Volume 95, Number 3, May–June 1990
Journal of Research of the National Institute of Standards and Technology

Contents

Articles

Conference Reports

News Briefs

Volume 95, Number 3, May–June 1990
Journal of Research of the National Institute of Standards and Technology

[J. Res. Natl. Inst. Stand. Technol. 95, 219 (1990)]

Operation of NIST Josephson Array Voltage Standards

Volume 95 Number 3 May–June 1990

Clark A. Hamilton,
Charles Burroughs,
and Kao Chieh

National Institute of Standards
and Technology,
Boulder, CO 80303

This paper begins with a brief discussion of the physical principles and history of Josephson effect voltage standards. The main body of the paper deals with the practical details of the array design, cryoprobe construction, bias source requirements, adjustment of the system for optimum performance, calibration algorithms, and an assessment of error sources for the NIST-developed Josephson array standard.

Key words: Josephson array; Josephson junction; superconductivity; voltage standard.

Accepted: January 2, 1990

1. Introduction

1.1 Physical Principles

In 1962 Brian Josephson derived an equation for the superconducting tunnel current that flows through a thin insulating barrier separating two superconductors [1]:

$$I=I_0 \sin\left(\frac{4\pi e}{h}\int V\,\mathrm{d}t\right). \qquad (1)$$

In this equation, I is the junction current, I_0 is the critical current (a constant of the junction), V is the junction voltage, and e/h is the ratio of the elementary charge to Planck's constant. When a dc voltage, V, is applied across the junction, eq (1) shows that the current will oscillate at a frequency $f=2eV/h$, where $2e/h \simeq 484$ GHz/mV. The very high frequency and low level of this oscillation make it difficult to observe directly. However, if an ac voltage at frequency f is applied to the junction, the junction's self-oscillation has a strong tendency to phase-lock to the applied frequency. During this phase lock, the junction voltage must equal $hf/2e$. This effect, known as the ac Josephson effect, is experimentally observed as a constant-voltage step at $V=hf/2e$ in the I-V curve of the junction. It is also possible for the junction to phase-lock to harmonics of f. This results in a series of steps at $V=nhf/2e$, as shown in figure 1.

1.2 History

Early experiments [2] showed that the Josephson voltage-frequency relationship implied by eq (1) is extremely precise. Initially these experiments used this relation to measure the ratio $2e/h$. It was soon realized that such measurements were limited by the accuracy of the voltage measurements. Thus, in 1972, NIST (then the National Bureau of Standards or NBS) adopted the value 483 593.42 GHz/V for $2e/h$ for the purpose of measuring voltage. Since then the NBS/NIST Legal Volt has been based on the ac Josephson effect. The Josephson volt, however, is not a fundamental derivation of the volt but rather a means of providing a very stable and reproducible voltage reference. In the International

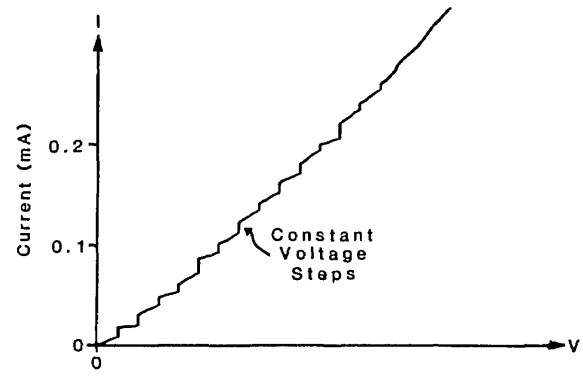

Figure 1. The I-V curve of a Josephson junction in a microwave field. The vertical steps are regions where the Josephson frequency $2e/h$ phase-locks to harmonics of the microwave frequency.

System of Units (SI), the volt is derived from a number of experiments that relate electrical and mechanical units. When the above value for $2e/h$ was first adopted in 1972, the uncertainty in realizing the SI volt was about 10 parts per million (ppm). Since then this uncertainty has been considerably reduced. As a result, an international agreement has been reached to define the Josephson voltage by the equation $V=nf/K_J$ with $K_{J-90}=483$ 597.9 GHz/V as the adopted value for the Josephson constant K_J. The new definition was effective on January 1, 1990 [3-4].

Although the ac Josephson effect provides a better voltage reference than standard cells, the first Josephson standards were difficult to use, mainly because a single junction produces a very low voltage—from 1 to 10 mV. Early Josephson voltage standards were unique systems, custom-built for national standards laboratories.

The accuracy of Josephson voltage standards improves substantially when many junctions are connected in series to generate a large voltage. This approach has been used to achieve a level of 100 mV from 20 individually biased junctions [5]. Extension of this approach to larger voltages rapidly becomes impractical because it is necessary to bias each junction onto one of the constant voltage steps shown in figure 1.

In 1977 Levinsen *et al.* suggested a method to avoid the multiple bias problem by using constant-voltage steps that cross the zero-current axis of the junction I-V curve [6]. These zero-crossing steps occur when highly capacitive junctions are exposed to microwave radiation at a frequency well above the junction's natural resonant frequency. Figure 2 is an example of an I-V curve with zero-crossing steps; an important feature is the lack of stable regions between the first few steps. Thus for small bias currents, the junction voltage must be quantized. With a common bias current at or near zero, the voltage across a large array of these junctions must also be quantized. With arrays of up to 19 000 junctions, quantized voltages above 10 V are possible. After more than 10 years of effort, the problems of fabrication, stability, and rf distribution are largely solved, and Josephson array voltage standards are a reality in many laboratories around the world [6–18].

2. Josephson-Array Voltage Standards

2.1 Chip Layout

The layout for a 1500-junction array is shown in figure 3. The rf-drive power is collected from a waveguide by a finline antenna, split four ways, and injected into four arrays of 375 series-connected junctions. The arrays are spaced 1 μm above a superconducting ground plane. Since the junctions are highly capacitive, they have a very low impedance at the microwave frequency. The array thus acts as a microstripline. Typical attenuation is about 0.15 dB/mm. Matched loads terminate each stripline so that each junction in the array receives the same level of rf drive. Addition of the dc voltages across the four arrays produces the 1-V output. Capacitors prevent the dc voltage from shorting through the rf distribution network. The rf drive is applied by inserting the finline end of the

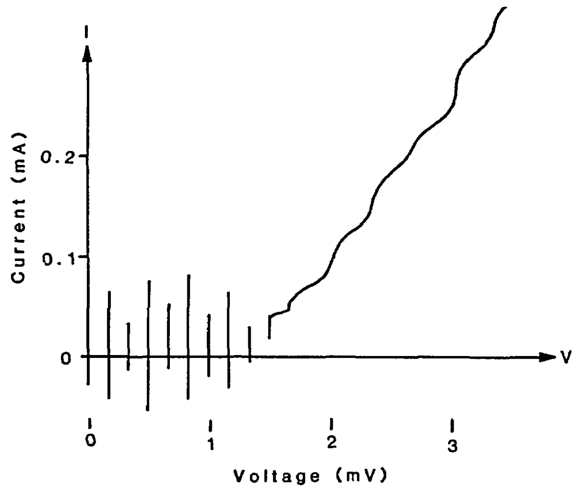

Figure 2. A single junction I-V curve showing constant voltage steps that cross the zero-current axis.

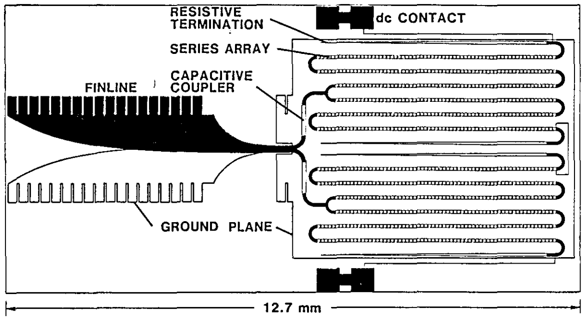

Figure 3. The layout of a typical Josephson-array chip.

chip into a slot parallel to the E-field in a WR-12 waveguide. The dc output appears across superconducting pads on the edge of the chip.

2.2 Operation

The operation of the array is illustrated in the *I*-*V* curves of figure 4. Figure 4a is a typical tunneling *I*-*V* curve for a single junction. This junction has a critical current of 360 μA and an energy-gap voltage of 2.7 mV. Figure 4b is the *I*-*V* curve of 2076 of these junctions connected in a series array; addition of the energy-gap voltages of all the junctions produces a current rise at 5.5 V. The upper horizontal branch of the curve consists of 2076 transitions which occur as the junctions switch to the energy gap in the order of increasing critical current. This branch of the *I*-*V* curve shows that the critical-current distribution varies from 270 to 340 μA for this array. When a 96-GHz current of about 15 mA is applied to a single junction, it develops constant-voltage steps in its *I*-*V* curve, as shown in figure 4c. Note that the steps below 1 mV cross the zero-current axis and that there are no stable regions between these steps. Figure 4d shows an *I*-*V* curve for the full array with 5 mW of rf drive (at the chip mount) at 96 GHz. This curve traces the envelope of about 15 000 constant-voltage steps that occur at 200-μV intervals from −1.5 to +1.5 V. In figure 4e, a section of this curve near 0.7 V is expanded to show nine individual steps.

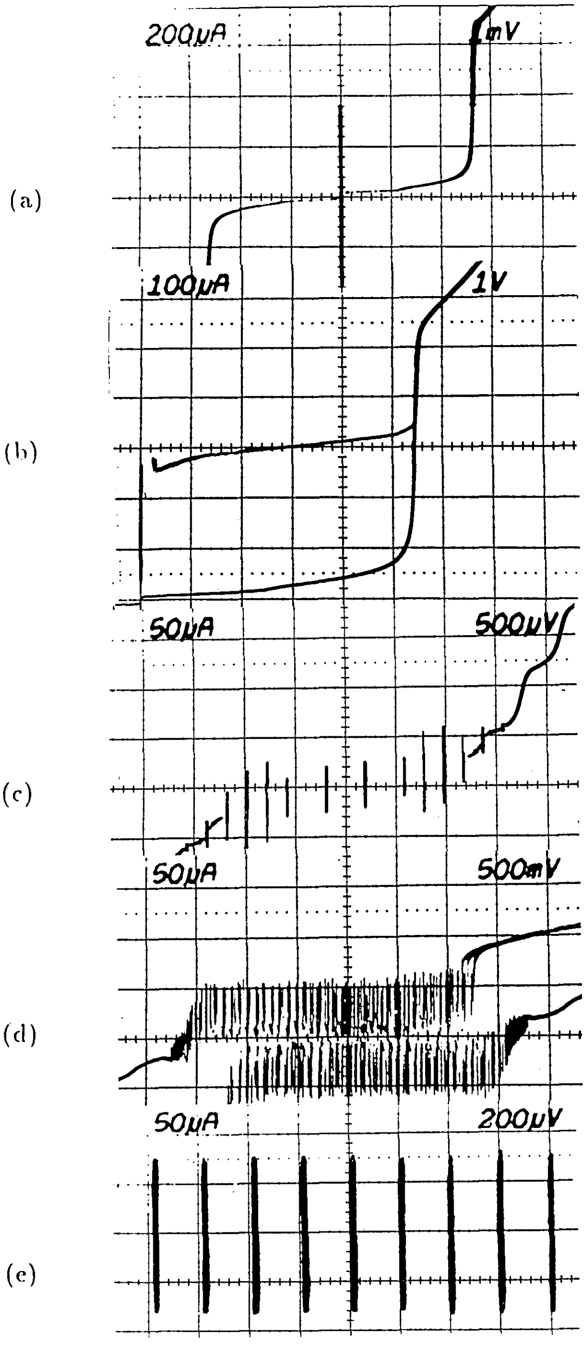

Figure 4. (a) A single-junction *I*-*V* curve, (b) an array *I*-*V* curve, (c) a single-junction *I*-*V* curve with applied rf, (d) an array *I*-*V* curve with applied rf, and (e) an expansion of curve (d) showing individual steps.

3. The Josephson-Array Voltage-Standard System

3.1 System Configuration

A block diagram of a typical voltage-standard system is shown in figure 5. The chip is mounted in a magnetically shielded cryoprobe and immersed in liquid helium. A Gunn diode, with an operating frequency in the range 70 to 100 GHz, provides microwave power to the chip. A microwave counter measures and phase-locks the Gunn diode frequency to an internal or external frequency reference. A dc-current source and a low-frequency triangle-wave generator provide current bias to the chip. The oscilloscope displays the bias current as a function of the array voltage. When the array is biased on a constant-voltage step, the oscilloscope displays a vertical line. If even one junction in the array is not biased on a step, the oscilloscope *I-V* display will have a slope which is easily detected on a suitably sensitive voltage scale, e.g., 10 μV/div. The voltmeter and frequency counter are connected via the IEEE-488 bus to a computer that can perform calibration, record-keeping, and diagnostic functions.

3.2 Cryoprobe

Figure 6 shows a typical cryoprobe on which Josephson-array voltage standards are mounted for cooling in liquid helium. Microwave power is delivered to the chip using a WR-12 band waveguide that has low-thermal and low-microwave loss. Typical microwave loss is 6 dB or less for a carefully cleaned waveguide. Dirt or corrosion in the waveguide can increase the attenuation by as much as 10 dB. A suitable waveguide can be made by using either a continuous section of 90-10 bronze or two sections of coin silver waveguide separated by 15 cm of internally gold-plated stainless steel waveguide. The latter must be constructed so that the stainless steel section will be located in the neck of the Dewar when the probe is fully submerged in the helium. The waveguide is plugged at the chip mount flange by a tapered dielectric plug or a thin polyethylene sheet between the flanges. The plug prevents thermal helium oscillations from developing inside the guide.

Although much more expensive, a dielectric waveguide can achieve an attenuation as low as 2 dB and negligible thermal loss. This makes it possible to keep the cryoprobe continuously immersed in a 100-L storage Dewar for as long eight weeks between refills.

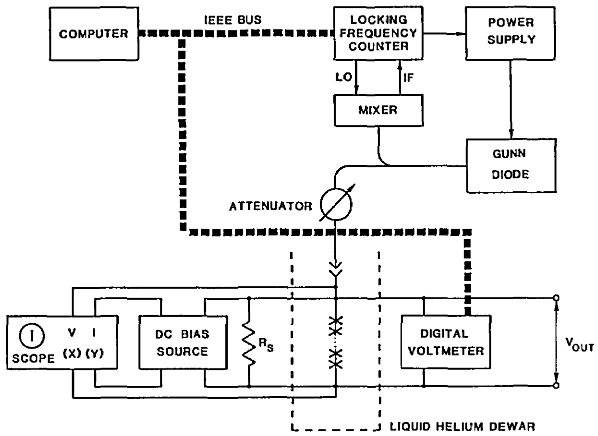

Figure 5. A block diagram of a Josephson-array voltage-standard system.

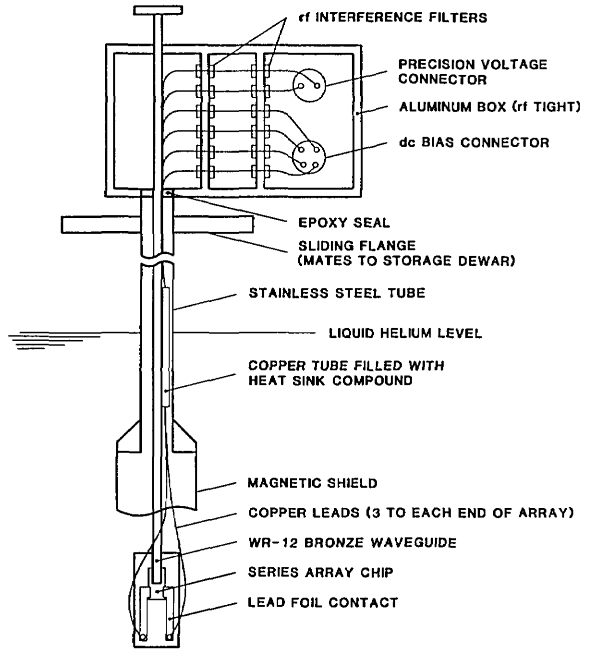

Figure 6. A typical cryoprobe used for cooling Josephson array voltage standards in a liquid-helium Dewar.

To prevent noise-induced transitions between constant voltage steps, the array chip must be completely covered by an rf and magnetic shield, and all connections to the chip must be through RFI filters at the probe top. These filters should have a minimum attenuation of 60 dB above 100 kHz and 100 dB above 1 MHz. If the array is to be connected directly to a DVM, it may be necessary to add additional low-frequency filtering to the reference output leads. To prevent ground loops, the microwave source and mixer must be isolated from the probe with a dc break that is made by removing the pins and separating the waveguide flanges at the top of the cryoprobe with a thin layer of polyethylene. The flanges are attached with nylon screws.

To minimize thermal voltage errors, the probe should be wired with thermocouple-grade copper wire that is bound to the waveguide with plumber's tape. A total of six wires, three to each side of the array, is typically used. Four wires are used to bias the array and to display its *I-V* curve; the other two wires supply the precise voltage output. The thermal voltage on the precise voltage leads may be checked by shorting the leads at the bottom end of the probe and measuring the voltage at the top connector as the probe is lowered into a Dewar of liquid helium. The voltage change after cooling should be less than 1 μV. Since there are six wires to the sample mount, performance can often be improved by selecting the pair with the smallest thermal voltage.

3.3 Bias Circuit

A suitable bias circuit, shown in figure 7, provides an output bias that is the sum of a triangle-wave sweep and a dc offset. The dc offset must be stable and adjustable at a level of about 200 μV. The output impedance is controlled by a 1-kΩ log-taper potentiometer. A pulse button provides the capability to momentarily increase the dc offset by about a factor of 3. This is often useful in achieving high-level, stable, array voltages. The bias current is measured by detecting the return current at the virtual ground input of a current mode amplifier. This means that current flowing into the RFI filter capacitance is not measured. The result is an *I-V* curve display (fig. 4) without the hysteresis caused by the filter capacitance and the associated distortion. The horizontal amplifier on the oscilloscope should have a differential input with a sensitivity of at least 100 μV. If this is not available, a differential preamplifier should be used.

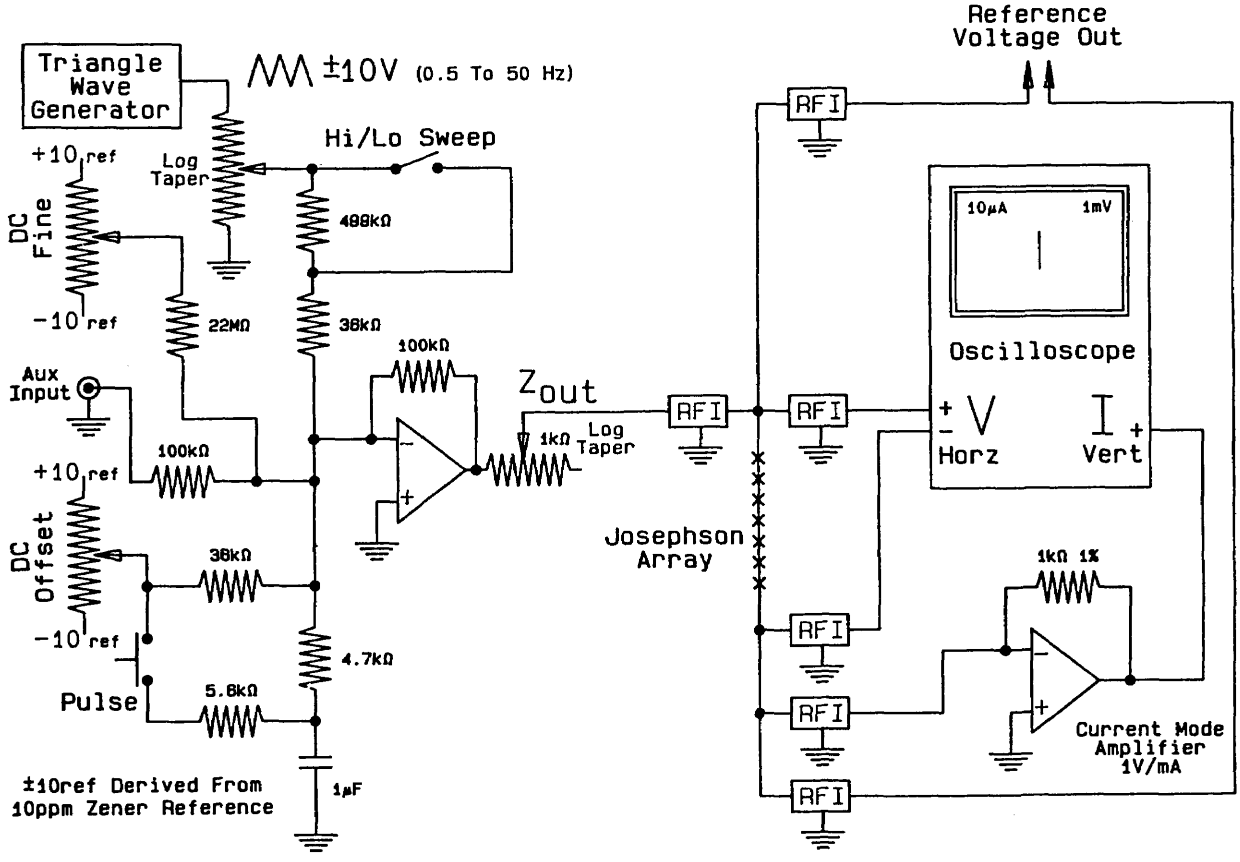

Figure 7. A circuit for supplying bias current to a Josephson array.

3.4 Grounding and Ground Leakage

Grounding of the array circuit at only one point (usually the return current side of the bias supply) is essential. In any case, most oscilloscopes have an input impedance to ground of not more than 1 MΩ. Thus, anything connected to the reference voltage output must be completely floating (more than 10^{10} Ω to ground). If there is a ground leakage path, the resulting current will cause voltage drops in the probe wiring resistance that lead to unpredictable errors. These errors are not detected or canceled by usual reversal procedures. A procedure for measuring leakage in the cryoprobe is described in section 6.4. Ground leakage and ac noise in reference standards can be eliminated by operating them in battery mode with line power completely disconnected. Leakage in the digital voltmeter (DVM) can be detected by performing calibrations with the DVM both at ground potential and at the array potential (1 V). If there is leakage in the DVM, these measurements will not agree.

4. Array Operation

4.1 Cooling and Warming

The probe should be cooled by lowering it slowly (over a period of about 15 min) into a liquid-helium Dewar. There should be no connections to the probe during the cooling process. The bias connections must be checked to ensure that the bias voltage is set to within 2 mV of 0 V. Once the probe is fully immersed in the helium and the bias level is verified, the bias leads can be connected. Failure to follow this procedure may lead to a number of problems caused by trapped magnetic flux in the array as described in section 4.2.

When the cryoprobe is removed from the Dewar, the Josephson array must be carefully warmed to avoid condensation on the chip. Any condensation on the chip or trapped inside the shield may lead to premature chip failure. Another approach is to store the probe with the chip mount raised into the neck of the Dewar. This is very safe for the chip but increases the chance of condensation in the waveguide. Unless a dielectric waveguide is used, storing the chip immersed in the liquid helium may cause excessive helium loss due to the thermal conductivity of the metal waveguide.

4.2 Array *I-V* Curve

Successful operation of a Josephson array demands careful adjustment of the dc and rf bias controls. The first step in the tuning procedure is to sweep the array *I-V* curve over a voltage range which includes the combined energy gap voltage of all of the junctions. This is typically ±10 V for a 3000 junction array. (For very large arrays designed to reach 10 V, there is usually a maximum voltage limit which will prevent observation of the combined energy gap voltage.) A source impedance of 1 kΩ or greater produces the best display. With the microwave power turned off, the curve should be like that in figure 8. The mean value of the critical current, I_0, and the combined energy-gap voltage, V_g, should be recorded each time the chip is cooled. If V_g is lower than expected, the array may be partially shorted or it may not be at the 4.2-K operating temperature due to insufficient liquid helium. Changes in I_0 may indicate moisture damage.

The array must be checked for trapped magnetic flux or junction failures. These problems can be observed by increasing the voltage sensitivity to 50 mV/div. The lowest critical current should not be less than about 60% of the mean critical current, as shown in figure 9. One or more junctions with small critical currents will result in small and unstable steps in the array *I-V* curve. Figure 10 is an example of an *I-V* curve in which about 35 junctions have reduced critical currents due to trapped magnetic flux. This usually is caused by cooling the array with the bias leads connected or by connecting the bias leads when the bias voltage is not set to zero. Trapped flux can be removed by raising the probe to warm the chip above the transition temperature (as indicated by a linear *I-V* curve), disconnecting all leads to the array, and then recooling. If a low critical current is not cured

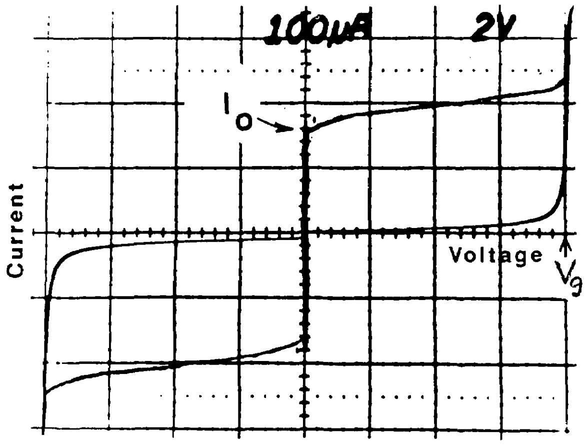

Figure 8. The full *I-V* curve of a typical Josephson array.

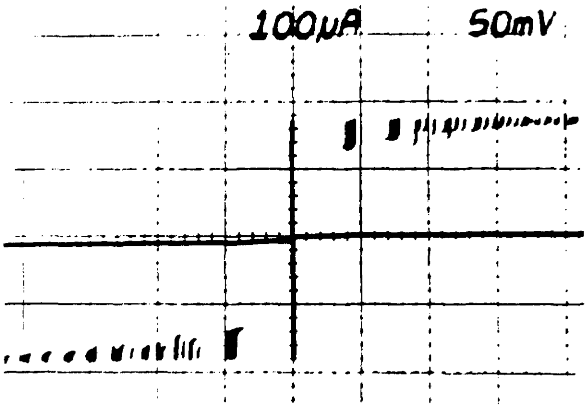

Figure 9. A typical array *I-V* curve with no trapped magnetic flux.

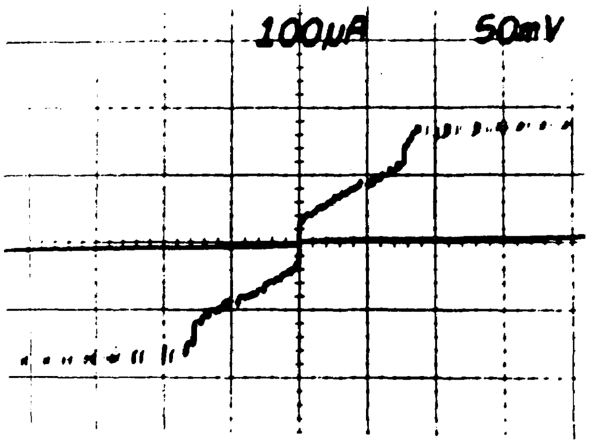

Figure 10. An array *I-V* curve with reduced critical currents caused by trapped magnetic flux.

by this process, it is probably caused by a junction failure. Such a failure will prevent the array from producing stable steps.

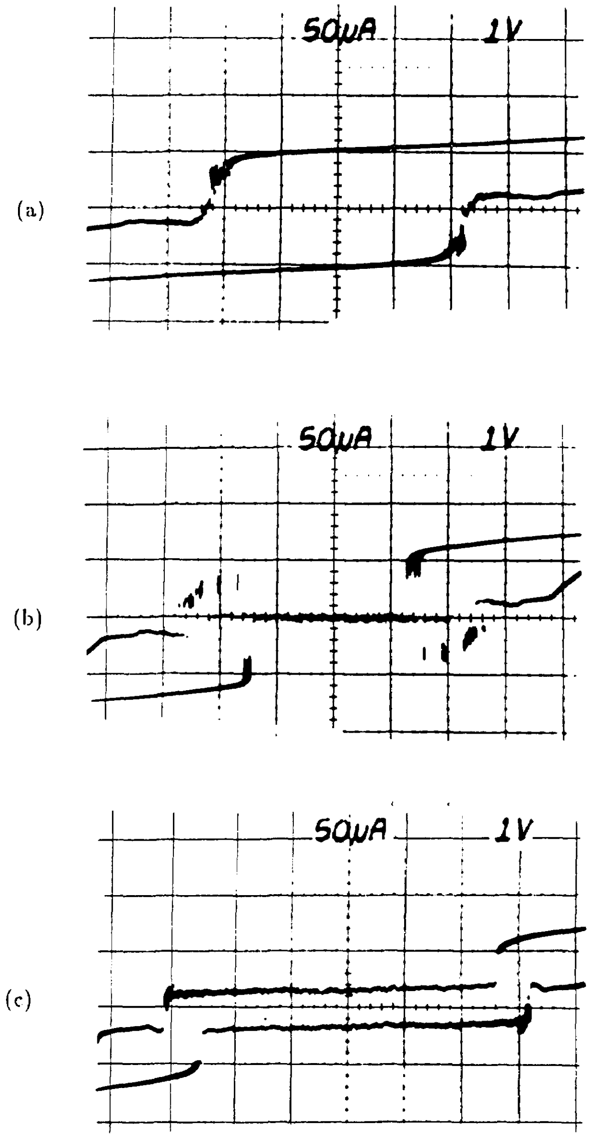

Figure 11. Typical array *I-V* curves for (a) low, (b) medium, and (c) high rf power levels.

4.3 Optimizing the Power and Frequency

Proper operation of a Josephson-array voltage standard requires the selection of a frequency where the array and microwave source work well together. The microwave power and frequency must be adjusted to obtain an *I-V* curve like those shown in figure 11. The important features of these curves are (1) they encircle the desired operating voltage on the voltage axis, *e.g.*, 1 V, and (2) the center part of the upper and lower branches of the curve are reasonably flat. The area encircled by these curves is an indication of the voltage range over which stable steps can be found. From top to bottom, the three curves show how the *I-V* curve evolves as the power is increased. Figure 11a illustrates stable steps to about 2 V; figure 11b, to about 2.5 V; and figure 11c, to about 3 V. The vertical spread of the curve can depend on the source impedance and sweep rate; it does not necessarily indicate the step amplitudes. Figure 12 shows the array *I-V* curve when the microwave power is too high. In this case, the steps are small and unstable. In figure 13, the microwave power is too low to generate stable steps above about 0.5 V. The best way to set the frequency is to adjust the power to obtain a curve like that in figure 13 (steps to about

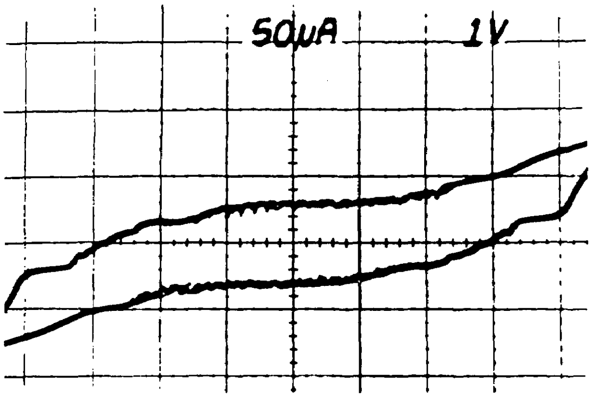

Figure 12. An array *I-V* curve showing the effect of too much rf power.

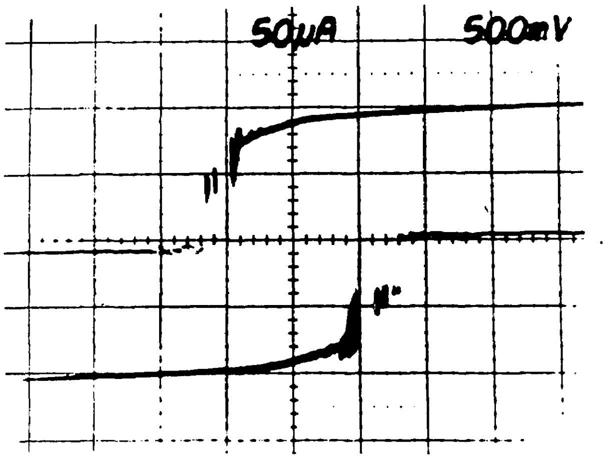

Figure 13. An array *I-V* curve showing the effect of too little rf power.

0.5 V) and then tune the frequency to maximize the width encircled on the voltage axis. The power can then be set to obtain a result like that in figure 11.

4.4 Setting the Array Voltage

When the array is used to calibrate a secondary reference, it is desirable to match the array and reference voltages as closely as possible. This is done by choosing appropriate values of n and f in the array voltage equation $V_a=nf/K_J$. The value of f is set by the frequency stabilization loop of the microwave source. The bias supply is used to force the array to the proper quantum voltage integer, n as follows: Once the frequency and power have been set as described above, the bias impedance is set to about 20 Ω, and the dc offset is set to force the array to a voltage near the desired final value. The *I-V* curve should then be observed with 1-mV sensitivity by using either ac coupling or a dc offset on the voltage amplifier. Figure 14 shows the ideal result: a small ac sweep causes the array to switch among about 25 steps. The power can now be fine tuned to obtain maximum step heights. In general, the steps grow larger and become unstable as the power is reduced below the optimum value. A typical result when the power is too low is shown in figure 15. Although the steps are very large, some junctions are being biased onto resistive portions of their *I-V* curves as seen in the sloped regions on the right side of the figure. If the power is too high, the steps are small and unstable, with sloped regions between them, as shown in figure 16. If there is trapped magnetic flux, the steps will be small at all power levels. Figure 17 shows a situation in which the *I-V* curve of a single junction with trapped flux appears at many points along

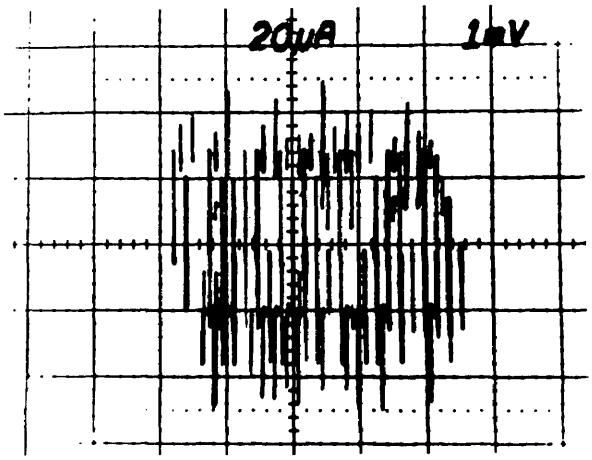

Figure 14. An ideal *I-V* curve display of quantum voltage steps.

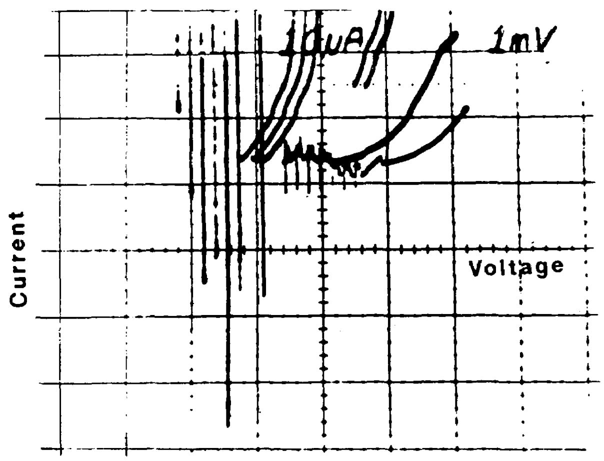

Figure 15. An expanded array *I-V* curve showing the effect of too little power.

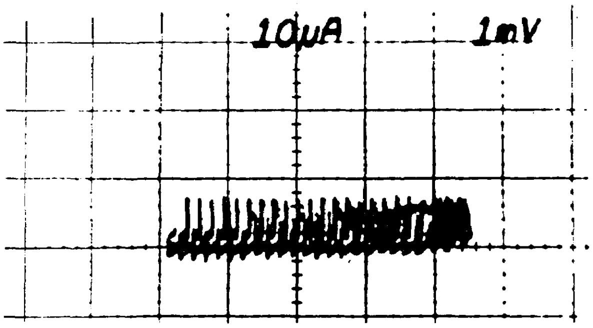

Figure 16. An expanded array I-V curve showing the effect of too much rf power.

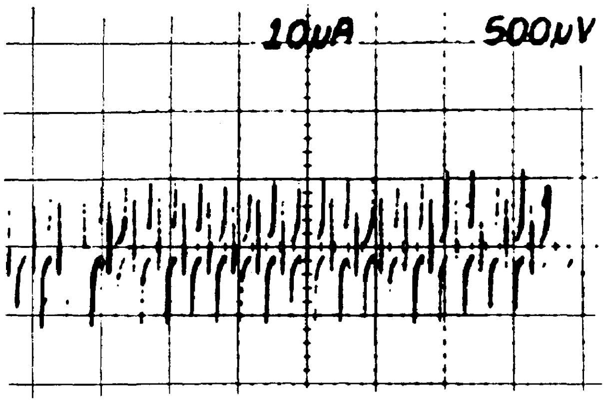

Figure 17. An expanded array I-V curve showing the effect of trapped magnetic flux.

the voltage axis. The changing offset of this curve is caused when other junctions in the array switch between steps.

Once the optimum power and frequency adjustments have been made, a single quantum voltage step is selected by reducing the ac sweep to about 10 μA. With a 15-Ω source impedance, any one of about six steps is selected at random. There are several ways to force the array to a specific step. For most arrays, an effective method is to reduce the sweep and bias impedance to minimum values. This may result in enough current noise to cause the array to switch among a few steps. The dc offset should then be adjusted to make the average array voltage as close as possible to the desired value, usually within 0.2 mV. When the bias impedance is increased, the array is very likely to lock onto the desired step. If increasing the bias impedance causes the bias point to move away from the $I=0$ axis, severe ground leakage probably exists somewhere, and any measurements are questionable. Some arrays go into a resistive state when the bias impedance is reduced. This may indicate that the operating frequency or power should be adjusted or that the array itself is marginal. Momentarily pulsing the bias voltage to a few volts above the desired value or turning the microwave power to zero may put the array back into the quantized voltage state.

Another method of selecting steps is to set the bias impedance to about 20 Ω and the sweep level to cause switching among about 25 steps, as in figure 14. Then set the dc offset to center the display on the desired step. When the sweep amplitude is reduced, the array is likely, after a few tries, to lock onto the desired step. Once the desired step is found, increasing the bias impedance to about 1 kΩ reduces the bias source current noise and improves the step stability.

5. Calibrations with an Array System

The most common use of a Josephson array is the calibration of a secondary reference standard, usually a Zener diode. Weston cells can be directly calibrated but the possibility of current transients caused by switching in the array makes this a risky procedure. Calibrations are typically done by putting the array and secondary reference in series opposition and measuring the difference voltage with a sensitive DVM. If the DVM has a gain error, E_g, its contribution to the calibration error will be $E_g\ (V_a - V_r)$. Thus, the error will be minimized by matching the array voltage, V_a, to the reference voltage, V_r, as closely as possible. Since the quantum voltage number, n, and the frequency, f, can be set, it is possible to obtain a nearly perfect null, thus eliminating any contribution from the DVM gain error. However, modern eight-digit DVMs are so accurate that it is not usually necessary to match V_a and V_r to less than a few millivolts. This means that any frequency can be used and any quantum step within a few millivolts of null is sufficient. This relaxation of the null requirement necessitates occasional calibrations of the DVM against the array but substantially simplifies the calibration procedure.

To find the array voltage, $V_a = nf/K_J$, it is necessary to determine the frequency, f, and the step number, n. The frequency is determined by phase-locking the microwave source to an accurately known frequency standard. The step number, n, is calculated from a knowledge of the difference voltage, V_{dvm}, and an estimate of the reference voltage, V_e, as follows: Assume that the DVM is connected so that $V_{dvm} = V_a - V_r$. Then n is given by

$$n = \mathrm{Round}[(K_J/f)(V_{\mathrm{dvm}} + V_e)], \qquad (2)$$

where "Round" means rounded to the nearest integer. The array voltage can then be calculated in the usual way; that is, $V_a = nf/K_J$. This procedure yields the correct value of n and V_a as long as the estimate V_e is within 50 μV of the actual reference voltage, V_r.

This procedure is more complicated than measuring the array voltage directly with the DVM, but it is much more convenient because it is not necessary to switch the array output to the DVM terminals. Such switching often induces a change in the step number, n.

In practice, there are always thermal voltages and offsets in the zero point of the DVM; these lead to errors in the measured difference voltage, V_{dvm}. If the offset and thermal voltages are stable, the resulting errors can be eliminated by making a second measurement in which the reference voltage and quantum number, n, are reversed. When these results are averaged, the thermal and meter-offset voltages cancel. A third measurement can be used to correct for first-order drift in the thermal and meter-offset voltages. More complex procedures involving further reversals of the reference or the DVM generally do not significantly improve the results.

5.1 Calibration Algorithm

The flow charts in figures 18 through 20 show a typical computer algorithm for calibrating reference standards. This algorithm has the following features:

1. The final uncertainty is controlled by a parameter, N, that specifies the number of difference readings to be averaged.
2. Any of about a hundred steps near the null point may be used for the measurement.
3. Spontaneous switching between steps is automatically accounted for during the measurement.
4. Frequency drift is tolerated with a corresponding increase in uncertainty.
5. The DVM and thermal offsets and first-order drifts are fully compensated.

The algorithm assumes that the DVM has a gain error, ϵ, less than 10 ppm. The DVM and thermal offsets and drifts are modeled by a combined offset voltage, V_0, and drift rate, m. The array and reference are first connected in series opposition so that

$$V_{\mathrm{dvm}} \simeq V_a - V_r + V_0 + mt, \qquad (3)$$

where t is the elapsed time since the first measurement. The array voltage, V_a, is then adjusted within a few millivolts of V_r and values of V_{dvm} are obtained. Each value is checked for consistency (± 2 μV) with the two previous values and then used to compute a data point,

$$V_i = V_a - V_{\mathrm{dvm}}. \qquad (4)$$

The elapsed time, T_i, is also recorded. The consistency check rejects readings affected by step transitions and enables a good data set to be obtained even when the array makes occasional transitions between steps. After N values of V_i and T_i have been obtained, the reference voltage and array bias are reversed and $2N$ more values of V_i and

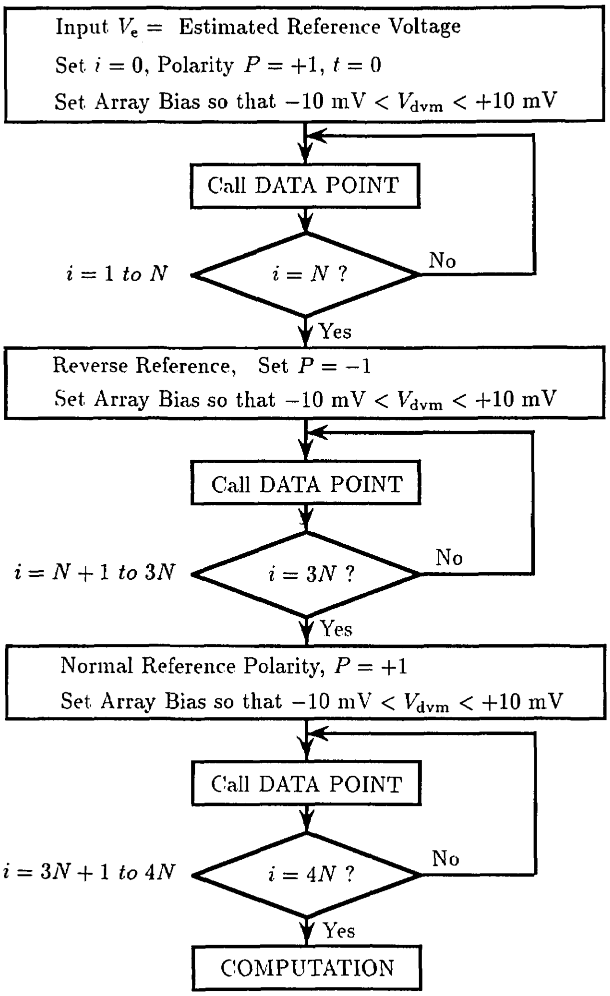

Figure 18. The flow chart for an algorithm used to calibrate a reference standard against a Josephson array.

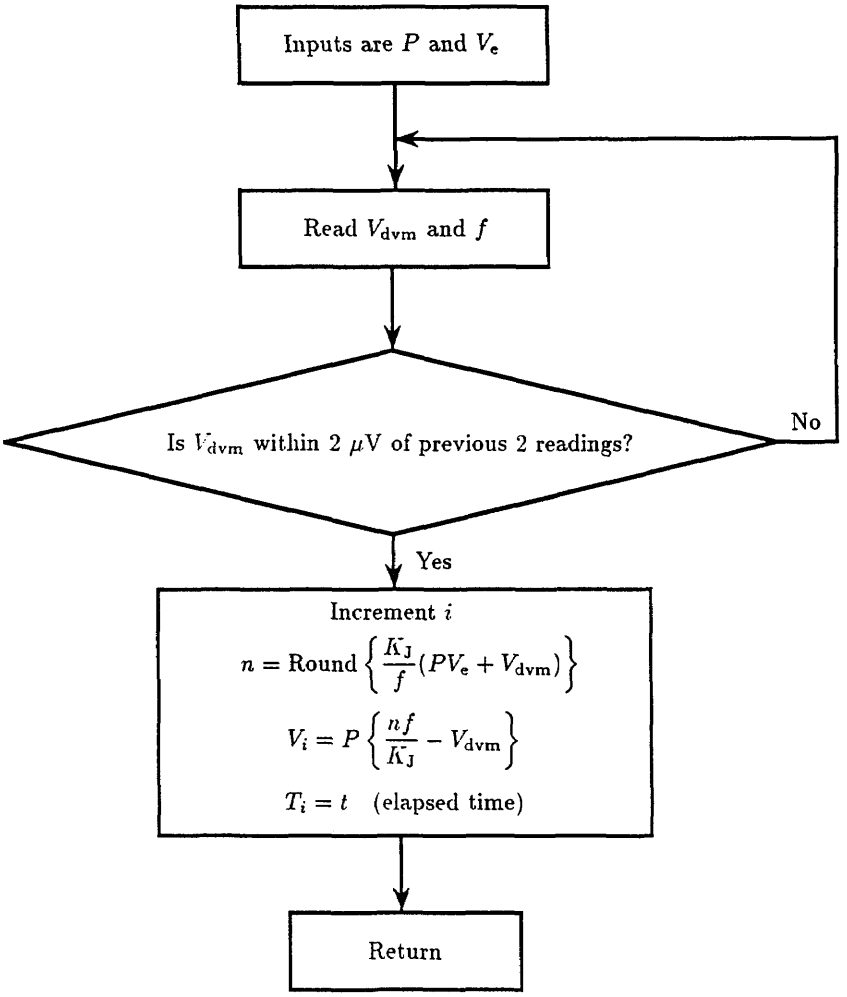

Figure 19. The flow chart for a subroutine used to obtain a single measurement of the reference voltage.

T_i are obtained. Finally, N more values of V_i and T_i are obtained with the original configuration. Figure 21 shows a typical data set obtained using $N = 10$.

In the computation flow chart of figure 20, the summation signs refer to data obtained with normal and reverse reference polarity and have the following definitions:

$$\sum_{\text{norm}} = \sum_{i=1}^{i=N} + \sum_{i=3N+1}^{i=4N}, \tag{5}$$

$$\sum_{\text{rev}} = \sum_{i=N+1}^{i=3N}, \tag{6}$$

$$\sum_{\text{all}} = \sum_{i=1}^{i=4N}. \tag{7}$$

A least-squares algorithm is used to compute values of $V_r - V_0$ and m that fit the $2N$ normal-polarity data points, V_i and T_i, with minimum error. This establishes the offset and drift line shown in figure 21. Reverse-polarity data are then used to estimate V_r and V_0.

The uncertainty due to reference and DVM noise is calculated from the differences between the measured data and the linear fit of figure 21. A standard deviation of the mean, σ_{norm}, is calculated for the normal data and σ_{rev} for the reverse data. The uncertainty in the value of V_r is calculated as the root-sum-square of σ_{norm} and σ_{rev}.

It is very important to reverse the array voltage by reversing the bias rather than by using a reversing switch. Any procedure that does not reverse the array quantum number, n, will not cancel the approximately 1-μV thermal voltage in the probe wiring.

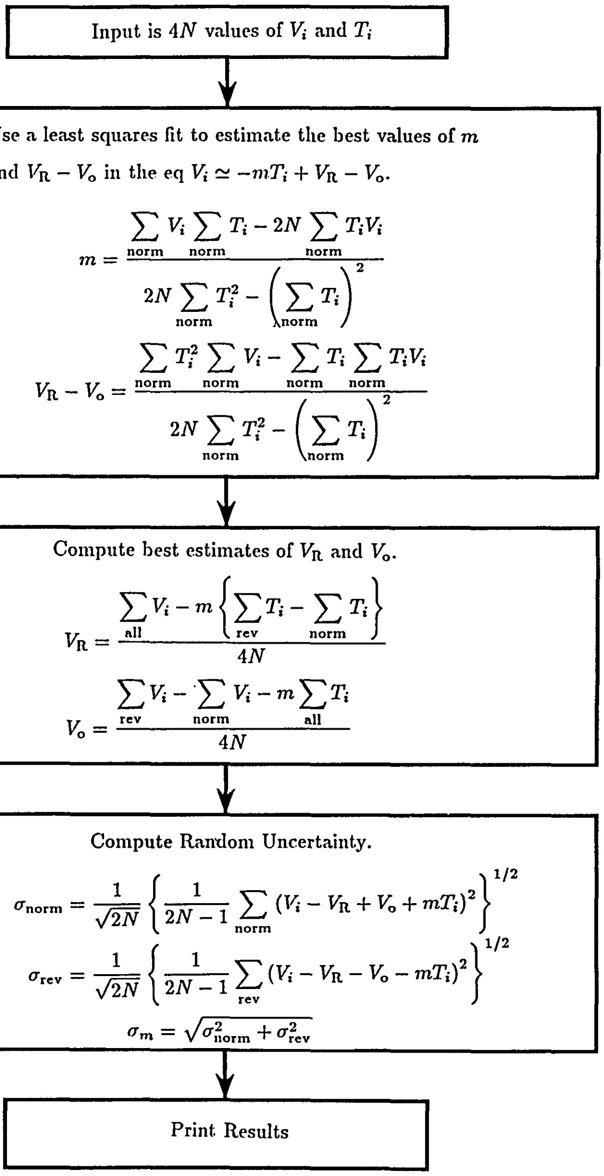

Input is $4N$ values of V_i and T_i

Use a least squares fit to estimate the best values of m and $V_R - V_o$ in the eq $V_i \simeq -mT_i + V_R - V_o$.

$$m = \frac{\sum\limits_{\text{norm}} V_i \sum\limits_{\text{norm}} T_i - 2N \sum\limits_{\text{norm}} T_i V_i}{2N \sum\limits_{\text{norm}} T_i^2 - \left(\sum\limits_{\text{norm}} T_i\right)^2}$$

$$V_R - V_o = \frac{\sum\limits_{\text{norm}} T_i^2 \sum\limits_{\text{norm}} V_i - \sum\limits_{\text{norm}} T_i \sum\limits_{\text{norm}} T_i V_i}{2N \sum\limits_{\text{norm}} T_i^2 - \left(\sum\limits_{\text{norm}} T_i\right)^2}$$

Compute best estimates of V_R and V_o.

$$V_R = \frac{\sum\limits_{\text{all}} V_i - m\left\{\sum\limits_{\text{rev}} T_i - \sum\limits_{\text{norm}} T_i\right\}}{4N}$$

$$V_o = \frac{\sum\limits_{\text{rev}} V_i - \sum\limits_{\text{norm}} V_i - m\sum\limits_{\text{all}} T_i}{4N}$$

Compute Random Uncertainty.

$$\sigma_{\text{norm}} = \frac{1}{\sqrt{2N}}\left\{\frac{1}{2N-1}\sum_{\text{norm}} (V_i - V_R + V_o + mT_i)^2\right\}^{1/2}$$

$$\sigma_{\text{rev}} = \frac{1}{\sqrt{2N}}\left\{\frac{1}{2N-1}\sum_{\text{rev}} (V_i - V_R - V_o - mT_i)^2\right\}^{1/2}$$

$$\sigma_m = \sqrt{\sigma_{\text{norm}}^2 + \sigma_{\text{rev}}^2}$$

Print Results

Figure 20. A flow chart of the calculation used to correct the calibration for thermal and DVM offsets and their first-order drifts.

6. Error Budget

Proper use of a Josephson-array voltage standard requires a careful assessment of all significant sources of error. This section develops an error budget appropriate to calibration of a 1-V reference standard that uses the calibration algorithm shown in figures 18 through 20. Both random and systematic errors must be considered. Random errors are obvious because they result in day-to-day fluctuations in calibration results. Even if the origin of the fluctuation is not known, the resulting uncertainty can be determined from a statistical analysis of the data. Systematic errors are more subtle because they generate a fixed or slowly drifting offset from the true value. Estimating the magnitude of systematic errors generally requires some special measurement procedure.

6.1 Difference-Voltage Measurement Noise

The dominant error in calibrations performed with a properly tuned Josephson voltage standard is the random noise of the difference-voltage measurement. Noise in the DVM and the reference standard combine to generate an uncertainty in the

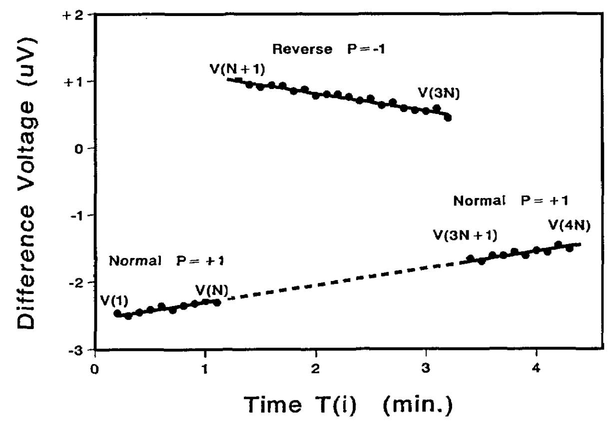

Figure 21. The data accumulated in a typical calibration of a reference standard.

final calculation of the reference value. This random error, E_n, is computed as shown in the algorithm of figure 20. Typical Zener reference calibrations at the 1-V level, using about one-minute averaging times for each of the normal and reverse measurements, should have 1σ E_n uncertainties of about 0.02 ppm.

6.2 DVM Gain and Linearity Errors

In a typical reference calibration with a Josephson standard it is inconvenient and unnecessary to match the array and reference voltages exactly. Thus, any error in the difference-voltage measurement results in an error in the final reference value. In addition to noise, DVMs have linearity and gain errors. At the low levels typically used in the difference-voltage measurement, the DVM linearity-error specification is a fixed percentage of full scale, and the actual error typically fluctuates randomly from one digital code to the next [18]. As a result of noise, the difference-voltage measurement is averaged over many digital codes. Thus, at the low level of the difference measurement, linearity errors are indistinguishable from DVM noise and are automatically included in E_n.

If the DVM gain, G, is not exactly 1, the error in the difference voltage is $(G-1)V_{\rm dvm}$, and this leads to an error, $E_{\rm d}$, in the reference value, $V_{\rm r}$, given by

$$E_{\rm d}=(G-1)\frac{V_{\rm dvm}}{V_{\rm r}} \tag{8}$$

For example, if the difference voltage is 1 mV and $G=1.000\,010$ (10 ppm error), the resulting error in a 1-V calibration is 0.01 ppm. The principal sources of uncertainty in G are the uncertainty in the initial DVM calibration and drift in the internal DVM voltage reference. Thus, the gain error, $E_{\rm g}$, can be written as a time-scaled quantity,

$$E_{\rm g}=G-1=E_{\rm cl}+D_{\rm v}t, \tag{9}$$

where $E_{\rm cl}$ is the DVM calibration uncertainty, $D_{\rm v}$ is the drift-rate specification of the DVM, and t is the elapsed time since the last calibration. The term $E_{\rm g}$ in eq (9) can be substituted for $(G-1)$ in eq (8) to give

$$E_{\rm d}=(E_{\rm cl}+D_{\rm v}t)\frac{V_{\rm dvm}}{V_{\rm r}}. \tag{10}$$

For a good-quality DVM, $D_{\rm v}$ is 10 ppm per year or less. This specification generally applies just after a self-calibration. If the DVM is subjected to the self-calibration daily, has its internal reference calibrated monthly, and the difference voltages are kept below 10 mV, then $E_{\rm d}$ will not add significantly to the total reference calibration uncertainty.

This point is illustrated in figure 22, which shows five sets of consecutive calibrations of a 1.018-V Zener reference standard all performed within 2 h. In the first three sets, the reference and Zener voltages were matched within 1, 5, and 10 mV. Since there is no apparent correlation between the reference values and the difference voltage, we can conclude that, with the DVM used in this measurement, difference voltages up to 10 mV can be tolerated without introducing significant errors. The fourth set of data in figure 22 shows three calibrations in which the array was deliberately forced to switch between steps many times during the

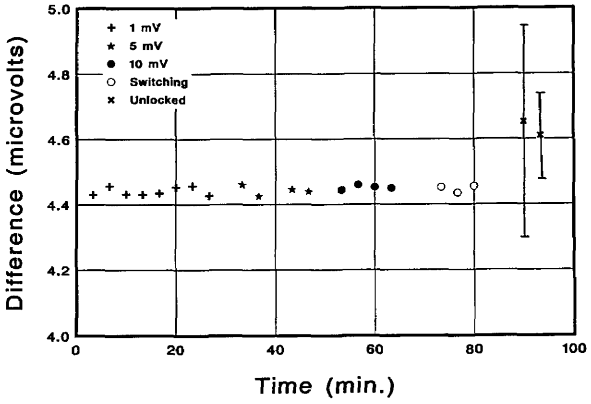

Figure 22. Calibration results of a 1.018-V Zener reference standard showing the effects of the difference-voltage amplitude, step stability, and frequency stability.

measurement. This slows the measurement somewhat but has very little effect on the final result. The 1σ uncertainty on the first four data sets is just slightly larger than the points themselves. This uncertainty results from a combination of Zener and DVM noise. In this case it is dominated by noise in the 1-V Zener reference.

The last two calibrations were made with the frequency source unlocked. The frequency typically drifted 5 ppm during these measurements. However, since the frequency is measured for each data point, the effect of the drift on the final result is much less than 5 ppm. Since the frequency and voltage are measured at slightly different times, frequency fluctuations result in an increase in the random noise of the difference voltage, E_n. Calibrations performed in the unlocked mode have an uncertainty that is highly dependent on the frequency stability. A typical value is about 0.3 ppm.

6.3 Frequency Error

Any error in the frequency reference that is used to measure and stabilize the microwave source translates directly into a voltage error. Josephson-array standards commonly rely on a precise quartz crystal frequency reference that is periodically calibrated. In this case, the fractional systematic error contributed by the frequency reference is

$$E_f = E_{c2} + D_f t, \tag{11}$$

where E_{c2} is the error in the initial calibration, D_f is the drift specification of the crystal, and t is the elapsed time since the frequency calibration. For example, if $E_{c2} = 10^{-10}$ and $D_f = 2 \times 10^{-10}$ per d, about three months after a frequency calibration, the frequency error is comparable to the noise error.

In an automated system, time-scaled errors E_f and E_d should be incorporated in the calibration results so that their effects cannot be ignored.

6.4 Leakage Currents

Significant errors may occur if there is leakage current between the array voltage leads or from these leads to ground. Leakage current causes a voltage drop across the resistance, R_p, of the probe filters and results in an error that is not corrected by the reversal process. Two kinds of leakage must be considered: resistive leakage and dielectric absorption. Resistive leakage can result from fingerprints on the filter elements, solder flux, or faulty capacitor dielectric. Dielectric absorption is a time-dependent process caused by a slow change in the orientation of electric dipoles in the filter elements.

Both resistive leakage and dielectric absorption sources may be checked with the circuit shown in figure 23. When a large resistance, R_s (typically 200 kΩ), is placed in series with the reference standard, the effects of leakage currents are magnified about 10 000 times. With the reversing switch S2 open, the DVM reads the reference voltage. If the DVM reading changes as a function of the position of switch S1, then ground-leakage current probably exists in the DVM. If the change is more than 10 μV, the DVM should be repaired or replaced.

When S2 is closed, any leakage current in the probe wiring causes an easily detected voltage drop in the DVM reading. A time plot of the DVM reading is shown in figure 24, first with the switch open, then in the (+) position, and finally in the (−) position. During these measurements, motion around the apparatus must be minimized because it induces capacitive currents that add considerable noise to the signal.

The systematic error due to cryoprobe leakage is calculated as follows: Let the deviation of the DVM voltage from the open switch voltage be ΔV. The leakage current is then given by $I_L = \Delta V / R_s$. When the probe is used with an array, this leakage current generates a normalized error,

$$E_l = \frac{I_L R_p}{V_r} = \frac{\Delta V R_p}{V_r R_s}, \tag{12}$$

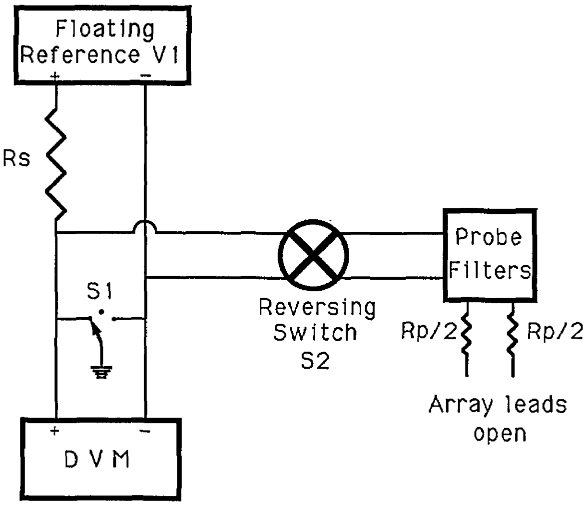

Figure 23. A circuit for measuring leakage currents in the cryoprobe.

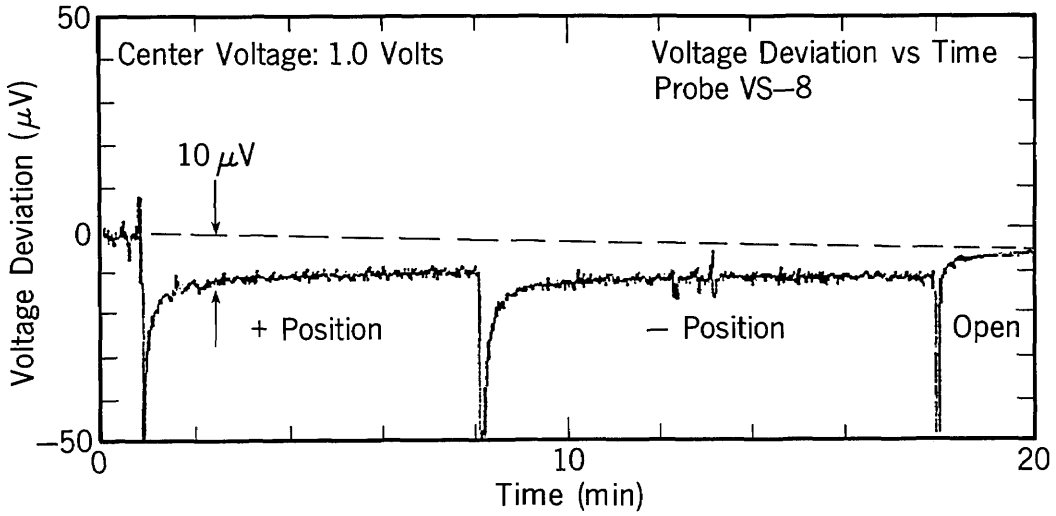

Figure 24. A plot of the DVM voltage vs. time generated using the circuit of figure 23. This plot is used to measure leakage and dielectric absorption in the cryoprobe.

where V_r is the reference voltage used in the leakage-current measurement. It is convenient to choose $R_s=10^4\ R_p$ since this makes ΔV exactly 10^4 times the actual error voltage. Figure 24 is an example of the result of this procedure for a probe with $R_p=20\ \Omega$ and $R_s=200\ \mathrm{k}\Omega$. The large spikes at the reversal points are caused by the current required to charge the filter capacitors. The exponential response is due to dielectric absorption and demonstrates that at least 20 s is required between a reversal and the beginning of a difference voltage measurement. The offset of about 10 μV from the open-switch voltage indicates that the error due to probe leakage is about $10\ \mu\mathrm{V}/10^4=1$ nV. Most of this leakage is contributed by the filter elements. For the specific results shown in figure 24, this error does not contribute significantly to the total uncertainty.

Leakage current in the leads connected to the reference standard will result in a voltage drop across the internal resistance, R_r, of the standard. The fractional error in the reference voltage is R_r/R_l where R_l is the leakage resistance. Since R_r is typically about 1 kΩ, leakage resistance greater than $10^{12}\ \Omega$ is required to keep this error below 1 part in 10^9. This can be easily achieved by using an appropriate reversing switch, insulated wire, and by floating the reference standard. The error caused by the leakage resistance R_l can be evaluated with the same procedure used to determine the probe leakage error as described above. Leakage current errors should be checked a few times a year and every time the precise voltage wiring is changed.

6.5 Uncorrected Thermal Offsets

Any thermal voltages in the wiring between the reversing switch and the reference standard are not corrected in the reversal process described in section 5. For this reason, very low thermal wire should be used and the distance between the reversing switch and the reference standard should be as short as possible. Uncorrected thermal voltages may be divided into a constant part and a part that may change with each switch operation. Both parts can be estimated by replacing the reference source with a low thermal short and connecting the DVM to the reversing switch output. The DVM should be set for a long averaging time so that voltages of a few nanovolts can be resolved. A series of $n \simeq 10$ DVM readings should then be taken to determine the 1σ uncertainty due to DVM noise, σ_{dvm}. If this is more than a few nV, then a longer DVM averaging time should be selected. Next, a series of $2n$ measurements with alternating switch polarities should be recorded. Let these be called V_{+i} and V_{-i}, $i=1...n$. If the 1σ values for V_{+i} and V_{-i}, σ_+, σ_-, are significantly greater than σ_{dvm}, then there is a fractional error E_r due to switch repeatability given by

$$E_r=\frac{1}{V_r}\sqrt{\left(\frac{\sigma_+ + \sigma_-}{2}\right)^2-\sigma^2_{\mathrm{dvm}}}. \tag{13}$$

The offset voltage, V_w contributed by the wiring is given by

$$V_w=\frac{1}{2n}\sum_{i=1}^{l} V_{+i}-V_{-i} \tag{14}$$

with an uncertainty given by

$$\Delta V_w = \sqrt{\frac{1}{n}(\sigma_+^2 + \sigma_-^2)}. \qquad (15)$$

The resulting fractional error in V_r is

$$E_w = \Delta V_w / V_r. \qquad (16)$$

If V_w is significant relative to ΔV_w, it should be subtracted from the reference voltage V_r. E_w should then be included in the combined uncertainty. Uncorrected thermal voltages are typically less than 10 nV, which is near the detection threshold.

There still remains the possibility of an error due to thermal voltages in the short or its connections. This error cannot be determined because any procedure to measure it requires altering the connections which may be the source of the error. Since it cannot be measured, this error is generally ignored.

6.6 Combined Uncertainty

If the previously described uncertainties are uncorrelated, the total 1σ uncertainty is obtained by adding them in quadrature:

$$E_{tot} = \sqrt{E_n^2 + E_d^2 + E_f^2 + E_l^2 + E_r^2 + E_w^2}. \qquad (17)$$

7. Common Problems

7.1 Inadequate Microwave Power

The frequency response of typical microwave sources and Josephson arrays is not very flat. Therefore, the power coupled into the array can often be substantially increased by tuning the source.

If the array response indicates that the available power is lower than expected from experience, it is likely that moisture has condensed in the waveguide. In this case, both the chip mount and microwave source must be removed from the probe and warm dry gas blown through the waveguide for about 5 minutes.

7.2 Erratic Calibration Results

A common mode of chip failure is the appearance of a slope on the *I-V* curve of the quantum-voltage steps. A slope occurs when a resistance develops in any part of the array circuit, usually as a result of corrosion or physical damage. Sloped steps can easily produce a scatter of up to 10 ppm in calibration results. Since this slope may have a value of 0.1 Ω or less, the maximum available voltage sensitivity (typically 10 μV) must be used to search the *I-V* curve for this problem.

If the polarity of the array, reference, or DVM does not conform to the assumptions made in the calibration algorithm, unpredictable errors up to about 70 ppm will occur in the calculated reference value.

The calibration algorithm computes the array step number based on an estimate of the reference voltage. If this estimate is in error by more than about 70 ppm, the computed step number will be wrong and the calibration result will therefore be meaningless.

7.3 Unstable Steps

Frequent switching between steps is, perhaps, the most common problem encountered with Josephson-array voltage standards. Good stability requires proper adjustment of the bias level, bias impedance, and microwave power, as discussed in section 4.3. Noise pick-up in the wires connected to the array can easily cause spontaneous transitions between the quantized voltage levels. Such noise is typically caused by switching of high-power equipment and by local radio transmitters. The "walkie-talkies" often used by service personnel can be a particularly uncontrollable and unpredictable source of interference. Usually, interference problems can be substantially reduced by careful shielding and grounding. In most environments, a shielded room is not necessary.

If the array is not fully immersed in liquid helium, it is likely to generate unstable steps. This possibility is easily checked by comparing the array energy-gap voltage, V_g, with its nominal value. A reduction of more than 5% indicates inadequate cooling.

Nonuniform critical currents in the array junctions also lead to unstable steps. This may be caused by trapped magnetic flux or the failure of one or more junctions. If the problem is not cured by warming and recooling the array, then a junction failure is the probable cause, and the array must be replaced. When care is taken to avoid physical damage and exposure to moisture, and thermal cycling is minimized, typical arrays have a lifetime of several years or more.

8. Acknowledgments

The authors gratefully acknowledge many helpful suggestions from Norman Belecki, Richard Steiner, Richard Harris, and Richard Kautz. None of this work would have been possible without the integrated-circuit process development efforts of Michael Cromar, Jim Beall, Ronald Ono, and Diane Go. Finally, we acknowledge the fabrication expertise of Frances Lloyd who has fabricated all of the Josephson array devices used at NIST and many other laboratories around the world.

About the authors: *Clark A. Hamilton, a NIST Fellow, is an electrical engineer in the Cryoelectronic Metrology Group of the Electromagnetic Technology Division. Charles Burroughs and Kao Chieh also work in this group, which is located at NIST in Boulder, Colorado. Charles Burroughs is an electrical engineer. Kao Chieh, a physicist, is a Visiting Scientist from the National Institute of Measurement and Testing in Chengdu, China.*

9. References

[1] Josephson, B. D., Phys. Lett. **1**, 251 (1962).
[2] Langenberg, D. N., Parker, W. H., and Taylor, B. N., Phys. Rev. **150**, 186 (1966).
[3] Taylor, B. N., J. Res. Natl. Inst. Stand. Technol. **94**, 2 (1989).
[4] Belecki, N. B., Dziuba, R. F., Field, B. F., and Taylor, B. N., NIST Tech. Note 1263, 1989.
[5] Endo, T., Koyanagi, M., and Nakamura, A., IEEE Trans. Instrum. Meas. **IM-32**, 267 (1983).
[6] Levinsen, M. T., Chiao, R. Y., Feldman, M. J., and Tucker, B. A., Appl. Phys. Lett. **31**, 776 (1977).
[7] Kautz, R. L., Appl. Phys. Lett. **36**, 386 (1980).
[8] Niemeyer, J., Hinken, J. W., and Meier, W., IEEE Trans. Instrum. Meas. **IM-33**, 311 (1984).
[9] Kautz, R. L., and Costabile, G., IEEE Trans. Magn. **MAG-17**, 780 (1981).
[10] Niemeyer, J., Hinken, J. H., and Kautz, R. L., Appl. Phys. Lett. **45**, 478 (1984).
[11] Hamilton, C. A., Kautz, R. L., Steiner, R. L., and Lloyd, F. L., IEEE Elec. Dev. Lett. **EDL-6**, 623 (1985).
[12] Niemeyer, J., Grimm, L., and Meier, W., Appl. Phys. Lett. **47**, 1222 (1985).
[13] Steiner, R. L., and Field, B. F., IEEE Trans. Instrum. Meas. **IM-38**, 296 (1989).
[14] Wood, B., Inglis, A. D., and Dunn, A. F., IEEE Trans. Instrum. Meas. **IM-38**, 302 (1989).
[15] Sakamoto, Y., Endo, T., Murayama, Y., and Sakuraba, T., IEEE Trans. Instrum. Meas. **IM-38**, 304 (1989).
[16] Jaeger, K. B., and Zack, C. A., IEEE Trans. Instrum. Meas. **IM-38**, 308 (1989).
[17] Hamilton, C. A., Lloyd, F. L., Chieh, K., and Goeke, W., IEEE Trans. Instrum. Meas. **IM-38**, 314 (1989).
[18] Goeke, W. C., Swerlein, R. L., Venzke, S. B., and Stever, S. D., Hewlett-Packard J. **40**, 22 (1989).

Volume 95, Number 3, May-June 1990
Journal of Research of the National Institute of Standards and Technology

[J. Res. Natl. Inst. Stand. Technol. 95, 237 (1990)]

The Calibration of dc Voltage Standards at NIST

Volume 95 Number 3 May-June 1990

Bruce F. Field

National Institute of Standards and Technology,
Gaithersburg, MD 20899

This document describes the procedures used at NIST to calibrate dc voltage standards in terms of the NIST volt. Three calibration services are offered by the Electricity Division: Regular Calibration Service (RCS) of client standard cells at NIST; the Volt Transfer Program (VTP) a process to determine the difference between the NIST volt and the volt as maintained by a group of standard cells in a client laboratory; and the calibration of client solid-state dc voltage standards at NIST. The operational procedures used to compare these voltage standards to NIST voltage standards and to maintain the NIST volt via the ac Josephson effect are discussed.

Key words: calibration services; dc volt; standard cells; voltage standards; Zener diode standards.

Accepted: February 23, 1990

1. Introduction

To maintain a "practical" unit of electromotive force (emf), that is, a representation of the volt as defined in the International System of Units (SI), standards laboratories may use one or more groups of electrochemical cells called standard cells[1]. Such cells are used as reference standards against which the emf of other cells or the electric potential difference of systems are compared. Typically, saturated cadmium-sulfate-type (Weston) cells are used when high accuracy, one part per million (1 ppm) or better, is required in maintaining a unit traceable to NIST. However, dc voltage standards based on solid-state devices are now available with stabilities approaching 1 ppm/yr. Such standards can be used to maintain and disseminate (transfer) a laboratory unit of voltage with accuracies approaching those obtainable with good saturated standard cells.

Standard cells are electrochemical systems composed of two dissimilar electrodes immersed in an electrolytic solution [1]. They are not intended to supply electric current and, therefore, are of different design from those electrochemical systems (e.g., storage batteries) which are intended for such purpose. The stability of the emf of the cell depends on the chemical equilibrium within the cell. Although the emf of a cell is highly reproducible and generally exhibits a fairly constant emf, it must be periodically recalibrated to eliminate the effects

---

[1] The dominant system of units used throughout the world to express the results of physical measurements is Le Système International d'Unites or International System of Units, abbreviated SI. The Consultative Committee on Electricity (CCE) of the International Committee of Weights and Measures believes that the appearance of creating of new unit system outside of the SI must be avoided. Thus, all "practical units of voltage" are to be viewed as representations of the (SI) volt. Further, the CCE believes that the representations of the volt of national standards laboratories are sufficiently close to the Si volt that it will rarely be necessary to distinguish between them and the SI volt. However, for clarity within this paper, the representation of the volt as maintained at NIST will be denoted as the NIST volt or V(NIST).

of long term drift. The frequency with which recalibrations are required is a function of the client's accuracy requirement, the number of cells used to maintain their volt, and the stability of their individual cells. This recalibration interval must be determined by the client laboratory based on their accuracy requirements and cannot be specified by NIST.

Presently available solid-state voltage standards contain at least one (and sometimes more) Zener-diode reference devices each of which develop an electric potential difference that is scaled using internal resistive dividers and low-noise amplifiers to produce a number of fixed-value output voltages in the range from 1 to 10 V. Outputs are typically provided at 1, 1.018, and 10 V, although the unscaled Zener voltage of about 7 V is also occasionally provided. These standards usually have their best stability at the Zener voltage (if available) or at 10 V rather than at the 1.018-V level of standard cells, as the scaling process from 10 to 1.018 V introduces additional uncertainty.

Calibration of dc voltage standards in terms of the NIST volt is accomplished via three services offered by the Electricity Division of the NIST. These calibration services are described briefly below, while the measurement approach, operational procedures, maintenance of the volt, and calibration uncertainties are described more fully in sections 2–5 of the paper. Additional details about the calibration services and their measurement procedures can be found in references [2] and [3].

1.1 Regular Calibration of Standard Cells

Clients may send standard cells to NIST for direct comparison to NIST cells which are in turn calibrated in terms of the NIST volt. Upon receipt of the standard, its cell emfs are compared directly to the NIST voltage standards on a daily basis and, after the emfs have stabilized, 10 additional comparisons are made. The averages of the cell emfs obtained from these comparisons are taken as the measured values of the cells. At the conclusion of the test a report is issued with a statement of the cell emf values and the estimated uncertainties for the emf values. These uncertainties apply only to the measurements made while the cells were at NIST. Since no additional components of uncertainty are included for transportation effects, long term drifts of the emfs, or measurement errors in the client's laboratory, such uncertainty components must be evaluated and included by the client as part of a complete analysis of the uncertainty of the standard.

1.2 Volt Transfer Program for Standard Cells

The Volt Transfer Program (VTP) is a measurement assurance program (MAP) designed to determine the difference between the unit of voltage maintained by a client laboratory using standard cells and the NIST volt. In this program, a group of NIST-owned cells in a thermoregulated enclosure is measured at NIST, shipped to the client laboratory, compared by the client to their reference cell group, and finally returned to NIST for concluding measurements. The measurements at the client laboratory are made using the client's measuring apparatus but using procedures specified by NIST. As data are taken they are transmitted to NIST and reduced and reviewed by NIST. At the conclusion of the test, a report is issued giving the difference between the client unit of voltage and the NIST volt as observed during the time of the test, along with an uncertainty for the difference. In this experiment, the uncertainty caused by the transportation of the standard cells is estimated and included in the final uncertainty.

1.3 Calibration of Solid-State Standards

Solid-state voltage standards to be calibrated by NIST must be calibrated at NIST (no MAP is presently available) and they must be complete instruments that continuously produce one or more stable voltages. When sent to NIST, these standards are compared indirectly to NIST standard cells which are in turn calibrated in terms of the NIST volt. NIST uses a specialized measuring/scaling system that automatically compares the output of any arbitrary voltage source within the voltage range of 1 to 10 V to a 1.018-V reference standard. Ten comparisons are made (one each working day) over a 2 week period as a minimum. At the conclusion of the test, a report is issued stating the values of the voltage outputs of the standard and their estimated uncertainties while the standard was at NIST. No additional uncertainty is included for transportation effects, long term drifts of the outputs, or measurement errors in the client's laboratory.

2. Measurement Approach

2.1 Standard Cell Voltage Difference Measurements

All cells at NIST are calibrated by comparing them directly to NIST-owned standard cells using a series opposition method and redundant measurement designs [5]. Figure 1(a) shows a simplified schematic of the measuring circuit used for the series opposition measurement method. Two cells (one of known value) are connected in series opposition and the small voltage difference is read using a digital voltmeter (DVM). However, in any real measurement circuit there will be unwanted spurious emfs as illustrated by the emf source P in figure 1(a). In general these spurious emfs can be classified into two categories:

1. Those emfs that remain constant, or relatively so, in relation to the interval over which a complete set of measurements is made.
2. Those emfs that vary rapidly (referenced to the interval over which a complete set of measurements is made).

If the emfs are of the second type they will have the effect of decreasing the precision of the process. On the other hand, if they are of the first type they will have the effect of introducing a systematic error into the measurement result such that

$$\Delta E = E_1 - E_2 + P$$

where E_1 and E_2 are the emfs of the two cells being compared and P is the constant, and as yet unknown, emf. It is possible to estimate P by reversing the position of the cells in the circuit and taking a second measurement $\Delta E'$ as shown in figure 1(b), where

$$\Delta E' = E_2 - E_1 + P.$$

Taking the difference between the two expressions gives

$$\Delta E - \Delta E' = 2(E_1 - E_2),$$

thus yielding an estimate of $E_1 - E_2$ free of P. The pair of measurements are said to be "left-right" balanced. That is, if there is a positional effect in the circuit it is balanced out of the final result. This technique is analogous to that used to eliminate the inequality of balance arms in precision weighing on a two-pan "equal-arm" balance. In order to identify the cell positions from the operational point of view, they are frequently designated as left and right relative to the input terminals of the measuring instrument. In practice more complex measurement patterns, i.e., redundant measurement designs, are used for intercomparing standard cells, see section 2.3.

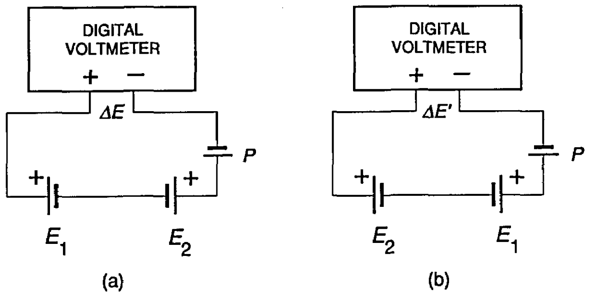

Figure 1. Simplified schematic of the measuring circuit used for series-opposition comparison of standard cells. (a) The "normal" measurement. (b) The "reversed" measurement with the cells interchanged to eliminate the constant positional effect denoted as a fixed emf P.

2.2 Standard Cell Measurement Apparatus

Two fully-automated voltage measuring systems are currently in use at NIST for all cell comparisons. Except for the switching systems, they are identical; one system (VTP) has a low-thermal-emf scanner with 80 voltage (cell) inputs and the second system (RCS) has a low-thermal scanner with 300 inputs. Figure 2 is a simplified diagram that generally represents both systems (the scanners vary in minor details). In addition, both systems contain a high resolution 6-1/2 digit voltmeter, a desktop computer, and a shared hard disk system (not shown).

The scanner permits selection of any pair of standard cells and connects them, in series opposition, to a digital voltmeter. The scanner effectively consists of two scanners: one cell is connected to the "A-bus" (see fig. 2) and a second cell is connected to the "B-bus." The bus (cell) negative terminals are connected together and the positive terminals are connected to the DVM through additional reversing switches. The switch assemblies are specially modified mechanical crossbar-matrix switches that use phosphor bronze springs and gold contacts and are actuated by magnetically latching solenoids. The use of latching solenoids reduces the heat input from the solenoid to the switch assembly (and thus the thermal emfs) when the switches are actuated. As the switches have relatively large thermal emfs when placed unprotected in the labo-

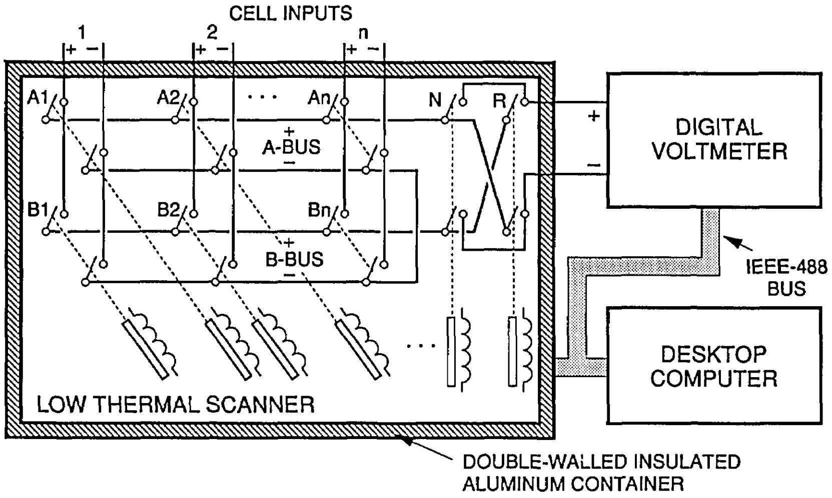

Figure 2. A diagram of the automated cell comparison systems showing some details of the low-thermal scanner. The scanner and digital voltmeter are controlled by a desktop computer.

ratory, they are mounted in a nested-pair of heavy-walled aluminum chambers with insulation between them. Additionally, thermal shunts are tied to the incoming leads. These thermal management techniques reduce the total thermal emfs in the scanner to typically 15 and 30 nV, respectively, for the 80- and 300-input switches. The difference in the thermal emfs of the two scanners is attributed to small deliberate differences in the construction of the switches to accommodate different numbers of cells. The scanners are controlled through an instrumentation bus [6].

The voltmeters were selected (and individually tested) for low input bias current and low random measurement error. Since the saturated standard cell emf stability depends on an electrochemical equilibrium within the cell, small charging or discharging currents that are present at the input of the DVM will produce changes in the cell emf that may be significant. The voltmeters used at NIST have been tested and determined to have an input bias current of 12 pA which contributes a negligible error to the measurement. A total measurement time of 18 s for each measurement is used by averaging six 3-s duration DVM readings which results in a typical single measurement standard deviation of 0.034 μV. In additional experiments, identical cell comparisons were made using both the DVM and classical potentiometers and the measurement results agreed well within 0.03 μV, the combined uncertainties of the instruments.

2.3 Redundant Measurement Designs

As used in this context, redundant measurement designs are a specified sequence of measurements used to compare pairs of standards. The measurement sequence is chosen to provide an optimum amount of information with as few measurements as possible. For the NIST measurements, the parameters that are estimated by the designs are: the difference of each cell emf from the reference group mean emf, the within-day standard deviation (the process precision), and the left-right (positional) effect in the measuring system. In addition, the designs provide diagnostic information about possible errors or problems with the measuring system. The within-day standard deviation permits laboratory personnel to estimate the quality of the measurements immediately and the redundant measurements allow them to eliminate anomalous observations mathematically from the measurement design and re-compute the cell emfs with little loss in accuracy.

Two specific designs are generally used at NIST, one for comparison of two groups of four cells, and one for comparison of one group of six cells to one group of four cells. In both cases a "full" design is used where all possible pair differences that involve cells from different groups are measured (16 and 24 measurements respectively). For other larger groups of cells, some observations may be eliminated from the "full" design. The cell emfs are estimated from the cell difference measurements by solving the over-determined set of equations using the least-squares method and including the constraint that the mean emf of a given group of cells (i.e., the reference group) is known. (When comparing client cells to NIST cells, the NIST cells are specified as the reference group.) This results in an assignment of individual emf values to all the cells in terms of the mean emf of the reference group.

When a well-designed classical potentiometer is used as the cell comparison instrument the left-right effect P does not vary significantly over the time of the measurement design and it is sufficient to require that the total design be left-right balanced, i.e., each cell appears on the left side and right side of the measuring system an equal number of times irrespective of their order of appearance in the design. Digital voltmeters, however, have been found to introduce a small time-varying dc offset that must be eliminated by immediately reading every cell pair a second time with the polarity of the input reversed. The algebraic difference of these two measurements divided by two is considered to be a single measure of the cell difference with the DVM offset eliminated.

2.4 Temperature Measurements

All saturated standard cells exhibit an emf change with temperature and must be maintained at a constant temperature. Cells sent to NIST for calibration are either housed in their own portable thermoregulated enclosures, or are immersed in NIST-provided constant-temperature oil baths. Thermoregulated enclosures generally contain a temperature sensing element which can be used to monitor the small temperature variations (usually less than 0.01 °C) within the cell enclosure. Typical devices are mercury-in-glass thermometers, thermistor bridges, and platinum resistance thermometers. NIST follows manufacturers' recommended procedures for monitoring the temperature using these devices. The temperature scale embodied in the temperature device is generally taken as correct, primarily because accurate knowledge of the temperature is unnecessary. Cell emfs are corrected only for small changes in temperature, referenced to a nominal temperature as established by the temperature device.

For cells housed in the NIST oil baths, calibrated platinum resistance thermometers and an ac resistance thermometer bridge are used to measure the temperature. The temperature of the oil bath is stable and uniform to at least 0.001 °C. The estimated uncertainty of the temperature measurement with respect to the International Temperature Scale of 1990 (ITS-90) is 0.005 °C (3 standard deviation estimate), and includes uncertainty components for the power dissipation in the thermometer, the determination of the triple point of water, and the drift of the calibration constants between calibrations.

Cell emfs are corrected for small day-to-day temperature changes by monitoring the temperature as described above and applying an emf correction based on the International (or Wolff) Temperature Formula [1]:

$$E_t = E_{20} - 0.00004060(t\text{-}20) - 0.000000950(t\text{-}20)^2 + 0.000000010(t\text{-}20)^3$$

where E_t is the emf in volts at temperature t and E_{20} is the emf at 20 °C. This equation is used to correct the cell emfs to any arbitrary nominal temperature by computing the correction for the actual temperature with respect to 20 °C and subtracting the correction for the nominal temperature with respect to 20 °C. The formula is an approximation and is not exact for all cells although it provides reasonable accuracy (better than 0.1 μV) if the total correction is less than 1 μV.

2.5 Solid-State Voltage Reference Measurements

Solid-state voltage standards are calibrated at NIST using a specially designed measurement system (denoted "ZCS"). It employs a potentiometric method allowing voltage measurements to be made without loading the standard. (An earlier version of this system is described in reference [7]). The system is a fully-automated scaling device for comparing arbitrary voltage standards to 1.018-V standard cells. A three step procedure is used to make a measurement of an unknown voltage: 1) the system is self-calibrated using a group of standard cells of known emf, 2) the unknown solid-state standards are compared to the calibrated system, and 3) the system is self-calibrated again to make sure that no significant drifts in the system have occurred.

Figures 3a and 3b show a simplified diagram of the measuring system configured for self-calibration and for measurement of unknown solid-state standards respectively. A modified 10.18-V Zener reference is permanently connected to a resistive divider; this combination (the Transfer Reference) is considered to be a stable voltage source with 10 series-connected 1.018-V outputs. The Transfer

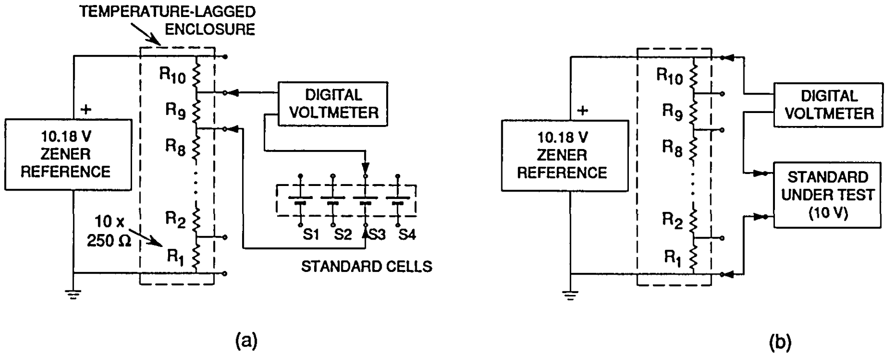

Figure 3. A simplified diagram of the "ZCS" calibration system used to calibrate solid-state standards. (a) The system arranged for self-calibration of the 1.018-V voltage drops across each of the 10 resistors. (b) The system configured for calibration of an unknown standard-under-test of approximately 10 V.

Reference is calibrated by comparing the voltage drop across each resistor in turn to the emf of each cell in a four cell group, measuring the microvolt-level difference voltages with the digital voltmeter for a total of 40 measurements. (Not shown in fig. 3 is a low-thermal scanner, similar to the ones described previously, which permits selecting the various voltage differences. Also not shown is the desktop computer and the shared hard disk system.) After calibration, the Transfer Reference is used as a calibrated source producing 10 voltages from 0 to 10.18 V in steps of 1.018 V by referencing each output tap to the bottom tap. Then (as shown in fig. 3b) the output voltage developed across N of the divider resistors is compared to the voltage of the unknown standard-under-test using the DVM. N is chosen to minimize the magnitude of the DVM reading. After all the standards under test have been measured, a second self-calibration of the Transfer Reference is performed to reduce any error caused by its drift during the measurements.

The final value for each solid-state standard under test is computed by correcting the measured difference between the standard-under-test and the Transfer Reference for the gain error of the DVM, and adding to this the value of the appropriate tap of the Transfer Reference. The calibrated values of the Transfer Reference are determined using a least-squares analysis of the redundant measurements that compared the 10 outputs of the Reference to the four-cell reference standard cell group. The mean of the "before" and "after" calibrations is used.

With this system the DVM is used to read only a fraction of the voltage of the standard-under-test which reduces the contribution of the DVM uncertainty to the overall measurement uncertainty. When comparing the standard-under-test to the Transfer Reference (with voltage taps at 1.018 V increments) the maximum possible reading required of the DVM is 0.509 V. Thus,

$$U=\frac{V_z-(N)1.018}{V_z}U_{\mathrm{DVM}}$$

where U_{DVM} is the DVM uncertainty expressed as a percentage of reading, V_{Z} is the voltage of the solid-state standard, N is the number of resistors, and U is the final DVM uncertainty as a percentage of V_{Z}. For a worst case of $V_{\mathrm{Z}}=5.6$ V, $U=0.09\ U_{\mathrm{DVM}}$, and for $V_{\mathrm{Z}}=10$ V, $U=0.02\ U_{\mathrm{DVM}}$. If, for example, the DVM were calibrated to an accuracy of 1 ppm of reading (not an unreasonable assumption) the DVM error contribution at 10 V would be 0.02 ppm.

The two largest contributions to the DVM uncertainty are the linearity error of the DVM and the gain error. (All DVM measurements are combined measurements of a "normal" and a "reversed" DVM reading to eliminate the DVM offset error.) The linearity of the DVM is checked periodically using an independent calibration system. The gain of the 1 V range of the DVM (the one used for all high accuracy measurements) is calibrated as part of step 2 of the measurement procedure by making two 1.018-V measurements of the voltages developed across two resistors in the Transfer Reference. Two measurements are made to evaluate the effect of measuring voltages with the DVM at ground and above ground. These gain calibrations are used by the system as previously described to correct the DVM readings to reduce the overall measurement uncertainty.

The DVM is used on the 0.1-V range for improved resolution in the comparisons of 1.018-V solid-state standards and of the reference standard cells to the Transfer Reference. The gain error of the 0.1-V range is not measured daily by the system but, the largest expected voltage difference for these comparisons is only 200 μV. Thus, for an overall measurement error of 0.005 ppm (of 1.018 V), the gain need only be known to 250 ppm. The gain of the 0.1-V range is periodically checked using external standards to ensure that it is within this limit.

3. Maintenance of the NIST Volt

By international agreement, starting on January 1, 1990, a highly accurate representation of the volt based on a new constant for the Josephson effect has come into effect worldwide [8]. This representation is defined in terms of the Josephson constant K_J, the frequency-to-voltage quotient of the ac Josephson effect in superconductors. The value of K_J used for maintaining the volt representation at NIST is 483 597.9 GHz/V. This value is believed to define a volt representation consistent with the SI volt to within 0.4 ppm (one standard deviation estimate). The operational procedures and apparatus used to maintain the NIST volt are described briefly below; additional details can be found in reference [9].

3.1 The ac Josephson Effect

When two weakly coupled superconductors are irradiated with microwave energy, the assembly (a Josephson junction) can be used to produce a number of precise voltages, $U_J(n)$, described by the following equation:

$$U_J(n)=nf/K_J,$$

where n is an integer, f is the frequency of the irradiating microwave energy, and K_J is as described above. A variety of experimental tests (for material dependence, temperature dependence, etc.) and theoretical investigations of the Josephson relation have been made which indicate that this equation is exact [10].

3.2 The Josephson Array

Arrays consisting of from 1500 to 2076 Josephson junctions are used to produce a total voltage of up to 1.2 V [11,12]. These arrays do not require control of the bias currents for the individual junctions as was the case in the past because they use constant-voltage steps which cross the zero current axis of the junction I-V curve. This arrangement allows a large array of junctions to share a common current bias at or near zero. The arrays are fabricated using niobium and lead alloys and are stable at room temperature.

3.3 Measurement Apparatus

Figure 4 is a simplified diagram of the Josephson array measurement apparatus. The microwave radiation is supplied to the Josephson array by a 60-mW Gunn diode oscillator at 94 GHz which is frequency-stabilized by a frequency-locking counter containing a quartz-crystal oscillator. The short

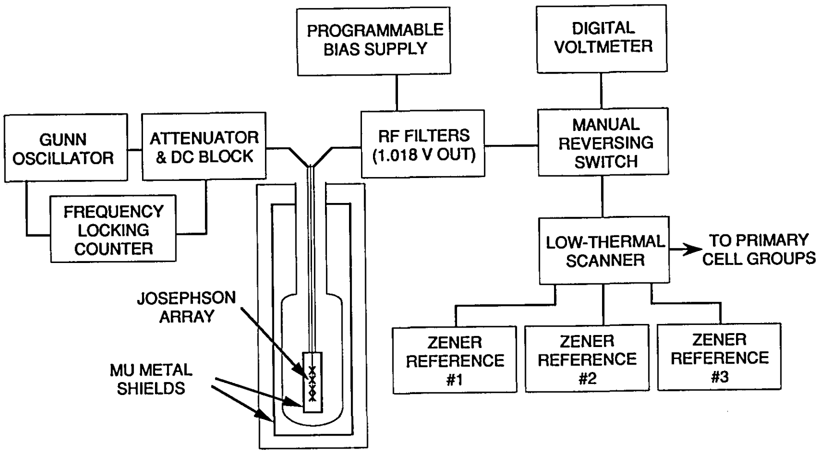

Figure 4. Diagram of the voltage measurement system based on the Josephson array.

term frequency stability of the microwave radiation (15 min) is about 1 part in 10^9. The frequency is measured by the frequency counter with a resolution of 1 part in 10^{10}. The accuracy of the counter time base is regularly checked against the U.S. frequency standard by comparing the counter time base to a 100 kHz high-stability oscillator which is simultaneously compared to the signal from WWVB using a VLF comparator.

Also shown in figure 4 is the dc measurement apparatus used to compare the array voltage at 1.018 V to a 1.018 V Zener reference standard. The bias source supplies a small current to force the Josephson array to operate at the desired step. RF filters are incorporated at the top of its probe to prevent externally generated noise from disturbing the array. The manual reversing switch contains multiple switches to perform two functions: reversing the polarity of the signal to the DVM, and reversing the polarity of the Zener reference (selected by the scanner) to match the polarity of the array. Thus, to measure the voltage of a Zener reference, the array is adjusted to produce a voltage nearly equal to the Zener reference by (a) adjustment of the bias current and microwave power to select a suitable voltage step, and (b) adjustment of the microwave frequency to fine-tune the step voltage. The step is observed on an oscilloscope (not shown in the figure) to check for any abnormalities. The difference between the array and Zener reference is then measured by averaging several readings (E_1) of the digital voltmeter. The polarity of the DVM is reversed and several more readings (E_2) are taken to eliminate offsets in the digital voltmeter. The bias current and microwave power are then adjusted to produce an array voltage of -1.018 V and the polarity of the Zener reference is reversed to match the array voltage. Two more sets of readings (E_3 and E_4) are taken with the DVM in its normal and reversed polarities respectively. This action is required to eliminate thermal emfs in the leads from the array to the reversing switches. The Zener voltage is calculated as $(E_1-E_2-E_3+E_4)/4+nf/K_J$ where n is the integer step number, f is the microwave frequency, and K_J is as defined above. This measurement sequence is repeated five times with a typical standard deviation of 0.009 μV for the five measurements, and takes about 12 min.

A final check is made on the thermal emfs in the leads from the Zener reference to the manual reversing switch by replacing the Zener reference with a short and adjusting the array to operate on the zero-voltage-step with the microwave power set to zero. The same measurement sequence is run as for the 1.018-V measurement. The residual thermal emfs thus determined are subtracted from the 1.018-V measurements.

4. Operational Procedures

Although it is theoretically possible to compare all 1.018-V client standards directly to the Josephson array, it would be inconvenient to do so as the Josephson measuring system is still partially manually controlled at present and the large number of measurements required each day could not be accomplished with just one measuring system. Instead, a hierarchical path of cell groups has been established to enable client standards to be calibrated in terms of the Josephson array.

Figure 5 shows the path of measurements from the Josephson array to client standards to be calibrated and the three measuring systems used (VTP, RCS, and ZCS). The details of these measuring systems have been described above (in secs. 2 and 3).

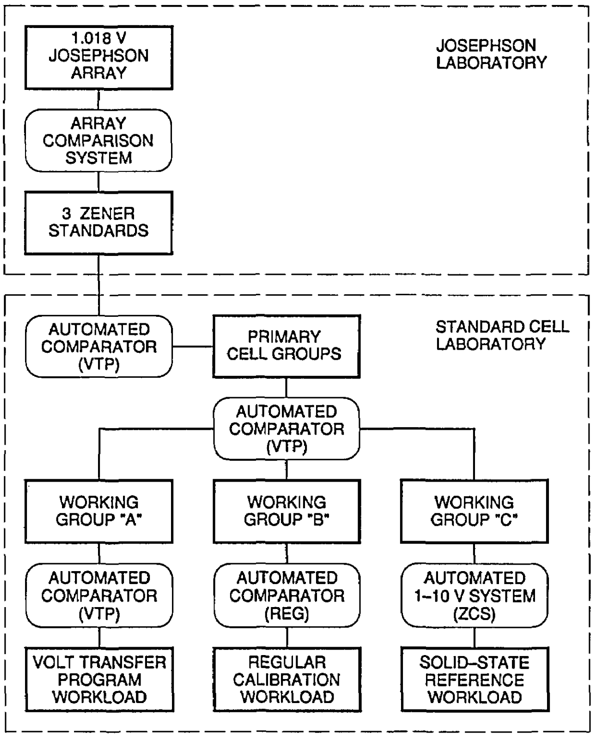

Figure 5. Plan of the voltage traceability process from the Josephson array to the workload for the three calibration services.

4.1 Calibration of the Laboratory Primary Cells

Comparison of the Josephson array to groups of cells considered to be "primary" cells (Josephson measurements) are made at approximately weekly intervals. Modular switches (using components similar to the previously described low-thermal scanners) permit comparing standards in the Josephson laboratory to cells situated in the Volt Facility (adjacent to the Josephson laboratory) with very small thermal emfs being introduced in the measurements. The weekly comparisons of the three Zener standards in the Josephson laboratory to the primary cells consist of three steps. 1) The three Zener standards are compared to the primary cells using redundant measurement designs and the VTP automated comparator. 2) The Zener standards are compared to the Josephson array and assigned voltage values. 3) The Zener standards are again compared to the primary cells. Every 4 weeks additional cell comparisons between the primary and working cell groups are made to investigate the possibility of new systematic errors that may have developed in the measuring systems. This is designated a "cardinal" measurement.

Standard cell emfs drift with time so the use of a simple time invariant model for the cell emf can lead to unacceptably large step changes in the cell value each time the value is reassigned from the Josephson measurements. In addition, it is desirable to "average" several Josephson measurements to reduce the random error associated with the short term fluctuations of the cell emfs as well as with the measurements. Accordingly, we use a model for the primary cell group emfs that predicts a linear drift with time, and new model coefficients are calculated after every cardinal Josephson measurement. Figure 6 shows the typical behavior of the mean emf of the primary group plotted against time.

In addition, since the workload calibration process is continuous, it is not possible to wait for the next Josephson measurement before assigning values to client cells. Therefore, weekly values for the means of the emfs of the cell groups are predicted using a least-squares fit based on the last five or so cardinal measurements. (The solid line in fig. 6 is such a prediction.) The exact number of measurements chosen for the fit depends on (a) how well the cell emfs fit a linear model, and (b) the random scatter in the Josephson measurements of the cell emfs. The judgement and experience of the laboratory staff are used to determine the models. A fit to all the cardinal measurements in figure 6 (the broken line) has been included to emphasize that the cell emfs do not follow a straight line model for an extended time period; additional structure (possibly humidity related) appears in the data.

The three Josephson measurements made on "off-weeks" each month are used to check the prediction of the assignment of the primary cells. The collection of cell groups that constitute the primary groups changes as cells need replacement or enclosures need repair. In general, the primary groups

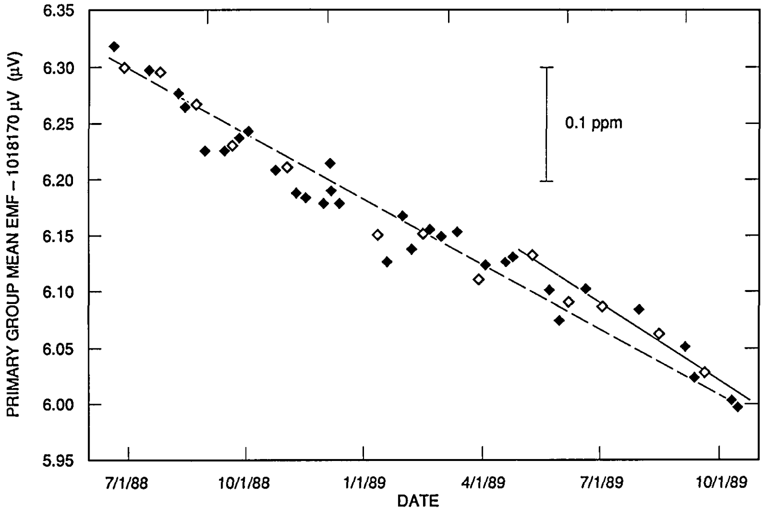

Figure 6. Josephson array measurements of the mean emf of the Primary Group. The open symbols indicate a cardinal measurement where new predictions for the cell values are computed. The meaning of the solid and dotted lines is described in the text.

consist of two or three groups of four to six cells each, with about 10 to 12 cells total. The primary cell groups also serve as a check standard for the Josephson measurements. If an individual Josephson measurement assigns values to the primary cells that are inconsistent with the predicted values (different by more than 0.07 ppm), all of the measurement systems are investigated to determine the source of the inconsistency. If the problem cannot be resolved, the Josephson measurement is usually repeated. In the exceptional circumstance where later Josephson measurements confirm the deviation from the predicted model, appropriate past workload data are corrected to reflect the change.

4.2 Calibration of Working Cell Groups

As previously discussed, in order to minimize the possibility of disturbing the primary cells, and because large numbers of standards are calibrated each day with three simultaneously operating measurement systems, the client cells cannot be compared directly to the primary cells. Instead, as shown in figure 5, the primary cells are compared to three working groups of cells once each day and then the working-group cells are compared to the client standards and NIST transport standards. The working-group cell emfs for each day are determined from the predicted values of the primary cells and the results of the comparisons of the working-group cells to the primary cells for that day. This process of using several working groups is feasible because only a small within-day uncertainty is introduced by the extra intercomparison measurements.

The constituents of the working groups (and the primary groups) are modified as necessary when cells show erratic behavior or temperature-regulated enclosures fail. (Historically substitutions have occurred every few years.) Changing cells occasionally is not a problem, particularly for the working groups, as no long-term history is required for operation of the system; the working groups are calibrated each day and must remain stable only throughout the day. The primary groups are required to be predictable for up to 1 month, this requires that candidate cells exhibit stable emf behavior for about 5 or 6 months before being eligible for use as primary cells. In addition to the cell groups considered to be primary and working, we have additional groups that are measured daily; these could substitute for the presently used groups.

4.3 Calibration of Client Saturated Standard Cells

Cells received for calibration may be subjected to a stabilization period before measurements are begun. The length of the stabilization is usually not longer than 4 weeks and depends on whether the cells were shipped to NIST under constant temperature control or not. If space is available on the measuring system, and cells have been shipped under temperature control, they are connected to the measuring system immediately. However, later review of the data generally results in these early measurements being discarded.

Three types of saturated standard cells are calibrated: cells intended for immersion in oil at 28 or 30 °C, and groups of cells in their own temperature-controlled enclosures. The first two types are placed in oil baths the temperatures of which are stable and uniform to at least 0.001 °C and are determined using NIST-owned platinum resistance thermometers. Temperature-controlled standard cell enclosures are tested under the following ambient conditions:

Temperature	(23±1) °C
Relative humidity	50% or less

The operating temperature of the cells in temperature-regulated enclosures is determined using the temperature measuring device supplied with the enclosure. If the enclosure has a temperature indicating bridge, a NIST-owned null detector is used to make the readings to within the resolution of the bridge, usually 0.001 °C. A NIST or customer-owned platinum resistance thermometer may be used if requested. Temperature measurements are made each day before the cell emf measurements are started.

4.4 Calibration of Volt Transfer Program Standards

The Volt Transfer Program involves sending a NIST-owned transport voltage standard to the client laboratory. The transport cells are compared to NIST working standards at NIST before and after shipment to the client laboratory and to the client reference group of standard cells while at the client laboratory. The process is described in more detail below.

4.4.1 Measurement of the Transport Standard at NIST The transport standard consists of a commercial thermoregulated enclosure usually containing four shippable saturated standard cells, operating at an internal temperature of 30 or 32 °C. The temperature is measured using the internal temperature bridge and an external null detector to provide 0.001 °C resolution. Temperature corrections to the cell emfs are applied according to the discussion given in section 2. Transport standard cells are compared daily to Working Group A using redundant measurement designs and the VTP measurement system (see fig. 5). Before shipment to a client laboratory, the cell emfs are plotted and examined for stability. A minimum of 15 stable measurements are required before the enclosure will be shipped.

The transport standard is shipped in a special container designed to provide physical shock protection and ambient temperature lagging. It also contains an external power supply to provide regulated power to the transport standard to maintain the cells at a constant temperature while at NIST and the client laboratory. In addition, batteries within the supply power the transport standard during shipping for up to 24 h during normal conditions. Since the temperature control system cannot supply cooling to the enclosure, shipment to warmer locations is avoided during extremely hot weather to prevent the enclosure from overheating. The standard is shipped either via air freight or hand-carried by laboratory personnel. In the former case, the client laboratory personnel are notified of the flight time of the standard and are expected to provide transportation from the airport to their laboratory within the 24-h lifetime of the batteries.

4.4.2 Comparison of the NIST Transport Standard to the Client Standard Each laboratory participating in the Volt Transfer Program must identify a group of saturated standard cells that are considered to be the "laboratory reference group" and constitute the "laboratory volt." The transport standard cells are compared to the cells of the laboratory reference using the normal laboratory measuring equipment and procedures with the exception that a NIST-specified measurement design must be used. NIST provides data sheets to record the measurement results. The data sheets are then immediately returned to NIST where the cell comparison data are reduced to determine the transport (and laboratory reference) cell emfs in terms of the client laboratory volt. Laboratories are required to make daily measurements and the results are reviewed by NIST to determine when sufficient data have been obtained to permit shipment of the standard back to NIST. A minimum of 10 measurement designs over 10 days is required for the transfer; however, the number is more typically in the range from 12 to 20. In addition, the within-day standard deviations and left-right components from the measurement designs are tested to see if they are in statistical control with respect to the expected values as determined from similar measurements at NIST and other laboratories.

4.4.3 Final Report Upon its return to NIST, the standard is again compared to Working Group A as before and, when the standard has stabilized and sufficient data has been taken, a final report is issued. Typical measurement data, the emfs of two of the four cells in a transport standard, are plotted in figure 7. Anomalous cell emf changes, typically caused by shipment or temperature problems, are eliminated from the final data analysis. (In fig. 7 the first measurement at the client laboratory for both cells appears slightly inconsistent with the succeeding data.) The data are also reviewed for abnormal temperature readings and to determine if they reasonably conform to a linear model.

Because the before and after NIST data do not usually exactly agree, a least-squares fit is made to them for each transport cell, and values are interpolated for each of the times (dates) the cell was compared to the client laboratory cells. V(LAB)-V(NIST) is determined using each cell in the transport enclosure by subtracting the NIST interpolated values of the transport cell from the respective client laboratory emf assignments, and taking the mean of these differences (0.698 and 0.715 μV for the data of fig. 7). The difference V(LAB)-V(NIST) as determined from each of the four cells in the transport standard should agree, but on occasion there is disagreement caused by abnormal cell behavior, such as excessive drift, or poor recovery from a physical shock or a temperature disturbance. The judgement and experience of the laboratory staff are used to determine when to exclude a cell from the analysis or, on rare occasions, to use only the NIST data taken before or after the transfer, but not both.

4.5 Calibration of Solid-State Standards

Solid-state voltage references sent in for calibration are connected to measuring system ZCS as soon as they are received. These references are measured starting the day after their receipt without a stabilization period, since none is usually required. Most standards sent in for calibration provide some method for monitoring the temperature of the reference element(s) of the standard. For these standards, the temperature is measured

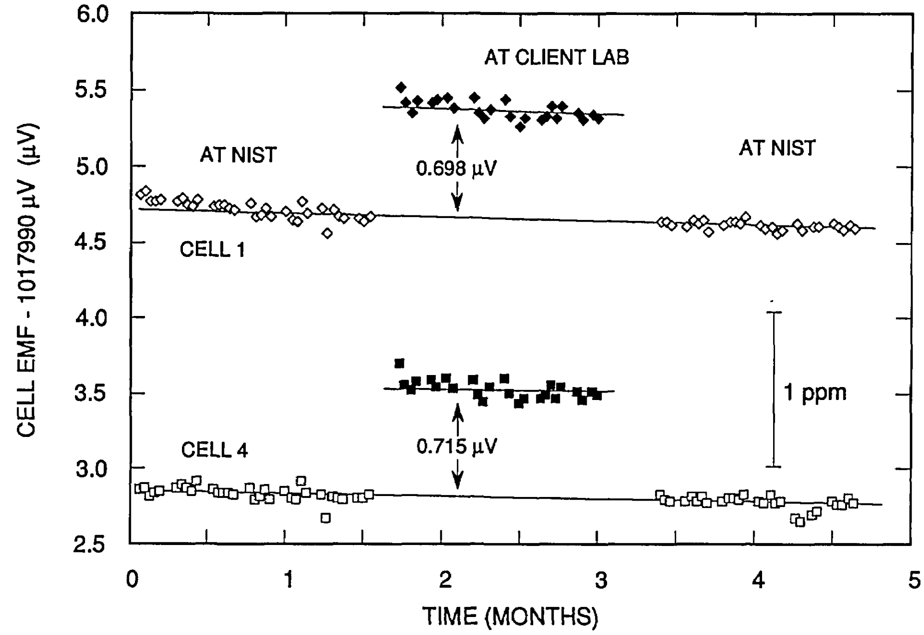

Figure 7. Typical measurement data for two of the four cells used for a Volt Transfer Program determination with a client laboratory.

before the voltage measurements are begun on the first day to determine if the internal temperature of the reference is at or near its normal operating temperature. Temperature measurements are not made on succeeding days unless specifically requested by the client. The relationship between small day-to-day temperature fluctuations and output voltage changes is different for each individual reference device and generally is not known; thus the temperature readings are not useful for correcting voltage readings. Voltage measurements are taken once a day for a minumum of 10 d. The data are reviewed at the conclusion of the measurement period and, if the voltages are sufficiently stable, the average of the measurements is reported as the calibrated value.

5. Calibration Uncertainties

The uncertainty assigned to the calibrated value of a client standard is a combination of three uncertainties: (1) the uncertainty of assigning a value to the primary cells from the Josephson array, (2) the uncertainty of assigning a value to the working cells from the primary cells each day, and (3) the uncertainty of assigning a value to the client standards considering the NIST measurement uncertainties and the performance of the client standard.

5.1 Uncertainty in the Assignment of the Mean Emfs of the Primary Groups

Table 1 summarizes the sources of uncertainty in assigning a value to the mean emf of a primary cell group at the time of a Josephson measurement.

Table 1. Uncertainties in the assignment of the mean emfs of the primary group

Source of uncertainty	1 std. dev. estimate (ppm)
Microwave frequency	0.005
Assignment of Zener reference group using array	0.006
Random uncertainty of comparison of Zener reference group to the mean of the Primary Group	0.009
Change in the Zener reference group during the Josephson measurement	0.019
Uncompensated thermal emfs in the cell switches	0.005
RSS total	0.023

The microwave frequency is measured by a frequency counter which is calibrated in terms of WWVB. An uncertainty is included for measurement uncertainty and drift of the Gunn oscillator frequency.

During a Josephson measurement each Zener reference is compared to the array five times. The pooled standard deviation of the mean calculated from individual comparisons is 0.0042 μV (60 degrees of freedom). This value, divided by the square root of three (i.e., 0.0024 μV, 0.002 ppm), is used as the random component of uncertainty in comparing the mean of the three Zener standards to the Josephson array. In addition, the thermal emfs in the leads to the Zener reference are measured and subtracted from the Zener values. The uncertainty of determining the thermal emfs is 0.0042 μV (0.004 ppm). As a conservative approach we add these two sources of uncertainty directly to obtain a total uncertainty of 0.0066 μV (0.006 ppm). All other known sources of systematic error are negligible.

The random component of uncertainty in comparing the Zener standards to the Primary Group is estimated from the 0.034 μV pooled standard deviation of a single cell-Zener comparison. Because of the redundancy of the measurement design, the uncertainty of the difference of the mean of the Zener reference group to the mean of the Primary Group is 0.012 μV. Two measurement designs are made for the Primary Group (before and after the Josephson measurements); thus, the uncertainty of its mean emf is reduced by the square root of two for a total uncertainty of 0.009 μV (0.009 ppm).

The difference of the mean Zener group emf minus the mean Primary Group emf typically shows a change of (0.008±0.011) μV in the before and after comparisons described above. These appear to be caused by small shifts in the Zener references emfs between the two measurements. Although statistically the bias in the shift (0.008 μV) is not significant compared to 0.11 μV, it is felt that a bias does exist but no correction is made. Rather, an uncertainty of 0.019 ppm (0.008+0.011) is assigned for changes in the mean Zener group emf during the measurements.

Modular low-thermal switches (similar to those described in sec. 2) are used to connect the various primary cells and the three transfer-Zener-standards to the VTP measuring system. The thermal emf variations in these switches that do not cancel on cell reversal have been measured to be 0.005 μV (0.005 ppm).

The root-sum-square (RSS) total is an estimate of the uncertainty in assigning a value to the mean emf of the Primary Group based on one Josephson measurement. This is an estimate of how well the present system would agree with another totally independent Josephson system. Based on data from actual multiple Josephson measurements from our one system we observe a reproducibility of the assignments of the mean emf of a group of standard cells of about 0.020 ppm.

5.2 Uncertainty in the Assignment of the Mean Emfs of the Working Groups

Table 2 summarizes the uncertainties in assigning a daily value to the mean emf of one of the working groups.

Table 2. Uncertainties in the assignment of the mean emfs of a working group

Source of uncertainty	1 std. dev. estimate (ppm)
Assignment of Primary Group (from table 1)	0.023
Day-to-day fluctuation of Primary Group	0.028
DVM scale error	0.005
Random uncertainty in comparison of Primary Group to Working Group	0.004
Uncompensated thermal emfs in cell switches	0.015
Uncertainty of assignment to Working Group RSS total	0.040

The uncertainty for the day-to-day fluctuations of the primary groups also includes an additional uncertainty produced by the inexact prediction of the values of the primary groups. The effect of these combined uncertainties has been estimated by an experiment lasting several months where values were assigned to the working groups using different groups of primary cells and comparing the differences in the assignments.

The DVM scale error is estimated based on daily readings of a calibrated 1000 μV source. The random uncertainty of the cell comparisons is estimated from the redundant measurement designs as before with a pooled standard deviation of a single measurement of 0.034 μV. The thermal emf variations in the switches that connect the various cells to measuring system VTP have been measured to be 0.015 μV (0.015 ppm).

The RSS total uncertainty in assigning a value to the mean emf of either working group is thus estimated to be 0.040 ppm.

5.3 Uncertainty in the Assignment of the Mean Emf of a Client Cell

Table 3 summarizes the sources of uncertainty in calibrating a client cell in terms of the NIST volt via the regular calibration method (RCS). The uncertainty of the Working-Group assignment is carried over from table 2.

Table 3. Uncertainties in the assignment of the mean emf of a client cell

Source of uncertainty	1 std. dev. estimate (ppm)
Uncertainty of assignment to Working Group (from table 2)	0.040
Change in Working Group during the day	0.040
DVM scale error	0.010
Random uncertainty of comparison of the Working Group to client cell	0.007
Uncompensated thermal emfs in the cell switches	0.030
Uncertainty of assignment to client cell (not including temperature measurement errors and day-to-day client cell emf fluctuations; see text)	
RSS total	0.065

The uncertainty introduced by the within-day changes in the Working-Group was estimated by a several-month-long experiment comparing the Working Group cells to the Primary-Group cells both before and after the normal workload measurements and recording the changes.

The DVM scale error is calculated as described for table 2, except that cell differences as large as 120 μV may be measured. The random measurement uncertainty of the working group—client cell comparison is estimated from the redundant measurement design as before. The thermal emfs in the crossbar scanner are measured periodically as described before and an uncertainty is included for their variations.

The final reported uncertainty for a client-cell emf is the direct sum of three components: (1) the assignment uncertainty from table 3 (0.065 ppm), (2) the uncertainty from the day-to-day cell fluctuations, and (3) the uncertainty caused by the imprecision of the cell temperature measuring device.

The day-to-day random component of the uncertainty of the client-cell emf is based on the standard deviation of the measured cell emfs from the 10 daily measurement designs. This standard deviation is compared to the pooled standard deviation of a large population of measurements of similar standards (0.135–0.188 μV, depending on the type of enclosure) using an F-test at the 99% confidence interval (CI). If the standard deviation is determined to belong to that population, then the population standard deviation of the mean is used as the estimate of the random component. If not, the computed standard deviation of the mean is used as the estimate.

The uncertainty of the assignment of values to the cell emfs due to the imprecision of the temperature monitoring device is estimated by calculating the change in cell emf (according to the International Temperature formula) for a change of one least count of the temperature monitoring device. For cells in enclosures containing internal thermistor bridges, where a least count of 0.001 °C is possible, an additional uncertainty of approximately 0.05 ppm is included. Enclosures monitored by mercury-in-glass thermometers are assigned an uncertainty equivalent to half the smallest graduation marked on the thermometer, approximately 0.5 ppm for a resolution of 0.01 °C. For cells calibrated in NIST oil baths an emf uncertainty equivalent to a temperature uncertainty of 0.005 °C is used to account for possible calibration errors in the platinum resistance thermometers used at NIST.

The final reported uncertainty contains no allowance for long term drift of the cells under test. Long term behavior must be determined by the client by analysis of the history of each individual standard. In addition, no allowances are made for the possible effects of transporting the standard between laboratories or the possible existence of a gross temperature dependence on ambient (room) temperature of the standard.

5.4 Uncertainties in the Determination of V(LAB)–V(NIST)

Table 4 summarizes the sources of uncertainty in the determination of V(LAB)-V(NIST) obtained via the Volt Transfer Program.

Table 4. Uncertainties in the determination of V(LAB)-V(NBS)

Source of uncertainty	1 std. dev. estimate (ppm)
Uncertainty of NIST assignment to transport group	0.061
Correlated temperature effects of the transport	0.050
Temperature resolution	0.050
Random component due to individual cell assignments and changes during transport	0.093
Uncertainty of V(LAB)–V(NIST) determination using a four cell transport enclosure	
RSS total	0.132

The uncertainty in assigning a value to the transport standard while at NIST is obtained through an analysis identical to table 3, except the switches used for the VTP transport standards have somewhat lower uncompensated thermal emfs (0.020 μV as opposed to the 0.030 μV shown in table 3).

The transport standards used for the Volt Transfer Program all contain thermistor bridges with 0.001 °C resolution; an uncertainty for the cell emf equivalent to this temperature change is included. In addition, the cell temperature within the enclosures changes slightly with changes in ambient temperature. The thermistor bridge does not properly reflect the change of the temperature of the cell in this case, probably due to a temperature sensitive component of the bridge circuitry that is at ambient temperature. Based on experiments on similar enclosures, an uncertainty estimate of 0.05 ppm is included to account for a difference between the client laboratory ambient temperature and the NIST laboratory ambient temperature.

Each of the four cells in the transport standard is used to determine a value for the difference in laboratory units, V(LAB)−V(NIST). The standard deviation of these four values arises from the uncertainty in predicting the cell emfs while at the client laboratory, the uncertainty in comparing the client laboratory reference to the transport standard, and the uncertainty due to random changes in the cell emfs due to shipment. A pooled standard deviation of 0.19 μV has been computed from 50 transfers and is used as the population standard deviation. The calculated standard deviation for each new transfer is compared to the population standard deviation at the 99% confidence interval using an F-test. If the statistic is determined to belong to that population, then the population standard deviation of the mean is used as the uncertainty estimate; if not, the actual standard deviation of the mean is used. Thus the uncertainty estimate for a four cell transport standard, based on the population standard deviation, is $(0.19\ \mu V)/\sqrt{4}$ or 0.095 μV (0.093 ppm).

If the difference V(LAB)−V(NIST) exceeds 0.14 ppm (≈1.5 times the uncertainty based on the population standard deviation), the report will recommend adjusting the assigned values of the client reference cell emfs to reduce the difference to zero. Adjusted values for the client cell emfs are calculated based on the measurements made in the client laboratory comparing the client reference group to the NIST transport standard. Each comparison results in a determination of the difference of each client reference cell emf from the mean emf of the client reference group. The average difference for each cell, obtained from all the comparisons, is added to the newly determined mean emf of the reference group to calculate the new values for each of the client reference cells.

5.5 Uncertainty in the Calibration of Solid-State Standards

The ZCS measuring system was designed principally to measure voltage standards in the range of 5 to 10 V. Table 5 lists the sources of uncertainty in the measuring system extrapolated to the worst case unknown voltage in the 5 to 10 V range. The system may be used over the 1 to 5 V range but with somewhat reduced accuracy except when the unknown voltage is near a cardinal value (1.018, 2.036, 3.054,... V).

Table 5. Uncertainties in the assignment of the mean emf of a solid-state standard

Source of uncertainty	1 std. dev. estimate (ppm)
DVM gain uncertainty	0.020
DVM linearity uncertainty	0.062
DVM leakage/bias currents	0.023
Standard cell leakage currents	0.006
Scanner switch thermal emfs	0.013
Random uncertainty in calibrating the Transfer Reference	0.007
Random uncertainty in calibrating the client standard (within-day)	0.013
RSS subtotal	0.072
Uncertainty in value of the Working Group	0.040
Change in Working Group during the day	0.047
Uncertainty of the value assigned to the client standard RSS Total	0.095

By far the most critical component of the system is the digital voltmeter. The DVM gain of the 1-V range is measured during the course of the Zener measurements and the gain error is calculated and applied as a correction to the appropriate DVM readings. An allowance is included in table 5 for the inaccuracy of this gain measurement.

The DVM linearity was initially checked on the 10-V range using a calibrated, manual 7-dial Kelvin-Varley divider, and measurements on similar DVMs indicate little or no change in the linearity with time. The linearity error is typically a maximum of 0.7 ppm or less at half-scale input and no correction to the data is made for it. Provision has been made for the system to calibrate automatically the linearity of the DVM at 10 points on the 10-V range by measuring the 10 voltages 1.018, 2.036, ..., 10.18 V, although this has not been necessary. Estimates of the uncertainties for the other sources of error are calculated as described previously.

6. Quality Control Procedures

Several additional quality control procedures are performed periodically to estimate or eliminate potential sources of error in the measurement systems that may go undetected by the redundant measurement designs. These procedures include measuring the scaling or gain errors in the digital voltmeters, the uncompensated thermal emfs in the crossbar switches and input leads, the leakage currents to ground from the measurement apparatus, and the circulating ground currents.

Before each daily set of cell comparisons each cell measurement system reads the output of its own 1000 μV Zener source to monitor the gain error of the 0.1 V range of the digital voltmeter. All voltmeter measurements are taken with the applied voltage in the normal polarity and again with the polarity reversed by the crossbar switch to eliminate any uncertainty due to zero offset of the voltmeter and thermal emfs in the leads to the voltmeter. The daily measured values of the 1000 μV source are plotted on a control chart and compared to predetermined limits. The gain error of the DVM in the solid-state measurement system (ZCS) is evaluated and corrected at the time of the measurement as described in section 2.

Thermal emfs in the leads from the client standards to the crossbar switch are evaluated regularly. The positive and negative leads are shorted together at the end where they would normally connect to the standard and a redundant measurement design is made between two sets of shorted leads. These thermal emf measurements are performed frequently, usually every 2 months or so as cell enclosures leave the laboratory and leads become free. Experience has shown that the thermal emfs in individual switches are usually small and fairly constant (typically less than 15 and 30 nV for measuring systems VTP and REG, respectively).

A standard cell group that can be used exclusively as a long term check standard is not available because of a shortage of good quality temperature regulated enclosures and long-term stable cells. Instead, the daily change in the average emf of the cell workload is calculated and compared to control limits. For the solid-state measuring system, a 10-V standard that is not moved is measured every day as part of the workload and serves as a check standard to monitor the long term stability of the measurement system.

Additional tests are also occasionally performed on the automated cell systems. Measurements of the insulation/leakage resistance of the measuring systems are done and recorded in laboratory notebooks. Closure experiments are done monthly (at least) to detect systematic errors due to leakage resistance. Closure experiments consist of redundantly comparing three cell enclosures with the pattern, A-B, B-C, and C-A. Summing the three mean emf differences should yield a value of zero; the deviation of the actual value from zero is an indication of measurement error. Using 24 such experiments performed on different enclosures between July 17, 1986 and October 1, 1986, the mean closure error was determined to be −0.9 nV with a standard deviation of the mean of 1.7 nV.

7. Conclusions

We are currently calibrating about 400 voltage standards per year. Although the measurement of the standards and the initial data reduction are nearly fully automated, the final analysis of the data and the generation of test reports still requires considerable attention from NIST laboratory personnel. We are presently in the process of developing advanced data handling and reduction tools (i.e., computer programs) to minimize the staff time required to generate the test reports.

About the author: Dr Bruce F. Field is an electronics engineer in the Electricity Division of the NIST Center for Electrical and Electronics Engineering, National Engineering Laboratory.

8. References

[1] Hamer, W. J., Standard cells, their construction, maintenance, and characteristics, Natl. Bur. Stand. (U.S.) Monogr. 84 (1965) 38 pp.

[2] Field, B. F., NBS Measurement Services: Standard Cell Calibrations, Natl. Bur. Stand. (U.S.) Spec. Pub. 250-24 (1987) 52 pp.

[3] Field, B. F., NBS Measurement Services: Solid-State DC Voltage Standard Calibrations, Natl. Bur. Stand. (U.S.) Spec. Pub. 250-28 (1988) 39 pp.

[4] Quinn, T. J., Metrologia **26**, 69 (1989).

[5] Eicke, W. G., and Cameron, J. M., Designs for Intercomparing Small Groups of Saturated Standard Cells, Natl. Bur. Stand. (U.S.) Tech. Note 430 (1967) 19 pp.
[6] Standard Digital Interface for Programmable Instrumentation, ANSI/IEEE 488.1 (1987).
[7] Field, B. F., IEEE Trans. Instrum. Meas. **IM-34**, 327 (1985).
[8] Belecki, N. B., Dziuba, R. F., Field, B. F., and Taylor, B. N., Guidelines for Implementing the New Representations of the Volt and Ohm Effective January 1, 1990, Natl. Inst. Stand. Tech. (U.S.), Tech. Note 1263 (1989) 72 pp.
[9] Steiner, R. L., and Field, B. F., IEEE Trans. Instrum. Meas. **IM-38**, 296 (1989).
[10] Taylor, B. N., and Witt, T. J., Metrologia **26**, 47 (1989).
[11] Hamilton, C. A., Kautz, R. L., and Lloyd, F. L., IEEE Elec. Dev. Lett. **EDL-6**, 623 (1985).
[12] Hamilton, C. A., Kautz, R. L., Lloyd, F. L., Steiner, R. L., and Field, B. F., IEEE Trans. Instrum. Meas. **IM-36**, 258 (1987).

Volume 95, Number 3, May–June 1990
Journal of Research of the National Institute of Standards and Technology

[J. Res. Natl. Inst. Stand. Technol. 95, 255 (1990)]

NBS/NIST Gas Thermometry From 0 to 660 °C

Volume 95 Number 3 May–June 1990

J. F. Schooley

National Institute of Standards and Technology,
Gaithersburg, MD 20899

In the NBS/NIST Gas Thermometry program, constant-volume gas thermometers, a unique mercury manometer, and a highly accurate thermal expansion apparatus have been employed to evaluate temperatures on the Kelvin Thermodynamic Temperature Scale (KTTS) that correspond to particular temperatures on the 1968 International Practical Temperature Scale (IPTS-68). In this paper, we present a summary of the NBS/NIST Gas Thermometry project, which originated with planning activities in the late 1920s and was completed by measurements of the differences *t*(KTTS)-*t*(IPTS-68) in the range 0 to 660 °C. Early results of this project were the first to demonstrate the surprisingly large inaccuracy of the IPTS-68 with respect to the KTTS above 0 °C. Advances in several different measurement techniques, development of new, specialized instruments, and two distinct sets of gas thermometry observations have resulted from the project.

Key words: gas thermometer; IPTS-68; thermodynamic temperature; thermometry.

Accepted: January 18, 1990

Contents

1. Introduction

The terms "thermodynamic temperature" and "absolute temperature" are used synonymously to refer to the parameter that occurs in many theoretical equations in physics and chemistry. By the middle of the 19th century, Carnot, Kelvin, and others had elucidated the principles of thermodynamics, and Kelvin had devised a universal scale of temperature that could be shown to be independent of the properties of any particular material [1]. His scale was very general, depending only upon the efficiency of Carnot's ideal heat engine; a natural consequence of his idea was the existence of an absolute zero of temperature defined by the absence of any heat energy in the substance under test.

Kelvin suggested that his scale could be particularized by specifying a number value for some reproducible state of matter; taking note of contemporary work on the thermal expansion of gases between 0 and 100 °C (the freezing and boiling points of water on the centigrade scale that was then in common use), he suggested that a workable thermodynamic scale could be obtained by adding 273 to all temperature values obtained by use of that centigrade scale.

The fact that the thermal expansion of gases was an important topic in 19th century science made the gas thermometer a natural choice for realizing Kelvin's new thermodynamic temperature scale. Measurements of thermodynamic temperature over a wide range can be performed with reasonable accuracy by use of gas thermometers, providing that proper account is taken of the properties of the real substances used in the experimental work. In principle, the ideal gas law,

$$PV=nRT, \tag{1}$$

where P represents the thermodynamic pressure, V stands for the volume of a bulb that contains n moles of an ideal gas, R denotes the gas constant, and T indicates the thermodynamic temperature, can be employed to realize the KTTS through the use of gas thermometers of various types. For instance, the unknown KTTS temperature T_u of a constant-pressure or a constant-volume gas thermometer can be evaluated approximately in terms of the Celsius reference temperature t_r by using the equation

$$T_\mathrm{u}=(t_\mathrm{u}+273)=(t_\mathrm{r}+273)(V[P,t_\mathrm{u}]/V[P,T_\mathrm{r}]) \tag{2}$$

or

$$T_\mathrm{u}=(t_\mathrm{u}+273)=(t_\mathrm{r}+273)(P[V,t_\mathrm{u}]/P[V,t_\mathrm{r}]), \tag{3}$$

respectively. Kelvin's original constant additive term, 273, approximately converts Celsius scale temperatures to thermodynamic Kelvin temperatures. In the constant-pressure case [eq (2)], the Kelvin reference temperature is multiplied by the ratio of volumes that contain a fixed number of moles of an ideal gas at a fixed pressure and at the unknown and reference temperatures, respectively, to produce a value of the unknown Kelvin temperature. In the constant-volume case [eq (3)], the multiplicative factor is the ratio of pressures at constant volume and at the two respective temperatures.

It is not difficult to discover that the simple equations given above apply only at a very elementary level of accuracy. For example, the present definition of the Kelvin Thermodynamic Temperature Scale assigns the value 273.16 K to the temperature of the triple point of water, so that the constant in eqs (2) and (3) must be modified accordingly. In addition, substantial corrections must be made to account for the facts that real gases do not behave ideally over any considerable range of temperature, so that so-called "virial corrections" must be incorporated into the equations; that gas bulb materials undergo thermal expansion as well as dilation or contraction from any pressure differences that exist across the bulb walls, changing the actual volumes of the gas bulb; that "dead space" volumes inevitably enter gas thermometric apparatus and must be properly considered; that accurate pressure and volume measurements can be made only with great difficulty; and that laboratory instrumentation generally can be calibrated only within certain limits. As a result of these problems, the evaluation of thermodynamic temperatures by gas thermometry has always been uncertain, with 0.01% representing the limiting accuracy until the work of Guildner and Edsinger established a new level of accuracy for this method. Berry [2] and Kemp et al. [3] have since accomplished gas thermometry of similarly high quality to elucidate the KTTS in the range below 273 K. Beattie [4] has given a thorough discussion of the experimental problems inherent in performing accurate gas thermometry.

2. Principles of the NBS/NIST Gas Thermometer

Very little has been written about the origins of the NBS gas thermometry program. Although Guildner et al. [5] refer to early developments in precision manometry for gas thermometers at NBS by Cragoe, Godfrey, Meyers, and Thompson, only internal NBS reports [6] contain information about NBS gas thermometry studies prior to the brief description given by Stimson during the Third Temperature Symposium in 1954 [7]. These internal reports date from 1928; they reflect, even then, efforts to employ many of the primary features of the present NBS gas thermometer—the use of a mercury manometer for accurate measurements of the pressure ratios arising in the use of a constant-volume gas thermometer as given in eq (3), the use of gage block end standards to support the reference cell of the manometer, and the careful isolation of the gas thermometer system from both mechanical and thermal disturbances.

Most of the significant features of the manometer used in the present-day NBS gas thermometer can be observed in figure 1, taken from reference [7]. Although this figure actually portrays an NBS thermometer calibration facility dating from the early 1950s, Stimson notes that the manometer shown at the left of the figure was designed for precision gas-thermometer measurements. The manometer was contained in a mechanically isolated, temperature-controlled room. The measuring and reference mercury surfaces were placed in large, carefully designed cells. They were connected by a small mercury line that contained swivel joints to permit the raising and lowering of the upper cell. The mercury levels in both cells were sensed by capacitor plates. (Initially, interferometric sensing of the mercury levels was considered for the level-sensing, but the existence of ripples on the mercury surfaces—which never have been completely eliminated—spoiled the sensitivity of that method. In contrast, the use of capacitance level-sensing was shown to "average out" standing waves on the uneven mercury surface rather accurately.) Since the mercury surfaces in the upper and lower cells could be maintained at very nearly fixed, equal distances from the bases of the cells, the height of the mercury column in any measurement would depend only upon the height of the stack of end standard gage blocks and the verticality of the stack. Accurate knowledge of the overall pressure generated in the manometer depended as well, of course, upon accurate knowledge of the density of the mercury in the manometer and of the value of the gravitational constant at the location of the instrument. In turn, the "fixed, known density" requirement placed tight restrictions upon the cleanliness of the manometer system and upon regulation and measurement of its temperature.

Besides the specialized manometer system, figure 1 shows, in conjunction with the oxygen boiling-point apparatus, the use of a metal diaphragm to separate the manometer's working gas from the gas employed in the test environment. Once again, electrical capacitance was employed to sense position; the deviation of the differential pressure across the diaphragm was measured in terms of changes from the null-point capacitance between the diaphragm and a fixed reference plate in its casing.

In 1955, Stimson [7] estimated the levels of uncertainty that reasonably could be expected in the use of the NBS manometer. These include uncertainty in the density of mercury, about 20 ppm; in the gravitational constant, about 10 ppm, and in the end standards, about 2 ppm.

The original plan for the NBS gas thermometer was to measure the ratio of the pressures generated in the gas thermometer at two temperatures, one of which would approximate the ice point (later refined to the more precise triple point of water). By fixing the number of moles of gas involved and using the ratio technique, Stimson and his colleagues planned to employ a more advanced form of eq (3) to evaluate the unknown temperature in thermodynamic terms, relative to the first. Initial NBS discussions probed the possibility of using a gas-bulb material made of an alloy whose thermal expansion might be nearly zero over a limited range of temperature. They also considered the relative advantages of utilizing a working gas of known non-ideality, versus the technique of making measurements over such an extended range of filling pressures that an extrapolation to zero pressure might be valid.

3. Present Manometer and Its Uncertainties

The present NBS/NIST gas-thermometer manometer became a reality following the addition of L. A. Guildner, R. E. Edsinger, and R. L. Anderson to the NBS staff during the late 1950s [8]. Many refinements of the original manometer were incorporated into later versions by this group, as well as one completely new feature—a second

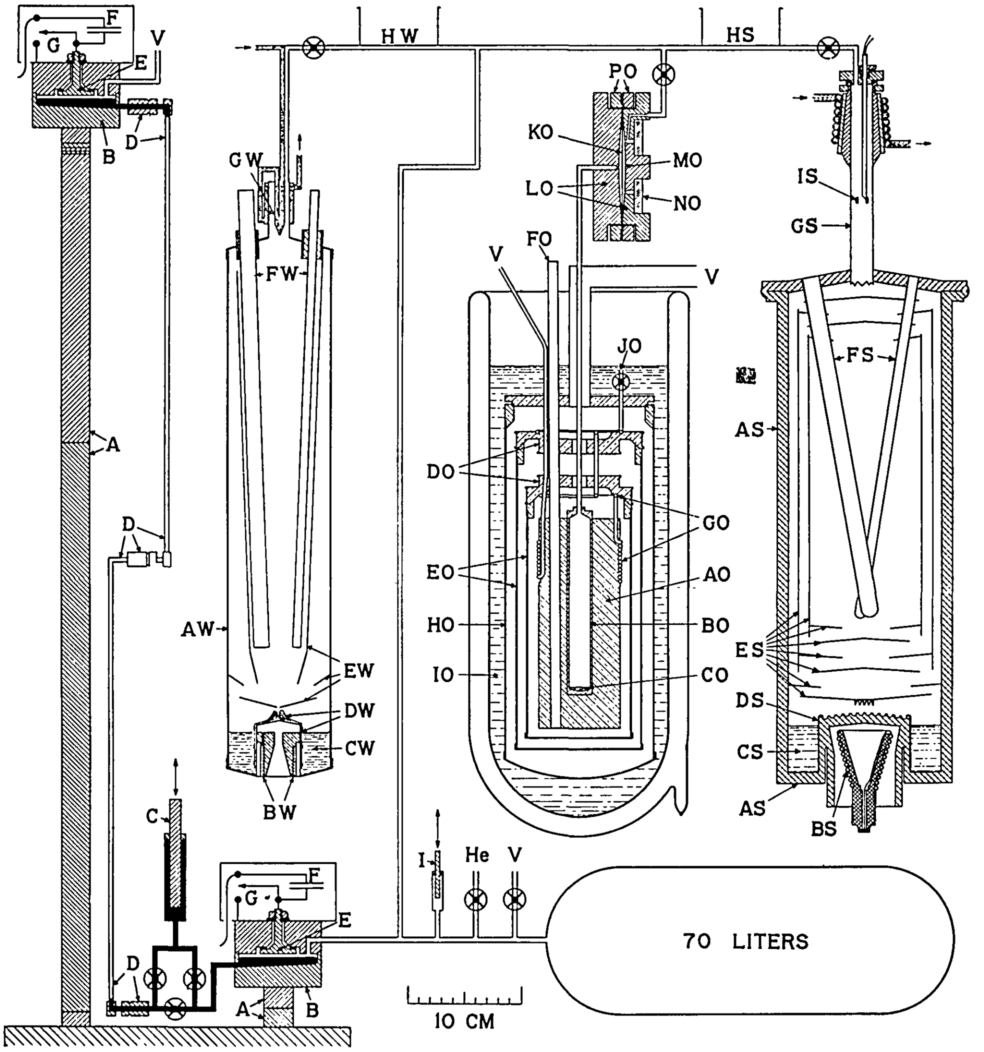

Figure 1. Diagram of NBS thermometer calibration apparatus used during the early 1950s. The diagram shows, from the left, a precision manometer that is similar in many respects to the one used in all of the NBS/NIST gas thermometry measurements, a steam-point boiler, an oxygen-point apparatus, and a sulfur-point boiler. A—End standard gage blocks, intended to be wrung together to define the cell separation. B—Large-meniscus (~7.3 cm inside diameter) mercury cells. C—Mercury pump for the adjustment of the mercury levels in the manometer. D—Movable mercury lines with rotating joints. E—Fixed capacitor plates for mercury level sensing. KO, LO, MO—Components of a capacitance diaphragm gage used to separate the helium gas used in the manometer from the oxygen used in the oxygen-point apparatus. (Reprinted from reference [7].)

lower mercury cell that served to evaluate the verticality of the gage-block stack.

The first detailed discussion of the components of the manometer system was published in 1965. This paper [9] noted the value of transformer ratio-arm bridges with three-lead capacitors for the precise measurement of capacitance, and it provided details of the construction and wiring of such a bridge as it applied to sensing the mercury level in a manometer and to determining the inside diameter of a relatively long metal capillary.

A schematic drawing of the capacitance bridge appears in figure 2. The bridge was especially designed to permit use of two test capacitors with one plate of each grounded, as would be the case in the manometer application. A double-shielding arrangement facilitated this design. In addition, elimination of the effects of capacitive coupling between the primary and secondary windings was achieved by the introduction of two electrostatic shields. Attention was also given to the problems involved in comparison measurements with a reference capaci-

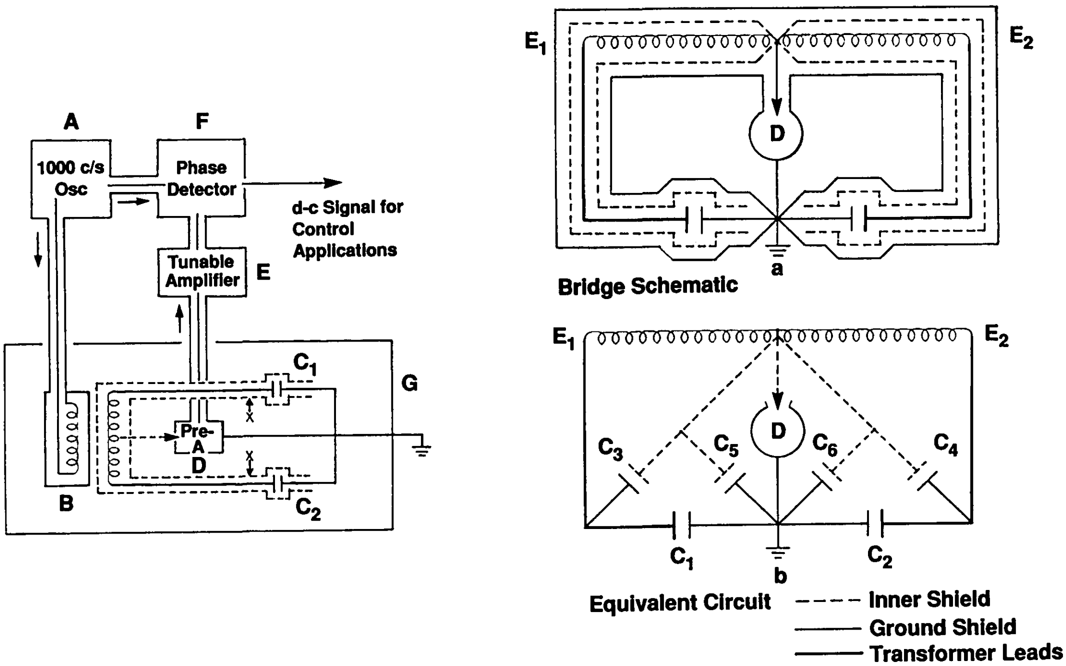

Figure 2. Left side—Block diagram of the capacitance bridge used to match the mercury levels in the gas thermometer manometer. Right side—Capacitance bridge schematic, shown without the primary windings (upper drawing), and its equivalent circuit (lower drawing). E_1, E_2—voltages opposite in phase, and with a ratio that is fixed within 1 ppm of the turns ratio. C_1, C_2—active capacitor elements. C_3, C_4—minimized capacitance between the inner shield and the transformer leads. C_5, C_6—minimized capacitances between the inner shield and the ground shield. D—High-impedance detector. (Reprinted from reference [9].)

tor. The estimated sensitivity of the bridge was 1×10^{-5} pF. The manometer pressure uncertainty arising from its use was estimated as not larger than 0.15 Pa.

A technique for utilizing fluorocarbon elastomers for high-vacuum seals in several articulating-arm and demountable-seal systems throughout the gas thermometer was discussed in a separate paper [10]. The seals were based upon the principle of stressing the fluorocarbon beyond its yield point; then it behaves as a highly viscous fluid, accommodating to mating surfaces even of relatively poor quality, and it also becomes much less porous, preventing leaks larger than 2×10^{-10} cc/s. Figure 3 shows the critical features of this type of seal. Polytetrafluoroethylene, which has a rather small coefficient of friction, was used in seals in which the component parts were intended to move, whereas polytrifluorochloroethylene was used in locking seals.

A full description of the manometer was published [5] in 1970. By that time, the instrument in its final form was installed and operating in the Gaithersburg gas thermometry laboratory of the NBS.

The manometer was installed in a specially prepared room below the basement of the Physics building at the new site. Figure 4 shows in schematic form a cross section of this two-level cellar, which provides protection from electromagnetic interference, from temperature inhomogeneity beyond the millikelvin level, and from most sources of vibration. The air conditioning flow moves through a multi-ducting system that incorporates temperature-controlled dampers; the relative humidity is held at 50% (referred to a temperature of 20 °C), and the temperature can be held constant within 2 mK/d.

The manometer itself was installed on a free-standing pier with a cap consisting of a sheet of steel 0.86 m square and 7.6 cm thick. An Invar[1] bar, resting upon knife edges, supports the two lower mercury cells and the gage block stack that in turn supports the upper cell. Great care was taken to provide flat, co-planar (within 0.1 μm) surfaces atop the Invar bar onto which could be wrung the

---

[1] Certain commercial equipment, instruments, or materials are identified in this paper to specify adequately the experimental procedure. Such identification does not imply recommendation or endorsement by the National Institute of Standards and Technology, nor does it imply that the materials or equipment identified are necessarily the best available for the purpose.

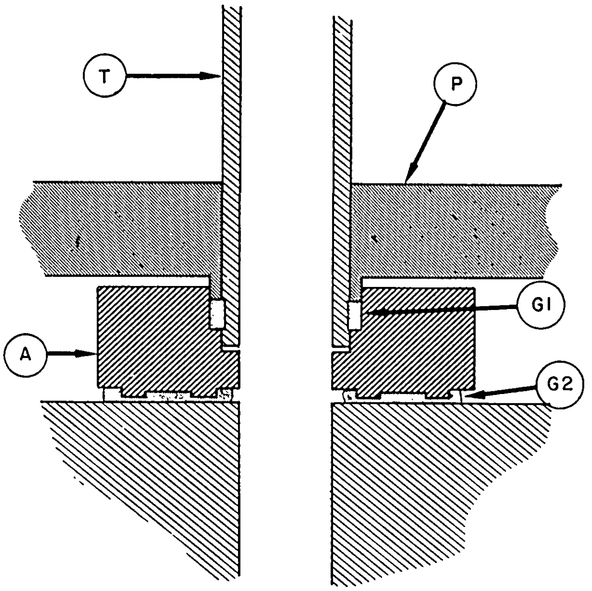

Figure 3. Details of two types of captured-elastomer seals used in the NBS/NIST manometer system. Ring A is fabricated with a land and groove on its bottom face and a compound receptacle for a locking seal on its top surface. Tube T is grooved to receive a polytrifluorochloroethylene gasket G1 which is then compressed by the force of a pusher P. The pusher also compresses polytetrafluoroethylene gasket G2. The total effect is to lock the tubing into a demountable assembly that both seals and locks it in place. (Reprinted from reference [10].)

cells and gage blocks. Provision was made for pumping a vacuum in axial holes in the gage blocks as a check on the quality of the wringing. The temperature of the manometer is measured by a dedicated platinum resistance thermometer, while the stability of the articulating-arm system is determined from measurements of a set of thermocouple thermometers arrayed along the arms. Operation of the manometer can be accomplished from the main laboratory control panel.

Details of the capacitance level-sensing and other techniques used in the construction of the mercury cells are illustrated in figure 5. The flatness of the mercury meniscus, the effect of ripples on the measured height of the mercury, and the stability of the mercury level afforded by this technique are discussed in some detail.

Also discussed in the 1970 paper are the components of uncertainty that make up the overall accuracy of the manometer when it is used as a part of the gas thermometer in the range 10-130 kPa (0.1-1.3 atm). In table 1 is given a short summary of this analysis. Note that the overall uncertainty of the manometer as a pressure standard is approximately 2 ppm; the uncertainty drops to 1.5 ppm if the manometer is used to compare pressures.

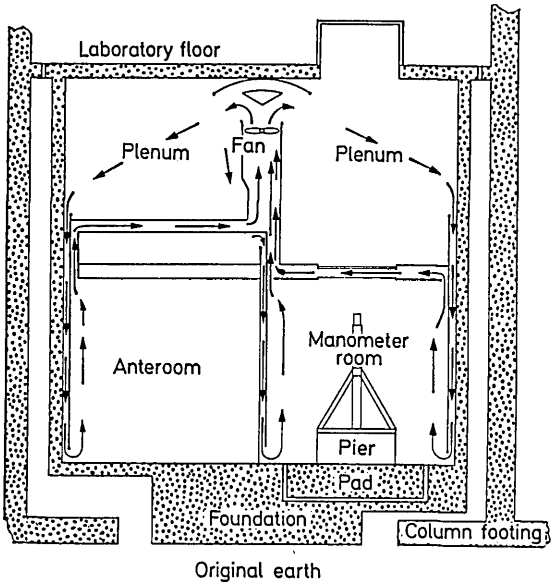

Figure 4. Schematic cross-section of manometer cellar beneath the NBS/NIST gas thermometer laboratory. The manometer is mounted upon a concrete pier that was made separate from the laboratory building to minimize vibration. A dedicated air conditioning system, vigorous air circulation, multi-point air-temperature sensing, and carefully designed controllers maintain millikelvin stability in the cellar temperature. The anteroom is used to temper and store a collection of end standard gage blocks and as a toolroom. (Reprinted from reference [5].)

4. First NBS Gas Thermometer

In its first version, the gas-bulb/thermostat assembly of the NBS/NIST gas thermometer had been intended to consist of a spherical gas bulb with a heavy protective casing, enclosed by a multi-layered, electrically heated furnace. The furnace was to be placed above the manometer connection [8]. The spherical shape is a strong one, and it permits relatively simple thermal expansion corrections to the bulb volume. The protective casing would allow a thin layer of gas at the working pressure to surround the gas bulb as a guard against pressure deformation of the bulb. Connecting the capillary to the bottom of the gas bulb and placing the assembly above the level of the pressure sensor would then minimize the likelihood of convective heat flow within the capillary, allowing it to be made slightly larger in diameter than would be the case if the temperature gradient were reversed. In practice, however, both the shape and the positioning of the thermometer were modified; machining and assembly of a protected spherical gas bulb and the establishment of a homogeneous temperature environment within a multi-shell configuration

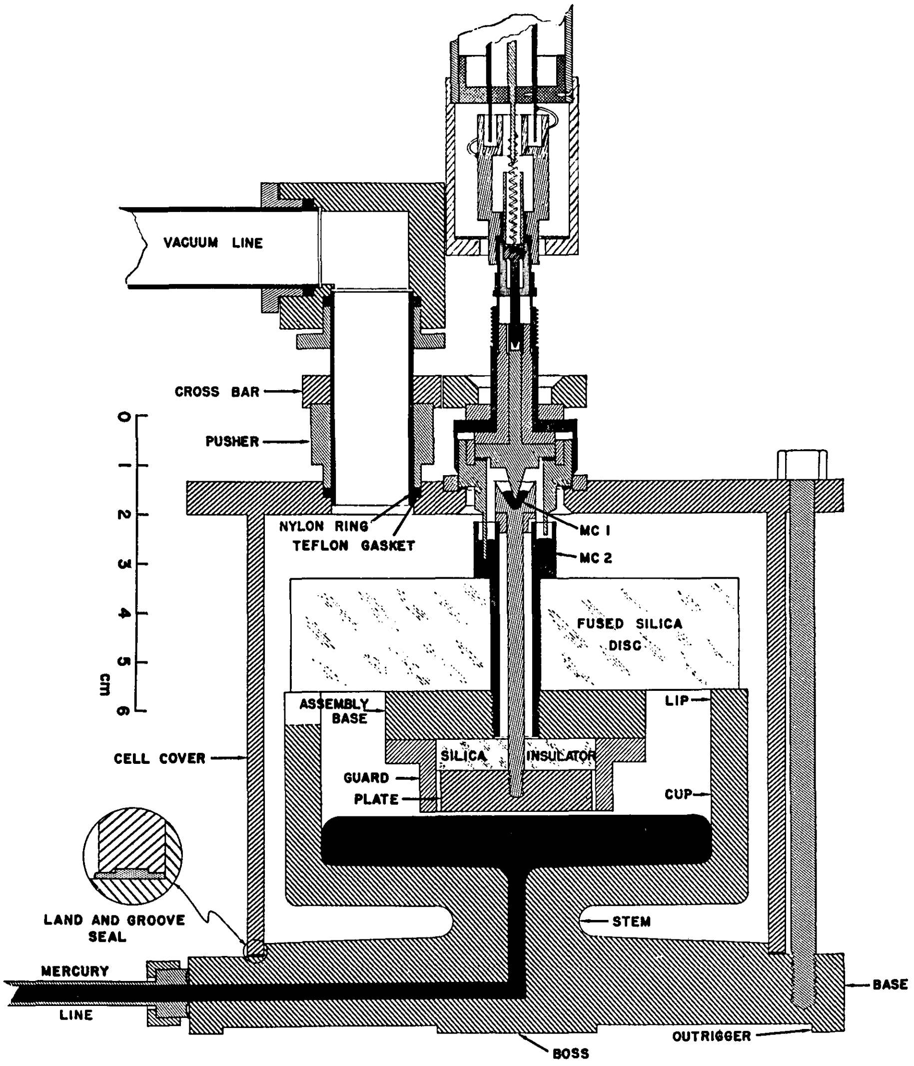

Figure 5. Cross-section of upper mercury manometer cell, showing details of the three-lead capacitance level measurement and the seals. The mercury cup was designed to maintain a stable position independent of pressure, and to be wrung to a gage block at the bottom and to a fused silica mounting disc at the top. Wringing the components of the capacitance level-detection assembly to the fused silica disc minimized the likelihood of drift in the mercury level, as well as deviations from co-planarity between the mercury surface and the capacitor plate. Mercury contacts MC1 and MC2 minimized stress arising from stiffness in the electrical contacts. (Reprinted from reference [5].)

proved difficult. Therefore, a cylindrical bulb protected by a cylindrical casing and the use of stirred-liquid thermostat baths, entered from the top, were adopted.

The first working version of the NBS/NIST gas thermometer [11] made use of the manometer as described in the previous section. Gage blocks for use in the manometer were specially calibrated (with an estimated uncertainty of ±0.3 ppm) by the NBS Dimensional Metrology Laboratory. The acceleration due to gravity at the location of the manometer was measured by the U.S. Geological Survey (with an estimated uncertainty of ±0.5 ppm). A 5-m tube, with an accompanying set of thermocouple thermometers to establish its temperature profile, was installed to carry the manometer gas (^{4}He) from the manometer cellar to the upper laboratory level. Remote control of the operating valves for opening and closing the mercury connections between the manometer cells from the upper laboratory was arranged. Finally, the capacitance bridge for monitoring the mercury levels

Table 1. Estimated uncertainties associated with mercury manometer

Feature	Uncertainty
Angle of bottom boss with respect to the mercury cell.	3 μ rad
Co-planarity of level-sensing capacitor and its guard.	6.6 mPa
Maximum depression of meniscus.	0.013 mPa
Maximum effect of ripples on measured meniscus height.	0.13 mPa
Maximum effect of tilt of sensing capacitor on measured miniscus height.	0.13 mPa
Maximum difference in electrostatic attraction effect between upper and lower cells.	0.06 mPa
Maximum effect of tilt of base on measured mercury height.	0.13 mPa
Maximum uncertainty of mercury level resulting from capacitance bridge imbalance.	0.12 Pa
Maximum flexure of Invar base as a result of weight of gage blocks under upper cell.	13 nm/atm
Maximum angle of wrung gage-block joints.	1 μ rad
Maximum temperature drift in cellar.	2 mK/d
Maximum uncertainty in ratio of gage-block heights at two measured temperatures.	0.5 ppm
Maximum uncertainty in ratio of mercury densities at two measured temperatures.	0.5 ppm
Maximum uncertainty in ratio of hydrostatic heads in measuring arm of manometer at two measured temperatures.	0.3 ppm
Overall uncertainty as a pressure-ratio device, (99+% confidence level)	1.5 ppm
Note that, for the measurement of a single pressure, the uncertainties are larger:	
Maximum uncertainty in mercury density.	1 ppm
Maximum uncertainty in mercury height.	0.5 ppm
Maximum uncertainty in gravitational acceleration.	0.5 ppm
Maximum uncertainty in hydrostatic head depends upon the situation; if the gas-tube height is known to 1 cm and the temperature profile for helium gas is known to 0.5 K, then	0.3 ppm
Overall uncertainty as a pressure standard, (99+% confidence level)	2 ppm

"With helium gas, the manometer operates as an absolute measuring device over the range 10–130 kPa with an (uncertainty) of about 2 ppm, and as a ratio device with an (uncertainty) of about 1.5 ppm. (Further improvement in this range) depends upon improvement in the measurement of the density of mercury, the acceleration of gravity, and in length metrology" [5].

(and a mechanism for slightly adjusting those levels) was installed in the upper laboratory. Thus, once the gage blocks appropriate for the production of a desired pressure were chosen and assembled into the manometer, final checking and adjustment of both the mercury level and the working gas pressure could be performed from the upper laboratory without disturbing the temperature in the manometer cellar.

The manometer was separated from the gas thermometer bulb by the diaphragm of a capacitance diaphragm gage, by a set of constant-volume valves, and by a capillary tube. The gas bulb could be lowered by a hydraulic mechanism into any of several movable variable-temperature baths; both the bulb and its connecting capillary were protected from exposure to the bath liquids by protective casings made of Inconel.

A schematic diagram of the gas bulb, its protective casing, and a portion of the gas handling and analysis system is shown in figure 6. The gas bulb was a relatively thin-walled (0.94 mm sides and bottom, 2.79 mm top) right circular cylinder of Pt-Rh alloy; its volume was about 430 mL. Most versions were constructed from sheets of a single alloy (80 Wt% Pt, 20 Wt% Rh) or (88 Wt% Pt, 12 Wt% Rh), although in one case, the bulb inadvertently was fabricated from two different alloys. The working gas in all cases was ^{4}He. Use of a residual gas analyzer allowed the evaluation of the purity of the working gas at a level sufficient to improve markedly the accuracy of the gas thermometer.

The designs of the gas bulb, the capillary, and the protective casing were intended to provide several results, as shown in figure 7. The Pt-Rh alloy composition was chosen for its uniform thermomechanical properties, its high-temperature stability, and its stiffness relative to that of pure platinum. As mentioned above, the cylindrical shape of the bulb allowed for closer tolerances in construction and for greater ease in assembly than the spherical shape first considered. The flat top of the bulb was

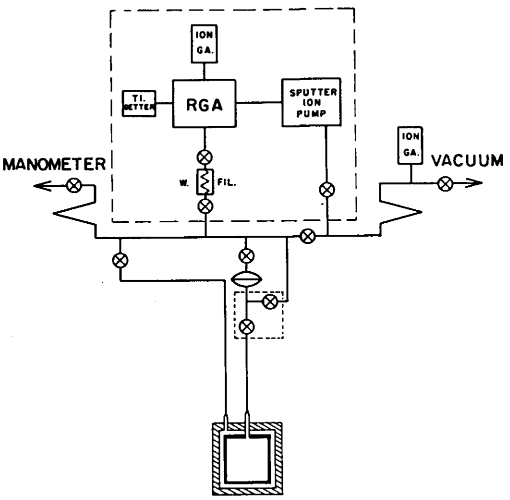

Figure 6. Elements of the first NBS/NIST gas thermometer. The gas bulb, a right circular cylinder of volume about 450 cm^3, was made from sheets of a platinum-rhodium alloy. It was surrounded by a heavy casing of Inconel. Constant-volume valves and a capacitance diaphragm gage separated the gas bulb from the manometer and from a gas purification and analysis system composed of a tungsten filament, a titanium getter, and a residual gas analyzer pumped by an ion pump. (Reprinted from reference [11].)

made of 2.8-mm stock to give it reasonable strength against deformation; by making the sides and bottom of thinner material (~1 mm) than the top, one could achieve a faster thermal response and a lighter weight to be suspended from the top. The capillary was made of approximately 1.6 mm o.d., 0.9 mm i.d. tubing of 90 Wt% Pt/10 Wt% Rh alloy. Use of that alloy for the capillary itself permitted the formation of a series of Type S thermocouple junctions along the capillary by simply welding Pt wire to the tube at appropriate intervals, and insulating the gas bulb, the capillary, and the wires from the Inconel protecting case and tube. Provision was also made for the difference in thermal expansion between the capillary and its Inconel protection tube. The gas bulb was isolated from the thermostating bath fluids and from pressure imbalances across its wall by a close-fitting, heavy-walled Inconel case. The wall of the protective case provided wells for four standard platinum resistance thermometers. The helium working gas was purified by passing it through molecular sieve material held at 78 K; its purity was evaluated through the use of a residual gas analyzer. As mentioned above, the working gas was separated from the manometer gas, also ^{4}He, by a brass diaphragm whose position was monitored by a capacitance plate, forming a capacitance diaphragm gage. With its use, measurement of the pressure null was found to be accurate within approximately 4 mPa (0.03 μm Hg).

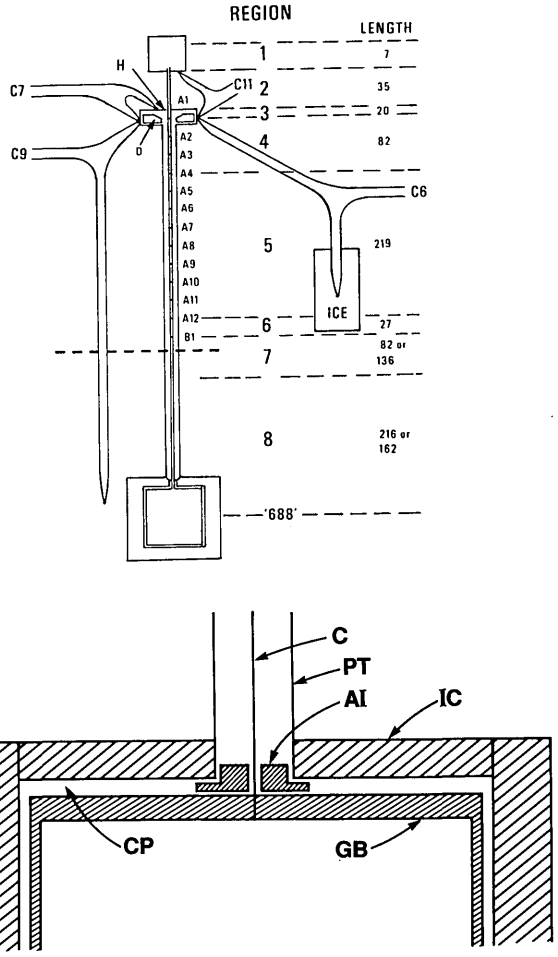

Figure 7. Schematic drawings of the NBS gas thermometer gas-bulb assembly and the capillary temperature-profile measurement system used with the stirred-liquid thermostat baths. The upper portion of the figure, reprinted from reference 21, shows the gas bulb and capillary with their protective casings. Sliding seal H allowed for the difference in thermal expansion between the capillary and its protective case. The drawing also shows the location of Pt wires welded to the capillary to form Pt vs. (Pt+10 Wt% Rh) thermocouple thermometers A1-A12 and B1, used to determine the temperature distribution along the capillary. The lower portion of the figure shows details of the gas thermometer construction in the region of the connection between the gas bulb GB and the capillary C, both made of Pt-Rh alloys. The capillary protection tube PT and the gas-bulb protective casing IC were made of Inconel alloy. AI denotes an alumina collar used to insulate the bulb electrically from the case and to create a gap CP between them. The gap, known as the counterpressure space, was filled with ^{4}He gas held at the gas-bulb pressure. Both the bulb and case were constructed by welding, using the heliarc technique.

Details of an application of the three-lead capacitance bridge (see sec. 3) employed to minimize the uncertainty of the dead-space correction in the gas thermometer were given in a 1971 paper [12]. In this application, the average diameter of the capillary tubing (see fig. 7) used to communicate the gas-bulb pressure to the manometer could be measured accurately within $\pm 6\times 10^{-5}$ cm. The measurements were accomplished before assembly by the introduction into the capillary of a carefully designed probe; the capacitance between the probe and the tube could be measured as a function of the tube length. This information, coupled with the temperature profile obtained by the use of the thermocouples shown in figure 7, permitted detailed calculation (at ~1-mm intervals) of the capillary dead-space correction to be made. The method used to compute the dead-space correction from this source follows. The total quantity of gas in the gas thermometer during any particular measurement, n_0, can be separated into two portions

$$n_0=n_\mathrm{b}+n_\mathrm{ds}, \tag{4}$$

where n_b denotes that portion of the gas that is contained in the gas bulb itself and thus is maintained at a uniform temperature, and n_ds denotes the portion of the gas that is contained in the "dead space," that volume of the gas thermometer that experiences a temperature different from that of the gas bulb. The dead space in the NBS/NIST gas thermometer comprises the capillary up to the first valve, as shown in figure 6. Although it might be expected that the dead space would include one side of the capacitance diaphragm gage and the tube that connects it to the first valve, such need not be the case. If the pressure of the gas above the first valve is made equal to the pressure below the valve whenever it is to be opened, then no gas will pass through the valve during a set of measurements, and the gas thermometer may be considered to terminate at the first valve. In fact, this technique was used consistently throughout the NBS/NIST Gas Thermometry program.

For the capillary gas

$$n_\mathrm{ds}=[P_0/R][\sum_k\{V_k(1+\beta_k t_k)\theta_k\}]. \tag{5}$$

In eq (5), P_0 denotes the gas pressure at the capacitance diaphragm gage above the gas bulb, R stands for the gas constant, V_k represents the volumes at 0 °C of approximately 1-mm segments (see fig. 7) of the capillary as measured capacitatively, β_k indicates the average volume thermal expansion of the capillary material from 0 °C to t_k, the Celsius temperatures of the capillary segments that are determined from measurements on thermocouples A1-B10, θ_k indicate Celsius-to-Kelvin temperature conversion factors, and the summation occurs over the length of the capillary from the gas bulb up to the first valve.

In order to restrict the effective dead space of the gas thermometer to the capillary, as described above, it was necessary to design a small, constant-volume valve to separate the gas bulb from the pressure-measurement system. The aim of the NBS workers was to limit the uncertainty in the ratio of the dead-space volume in the valve system to the volume of the gas bulb to 1 ppm. To accomplish this purpose, Anderson and Guildner designed a valve whose volume is constant within 0.1 mm^3 at any position [13]. Details of the valve design are shown in figure 8.

Carefully designed, stirred liquid baths capable of temperature homogeneity at the level of a millidegree or so at temperatures up to 500 °C have been described by Beattie [14]. Baths of similar design were built for the NBS/NIST gas thermometer. Each bath was enclosed in a large, heavy container that was fitted with wheels. The bath enclosure rested upon firebrick and was encircled by a helically coiled outer heater wire. Mineral insulation retarded radial heat flow to the outer shell. A steady voltage was applied to the outer heater at such a level that the bath temperature reached 2–3 °C below the desired value. A regulating heater took the form of a second helical coil that surrounded a central flow-directing cylinder that was open at both ends. At the bottom of the cylinder, a high-speed stirrer circulated the bath liquid, which flowed upwards past the gas thermometer assembly, outwards to the edge of the bath, and downwards to the bottom again. The gas thermometer assembly and the platinum resistance thermometers were thus continually bathed by the tempering bath liquid. The baths built with this design provided stable temperature environments for the gas bulb; the measured gas thermometer temperature was found to remain steady over a typical 1-week period within 0.4 mK, and within 0.04 mK over a typical 2-h period. Use of this type of thermal environment for the gas thermometer bulb, however, necessitated the construction of a hydraulic lifting system for the bulb assembly and the installation of articulating vacuum joints for the working gas lines. The latter were made similar to those employed in the manometer.

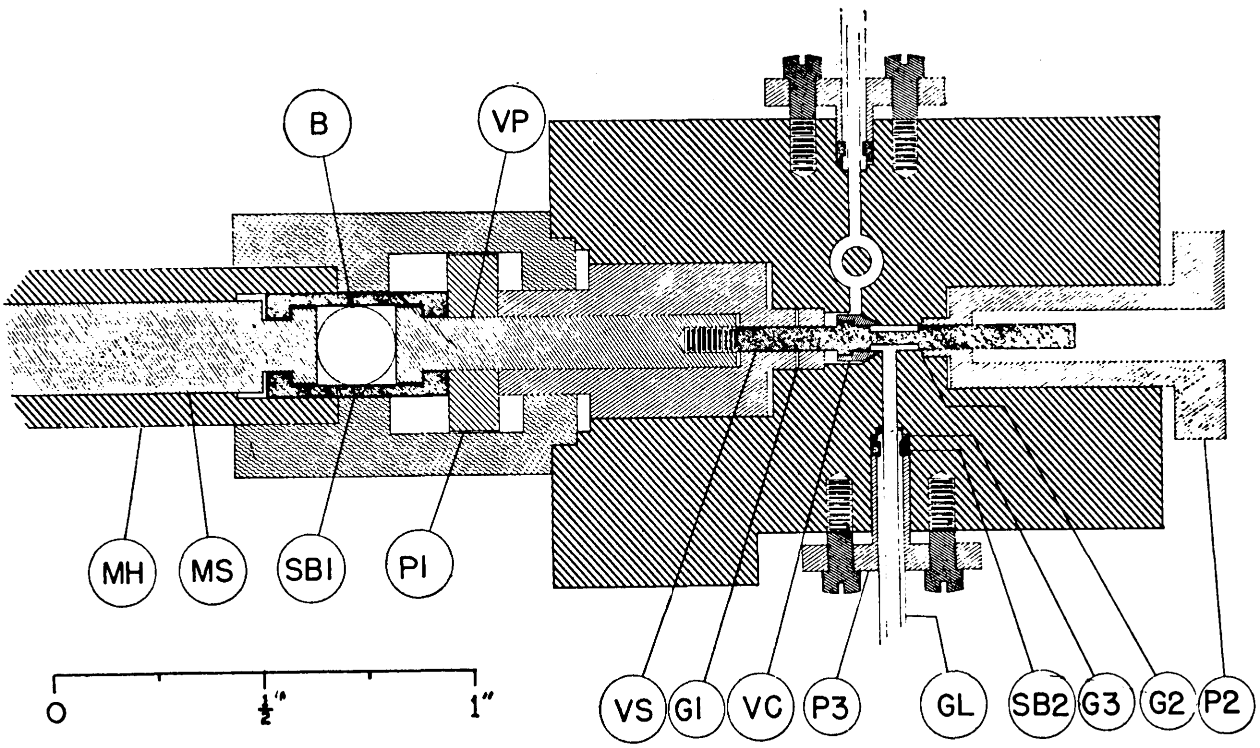

Figure 8. Cross section of constant-volume valve. A micrometer head, MH, is graduated in units of 0.0001". It moves the spindle, MS, which in turn moves a steel ball, B, a push rod, VP, and the valve stem, VS. The valve cone, VC, was made with an included angle of 58 ° so that it would seal near its tip into a 60 ° seating hole. The stem is made uniform within ±0.00013 mm in diameter in order to ensure constant volume within 0.005 mm^3. (Reprinted from reference [13].)

5. Scale Differences From 0 to 142 °C

After flushing the gas bulb with purified helium, it was necessary to spend a full month pumping the bulb to remove contaminating gases before commencing a set of gas thermometer measurements. After such a vacuum bakeout, however, a week's isolation of the gas bulb resulted in a pressure rise of only 0.03 Pa. In preparation for a run, the gas bulb was filled with purified helium gas at the highest temperature to be measured, its pressure was verified over a three-hour period, and the bulb temperature on the IPTS-68 was recorded by three platinum resistance thermometers (PRTs) prior to reducing the bulb temperature to a lower unknown temperature or to the reference value near 0 °C. In these first experiments, six different filling pressures were used for each KTTS temperature that was to be determined. By plotting the apparent gas thermometer temperature as a function of pressure, Guildner, Anderson, and Edsinger could extrapolate the results to zero pressure with confidence, obviating the need for highly accurate second-virial-coefficient data on the ^{4}He working gas.

The care with which the gas bulb and the gas purification and handling systems were prepared, together with the availability of sensitive in-line gas analysis equipment, paid immediate dividends as the first determinations of the steam-point temperature relative to the ice point were completed [11].

Three different gas bulbs were employed in this first series of measurements; the third was constructed so as to permit vacuum bakeout at temperatures as high as 800 °C. The KTTS temperature corresponding to the steam point as determined from the gas thermometer was found to decrease noticeably as the gas bulb cleanup proceeded. Eventually, the results stabilized. At that juncture, the steam point registered 99.973 °C on the thermodynamic Celsius scale, indicating that the International Practical Temperature Scale of 1968 was too high by 0.027 °C.

Because the Gas Thermometry group had not measured the thermal expansion of the metal from which the gas bulb had been constructed, and because they were not yet convinced that they had effectively eliminated the problem of sorption of impurity gases, they refrained from attaching an overall uncertainty to this first determination of the steam point. Nevertheless, it was apparent that the IPTS-68 might not have been as close an approximation to the Kelvin Thermodynamic Temperature Scale as had been generally thought (the estimated thermodynamic uncertainty of the IPTS-68 at the steam point had been assigned—conservatively, it had been supposed—as ±0.005 °C when the scale was formulated). Also apparent was the importance of cleanliness and the elimination from thermodynamic gas thermometry of sorbable impurities, which show such deviations from ideality that their presence had noticeably compromised most of the earlier work of this type.

After the gas thermometer measurements at the steam-point temperature were completed, Guildner and Edsinger [15] quickly introduced a new thermostated bath in which the fluid was a solution of water and potassium chromate. With this bath, they extended the study of the differences between the KTTS and the IPTS-68 to cover the range 0 to 142 °C.

In completing this portion of the study, they also improved the method of purifying the ^{4}He working gas: the gas was made to pass through a trap containing Ti chips held at 900 °C, where chemically reactive substances would combine with the Ti to form non-volatile compounds and, in some cases, hydrogen gas; then through a CuO trap, also held at 900 °C, to convert the hydrogen to water; and finally through a cooled (78 K) zeolite trap, to adsorb the water. They also arranged to allow the ion pumps to be valved off from the gas system to avoid possible contamination by outgassing when the ion pumps were turned off. As before, pressure-ratio measurements were made at several gas filling pressures, allowing extrapolation of the results to zero pressure.

The differences between the derived values of the Kelvin thermodynamic scale and the IPTS-68 over the range 0 to 142 °C were expressed [15] as

$$t(\mathrm{KTTS})-t(\mathrm{IPTS\text{-}68})=-1.57478\times10^{-4}t -2.04508\times10^{-6}t^2+6.08088\times10^{-9}t^3\ ^\circ\mathrm{C}. \quad (6)$$

The thermodynamic value of the steam point was given as 99.970±0.0035 °C at the 99% confidence level. The authors noted that, since it had been desired to maintain a truly centigrade International Temperature Scale (i.e., to maintain the ice and steam points exactly 100 Celsius degrees apart), then the ice point temperature should have been given the value 273.23 K rather than 273.15 K when the IPTS-68 was prepared. They also acknowledged that their present and future results on the KTTS could be incorporated into a table or equation of differences between that scale and the International one, rather than by replacing the International Scale with one that more closely approximates thermodynamic temperatures.

6. Second Version of the NBS/NIST Gas Thermometer

As a result of the experience gained in measurements to 142 °C, many other changes were made in the NBS/NIST gas thermometer and in the procedures for its use. Some of the changes were concerned with the problems of making measurements at still higher temperatures; others resulted from a desire to improve the quality of the observations.

Among the changes in equipment were the following:

- improvements in the ^{4}He pumping system, both in capacity and flexibility;
- new thermostated bath for gas-bulb temperature equilibration;
- addition of an ac resistance bridge for PRT measurements and a digital voltmeter for thermocouple emf measurements; and
- addition of a thermomolecular-pressure-effect measurement capability.

Procedural changes during this period included:

- care to exclude sources of hydrogen gas from the gas-bulb environment;
- care to avoid pressure inequalities across the gas-bulb wall, particularly above 327 °C;
- greater use of "integrity checks" to discover the presence of impurity gases or leaks in the gas thermometer;
- use of an improved procedure for evaluation of the dead-space correction;
- use of greater care in handling and evaluating PRTs;
- use of virial coefficients to calculate the non-ideality correction for ^{4}He instead of multiple pressure values in the gas thermometer measurements; and
- introduction of computers for data analysis.

6.1 Fused Salt Bath

In order to attain still higher temperatures in the gas thermometer bulb assembly, Guildner and Edsinger built a stirred liquid bath of the same general type described in section 4, but containing as the bath medium a eutectic mixture of lithium, sodium, and potassium nitrates. The use of this medium for thermostat baths has been described briefly by Beattie [14]. As before, the gas bulb assembly, along with the constant-volume valve block, the thermostated capacitance diaphragm gage, and the gas analysis system, was lifted hydraulically in order to change the environment from an ice/water or water/potassium-chromate bath to the fused salt bath.

The fused salt bath could be used only to 457 °C, owing to increasing tendencies of the liquid nitrate mixture to attack the thermometer sheaths and to migrate from the reservoir into the heater-insulator portion of the bath. Therefore, it was decided to investigate the temperature region from 0 to 457 °C before building a new thermostat for higher temperatures.

6.2 Thermal Expansion Measurements

Although the Pt-Rh alloys from which all the NBS/NIST gas bulbs have been fabricated are stable, high-temperature materials, they also exhibit large coefficients of thermal expansion. In order to determine thermodynamic temperatures at a level adequate for use in the NBS/NIST gas thermometry program, it was necessary for Guildner and his colleagues to obtain linear thermal expansion measurements from the gas-bulb materials over the entire range of the gas thermometry measurements with an accuracy approaching 1 ppm. This level of accuracy was not easy to achieve by use of ordinary thermal expansion equipment (even with Fizeau interferometry), because it utilized thermocouple sensors of limited accuracy [16,17].

During the mid-1960s, a special thermal expansion apparatus was designed and constructed for the accurate determination of the linear thermal expansion of materials from which NBS/NIST gas thermometer bulbs had been prepared. Based upon the principles of Fizeau interferometry and precision thermometry, that apparatus consisted of a sample chamber surrounded by a copper block that was in turn enclosed within some seven concentric thermal shields [18,19]. Figure 9 shows the dilatometer furnace that enclosed the sample, figure 10 shows the interferometer that was employed to observe and register the sample thermal expansion, and figure 11 shows the sample assembly and the fringe pattern as recorded on panchromatic film. Temperature control of the sample was achieved by manual adjustment of some nine heaters located on the three inner shells of the furnace; the settings were arranged to minimize the interior temperature gradients as indicated by sets of differential thermocouples. The sample temperature was measured with an estimated accuracy of 0.01 °C by use of a specially constructed platinum resistance thermometer. Use of a homemade fringe-reading system allowed measurement of the sample thermal expansion with an imprecision of about 0.01 fringe.

Accurate determination of thermal expansion with the apparatus described above was a complicated process. It involved careful preparation of samples so as to obtain a suitable fringe pattern; recording on film the fringe pattern both at a series of stable, carefully measured temperatures and during the intervening temperature changes; regulating and measuring the pressure of the heat-exchange gas at the fixed-temperature points; and determining from the filmed patterns the fringe changes that accompanied each modification of the temperature. The thermal expansion coefficients were obtained by fitting the experimental data by means of equations such as

$$\Delta N(t_i,t_{i+1})=\sum_{n=1}^{m}A_n(t^n{}_{i+1}-t^n{}_i). \tag{7}$$

Detailed discussions of the thermal expansion apparatus, the measurement procedure, and one method of analyzing data obtained during experiments performed some time ago, are given in reference [19]. Here, we shall summarize the results obtained for the percent linear thermal expansion in the range 0 to 550 °C, with reference to 0 °C, for 100% Pt:

$$\begin{aligned}100\,\epsilon(t,0\ ^\circ\mathrm{C})&=100\,[L(t)-L(0\ ^\circ\mathrm{C})]/[L(0\ ^\circ\mathrm{C})]\\&=8.862\times10^{-4}\,t+1.760\times10^{-7}\,t^2\\&\quad-1.144\times10^{-10}\,t^3+8.93\times10^{-14}\,t^4.\end{aligned} \tag{8}$$

For 88 Wt% Pt+12 Wt% Rh

$$\begin{aligned}100\,\epsilon(t,0\ ^\circ\mathrm{C})&=8.763\times10^{-4}\,t+2.116\times10^{-7}\,t^2\\&\quad-1.455\times10^{-10}\,t^3+1.036\times10^{-13}\,t^4,\end{aligned} \tag{9}$$

and for 80 Wt% Pt+20 Wt% Rh

$$\begin{aligned}100\,\epsilon(t,0\ ^\circ\mathrm{C})&=8.674\times10^{-4}\,t+2.538\times10^{-7}\,t^2\\&\quad-2.081\times10^{-10}\,t^3+1.480\times10^{-13}\,t^4.\end{aligned} \tag{10}$$

The estimated standard deviation of the fit to the data in each case was less than 0.1 fringe (<1 ppm in sample length).

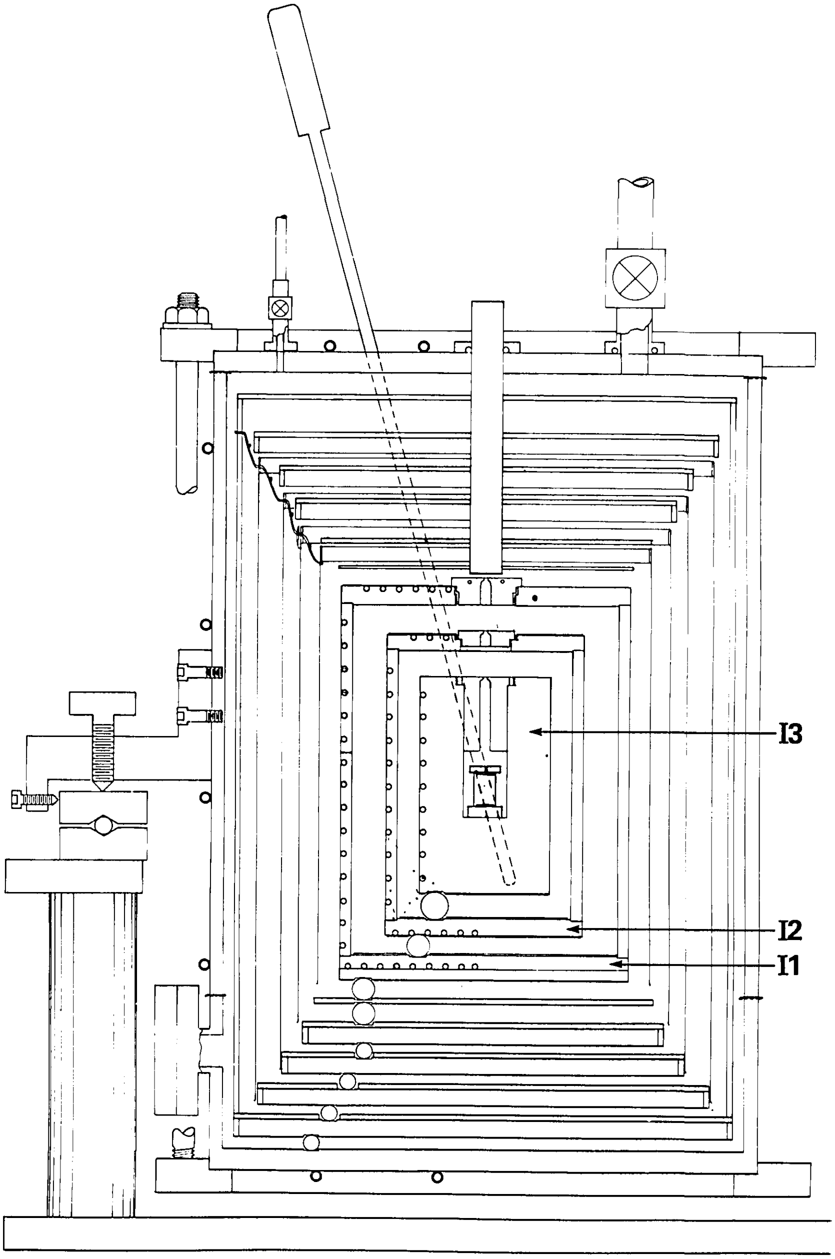

Figure 9. Cross-section drawing of original NBS/NIST gas-thermometry thermal expansion furnace. The outermost shell was made of brass in three sections. PTFE gaskets were employed at the joints to permit evacuation of the furnace. Cooling coils on the outside surface of the outer shell could be connected to refrigerated fluid in order to cool the furnace to temperatures as low as −30 °C. Successively smaller radiation shields of copper, silver (three shields), and gold enclosed three Inconel 600 shields, I1, I2, and I3. Shell I1 was equipped with separate resistive heaters placed in grooves in its top, bottom, upper sidewall, middle sidewall, and lower sidewall. Shell I2 supported heater circuits located on its top plate, on its sidewall, and on its bottom plate. The innermost shell, I3, was prepared from a solid cylinder of Inconel of 7.5-cm diameter and 13-cm length; a central hole was bored to house the sample assembly, and an off-center hole accommodated a calibrated PRT. Three-element "Platinel" thermocouples were arrayed along the surfaces of shells I1, I2, and I3; these thermocouples were connected in differential circuits for temperature control. A quartz window, 1.9-cm diameter and 16-cm thick, was sealed in place above the sample. Sample loading was accomplished by removal of the lids of the shields and the slotted plugs in the Inconel shells. All shields and shells rested upon steel balls that were constrained by slots in the next lower plate. The furnace could be rotated on a ball-bearing assembly; it was leveled by means of three sets of screws that contacted the circular rotation unit as shown in the figure. (Reprinted from reference [19].)

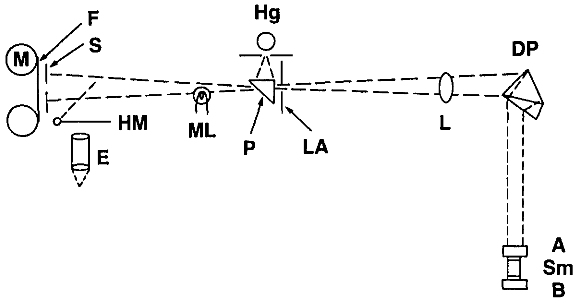

Figure 10. Schematic drawing of the recording interferometer [36,37,38]. A low-pressure electrodeless ^{198}Hg lamp, Hg, provides light for the interferometer through a prism, P, a limiting aperture, LA, lens L, and a double dispersing prism, DP. The light is partially reflected by the lower surface of optical plate A and then fully reflected by the upper surface of plate B; the two plates enclose the sample, Sm, and with it create the interference fringe pattern that falls upon the narrow horizontal slit S and is recorded on 35 mm panchromatic film F. A hinged mirror, HM, and eyepiece, E, allow the operator to view the fringe pattern before recording it. A drive mechanism, M, moves the film at one of three pre-chosen rates. A marker lamp, ML, can be used to identify particular locations on the film. (Reprinted from reference [19].)

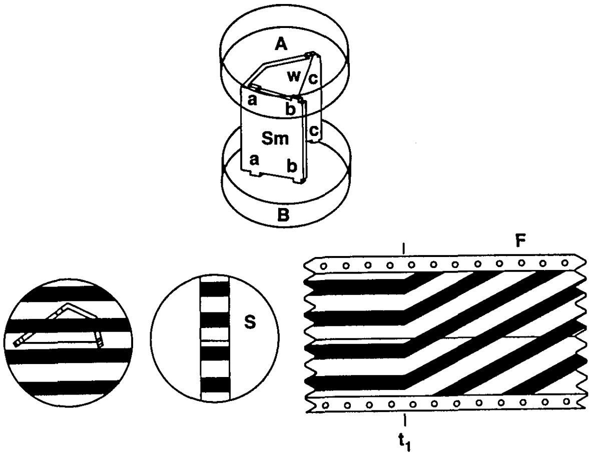

Figure 11. Sample assembly and fringe pattern. The upper surface of the upper optical plate, A, makes an angle of 20° with respect to the lower surface, so that its reflections do not appear in the field of view. The lower surface is coated with TiO_2 for 30% reflection. The upper surface of the lower optical plate, B, is coated for total reflection, while its lower surface was left rough. The sample, Sm, is shaped so as to provide three-point support for the upper plate. Three sets of tabs, a-a, b-b, and c-c were left on the upper and lower sample edges for fine adjustment of the plate separation, so as to produce a fringe pattern similar to that shown in the lower left corner of the drawing. The pattern is partially blocked by a slot S in the central copper tempering block, providing a filmed image that is fixed with respect to the fiducial wire, w, during steady-temperature recording. At time t_1, the film, F, moving leftward, begins to record the moving fringe pattern resulting from a change in sample temperature. (Reprinted from reference [19].)

Because of a slight difference in fitting procedure from that described in reference [19], the equation corresponding to eq (9) that was actually used for the (88/12) alloy in the gas thermometry calculations in the range 0 to 457 °C was as follows:

$$100\,\epsilon(t, 0\,^\circ\mathrm{C}) = 8.7509\times10^{-4}\,t + 2.2782\times10^{-7}\,t^2 - 2.4767\times10^{-10}\,t^3 + 3.462\times10^{-13}\,t^4 - 1.9117\times10^{-16}\,t^5. \qquad (11)$$

At 457 °C, use of the newer coefficients (from reference [19]) would have resulted in a higher calculated value of the Kelvin Thermodynamic temperature (see next section) by 0.003 °C.

7. Scale Differences From 0 to 457 °C

The characteristics of the second version of the NBS/NIST gas thermometer indicated the capability for determination of Kelvin thermodynamic temperatures up to 457 °C with very low uncertainty levels, although it still was necessary to record data by hand and to make use of the central NBS facility for the computation of results.

A comprehensive presentation of results from the NBS gas thermometer was published in 1976 by Guildner and Edsinger [21]. The work described in that paper embodied the changes from earlier efforts in both equipment and procedures that are mentioned briefly above. The earlier results were slightly modified, and they were substantially extended in range.

Measurements that were part of each determination of a Kelvin thermodynamic temperature with the revised apparatus included the following:

- Checks on the integrity of the capacitance diaphragm gage and of the capacitance bridge used in setting the manometer mercury levels, to ascertain that these vital systems were working properly;
- Resistances of three long-stem platinum resistance thermometers inserted into the gas-bulb protective case, followed later by measurements of the thermometers in a triple point of water cell, to provide an estimate of the gas-bulb temperature on the IPTS-68;
- Voltages of more than ten thermocouples that were ranged along the gas-bulb capillary, referred to ice junctions, to provide part of the dead-space correction;

- Resistance of a long-stem PRT placed on the manometer block, and voltages of a set of thermocouples ranged along the manometer mercury lines, to provide the temperature of the mercury in the manometer;
- Height of the stack of wrung gage-block end standards under the pumped cell of the manometer, to provide the height of the mercury column;
- Capacitance of the diaphragm gage that separated the manometer gas from the gas thermometer working gas, to provide a value of the pressure difference.

Most of the types of measurements made by Guildner and Edsinger became part of the procedures used in later measurements to 660 °C. Therefore it is useful to summarize the approach used in the measurements to 457 °C.

7.1 IPTS-68 Temperatures

Over the period during which the measurements to 457 °C were performed, four calibrations of the three PRTs used in the gas bulb and the PRT used to measure the temperature of the manometer were obtained. The fixed-point resistance values repeated at the level of 0.00045 °C. The constants obtained in the calibrations were employed in a Fortran IV program that was run as needed on the NBS computer in order to provide the mercury temperature and the gas bulb temperature corresponding to each pressure-temperature determination. The symbolic program was given in Appendix I of reference [21]. It was estimated that the uncertainty in the calculated IPTS-68 temperatures never exceeded 0.001 °C.

IPTS-68 temperatures of copper-constantan thermocouple thermometers were calculated from a standard table of emf vs. temperature [22]. IPTS-68 temperatures of Pt vs. (Pt+10 Wt% Rh) thermocouple thermometers were obtained by use of an equation derived from calibrations of thermocouples similar to those employed in the gas thermometer:

$$E=5.45846\times10^{-3}\,t+1.13497\times10^{-5}\,t^2 -1.52447\times10^{-8}\,t^3+9.06033\times10^{-12}\,t^4. \qquad (12)$$

The above equation represented the observed data within 0.47 μV from 25 up to 500 °C.

7.2 Manometer Pressure

Calculation of the pressure on the manometer side of the capacitance diaphragm gage is discussed at length in reference [5]. Each pressure value had several components:

(1) the height of the gage blocks stacked below the upper cell of the manometer, modified by thermal expansion (calculated from the difference between the calibration temperature and the measured manometer temperature) and by the compression resulting from the weight of the upper cell;

(2) the density of the mercury, obtained from the following relation: 1.354584×10^{-4} $[1-1.8110\times10^{-4}\,(t-20\ ^\circ\mathrm{C})+3.8\times10^{-11}\,p$ (in N/m^2)] kg/m^3 [40,41,42]. The temperature was obtained in each case by reading the manometer PRT. The pressure, arising from the head of mercury, was calculated for one-half the gage-block stack height;

(3) the acceleration due to gravity, g, 9.801022 $[1-3\times10^{-7}\,h$ (in m)] m/s^2 [43], where h was the vertical height of the capacitance gage above the reference level at which the value of g was originally determined;

(4) the hydrostatic head of ^{4}He gas between the manometer and the diaphragm, π_{m}, given by

$$\pi_{\mathrm{m}}=\sum_k [M g\, l_k]/[R\, T_k], \qquad (13)$$

where M denotes the molecular weight of the gas, l_k stands for an increment of length, R, the molar gas constant, is 8.3137×10^6 [cm^3 Pa]/[mol K], T_k represents the temperature of the kth element of length of the riser tube that connected the two instruments, and the summation occurs over the full length of the riser tube; and

(5) any difference in the partial pressure of mercury on the two sides of the manometer. One notes in this component of the pressure calculation that the use of a cooled mercury vapor diffusion pump to maintain a vacuum over the upper cell may result in a lower partial pressure of mercury over the upper cell than that existing in the riser tube above the lower cells.

7.3 Gas Bulb Pressure

To convert the pressure evaluated at the manometer side of the diaphragm to the value existing within the gas bulb, it was necessary to calculate or measure the pressure difference across the diaphragm, the pressure head between the diaphragm and the gas bulb, and the thermomolecular pressure correction for the capillary.

The sensitivity of the diaphragm gage was periodically re-determined by observing the values of capacitance that corresponded to small, measured gas pressures introduced into one side of the gage. It was necessary as well to maintain a frequent schedule of null-pressure measurements to verify the capacitance value that corresponded to equal pressures on the two sides of the diaphragm.

The pressure head between the diaphragm gage and the center of the gas bulb was obtained from a relation similar to eq (13), with the additional consideration of the thermal expansion of each element of the capillary:

$$\pi_c = [\{Mg\}/\{RK\}]\sum_k [l_k/T_k][1+\alpha_k \Delta t_k]. \tag{14}$$

In eq (14), the α_k and Δt_k represent, respectively, the linear thermal expansion, and the difference from 23 °C of the temperature, of each element. The summation runs over the length of the capillary from the diaphragm to the center of the gas bulb. Other symbols have the meanings given in eq (13).

The thermomolecular pressure correction appropriate for each measurement was estimated on the basis of experiments performed with a capillary similar to the one used in the gas thermometer. The substitute capillary was enclosed within a larger tube (about 9.6 mm i.d.). In the experiments, the capillary was connected to one side of the diaphragm gage and the larger tube to the other; the assembly was installed in a vacant gas-bulb thermometer well (see fig. 2 of reference [21]). By determining the pressure difference between the two tubes as functions of pressure and temperature, Guildner and Edsinger obtained values for the thermomolecular pressure corrections up to 457 °C that they estimated to be accurate within about 1%.

7.4 Gas Bulb Volume

The absolute interior volume of the gas bulb at the reference temperature needed only be known with moderate accuracy; a change of 8% in the evaluation of the bulb volume was estimated to effect only a 0.003 °C modification in the calculated thermodynamic temperature near 150 °C. Measurement of the volume better than this level of accuracy was readily accomplished by weighing the bulb empty and then weighing it filled with water at a known temperature.

Much more significant was any uncertainty in the thermal expansion of the gas bulb from the reference temperature to the test temperature. The volume of a gas bulb at any temperature t_u, $V(t_u)$, could readily be calculated once the linear thermal expansion of the gas-bulb material had been determined for the temperature range of interest:

$$\begin{aligned} V(t_u) &= V(t_r)\,[1+\beta(t_u-t_r)] \\ &= V(t_r)\,[1+\bar{\alpha}(t_u-t_r)]^3, \end{aligned} \tag{15}$$

where $\bar{\alpha}(t_u-t_r)=[\mathrm{l}(t_u)-\mathrm{l}(t_r)]/[\mathrm{l}(t_r)][t_u-t_r]$.

In the case of the experiments reported in reference [21], a complication arose because the gas bulb top had been fabricated from 80 Wt% Pt/20 Wt% Rh alloy, whereas the sides and bottom had been made from 88 Wt% Pt/12 Wt% Rh alloy. Because of the slight difference in thermal expansion coefficients, the shape of the cylindrical gas bulb could be expected to change with temperature. Considering the probable nature of the distortion, Guildner and Edsinger found that the change in volume of the bulb could be adequately calculated by using the mean thermal expansion coefficients characteristic of the 88/12 alloy.

7.5 Dead Space Evaluation

We noted in section 4 that the procedures used during gas-thermometer measurements restricted the dead space to the gas-bulb capillary and the constant-volume valve that closed it off from the capacitance diaphragm gage. We also mentioned there that the uncertainty contributed by the constant-volume valve was negligible. The temperature correction resulting from the amount of the working gas that was contained in the capillary could be calculated on the basis of eq (4). Dividing the total number of moles of working gas in the gas thermometer between the gas bulb and the dead space (essentially all of which consisted of the capillary) and neglecting, for this purpose, the non-ideality of the gas, we could evaluate the temperature correction arising from the dead space, δt_{ds}, as

$$\begin{aligned} \delta t_{ds} = {} & T_{bu}(\text{including dead space}) \\ & - T_{bu}(\text{no dead space}), \end{aligned} \tag{16}$$

where the two right-hand terms refer to the bulb temperatures calculated for the higher-temperature state first including the capillary and then neglecting the capillary. The first term can be written

$$T_{\mathrm{bu}}=[P_{\mathrm{bu}}V_{\mathrm{bu}}]/[\{P_{\mathrm{br}}V_{\mathrm{br}}/T_{\mathrm{br}}\}+\sum_k(P_{k\mathrm{r}}V_{k\mathrm{r}}/T_{k\mathrm{r}})$$

$$-\sum_k(P_{k\mathrm{u}}V_{k\mathrm{u}}/T_{k\mathrm{u}}], \tag{17}$$

where all volumes V are corrected for thermal expansion and the capillary pressures P_k are corrected for hydrostatic head and thermomolecular effects. The second term on the right-hand side of eq (16), in which the dead space correction is neglected, is simpler:

$$T_{\mathrm{bu}}=[T_{\mathrm{br}}P_{\mathrm{bu}}V_{\mathrm{bu}}]/[P_{\mathrm{br}}V_{\mathrm{br}}]. \tag{18}$$

With only a negligible error, eq (16) can be re-written in the form

$$\delta t_{\mathrm{ds}}=-[\{T_{\mathrm{br}}T_{\mathrm{bu}}\}/V_{\mathrm{br}}]\sum_k[\{V_{k\mathrm{r}}/T_{k\mathrm{r}}\}$$

$$-\{P_{\mathrm{bu}}V_{\mathrm{ku}}\}/\{P_{\mathrm{br}}T_{k\mathrm{u}}\}]. \tag{19}$$

The temperatures of the individual elements of the capillary were deduced from measurements of the thermocouples arrayed along its length.

7.6 Effect of Gas Non-Ideality

The method used in the earliest series of gas thermometry measurements to eliminate errors arising from the non-ideality of the ^{4}He working gas was to perform a set of measurements at the same unknown temperature with several filling pressures; extrapolation of the indicated gas thermometer temperature to the value corresponding to zero filling pressure could then compensate for the non-ideality of the gas. However, the magnitude of the thermomolecular correction at low pressures and high temperatures increased the uncertainty from that source, so that, in the work described in reference [21], the virial theorem was employed, with values of the second virial coefficient obtained from the existing literature.

An equation was developed to represent the second virial coefficients of ^{4}He over the range 0 to 600 °C:

$$B(\mathrm{cm^3/mol})=11.9967-4.48574\times10^{-3}\,t$$

$$+1.46724\times10^{-6}\,t^2. \tag{20}$$

The estimated uncertainties in the non-ideality corrections resulted in uncertainties in the KTTS temperatures that ranged from 0.12 mK at 100 °C and 20 kPa to 1.23 mK at 457 °C and 100 kPa (reference [21], sec. 9).

7.7 Summary of Results

As a result of a series of 123 sets of measurements with the gas thermometer over a period of 15 months, Guildner and Edsinger derived a relation (rounded off here to five significant figures) for the difference between the Kelvin Thermodynamic Temperature Scale and the IPTS-68 in the range 0 to 457 °C (273.15 to 730.15 K):

$$T/\mathrm{K}-T_{68}/\mathrm{K}_{68}=-1.2089\times10^5/T_{68}^{\;2}$$

$$+1.2135\times10^3/T_{68}-4.3160+6.4408\times10^{-3}T_{68}$$

$$-3.5664\times10^{-6}T_{68}^{\;2}. \tag{21}$$

The uncertainties associated with the major components of the measurements contributing to these results are summarized in table 2.

Table 2. Estimated uncertainties of 1976 NBS gas thermometer

Feature	Uncertainty
Dead space	0.9 mK (C)
Thermal expansion	0.5 mK (B)
Pressure ratio	0.5 mK (A)
	0.4 mK (B)
Gas imperfection	1.2 mK (C)
Thermomolecular	Negligible

[a] Three classes of uncertainty were recorded, all in terms of "one standard deviation":

A. Random errors.

B. Errors producing a constant bias but evaluable in terms of random errors of subsidiary experiments.

C. Systematic errors not evaluable in statistical terms.

The differences $t(\mathrm{KTTS})-t(\mathrm{IPTS\text{-}68})$ at the steam point, the tin point, the zinc point, and 457 °C (the highest temperature reached), along with their estimated uncertainties, are given in table 3. The results are shown in graphical form in figure 12.

Table 3. Scale differences at four reference temperatures

Point	t_{68}, °C	$(t_{\mathrm{th}}-t_{68})$, °C	Random, °C (3 s.d.)	Systematic, °C (3 s.d.)
Steam	100	−0.0252	±0.0018	±0.00054
Tin	231.9681	−0.0439	±0.0022	±0.0015
Zinc	419.58	−0.0658	±0.0028	±0.0028
	457	−0.0794	±0.0028	±0.0031

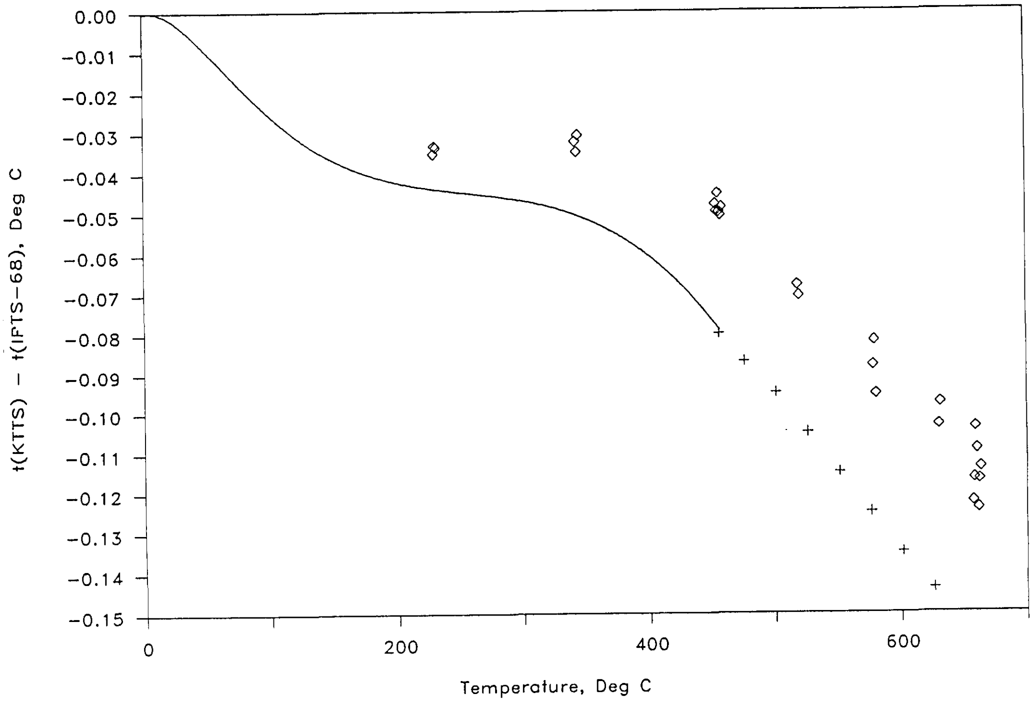

Figure 12. Temperature scale differences t(KTTS)$-t$(IPTS-68) as determined with various versions of the NBS/NIST gas thermometer. Solid line—results given in reference [21] by Guildner and Edsinger. Diamonds—results given in reference [35] by Edsinger and Schooley [35]. For comparison with the higher-temperature results of reference [35], the results (indicated by plus signs) obtained by Jung [25], using radiation thermometry based on the results of reference [21] at 457 °C, are included as well. (Reprinted from reference [35].)

Inasmuch as the NBS gas thermometry results showed deviations of the IPTS-68 from its thermodynamic counterpart that were everywhere at least twice as large as had been estimated during its formulation in 1968, considerable effort has been expended in other laboratories to seek corroboration of the gas thermometer determinations by different experiments. Recently, similar results below 140 °C have been found using the methods of total radiation thermometry [23] and acoustic thermometry [24].

8. Most Recent Version of the NBS/NIST Gas Thermometer

After Guildner and Edsinger reported on the deviation of the International Practical Temperature Scale of 1968 from the Kelvin Thermodynamic Scale in the range 0–457 °C, Jung [25], Coates and Andrews [26], and Coates, Andrews, and Chattle [27], performed spectral radiation thermometry experiments in order to realize the KTTS at still higher temperatures. To obtain measurements that were consistent with the NBS gas thermometry, they each utilized the NBS determinations near 457 °C as reference temperatures.

Because of the difficulty involved in performing spectral radiation thermometry at temperatures as low as 457 °C, experimental uncertainty at that temperature is considerably larger than it is at higher temperatures; furthermore, systematic errors in "low-temperature" radiation thermometry become increasingly difficult to evaluate. Since in principle gas thermometry can provide reference temperatures substantially above 457 °C that are referred to the principal KTTS defining temperature at 0.01 °C, it was desirable to continue study of the KTTS by gas thermometry at temperatures above 457 °C. A further advantage to be gained by such a step is that an extended range of the KTTS would be explored by two methods that possess intrinsically different systematic errors, allowing better evaluation of the uncertainty of thermodynamic temperatures throughout the overlapping range. For these reasons, R. E. Edsinger and the present author recently undertook experiments that continued the work of Guildner and Edsinger to up temperatures as high as 660 °C.

Some of the apparatus built at the NBS for gas thermometric studies above 500 °C was described by Guildner and Edsinger in 1982 [28]. It was necessary to modify that equipment in the course of using it to determine the difference t(KTTS)-t(IPTS-68) from 230 to 660 °C in the most recent experiments. It also proved desirable to modify the furnace used for the determination of thermal expansion; the gas bulb; the gas-bulb thermometers; the method used in purifying the ^{4}He working gas; and the technique for tracking the "counterpressure." No changes were required in the manometer.

8.1 High-Temperature Furnace

The major difference between the most recent gas thermometry experiments and those reported previously involved the thermal environment of the gas bulb. In the earlier experiments up to 457 °C, the gas-bulb/case system was immersed, as needed, in liquid baths; in an ice/water bath to provide the reference state, in a water/potassium-chromate bath to provide uniform temperatures between 0 and 140 °C, or in a bath containing a eutectic mixture of lithium, sodium and potassium nitrates to provide uniform temperatures between 140 and 457 °C. As noted in section 6, use of the molten salt bath above 457 °C, while providing quite uniform temperatures in the volume containing the gas bulb, nevertheless offered its own problems; not only did the hot molten salts attack the sheaths of the PRTs, but the solution also migrated out of the bath reservoir, occasionally damaging the electrical circuits.

A less homogeneous thermal environment was provided for the most recent experiments by an argon-filled furnace [28]. A schematic drawing of the high-temperature furnace is shown in figure 13. Although capable of providing gas-bulb temperatures as high as 1000 °C, some eight heaters required careful manual adjustment if the operator wished to eliminate very noticeable temperature gradients in the gas bulb. The furnace response time was an hour or more, depending upon its temperature; however, its thermal stability was quite high, permitting ample time for measurements after adjustment. As before, an ice bath was used to provide the reference state near 0 °C for the gas bulb.

8.2 Gas Bulb Assembly

The gas bulb in use during the most recent experiments was not the one that was used in the

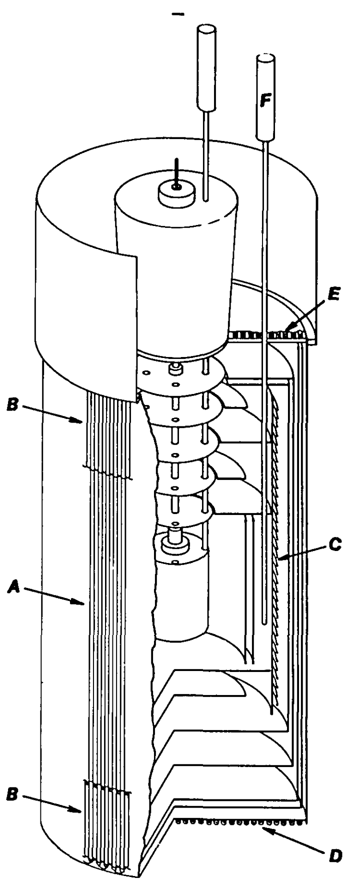

Figure 13. Cutaway drawing of the inner, heated portion of the high-temperature gas thermometer thermostat, shown with the gas thermometer assembly lowered into its measurement position. Like the other NBS/NIST Gas Thermometry thermostats, the 200–1000 °C furnace was movable. The exterior surface of the thermostat (not shown here) was cooled by chilled water flowing through coils brazed to it. The heat load on the exterior surface was reduced by the inclusion of 20 cm of Fiberfrax insulation between it and the heated portion shown here. The furnace was gas-tight except at the top. Argon gas was inserted through the exterior wall into the insulated space outside the heaters A,B and also into the volume surrounding the protective case of the gas bulb, in order to reduce the concentration of hydrogen and other active species in the thermostat. The inner parts of the furnace were made of Inconel alloys. The shields inside the heated portion of the thermostat provided isolation from the laboratory environment and support for some eight independent zone heaters. The main heaters, A, were composed of vertical windings of Nichrome wire threaded through single-hole ceramic insulators. The heater was divided into independently controlled quadrants to allow for slight misalignment of the gas-bulb assembly with respect to the furnace centerline. Band heaters, B, consisting of short sections similar to the main heaters, surrounded the top and bottom of the main heaters. A regulating heater, C, distributed its heat evenly over one of the shields. Its power was regulated by the temperature as sensed by a control thermometer, F. A bottom heater, D, a top heater, E, and three heaters in the gas-bulb suspension assembly could be adjusted independently to correct vertical temperature gradients. Approximately 750 W of overall heater power were required to maintain the gas bulb at 660 °C; less than 1% of the total was dissipated in heater C. A line conditioner was used to regulate the line voltage to the heater circuits, and specially designed controls were used on the heaters. A soft fiberglass rope was used to seal the conical plug on the gas-bulb suspension into its socket prior to each run. (Reprinted from reference [28].)

measurements reported earlier [21], although it was quite similar in its construction (see fig. 7). The major change in its construction was in its lower end cap, which was more than doubled in thickness for reasons to be discussed later. The gas bulb was made entirely of 80 Wt% Pt+20 Wt% Rh in the shape of a right circular cylinder of volume ~407 ml. As before, it was connected to a capacitance diaphragm gage via a capillary of composition 90 Wt% Pt+10 Wt% Rh. Because the thermostat provided a relatively poor level of temperature homogeneity in comparison to the liquid baths used in earlier versions of the gas thermometer, more capillary thermocouple stations were added to define the temperature profile along the capillary immediately above the gas bulb. The capillary/gas-bulb system was enclosed by the same heavy-walled Inconel 600 protective case and tube that had been used in the previous experiments. Helium gas again was introduced into the protective case and tube at nearly the same pressure (the "counterpressure") as that existing at any given time in the gas bulb [20].

Invariably, four platinum resistance thermometers (PRTs) were placed in the four wells in the wall of the protective case prior to measurements; these were used to determine IPTS-68 temperatures of the gas bulb. Radial temperature gradients within the gas bulb could be evaluated by comparing the temperatures of the PRTs at a fixed depth in the case, and minimized by adjusting separately the thermostat heaters (A, fig. 13). Vertical gradients could be detected by varying the vertical positions of the PRTs.

As before, the operating procedures were chosen so that the dead space correction applied only to the capillary above the gas bulb and to the constant-volume valve that was located directly above the capillary. The magnitude of the dead-space correction was now determined by measuring the emf of each of some 22 (Pt) vs (Pt+10 Wt% Rh) thermocouples that were arrayed along the capillary between the gas bulb and the constant-volume valve.

8.3 Platinum Resistance Thermometry

A set of calibrated high-temperature PRTs was used to control the furnace, to monitor the temperature uniformity in the gas bulb, and to provide its IPTS-68 temperature. The thermometers were especially designed for use at temperatures as high as 1000 °C; they were made with 2.5 Ω nominal ice-point resistance, bifilar helical windings, and synthetic vitreous silica sheaths. Most of these thermometers were made at the NBS, either by J. P. Evans [28,29,30] or by Guildner and Edsinger [28]; during the last stages of the experiments, however, two more were obtained from a commercial source [45].

Two resistance bridges of NBS construction were used to measure the resistances of the PRTs. One of these bridges, a 400-Hz, manually balanced model [31], monitored a PRT that was located near furnace heater C (see fig. 13); it was used for fine temperature control. The heater supply derived its signal from the bridge output. A second resistance bridge of more recent design [32] provided an automatic-balancing, computer-controlled monitor for the four PRTs that were used in the protective case of the gas-bulb system, as well as for a standard PRT that continually monitored the manometer cellar temperature.

8.4 Auxiliary Equipment

Purified ^{4}He gas was obtained from the same high-pressure cylinder that was used in the work published earlier. Before it was allowed to enter the gas bulb or manometer, the helium was passed slowly (~0.06 mol/h) through a copper trap that was surrounded by liquid ^{4}He at 4.2 K. This purification procedure is quite different from the one used previously (see secs. 4 and 5). Some of the helium gas was diverted to a 3-L storage volume so that small volumes of the system (typically, the constant-volume valves and the capacitance diaphragm gage) could be emptied and refilled during a measurement sequence.

A digital capacitance diaphragm gage was introduced to monitor the pressure in the manometer-counterpressure system while it was being filled or emptied, and during furnace temperature changes [44]. (At these times, the mercury system in the manometer was valved off to prevent flooding of the cells and consequent shorting of the level-sensing capacitance plates.)

A low-thermal, four-deck scanner was used in conjunction with a digital voltmeter and a laboratory microcomputer to monitor a variety of measurements. These included the following:

- •Resistance of the thermometer-bridge resistance standard contained in a thermostated enclosure;
- •Resistances of the four PRTs in the gas-bulb protective case;
- •Resistance of the PRT in the manometer cellar;
- •EMFs of the 22 [Pt vs. (Pt+10 Wt% Rh)] thermocouple thermometers located along the gas-bulb capillary, each measured against a reference junc-

tion held at the ice point, and emfs of the four thermopiles located on the mercury lines and cells of the manometer;

- Output of the capacitance diaphragm gage that monitored the counterpressure;
- EMF of the thermocouple thermometer that monitored the temperature of the main capacitance diaphragm gage; and
- Voltages appearing on the manually set high-temperature furnace heaters.

Calibration data recorded in the memory of the microcomputer allowed expression of all thermometer readings directly in °C and of the counterpressure capacitance diaphragm gage output in pressure units.

8.5 Recent Thermal Expansion Measurements

In section 6.2. we described the first of two devices for the precise measurement of thermal expansion, each comprised of a Fizeau interferometer, a thermally homogeneous sample furnace, and a calibrated PRT. The first apparatus was used to measure the thermal expansion of the materials from which the gas bulbs used in the earlier gas thermometer experiments were constructed [19,21,28]. The results obtained with this apparatus were of high quality, with an imprecision generally better than 1 ppm in sample length; however, setting the sample temperature to a stable, uniform value required the iterative adjustment of the current settings in nine furnace heaters. This technique proved to be both time-consuming and tedious. The advent of heat-pipe thermal equilibration techniques led to the re-building of the thermal expansion furnace, employing a heat pipe in place of the multiple shields.

The objective in modifying the earlier furnace was to simplify its operation while still retaining a satisfactory level of accuracy in the determination of thermal expansion. To reduce the uncertainty of the thermodynamic temperatures arising from uncertain knowledge of the thermal expansion of the gas bulb to the level of ±0.011 °C at 660 °C (approximately 12 ppm of the temperature in kelvins), it was necessary to measure the thermal expansion of the gas bulb material accurately within about 4 ppm in sample length. This objective appeared to be achieved with the construction of a simpler, computer-controlled furnace. A recent paper [33] contains a description of the construction of the new furnace and its use to determine the coefficients of linear thermal expansion of Pt and Pt-Rh alloys in the range −20 to +700 °C.

Figure 14 shows the heat-pipe furnace. A sealed outer wall was constructed in two parts that were screwed together onto a PTFE gasket. A six-turn copper cooling coil was brazed onto the outer wall of the furnace. Argon gas was fed into the furnace at a pressure slightly above ambient so as to reduce the likelihood of water or other unwanted impurity gases inside the furnace.

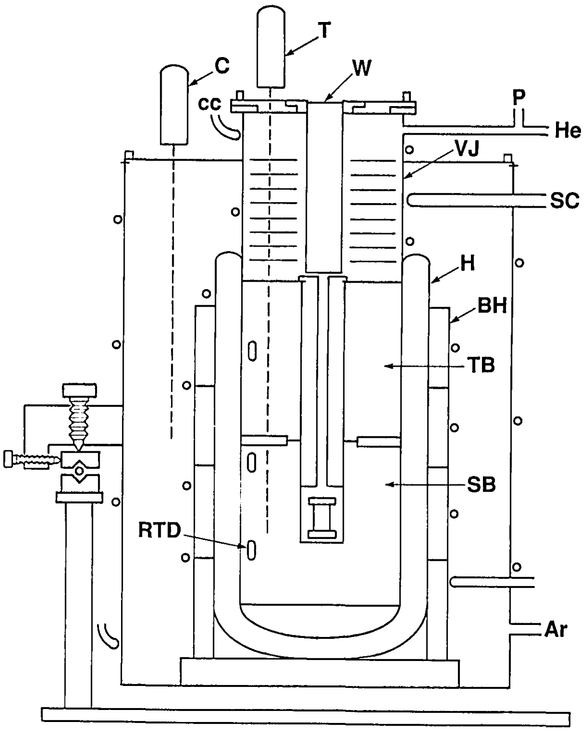

Figure 14. Cross-section drawing of heat-pipe thermal expansion furnace. The outer wall was made of brass; a cooling coil, cc, made of copper tubing was brazed to the outside. A slight overpressure of argon gas was maintained inside the outer wall through the connection Ar. The furnace was supported at three points on a turntable that rested upon the laboratory bench. A closed-end, Inconel heat pipe, H, loaded with 50 g of potassium metal, rested upon an insulating support. Four ganged band heaters, BH, provided heat to the heat pipe. A platinum resistance thermometer, C, sensed the temperature in the vicinity of the band heaters, allowing rough temperature control. A sealed tube, VJ, served as an evacuable enclosure for the sample assembly. The sample itself was centered within the lower of two copper blocks, SB, which also provided a socket to receive a calibrated platinum resistance thermometer, T. The upper copper block, TB, tempered the ^{4}He fill gas, thermometer T, and a central slotted copper block. A quartz window, W, tempered by a set of Inconel baffles, admitted light from the interferometer. A coil of stainless steel tubing, SC, was used to cool the sample chamber below room temperature. Ports P and He were used to monitor the fill-gas pressure and to evacuate the sample space, respectively. (Reprinted from reference [33].)

An Inconel heat pipe (labelled H in fig. 14) containing 50 g of potassium metal was obtained commercially. The lower end of the heat pipe was closed, providing a Dewar-like configuration. A close-fitting Inconel jacket, VJ, inside the heat pipe, provided a vacuum-tight sample chamber. The vacuum jacket permitted the sample chamber to be pumped and filled with gas of any desired composition and pressure. The heat pipe was surrounded by a set of four, 1250-W, cylindrical band heaters, BH, connected in electrical series. A long-stem platinum resistance thermometer, C, was mounted with its sensor near the band heaters to allow rough control of the heat pipe temperature.

Within the space tempered by the heat pipe were placed two copper blocks that were joined lightly as shown in figure 14. The lower copper block, SB, provided a central chamber for the sample assembly and a socket for a second long-stem PRT, T. This thermometer was monitored to obtain sample temperature values. Also included in block SB were two of three small, industrial-grade platinum resistance thermometers (RTD) to be used in evaluating the quality of temperature homogeneity throughout the sample chamber. The upper copper block, TB, of which the main function was that of tempering the PRT and the sample gas, contained the third RTD unit. On the outside of each copper block was wound a resistance heater. The two block heaters were connected electrically in such a way that the proportion of heater power deposited in each could be varied by the operator.

Outside the heat-pipe assembly, a coil of stainless steel tubing, SC, provided the means of introducing a refrigerant into the furnace to allow measurements below room temperature.

The amount of light that impinged upon the sample was restricted by a slotted copper plug above it, by a thick (15 cm) quartz window, W, and by a green filter in the Fizeau interferometer. Since no measurement of the light intensity was performed in these experiments, one can only estimate the level of stray heat from this source.

Potassium was selected as the working substance in the heat pipe despite the fact that its vapor pressure becomes substantial only above 400 °C. Given the relatively low radiative-to-conductive heat transfer properties of the components of the furnace up to that temperature, it seemed likely that the heat pipe would serve as a Dewar vessel up to temperatures at which it became active as a thermal element. The ease of control of the furnace and its thermal stability in use over the experimental range of temperature were consistent with this interpretation.

The interferometer, sample assembly, and fringe recording methods were unchanged from the earlier version of the thermal expansion apparatus. However, apart from the recording of the interference fringes, the acquisition of most of the experimental data was accomplished by the use of a dedicated laboratory microcomputer that was programmed to accept digital information from a high-accuracy resistance bridge of NIST construction [32] and from a digital voltmeter. Each of these instruments in turn was connected to several sensors, either directly or by means of low-thermal-emf scanners. The microcomputer was used also to activate digital-to-analog power supplies to energize the three furnace heater assemblies, to convert resistance values to temperatures, and to convert digital pressure data from voltage units to pressure units. The pressures thus calculated were further analyzed to yield values of the index of refraction of the sample-chamber gas. Figure 15 is a schematic drawing showing the interconnected components.

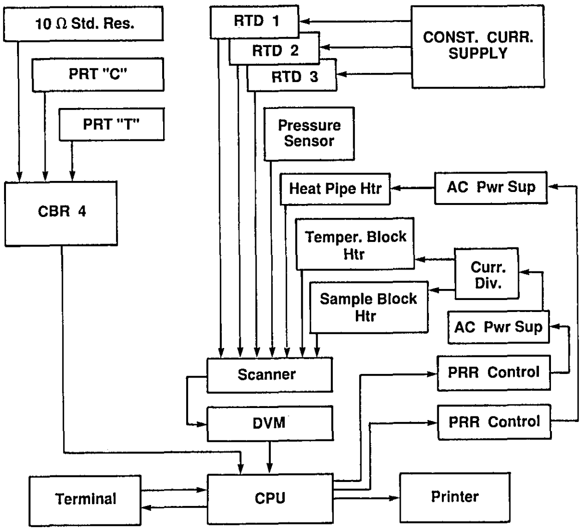

Figure 15. Schematic drawing showing the use of a laboratory microcomputer in acquiring resistance and voltage data and providing control information for dilatometry. The central processing unit, CPU, was programmed to obtain resistance data, using digital bridge CBR4 [32], from a 10-Ω thermostated standard resistor; from a control thermometer, C; and from the sample thermometer, T. The CPU converted those data to temperature values for use in control and evaluation. Through a low-thermal scanner, a digital voltmeter, DVM, provided data from three temperature sensors (RTDs), from a digital pressure sensor, and from various heaters. A portion of the operational program was used to send digital signals to temperature controllers of the proportional-rate-reset type; these, in turn, operated ac power supplies that activated heaters either directly or through current-divider circuits. The CPU also provided outputs to a terminal and to a printer.

The sample temperature was reduced to values as low as −20 °C by the manually regulated flow of nitrogen gas that had been cooled in a heat exchanger held at −195 °C in a bath of liquid nitrogen. As mentioned above, temperatures from ambient to 700 °C were attained by regulating the power to band heaters on the heat pipe assembly and to resistive heaters on the upper and lower copper blocks inside the heat pipe.

The temperature control technique was based upon the use of a dedicated laboratory microcomputer as shown in figure 15. The computer program allowed one to input target temperatures both for the PRT located near the heat pipe (C in fig. 14) and for PRT *T*, used to determine the sample temperature. An input time interval governed the frequency with which the resistances of those thermometers were measured, the corresponding temperatures calculated, and the information displayed on the terminal and, if desired, printed on the printer. The program compared the target temperatures with those determined by measurement, and called for more or less voltage to the heaters depending upon the differences. Limits to the heater voltages could be set by hand, and generally the heat-pipe target temperature was set so as to minimize the power to the tempering block and the sample block. The temperatures calculated for the RTDs were helpful in evaluating the uniformity of the temperature in the two copper blocks. However, the RTDs were not sufficiently stable to be used as the basis for setting the sample temperatures.

In general, use of these techniques allowed the achievement of stable sample temperatures with less than 30 W of power to the tempering block and 4–10 W to the sample block; in contrast, power to the heat pipe heaters ranged from 10 W at 100 °C to about 250 W at 700 °C.

The sample temperature could be resolved within approximately ±0.001 °C in the following manner. A specially prepared PRT was calibrated according to the IPTS-68 and installed in the sample block. The digital resistance bridge permitted the measurement of the resistance of the PRT with a resolution of 1 micro-ohm on command from the dedicated laboratory microcomputer as shown in figure 15. Use of a thermostated resistance standard provided evidence that the bridge measurements were accurate within about 1 ppm. During the times when the furnace temperature was stabilized as described in the previous section, the PRT resistance was read three times, the readings averaged, and the temperature calculated on the basis of the calibration coefficients stored in memory. This process was repeated until the sample temperature appeared to be stable. Then the RTD resistances, the heater voltages, and the sample-chamber pressure were recorded. PRT *T* was then monitored again and the temperature was changed at a pre-determined rate towards the next target temperature.

It may be useful to present here a synopsis of the analytical methods used to obtain values of the thermal expansion as well as certain results that have not been published heretofore. The following expression was used to represent the length of the sample at any Celsius temperature t_i:

$$L(t_i)=L(t\ ^\circ\mathrm{C})+\sum_{n=1}^{m} A_n[t_i^{\,n}-t^n]. \tag{22}$$

In practice, the length of each sample before installation in the dilatometer was measured accurately within about 5 ppm as described in section 6.2. The sample length in fringes of light of frequency 546.2271 nm in vacuum [39] could be expressed by use of the relation

$$N=2\,L/\lambda_0, \tag{23}$$

where N denotes the sample length in fringes of light of wavelength λ_0 cm and L represents the length of the sample expressed in cm. The values of N thus obtained corresponded to the sample length at the bench-top temperature at which the precision micrometer and the gage blocks were employed; later, these values could be corrected to t=0 °C by use of the fitting equations.

The observed fringe count at the steady-temperature points was corrected for the index of refraction of ^{4}He gas, included as a tempering medium in the sample chamber. The approximate 1-atm, 20 °C handbook value, 1.000 036, was corrected to the experimental pressure and temperature by the relation

$$n_i=1+0.000\,036[p_i/101]\,[(293)/(t_i+273)], \tag{24}$$

where p_i is expressed in kPa and t_i in degrees Celsius. The correction to the fractional fringe value from the measured to vacuum conditions was then obtained from the relation

$$\Delta N(t_i)_{\mathrm{vac-meas}}=2\,L_i(1-n_i)/\lambda_0, \tag{25}$$

where L_i indicates the sample length at temperature t_i.

To obtain the coefficients of eq (22), the function [47]

$$\Delta N_{\mathrm{vac}}(t_i,t_{i+1})=\sum_{n=1}^{m} A_n[t^n_{i+1}-t^n_i] \tag{26}$$

was fitted to the corrected fringe-temperature data sets. This is substantially the same equation that appears earlier in this paper as eq (7). The fitting procedure employed a least-squares computational program with $n \leqslant 6$ coefficients. The program provided an estimated standard deviation of the fit and a coefficient for the evaluation of the significance of each added term in the fitting equation [34].

Evaluation of the coefficients A_n yielded an expression for the linear thermal expansion in the usual form [19]

$$\begin{aligned}\epsilon(t,0\,^\circ\mathrm{C}) &= [L(t)-L(0\,^\circ\mathrm{C})]/L(0\,^\circ\mathrm{C})\\ &= [N(t)-N(0\,^\circ\mathrm{C})]/N(0\,^\circ\mathrm{C})\\ &= \sum_{n=1}^{m} [A_n/N(0\,^\circ\mathrm{C})]t^n. \end{aligned} \tag{27}$$

The thermal expansion can be obtained for any other reference temperature from the relation

$$\epsilon(t,t_{\mathrm{ref}})=[\epsilon(t,0\,^\circ\mathrm{C})-\epsilon(t_{\mathrm{ref}},0\,^\circ\mathrm{C})]/[1+\epsilon(t_{\mathrm{ref}},0\,^\circ\mathrm{C})]. \tag{28}$$

Two thermal expansion samples were prepared from the (80 Wt% Pt+20 Wt% Rh) alloy gas thermometer bulb used in the most recent NIST experiments, using the methods described in section 6.2. We present here details of measurements taken on these samples, labelled S-M and S-U, because they have not been reported heretofore. In addition, they show the level of precision of the thermal expansion measurements obtained using the thermal expansion apparatus described herein, and, most importantly, they modify slightly the calculated values of thermodynamic temperature given in reference [35]. The data on sample S-M were obtained both during warming and during cooling, while those on sample S-U were obtained only on cooling.

The length of sample S-M at 23.6 °C was found to be 2.528 388 cm, or 92,567.3 fringes of light at 546.2271 nm in vacuum. Some 45 fringe differences were obtained on this sample over the range −25 to +700 °C. Table 4 shows the experimental data used in obtaining the fringe differences ΔN that reflect the change in sample length between two stable temperatures, the fringe differences derived from the chosen fitting equation, and the differences between the experimentally derived values and the calculated values. The whole fringe differences occurring between the steady temperatures listed in column 2 were inferred from measurements made on other samples of the same alloy; the fractional fringe counts are given in column 3 of table 4. The fractional fringe values were corrected for the refractive index of the medium as obtained from the pressures given in column 4, thus obtaining the values given in column 5.

The resulting values of ΔN_{exp}, given in column 6, were fitted in the manner described above. The fitting parameters thus obtained are given in table 5. As one can see by examining table 5, there is little advantage in using a t^5 term in the fitting procedure, and none in using a t^6 term. The standard deviation of the four-term polynomial is somewhat smaller than 0.07 fringe, with the coefficients of the fitting equation as shown in table 5. Using these coefficients, one can obtain a set of ΔN_{cal} values for the experimental temperatures as given in column 7 of table 4. The deviations of the calculated data from the experimental data, listed in column 8, are shown in figure 16. No systematic differences appear between the data obtained during a cooling cycle and that obtained during warming.

It is clear from study of both table 5 and figure 16 that the newer apparatus provides linear thermal expansion values of excellent precision; 87% of the data points shown lie within ±1 ppm of a four-term fitting equation.

The linear thermal expansion for sample S-M can be expressed in terms of eq (27), using the coefficients given in table 5 and the sample length derived for 0 °C,

$$\begin{aligned}\epsilon(t,0\,^\circ\mathrm{C}) &= 8.707\times10^{-6}\,t+2.177\times10^{-9}\,t^2\\ &\quad -1.037\times10^{-12}\,t^3+5.729\times10^{-16}\,t^4. \end{aligned} \tag{29}$$

A second sample of the same alloy was prepared from the NIST gas thermometer bulb in the same manner as sample S-M. Designated S-U, the sample's bench-top (23.2 °C) length, expressed in fringes of light of 546.2271 nm, was measured as 90,445.6 fringes. The linear thermal expansion of sample S-U was measured in much the same way as S-M, although with fewer (15) steady temperatures. The results, however, were quite similar. Tables 6 and 7 show the information obtained from measurements on sample S-U, and figure 17 shows the differences between the experimental and cal-

Table 4. Experimental data for sample S-M (80 Wt% Pt+20 Wt% Rh) run 502, October-November 1987 N(23.6 °C)=92,567.3±0.5 fringes

1 Steady temp. no.	2 t(68), °C	3 F.F.[a].	4 Gas press. kPa	5 F.F. corr.	6 ΔN_{exp}[b]	7 ΔN_{cal}	8 Dev fr[c]
1	700.086	0.559	0.169	0.557			
1a					−50.154	−50.285	0.131
2	650.400	0.406	0.268	0.403			
2a					−50.071	−50.056	−0.015
3	600.202	0.334	0.184	0.332			
3a					−48.893	−48.899	0.006
4	550.449	0.442	0.275	0.439			
4a					−48.843	−48.868	0.025
5	500.009	0.601	0.392	0.596			
5a					−47.301	−47.334	0.033
6	450.451	0.297	0.149	0.295			
6a					−46.925	−46.983	0.058
7	400.551	0.372	0.127	0.370			
7a					−46.794	−46.892	0.098
8	350.007	0.582	0.411	0.576			
8a					−45.319	−45.316	−0.003
9	300.413	0.259	0.145	0.257			
9a					−44.504	−44.522	0.018
10	250.916	0.761	0.447	0.753			
10a					+0.948	+0.974	−0.026
11	252.007	0.705	0.211	0.701			
11a					−41.935	−42.000	0.065
12	204.567	0.769	0.136	0.766			
12a					−39.312	−39.224	−0.088
13	159.530	0.457	0.124	0.454			
13a					−38.989	−38.977	−0.012
14	114.001	0.469	0.155	0.465			
14a					−36.990	−36.982	−0.008
15	70.007	0.480	0.200	0.475			
15a					−37.054	−37.093	0.039
16	25.009	0.429	0.295	0.421			
16a					−40.308	−40.287	−0.021
17	−24.988	(0.115)[d]	0.060	(0.113)[d]			
18	−24.609	0.347	0.067	0.345			
18a					22.243	22.362	−0.119
19	+3.292	0.591	0.104	0.588			
19a					17.818	17.784	0.034
20	25.206	0.412	0.216	0.406			
20a					20.890	20.847	0.043
21	50.607	0.304	0.287	0.296			
21a					20.272	20.247	0.025
22	74.999	0.576	0.323	0.568			
22a					21.002	20.981	0.021
23	100.005	0.575	0.231	0.570			
23a					21.058	21.091	−0.033
24	124.882	0.628	0.016	0.628			
24a					21.991	21.958	0.033
25	150.521	0.620	0.039	0.619			
25a					21.024	20.995	0.029
26	174.802	0.646	0.165	0.643			
26a					22.026	21.995	0.031
27	200.007	0.673	0.227	0.669			
27a					21.803	21.862	−0.059
28	224.836	0.474	0.119	0.472			
28a					23.032	23.020	0.012

Table 4. Experimental data for sample S-M (80 Wt% Pt+20 Wt% Rh) run 502, October–November 1987 $N(23.6\ ^\circ\mathrm{C})=92{,}567.3\pm0.5$ fringes—Continued

1 Steady temp. no.	2 $t(68)$, °C	3 F.F[a].	4 Gas press. kPa	5 F.F. corr.	6 ΔN_{exp}[b]	7 ΔN_{cal}	8 Dev fr[c]
29	250.752	0.506	0.129	0.504			
29a					21.969	21.932	0.037
30	275.236	0.477	0.216	0.473			
30a					23.020	23.027	−0.007
31	300.734	0.495	0.113	0.493			
31a					22.124	22.094	0.030
32	325.007	0.620	0.209	0.617			
32a					22.916	22.929	−0.013
33	350.005	0.537	0.243	0.533			
33a					23.105	23.111	−0.006
34	375.011	0.643	0.333	0.638			
34a					23.811	23.890	−0.079
35	400.666	0.450	0.045	0.449			
35a					23.210	23.232	−0.022
36	425.430	0.660	0.080	0.659			
36a					23.011	23.019	−0.008
37	449.793	0.672	0.133	0.670			
37a					23.950	23.974	−0.024
38	474.986	0.622	0.173	0.620			
38a					24.812	24.638	0.174
39	500.689	0.433	0.119	0.432			
39a					24.067	24.053	0.014
40	525.601	0.501	0.184	0.499			
40a					23.980	23.938	0.042
41	550.220	0.481	0.220	0.479			
41a					24.861	24.663	0.198
42	575.404	0.344	0.355	0.340			
42a					24.260	24.260	0.000
43	600.000	0.602	0.148	0.600			
43a					25.008	24.842	0.166
44	625.006	0.611	0.267	0.608			
44a					25.002	25.005	−0.003
45	649.993	0.611	0.128	0.610			
45a					24.987	24.958	0.029
46	674.750	0.599	0.168	0.597			
46a					25.832	25.813	0.019
47	700.162	0.431	0.185	0.429			

[a] F.F.; fractional fringe count at the fiducial mark.
[b] ΔN_{exp}; corrected differences in sample length, expressed in fringes.
[c] Dev; $\Delta N_{\mathrm{exp}}-\Delta N_{\mathrm{cal}}$. These differences are plotted in figure 16.
[d] The experimental uncertainty of this value was unusually high.

culated values. Again, most of the differences (13 of the 15 points) lie within ±1 ppm of the sample length.

The linear thermal expansion for sample S-U, using the coefficients from table 7 and the sample length calculated for 0 °C, is

$$\epsilon(t,0\ ^\circ\mathrm{C})=8.730\times10^{-6}\,t+2.056\times10^{-9}\,t^2-7.999\times10^{-13}\,t^3+4.111\times10^{-16}\,t^4. \qquad (30)$$

It is useful to examine the relationship between the linear thermal expansion coefficients determined a decade ago on a sample of 80 Wt% Pt+20 Wt% Rh (see eq (10) in sec. 6.2 and reference [19]) and those of the two samples measured with the newer thermal expansion apparatus [eqs (29) and (30)]. Such a comparison can demonstrate the stability of the alloy to temperature cycling, and can show as well the practical similarity of two different thermal expansion facilities.

Table 5. Fitting parameters for the thermal expansion of sample S-M (80 Wt% Pt+20 Wt% Rh)

Equation used in least-squares fitting procedure:

$$\Delta N(t_i, t_{i+1}) = \sum_{n=1}^{m} A_n(t^n_{i+1} - t^n_i) \qquad (26)$$

Determination of number of polynomial terms for "best fit":

$p=45$ data points

m	σ^a	$F_m{}^b$	$F_{0.95}\,(1, p\text{-}m)$
1	2.169 2		
2	0.130 7	12073.4	4
3	0.084 7	60.4	4
4	0.066 7	26.6	4
5	0.061 8	7.8	4
6	0.060 4	2.9	4

Coefficients of 4th degree polynomial:

n	A_n	σ of A_n
1	0.805 840 5	0.000 897 4
2	0.000 201 509	0.000 005 967
3	−0.000 000 095 958	0.000 000 014 034
4	0.000 000 000 053 023	0.000 000 000 010 233

$N(0\ ^\circ\text{C})=92{,}548.2$ fringes (calc)

---

[a] σ: the estimated standard deviation of the fit.

[b] F_m: an index used to estimate the level of significance of the mth coefficient in the equation fitted to the data.

$$F_m = 1 + (p - m + 1)[(\sigma_{m-1}/\sigma_m)^2 - 1]$$

where p is the number of data points and m is the number of coefficients in the polynomial. The coefficient A_m is considered significant at the desired level of confidence if F_m is greater than the corresponding value given in the fourth column. (Entries in column 4 were taken from a standard table for the F-distribution, e.g., table 3 of reference [34].)

One method for comparing the three sets of results on the alloy in question would consist of a comparison of the thermal expansion coefficients obtained by fitting the separate sets of data. In table 8, we show the three sets of coefficients determined independently, along with the estimated standard deviations of the respective fits, normalized to unit sample length. Comparison of the three equations shows agreement within about two parts per million over the measured temperature range.

The similarity of the three sets of measurements can be demonstrated more clearly by fitting eq (26) to all of the data as a single set. This we have done, after normalizing the three sets of fringe differences $\Delta N(t_i,t_{i+1})$ to a uniform sample length. The thermal expansion coefficients thus determined for the pooled data are given in table 8, and the differences between the experimental and calculated values are shown in figure 18. One can see that no systematic difference larger than the imprecision of the fitting process is evident between any pair of samples. Furthermore, the estimated standard deviation of the pooled-data fit is quite comparable to those determined for the individual samples. These facts indicate that annealed samples of Pt-Rh alloy are extremely stable metallurgically, and that the two versions of the thermal expansion measurement apparatus are remarkably consistent in their performance.

The pooled-data thermal expansion equation,

$$\epsilon(t,0\ ^\circ\text{C}) = 8.70484\times10^{-6}\,t + 2.24455\times10^{-9}\,t^2 - 1.2136\times10^{-12}\,t^3 + 6.9642\times10^{-16}\,t^4, \qquad (31)$$

will be used later to correct the observed gas thermometry results that were reported in reference [35].

In addition to the random uncertainty levels of ±2 ppm, there are systematic uncertainties in the thermal expansion determinations whose magnitudes can only be estimated. These include differences between the sample temperature and thermometer T (fig. 14), used to obtain the sample temperature, which were estimated as no larger than 0.001 °C; uncertainty in the fringe counts, which were estimated as no larger than 0.01 fringe; uncertainty in the actual index of refraction of the gas that occupies the sample space, which was estimated to correspond to no more than 0.02 fringe; uncertainty in the vacuum wavelength of the spectrometer light source, which was estimated to be less than 1 ppm; and changes in the sample thermal expansivity or in expansion-related properties during the measurements, which were estimated as less than 2 ppm by virtue of the agreement shown in figure 18.

9. Scale Differences From 230 to 660 °C

As noted above, much of the gas thermometry data needed to calculate Kelvin thermodynamic temperature values in the range 230 to 660 °C was available in a laboratory microcomputer as soon as the measurements had been performed. Installation on the laboratory computer of the computational programs used earlier on the central NBS computer by Guildner and Edsinger [21] allowed the quick evaluation of the quantity t(KTTS)-t(IPTS-

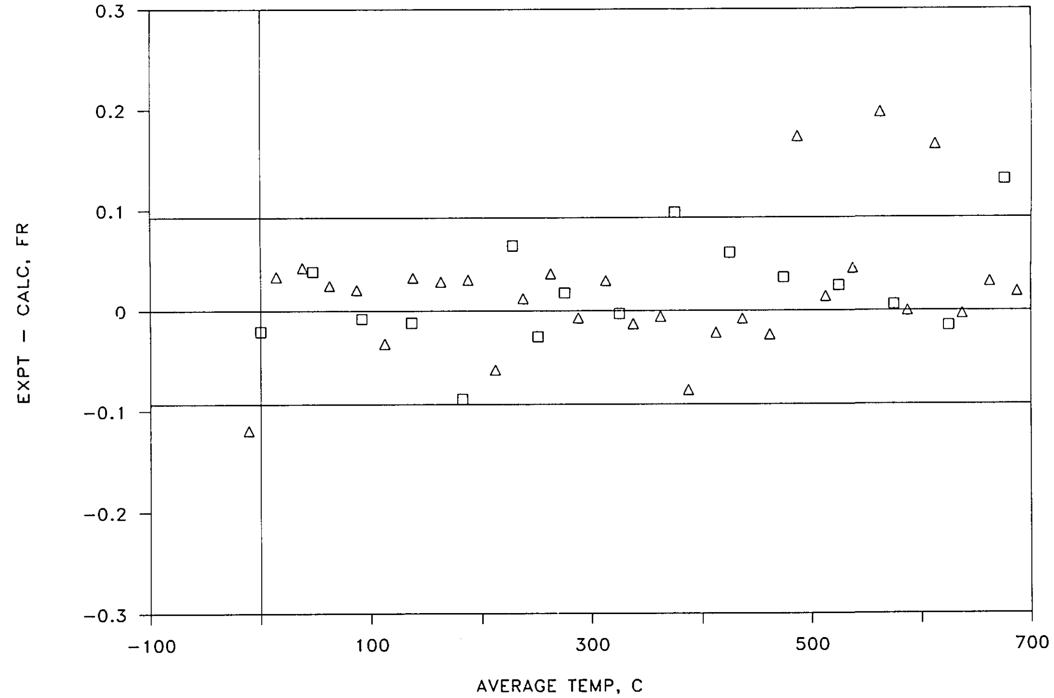

Figure 16. Differences in fringes of light at 546 nm between the length changes that were observed experimentally for sample S-M (80 Wt% Pt+20 Wt% Rh) and those that were calculated from a 4th degree fitting equation (see table 5). Squares—data taken during cooling cycle. Triangles—data taken during warming cycle. All data points but one were obtained over at least a 20 °C temperature interval. Horizontal lines are drawn at the levels that indicate ±1 ppm of the sample length.

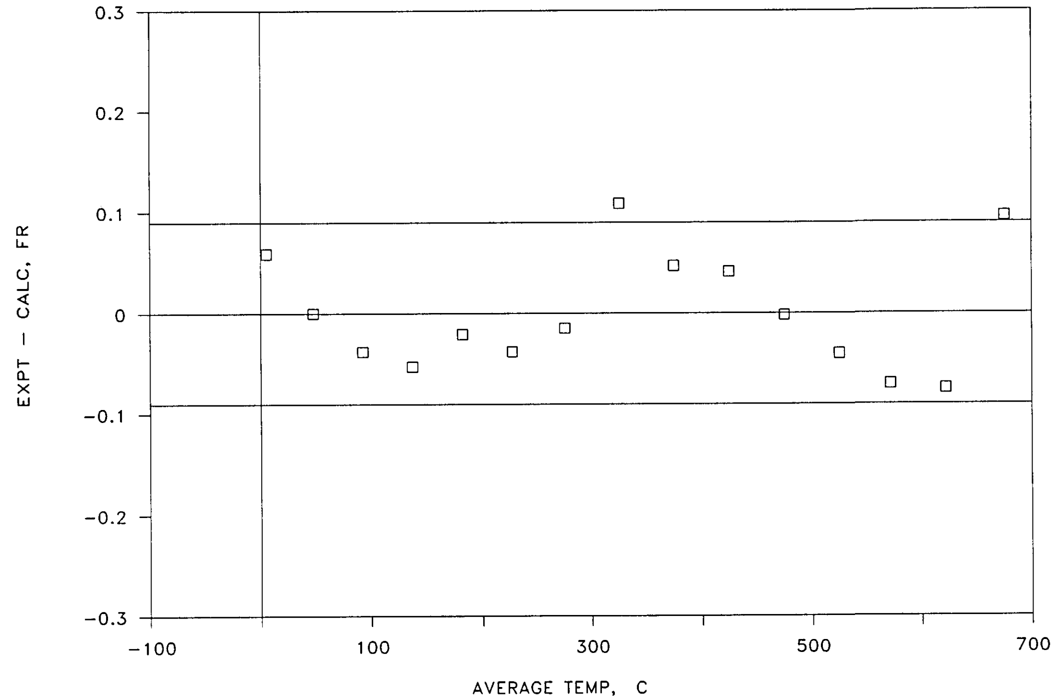

Figure 17. Differences in fringes of light at 546 nm between the length changes that were observed experimentally for sample S-U (80 Wt% Pt+20 Wt% Rh) and those that were calculated from a 4th degree fitting equation (see table 7). The data were obtained during one cooling cycle. Horizontal lines are drawn at the levels that indicate ±1 ppm of the sample length.

Table 6. Experimental data for sample S-U (80 WT% Pt+20 Wt% Rh) run 501, April-July 1987 $N(23.2\ ^\circ\text{C})=90{,}445.6\pm0.5$ fringes

1 Steady temp. no.	2 $t(68)$, °C	3 F.F.[a]	4 Gas press. kPa	5 F.F. corr.	6 ΔN_{exp}[b]	7 ΔN_{cal}	8 Dev fr[c]
1	700.801	0.482	0.305	0.479			
1a					−49.867	−49.963	0.096
2	650.201	0.615	0.331	0.612			
2a					−55.118	−55.043	−0.075
3	593.602	0.498	0.348	0.494			
3a					−41.874	−41.804	−0.070
4	550.005	0.624	0.363	0.620			
4a					−47.081	−47.041	−0.040
5	500.298	0.543	0.372	0.539			
6	500.305	0.500	0.424	0.495			
6a					−46.961	−46.959	−0.002
7	449.976	0.539	0.424	0.534			
7a					−45.916	−45.957	0.041
8	400.004	0.624	0.437	0.618			
8a					−44.994	−45.041	0.047
9	350.301	0.630	0.435	0.624			
9a					−44.257	−44.366	0.109
10	300.594	0.374	0.427	0.367			
11	300.608	0.309	0.613	0.299			
11a					−44.073	−44.058	−0.015
12	250.454	0.236	0.597	0.226			
12a					−39.848	−39.810	−0.038
13	204.404	0.389	0.596	0.378			
14	204.405	0.483	1.243	0.460			
14a					−37.801	−37.780	−0.021
15	160.001	0.684	1.200	0.659			
15a					−38.122	−38.069	−0.053
16	114.503	0.563	1.147	0.537			
16a					−36.207	−36.169	−0.038
17	70.505	0.358	1.093	0.330			
17a					−36.744	−36.744	0.000
18	24.954	0.616	1.028	0.586			
19	24.951	0.649	1.040	0.618			
19a					−31.368	−31.427	0.059
20	−14.766	0.264	0.408	0.250			

[a] F.F.; fractional fringe count at the fiducial mark.

[b] ΔN_{exp}; corrected differences in sample length, expressed in fringes, that accompany changes from one steady-state temperature to the next.

[c] Dev; $\Delta N_{\text{exp}}-\Delta N_{\text{cal}}$. These differences are plotted in figure 17.

68) for a given measurement and thus the modification of procedures or apparatus as needed. The linear thermal expansion coefficients for sample S-M [eq (29)] were incorporated into the program to calculate the gas bulb volume at the various gas thermometer temperatures.

9.1 IPTS-68 Temperatures

The specially prepared PRT's used in the high-temperature measurements were of sufficient quality to define the IPTS-68 by means of the usual calibration procedure. During the measurements, the thermometers were calibrated four times. One of the calibrations included measurements at the aluminum freezing-point temperature.

In use, the thermometers were re-calibrated at the triple point of water after each high-temperature run because of the possibility of drift as a result of mechanical shock or exposure to high temperatures.

IPTS-68 values of temperature near 660 °C were derived from the relation

$$t_{68}=t'+0.045\ ^\circ\text{C}, \tag{32}$$

Table 7. Fitting parameters for the thermal expansion of sample S-U (80 Wt% Pt+20 Wt% Rh)

Equation used in least-squares fitting procedure:

$$\Delta N(t_i,t_{i+1})=\sum_{n=1}^{m} A_n(t^n_{i+1}-t^n_i) \qquad (26)$$

Determination of number of polynomial terms m for "best fit":

$p=15$ data points

m	σ[a]	F_m[b]	$F_{0.95}$ (1, p-m)
1	2.898 0		
2	0.138 9	6081.2	4.67
3	0.075 8	31.7	4.75
4	0.058 1	9.4	4.84
5	0.026 4	43.4	4.96
6	0.020 5	7.6	5.12

Coefficients of 4th degree polynomial:

n	A_n	σ of A_n
1	0.789 424 4	0.001 161 2
2	0.000 185 896	0.000 007 379
3	−0.000 000 072 335	0.000 000 016 695
4	0.000 000 000 037 180	0.000 000 000 011 889

$N(0\ ^\circ\mathrm{C})=90{,}427.2$ fringes (calc)

[a] σ: the estimated standard deviation of the fit.

[b] F_m: an index used to estimate the level of significance of the mth coefficient in the equation fitted to the data.

$$F_m=1+(p-m+1)[(\sigma_{m-1}/\sigma_m)^2-1]$$

where p is the number of data points and m is the number of coefficients in the polynomial. The coefficient A_m is considered significant at the desired level of confidence if F_m is greater than the corresponding value given in the fourth column. (Entries in column 4 were taken from a standard table for the F-distribution, e.g., table 3 of reference [34].)

where t' has the meaning given in the IPTS-68 text [48]. This definition, while not the standard one for this range of temperature, is more precise than the standard one based upon the Pt vs. (Pt+10 Wt% Rh) thermocouple thermometer.

9.2 Non-Ideality of the Working Gas

Guildner and Edsinger used eq (20) to generate values of the second virial coefficient for ^{4}He in the range 0 to 457 °C. A review of more recent literature on this topic [46] indicated to Edsinger and Schooley that eq (19) still was adequate to represent the second virial data, and that it also would suffice for generating values up to temperatures as high as 660 °C within uncertainty limits that range from $\pm 0.2\ \mathrm{cm^3/mol}$ at 0 °C to $\pm 0.4\ \mathrm{cm^3/mol}$ at 660 °C.

9.3 High-Temperature Drift

For the most part, the gas-thermometry measurement procedures and computations used in the most recent experiments were very similar to those described in section 7. The accuracy of the computational programs was verified by re-calculating results obtained earlier, using the original data. One change in procedure, however, is worth noting because it yielded puzzling results. This change involved an attempt to repeat the filling conditions after obtaining a pair of measurements at 0 °C and the test temperature.

In this study, the gas bulb was filled to ~13.3 kPa while it was maintained at 0 °C in the ice bath. After filling, the gas bulb was closed off and the gas thermometer was moved from the ice bath to the high-temperature furnace. The furnace was

Table 8. Linear thermal expansion coefficients determined for three samples of 80 Wt% Pt+20 Wt% Rh

Sample[a]	t^1 coef.	t^2 coef.	t^3 coef.	t^4 coef.	σ_{fit}[b]
Ref [19] (25)	8.674×10^{-6}	2.538×10^{-9}	-2.081×10^{-12}	1.480×10^{-15}	0.062
S-M (45)	8.707×10^{-6}	2.177×10^{-9}	-1.037×10^{-12}	5.729×10^{-16}	0.073
S-U (15)	8.730×10^{-6}	2.056×10^{-9}	-7.999×10^{-13}	4.111×10^{-16}	0.065
Pooled (85)	8.705×10^{-6}	2.245×10^{-9}	-1.214×10^{-12}	6.964×10^{-16}	0.074

[a] Number of data points in parentheses.

[b] Estimated standard deviation of the 4th-degree fit normalized to a uniform sample length.

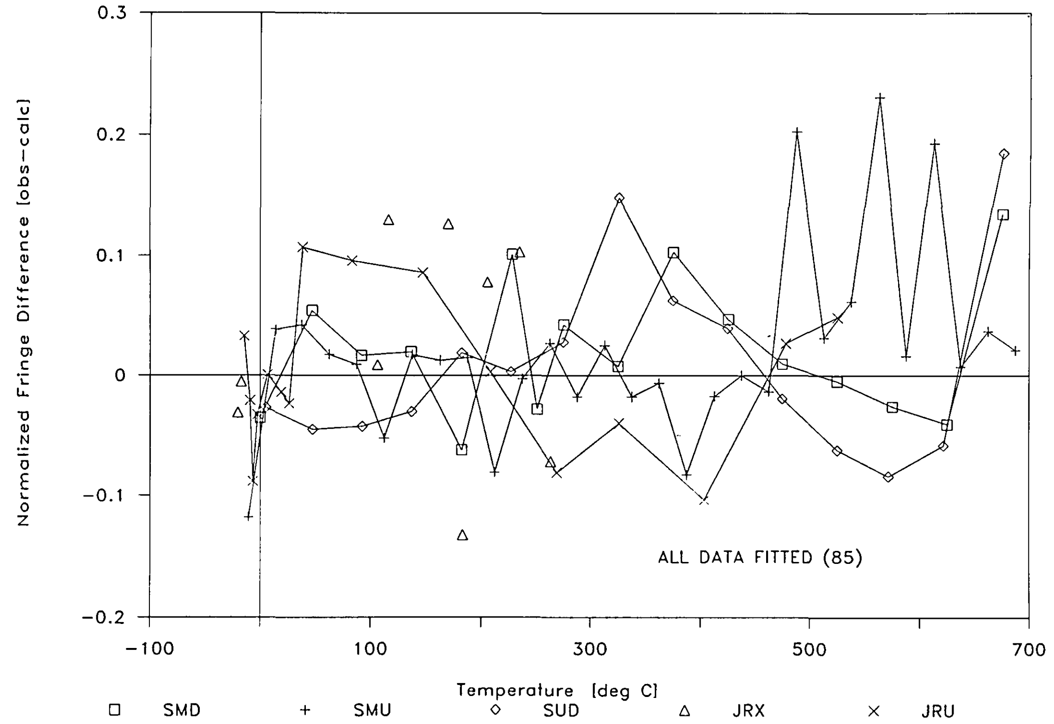

Figure 18. Differences in fringes of light at 546 nm, normalized to a uniform sample length, between the length changes observed experimentally and those that were calculated from eq (26) carried to the 4th degree, for three samples of 80 Wt% Pt+20 Wt% Rh alloy considered as a single set of pooled data. Triangles and x's—data from reference [19], obtained about a decade ago on a sample cut from a sheet of the stated composition. Triangles indicate data obtained in a more or less random sequence of heating and cooling; x's indicate data taken in a single warming sequence. Squares and +'s—data obtained during cooling and warming, respectively, on sample S-M. Diamonds—data obtained during cooling on sample S-U. Both of the latter samples were cut from the NBS/NIST gas thermometer bulb following the completion of the gas thermometry experiments. One ppm of sample length corresponds to ±0.1 fringe.

heated to a temperature in the range 230 to 660 °C, and the furnace controls were set so as to minimize the temperature gradients in the region of the gas bulb, making full use of the extra thermocouple thermometers arrayed along the capillary all the way down to the gas bulb. During the heating period, the height of the gage-block stack was changed, as usual, and the counterpressure was adjusted to track the calculated gas-bulb pressure within about 0.2 kPa. After measurements were completed at the upper temperature, the gas thermometer was returned to the ice bath and the manometer gage-block stack was returned to its original height.

This process, which typically lasted 7 d, invariably led to a final gas-bulb pressure that was lower than its starting value, the discrepancy being the larger, the higher the intervening furnace temperature and the duration of the high-temperature portion of the measurement. During one series of observations, the gas-bulb pressure was monitored while the gas thermometer was maintained for several days at various elevated temperatures. Typically, the observed drift amounted to −0.027 Pa/d at 231 °C, −0.067 Pa/d at 420 °C, and −0.27 Pa/d at 660 °C, as shown in figure 19. In terms of the thermodynamic temperature of the gas bulb, these quantities correspond to drifts of −0.54, −1.3, and −5.4 mK/d, respectively. No such drift in the gas-bulb pressure occurred while the gas thermometer was maintained at 0 °C, even for a period of several weeks.

There was no apparent explanation for this effect. The rather thin-walled (~1 mm) gas bulb was modified by replacing its bottom cap with thicker material (~2.5 mm), as noted in section 8.2, against the possibility that the pressure change had arisen from creep of the gas bulb, and subsequent gas-thermometry measurements of the type described above resulted in a high-temperature drift that, while still observable, was diminished by at least a factor of two at 660 °C.

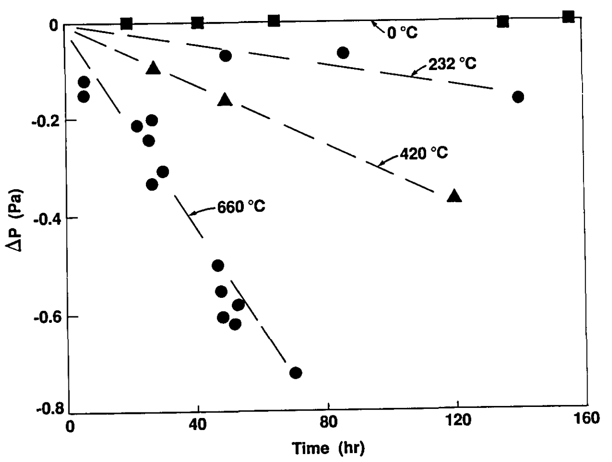

Figure 19. Temperature-dependent drift in the measured pressure of the NBS/NIST gas thermometer, observed while maintaining the thermometer at various elevated temperatures. This effect was found while using a cylindrical Pt-Rh alloy gas-thermometer bulb with a thin (~1 mm) bottom plate. Subsequent measurements with a heavier (~2.5 mm) bottom plate showed approximately one-half as much drift at a particular temperature. The working pressure typically ranged from 13.3 kPa at 0 to 45 kPa at 660 °C. Note that no effect was seen at 0 °C.

The gas thermometry measurement procedure was modified in order to minimize, insofar as possible, the effect of the high-temperature drift mentioned above. The gas bulb was evacuated at a temperature at least as high as that which was to be measured; then the furnace was set at the upper measuring temperature. The gas bulb and manometer were filled with the desired quantity of freshly purified ^{4}He, and both radial and vertical gradients in the furnace were carefully minimized (usually within ±0.003 °C). Then the gas thermometer was allowed to equilibrate. Following this step, the offset in the capacitance diaphragm gage was measured and all power to the furnace heaters was turned off. An ice-bath measurement and thus a determination of t(KTTS)-t(IPTS-68) at the chosen high temperature could be accomplished in this fashion within 48 h of the time when the gas bulb was filled. This procedure avoided long periods of heating and, although it permitted the evaluation of only one IPTS-68 temperature in any one measurement, it minimized any systematic error in the results arising from the unexplained high-temperature drift. The maximum uncertainty from this source was estimated as -0.0006 °C for our measurements at 230 °C and as -0.006 °C for those at 660 °C.

It is interesting to note that Guildner and Edsinger [21] found no such drift during their studies. It was generally their practice to fill the gas bulb at the highest temperature to be studied, then to measure gas-bulb pressures at several temperatures in a decreasing sequence. They did not generally return to the filling temperature to demonstrate the accurate recovery of the filling pressure, but they found no drift during several occasions in which they left the gas bulb at the same temperature for several days.

9.4 Results and Their Uncertainties

The results of 26 determinations of t(KTTS)-t(IPTS-68), obtained in the manner just described, were presented by Edsinger and Schooley in reference [35] and are shown in figure 12. The value 660.342±0.015 °C was obtained for the thermodynamic temperature of the aluminum freezing point.

Four different filling pressures were used in measurements at 660 °C in an effort to verify the accuracy of the thermomolecular correction, which had been obtained from an experimental study conducted on a capillary different from the one used in the gas thermometry experiments (see sec. 7.3). This range of pressures required the employment of thermomolecular corrections as large as 0.3 °C at 660 °C. As can be seen in table 2 of reference [35], the value of the thermodynamic temperature determined in this sequence of measurements varied by no more than 0.0045 °C, indicating that the thermomolecular correction was known within a few percent.

A summary of the estimated uncertainties of the measurements comprising a gas-thermometer temperature determination are given in table 9. At 450 °C, the overall random uncertainty was given as 0.02 °C at the 99% confidence level [35]. By comparison, the corresponding uncertainty of the determination by Guildner and Edsinger [21] at the same temperature was given as no larger than 0.005 °C. Thus the difference between the two sets of determinations (approximately 0.03 °C) is slightly larger than the combined uncertainties.

After the gas thermometry measurements were complete to 660 °C, the gas bulb was disassembled from its protective case and several samples were cut from it for measurement of its thermal expansivity as described in section 8.5. X-ray analysis was used to verify that the entire gas bulb consisted of the same alloy composition.

Table 9. Estimated uncertainties of gas thermometry results from 230 to 660 °C

Source	Type[a]	Magnitude 230 °C	Magnitude 660 °C
Manometer pressure ratio accuracy	C	±0.001	±0.0015
Gas bulb thermal expansion/creep	S	−0.0006	−0.006
Gas bulb thermal expansion measurements	R	±0.003	±0.006
Gas-bulb thermostat temperature inhomogeneity	R	±0.003	±0.005
PRT resistance-temperature relation	R	±0.001	±0.002
^{4}He purity	S	Unknown	
^{4}He virial correction	S	±0.001	±0.004
Thermomolecular pressure correction	S	<0.001	<0.001
Capacitance diaphragm gage imbalance	C	±0.0002	±0.0002

[a] S=Systematic; R=Random; C=Combination.

10. Comparison of Gas Thermometer Results

The largest sources of uncertainty in the work of Guildner and Edsinger were ascribed to uncertainty in the knowledge of the non-ideality of the working gas and to uncertainty in the dead space correction, as shown in table 2. The uncertainty in the thermal expansion of the gas bulb was estimated as ±0.5 mK at the "one-sigma" level; in retrospect, we find that an alternative treatment of the thermal expansion data would result in a ±0.003 °C shift in the calculated thermodynamic temperature at 457 °C. Such a shift would bring the data shown in figure 12 into slightly closer agreement. We also ascribe a slightly larger uncertainty to the calculation of the gas imperfection correction (about ±0.0025 °C at 457 °C) based upon an assessment of the present literature. Finally, one can recall the composite nature of the gas bulb in the previous work, and the necessity to predict its effect upon the overall thermal expansion. While no details were given of this prediction, Guildner and Edsinger considered that the problem had negligible impact upon the accuracy of their results.

On the other hand, the experiments of Edsinger and Schooley were notable for the rather larger uncertainties in the determination of IPTS-68 temperatures, arising from the difficulty of setting and measuring the gas-bulb temperature in the gaseous environment of the high-temperature furnace. Also notable in the more recent experiments was the curious drift in the gas-bulb pressure (see fig. 19), an effect that cannot be ascribed to leakage in the equipment, or, indeed, to any unequivocal source. Taking account of the completed thermal expansion results given in section 8.5 modifies the published results of Edsinger and Schooley only slightly. Replacing the coefficients of eq (29), which were employed in calculating the gas-thermometry results given in reference [35], with the coefficients of eq (31) has the effect of increasing the calculated thermodynamic temperatures by 0.002 °C at 250 °C, by 0.0033 °C at 400 °C, and by 0.001 °C at 630 °C. While these corrections are not large ones, they illustrate the great sensitivity of gas thermometry measurements to the thermal expansion of the gas bulb itself.

In comparing the two sets of experimental results at 457 °C, as shown in figure 12, one finds very similar levels of experimental variation in the results, about 0.006 °C in reference [21] and 0.005 °C in reference [35]. The estimated uncertainties associated with the determinations of thermal expansion, of gas-bulb creep, of the gas-bulb temperature, and of the non-ideality of the working gas in the more recent work [35], however, are considerably larger than their earlier counterparts, resulting in overall random uncertainties estimated to range, at the level of one standard deviation, from 0.0045 °C at 230 °C to 0.008 °C at 660 °C. The combined uncertainties at the 99% confidence level nearly overlap both at 230 and at 457 °C.

11. Summary and Conclusions

The work described herein has been pursued over the course of several decades. It has achieved its goal of evaluating the accuracy of the international scale of temperature with respect to the basic Kelvin Thermodynamic Temperature Scale. The IPTS-68 was shown to deviate from the Kelvin Thermodynamic Scale by amounts far in excess of those expected when the international scale was promulgated, leading to a world-wide effort to perfect a replacement scale. In fact, this replacement scale, to be known as the International Temperature Scale of 1990 (ITS-90) is essentially complete at the time of this writing.

In the course of preparing the equipment needed for this project, a mercury manometer facility was constructed that was, and very likely remains today, the most accurate pressure-measurement facility in the world. Similar advances in the construction of capacitance level sensing equipment, in constant-volume valves and articulating seals, and in high-accuracy dilatometry have resulted from this project.

The basic physical concepts of the gas thermometry experiments described herein involve techniques that are well understood, while their realization and refinement have occupied highly trained and dedicated workers during whole careers of meticulous effort. The work described herein has considerably improved our understanding of the Kelvin Thermodynamic Temperature Scale, but it is clear from a glance at figure 12 that the Kelvin Thermodynamic Scale still is uncertain in the range upwards from 200 °C by about ±20 ppm. Reducing this uncertainty is a task that we leave to future thermometrists, who well may employ a different technology.

12. Acknowledgments

The author is grateful to R. E. Edsinger and to L. A. Guildner for discussing many details of their work with him. He is also indebted to G. T. Furukawa, to M. L. Reilly, and to J. M. H. Levelt Sengers for careful reviews of the draft manuscript.

About the author: Dr. James F. Schooley, recently retired from NIST, served in the positions of Postdoctoral Research Associate, Heat Division; Staff Physicist, Heat Division; Chief of the Temperature Section, Heat Division; Chief of the Temperature and Pressure Division, National Measurement Laboratory; and most recently, Staff Physicist, Temperture and Pressure Division, National Measurement Laboratory. Besides gas thermometry, his research interest was cryogenic physics.

13. References

[1] Thomson, W., On an absolute thermometric scale founded on Carnot's theory of the motive power of heat, and calculated from Regnault's observations, Cambridge Phil. Soc. Proc., June 5, 1848.

[2] Berry, K. H., Metrologia **15**, 89 (1979).

[3] Kemp, R. C., Kemp, W. R. G., and Besley, L. M., Metrologia **23**, 61 (1986).

[4] Beattie, J. A., "Gas thermometry", Temperature, Its Measurement and Control in Science and Industry, **2**, Wolfe, H. C., Ed., Reinhold Pub. Corp., New York (1955) pp. 63–97.

[5] Guildner, L. A., Stimson, H. F., Edsinger, R. E., and Anderson, R. L., Metrologia **6**, 1 (1970).

[6] See, for example, data book "LAG Gas Thermometry No. 5."

[7] Stimson, H. F., "Precision resistance thermometry and fixed points," Temperature, Its Measurement and Control in Science and Industry, **2**, Wolfe, H. C., Ed., Reinhold Pub. Corp., New York (1955) pp. 141–168.

[8] Guildner, L. A., "A National Bureau of Standards Gas Thermometer," Temperature, Its Measurement and Control in Science and Industry, **3, Part 1**, Brickwedde, F. G., Ed., Reinhold Pub. Corp., New York (1962) pp. 151–155.

[9] Guildner, L. A. and Edsinger, R. E., J. Res. Natl. Bur. Stand. (U.S.) **69C**, 13 (1965).

[10] Anderson, R. L., Guildner, L. A., and Edsinger, R. E., Rev. Sci. Instr. **41**, 1076 (1970).

[11] Guildner, L. A., Anderson, R. L., and Edsinger, R. E., "Effects of sorption on the realization of the thermodynamic scale," Temperature, Its Measurement and Control in Science and Industry, **4**, Plumb, H. H., Ed.-in-Chief, Instrument Society of America, Pittsburgh (1972) pp. 313–322.

[12] Edsinger, R. E., Guildner, L. A., and Anderson, R. L., Rev. Sci. Inst. **42**, 945 (1971).

[13] Anderson, R. L. and Guildner, L. A., Rev. Sci. Instr. **36**, 615 (1965).

[14] Beattie, J. A., Rev. Sci. Instr. **2**, 458 (1931).

[15] Guildner, L. A. and Edsinger, R. E., J. Res. Natl. Bur. Stand. (U.S.) **77A**, 383 (1973).

[16] Kirby, R. K., J. Res. Natl. Bur. Stand. (U.S.) **71A**, 363 (1967).

[17] Hahn, T. A., J. Appl. Phys. **41**, 5096 (1970).

[18] Edsinger, R. E., "Method for obtaining accurate thermal expansion data on solids from 50 to 1000 °C," 1968 Symposium on Thermal Expansion of Solids, Paper #25.

[19] Edsinger, R. E., Reilly, M. L., and Schooley, J. F., J. Res. Natl. Bur. Stand. (U.S.) **91**, 333 (1986).

[20] The rate of change of pressure in the gas bulb was judged to be sufficiently slow that the pressure difference never exceeded 1 kPa.

[21] Guildner, L. A. and Edsinger, R. E., J. Res. Natl. Bur. Stand. (U.S.) **80A**, 703 (1976).

[22] Powell, R. L., Hall, W. J., Hyink, C. H., Jr., Sparks, L. L., Burns, G. W., Scroger, M. G., and Plumb, H. H., "Thermocouple reference tables based on the IPTS-68," NBS Monograph 125, 410 pp, March 1974.

[23] Quinn, T. J. and Martin, J. E., Phil. Trans. Roy. Soc. London Ser. A **316**, 85 (1985).

[24] Moldover, M. and Trusler, J. P. M., Metrologia **25**, 165 (1988).

[25] Jung, H. J., Metrologia **20**, 67 (1984).

[26] Coates, P. B. and Andrews, J. W., "Measurement of thermodynamic temperatures with the NPL photon-counting pyrometer," in Temperature, Its Measurement and Control in Science and Industry, **5**, Schooley, J. F., Ed., American Institute of Physics, New York (1982) pp. 109–114.

[27] Coates, P. B., Andrews, J. W., and Chattle, M. V., Metrologia **21**, 31 (1985).

[28] Guildner, L. A. and Edsinger, R. E., "Progress in NBS gas thermometry above 500 °C," in Temperature, Its Measurement and Control in Science and Industry, **5**, Schooley, J. F., Ed., American Institute of Physics (1982) pp. 43–48.

[29] Evans, J. P., J. Res. Natl. Bur. Stand. (U.S.) **89**, 349 (1984).

[30] Bass, N. and Evans, J. P., "Techniques in high-temperature resistance thermometry," NBS Tech Note 1183, Jan. 1984, 15 pp.

[31] Cutkosky, R. D., J. Res. Natl. Bur. Stand. (U.S.) **74C**, 15 (1970).

[32] Cutkosky, R. D., "Automatic resistance bridges for new and special applications," in Temperature, Its Measurement and control in Science and Industry, **5**, Schooley, J. F., Ed., American Institute of Physics, New York (1982) pp. 711–713.

[33] Edsinger, R. E. and Schooley, J. F., "A high-accuracy dilatometer for the range −20 °C to +700 °C," Tenth International Thermal Expansion Symposium, Boulder CO, June 6-7, 1989. To be published in Int. J. of Thermophys.

[34] Mandel, J., Chapt. 8 in The Statistical Analysis of Experimental Data, Wiley & Sons, New York (1964).

[35] Edsinger, R. E. and Schooley, J. F., Metrologia, **26**, 95 (1989).

[36] Candler, C., Chapt. IV in Modern Interferometers, Hilger & Watts, Ltd. (1951).

[37] Merritt, G. E., "Application of the interferometer to measurements of the thermal dilation of ceramic materials," Scientific Papers of the Bureau of Standards **19**, No. 485 (1924).

[38] Saunders, J. B., An apparatus for photographing interference phenomena, NBS Research Paper RP1668, J. Res. Natl. Bur. Stand. (U.S.) **35**, 157 (1945).

[39] Kaufman, V., J. Opt. Soc. Amer. **52**, 866 (1962).

[40] Cook A. H. and Stone, N. W. B., Phil. Trans. Roy. Soc. Lond., Ser A **250**, 279 (1957). The value given at 20 °C and 101.325 kPa is 13545.874 kgm/m^3±0.014.

[41] Patterson, J. B. and Prowse, D. B., Metrologia **21**, 107 (1985). The densities of mercury samples obtained from different sources vary by several ppm; therefore it is necessary to measure particular samples directly.

[42] CSIRO Measurement Report RS 14251, April 9, 1987. Quoted in Moldover, M. R., Trusler, J. P. M., Edwards, T. J., Mehl, J. B., and Davis, R. S., J. Res. Natl. Bur. Stand. (U.S.) **93**, 85 (1988).

[43] Measurements by the Coast and Geodetic Survey, Environmental Sciences Services Administration, U.S. Department of Commerce, June 19 and 21, 1968.

[44] MKS Baratron, 1000 Torr head.

[45] Chino Works. Inc, Model R-800-3.

[46] Kell, G. S., McLaurin, G. E., and Whalley, E., J. Chem. Phys. **68**, 2199 (1978).

[47] This function was inadvertently written incorrectly in reference [19]. As eq (8), the right-hand side was given incorrectly as $\Sigma A_n\,[t^n_i - t^n_{i+1}]$, the negative of the correct expression given in eq (26) of this paper.

[48] "The International Practical Temperature Scale of 1968, Amended Edition of 1975," Metrologia **12**, 7 (1976).

Volume 95, Number 3, May–June 1990
Journal of Research of the National Institute of Standards and Technology

[J. Res. Natl. Inst. Stand. Technol. 95, 291 (1990)]

Phase Equilibria and Crystal Chemistry in Portions of the System SrO-CaO-Bi_2O_3-CuO, Part II—The System SrO-Bi_2O_3-CuO

Volume 95 Number 3 May–June 1990

R. S. Roth, C. J. Rawn, B. P. Burton, and F. Beech

National Institute of Standards and Technology,
Gaithersburg, MD 20899

New data are presented on the phase equilibria and crystal chemistry of the binary systems SrO-Bi_2O_3 and SrO-CuO and the ternary system SrO-Bi_2O_3-CuO. Symmetry data and unit cell dimensions based on single crystal and powder x-ray diffraction measurements are reported for all the binary SrO-Bi_2O_3 phases, including a new phase identified as $Sr_6Bi_2O_9$. The ternary system contains at least four ternary phases which can be formed in air at ~900 °C. These are identified as $Sr_2Bi_2CuO_6$, $Sr_8Bi_4Cu_5O_{19+x}$, $Sr_3Bi_2Cu_2O_8$ and a solid solution (the Raveau phase) which, for equilibrium conditions at ~900 °C, corresponds approximately to the formula $Sr_{1.8-x}Bi_{2.2+x}Cu_{1\pm x/2}O_z$ $(0.0 \leqslant x \leqslant \sim 0.15)$. Superconductivity in this phase apparently occurs only in compositions that correspond to negative values of x. Compositions that lie outside the equilibrium Raveau-phase field often form nearly homogeneous Raveau-phase products. Typically this occurs after relatively brief heat treatments, or in crystallization of a quenched melt.

Key words: crystal chemistry; phase equilibria; single crystal diffraction; SrO-CaO-Bi_2O_3-CuO; superconductivity; x-ray powder diffraction.

Accepted: March 2, 1990

1. Introduction

The discovery of high transition temperature (T_c) superconductivity in cuprates by Bednorz and Müller [1] and its confirmation by Takagi et al. [2] as being due to the phase $La_{2-x}Ba_xCuO_4$ led to a world-wide search for other compounds with higher T_c. These researches first produced $La_{2-x}Sr_xCuO_4$ [3] and quickly led to the discovery of a mixed phase composition in the system BaO-Y_2O_3-CuO with a $T_c \sim 90$ K [4], well above liquid nitrogen temperature (73 K). Identification of the superconducting phase as $Ba_2YCu_3O_{6+x}$ [5] has resulted in hundreds of published reports on the properties of this phase. Our own phase equilibria studies of the system BaO-Y_2O_3-CuO [6,7] have shown that CO_2 is an important constituent of bulk ceramics that are prepared in air.

Phases with still higher T_c were found in the systems SrO-CaO-Bi_2O_3-CuO and BaO-CaO-Tl_2O_3-CuO [8,9]. These phases belong mostly to a homologous series $A_2Ca_{n-1}B_2Cu_nO_{2n+4}$ ($A=$ Sr, Ba; $B=$ Bi, Tl) although another series $A_2Ca_{n-1}BCu_nO_{2n+3}$ ($A=Ba$, $B=Tl$) can also lead to superconducting phases [10]. Still other compounds have been discovered with high T_c, i.e., $Pb_2Sr_2YCu_3O_{8+\delta}$ [11], $Ba_{1-x}K_xBiO_3$ [12] (with no Cu ions!) and $Nd_{2-x}Ce_xCuO_4$ [13]. The Tl^{+3} containing phases with the largest values of n, so far have the highest confirmed T_c, up to ~125 K [9]. However, the phases in the Tl^{+3} system are difficult to prepare as bulk single phase samples, and the relevant phase equilibria have not been determined, owing to the extreme volatility of Tl and the poisonous nature of Tl vapors. In the Bi^{+3} containing systems the phase with $n=2$ and $T_c \sim 80$ K is easily prepared. However, its exact single-phase region is not well known and a structure determination has not been completed because of very strong incommensurate diffraction that is apparently due to a modulation of the Bi positions. Higher n (and higher T_c) phases have not been prepared as single phase bulk specimens (without PbO). Thus, we undertook a comprehensive study of the phase equilibria and crystal chemistry of the entire four component system SrO-CaO-Bi_2O_3-CuO. It is hoped that a complete understanding of the crystal chemistry and thermodynamics of the many phases formed will lead to a better understanding of the processing parameters for the preparation of bulk ceramics with reproducible and useful properties.

A prerequisite to understanding the phase equilibria of the four-component system is adequate definition of the phase relations in the bounding binary and ternary systems. The ternary system SrO-CaO-CuO was the first to be investigated and the results were published separately [14]. The solubilities of CaO in the solid solutions that are based on SrO:CuO phases were determined, and a ternary phase $Ca_{1-x}Sr_xCuO_2$ ($x=0.14-0.16$) was discovered. The structure of this ternary phase was refined by Siegrist et al. [15]. The present paper discusses the experimental determination of the phase relations and crystal chemistry of the ternary system SrO-Bi_2O_3-CuO as well as its boundary binary systems. A portion of the binary SrO-CuO system was previously published [16], and the structure of the compound "$Sr_{14}Cu_{24}O_{41}$" was determined [17]. Because of the relative importance of the phase $Sr_2Bi_2CuO_6$, a separate paper was prepared concerning the composition, unit cell dimensions and symmetry of this phase [18]. The experimental details, phase relations and crystal chemistry of the binary CaO-Bi_2O_3 and the two remaining ternary systems CaO-Bi_2O_3-CuO and SrO-CaO-Bi_2O_3 are reported in separate publications [19,20].

In the following discussion of phase equilibria and crystal chemistry, the oxides under consideration will always be given in the order of decreasing ionic radius, largest first, e.g., SrO:$\frac{1}{2}Bi_2O_3$:CuO. The notation $\frac{1}{2}Bi_2O_3$ is used so as to keep the metal ratios the same as the oxide ratios. The standard cement/ceramic notation is used for short hand with S=SrO, B=$\frac{1}{2}Bi_2O_3$ and C=CuO. Thus compositions may be listed simply by numerical ratio, e.g., the formula $Sr_2Bi_2CuO_6$ can be written as S_2B_2C or simply 2:2:1.

2. Experimental Procedures

In general, about 3.5 g specimens of various compositions in binary and ternary combinations were prepared from $SrCO_3$, Bi_2O_3, and CuO. Neutron activation analyses of the starting materials indicated that the following impurities (in μg/g) were present: in CuO−3.9Cr, 2.8Ba, 28Fe, 410Zn, 0.09Co, 1.9Ag, 0.03Eu, 14Sb; in Bi_2O_3−2.1Cr, 0.0002Sc, 26Fe, 21Zn, 0.6Co, 0.5Ag, 0.0008Eu, 0.2Sb; in $SrCO_3$−320Ba, 0.001Sc, 6.3Fe, 3.7Zn, 0.1Co, 0.002Eu. The constituent chemicals were weighed on an analytical balance to the nearest 0.0001 g and mixed either dry or with acetone in an agate mortar and pestle. The weighed specimen was pressed into a loose pellet in a stainless steel die and fired on an MgO single crystal plate, or on Au foil, or on a small sacrificial pellet of its own composition. The pellets were then calcined several times at various temperatures from ~600 °C to 850 °C, with grinding and repelletizing between each heat treatment. Duration of each heat treatment was generally about 16–20 h. For the final examination a small portion of the calcined specimen was refired at the desired temperature (1–8 times), generally overnight, either as a small pellet or in a small 3 mm diameter Au tube, either sealed or unsealed. Too many heat treatments in the Au tube generally resulted in noticeable loss of Cu to the Au vessel.

When phase relations involving partial melting were investigated, specimens were contained in 3 mm diameter Au, Pt or Ag/Pd tubes and heated in a vertical quench furnace. This furnace was heated by six $MoSi_2$ hairpin heating elements with vertical 4-in diameter ZrO_2 and 1-in diameter Al_2O_3 tubes acting as insulators. The temperature was measured separately from the controller at a point within approximately 1 cm of the specimen by a Pt/90Pt10Rh thermocouple, calibrated against the melting points of NaCl (800.5 °C) and Au (1063 °C). After the appropriate heat treatment the specimen was quenched by dropping it into a Ni crucible, which was cooled by He flowing through a copper tube immersed in liquid N_2.

In order to approach equilibrium phase boundaries by different synthesis routes, many specimens were prepared from pre-made compounds or two-phase mixtures as well as from end members. These were weighed, mixed and ground in the same way as for the previously described specimens. Also, some specimens were: 1) annealed at some temperature (T_1) and analyzed by x-ray powder diffraction; 2) annealed at a higher or lower temperature (T_2) where a different assemblage of phases was observed; and 3) returned to T_1 to demonstrate reversal of the reaction(s) between T_1 and T_2. All experimental details are given in tables 1a and 1b. Phase identification was made by x-ray powder diffraction using a high angle diffractometer with the specimen packed into a 5 or 10 mil deep cavity in a glass slide. The diffractometer, equipped with a theta compensating slit and a graphite diffracted beam monochromator, was run at $\frac{1}{4}°2\theta$/min with CuKα radiation at 40 KV and 30 MA. The radiation was detected by a scintillation counter and solid state amplifier and recorded on a chart with $1°2\theta = 1$ in. For purposes of illustration and publication, the diffraction patterns of selected specimens were collected on a computer-controlled, step scanning goniometer and the results plotted in the form presented.

Equilibrium in this system has proven to be so difficult to obtain that a few specimens were prepared by utilizing an organic precursor route to obtain more intimate mixtures at low temperatures. It is relatively simple to make mixtures of SrO (with or without CaO) and CuO by utilizing acetate solutions or acrylic acid, but Bi_2O_3 is not soluble in these solutions. The carbonates of all three (or four) oxides were therefore dissolved in lactic acid and dried by slow heating in a container with a large surface-to-volume ratio. This procedure yields an essentially single phase amorphous precursor for all compositions that contain less than about 66.7 mole percent Bi_2O_3. At higher bismuth contents, pure Bi metal was formed by carbothermic reduction under even the lowest temperature drying procedures in air.

3. Experimental Results and Discussion

Most of the experiments performed on the binary and ternary mixtures of SrO:Bi_2O_3:CuO are reported in table 1a. Additional experiments specifically designed in an attempt to obtain crystals large enough for x-ray single crystal study are detailed in table 1b. Crystallographic data for various phases are reported in table 2.

3.1 The System Bi_2O_3-CuO

A phase diagram for this system was already published [21], and was redrawn as figure 6392 in Phase Diagrams for Ceramists (PDFC) [22]. It apparently contains only one compound, Bi_2CuO_4 (B_2C), which is tetragonal, space group P4/ncc, $a = 8.510$, $c = 5.814$ Å [23]. The x-ray powder diffraction data for Bi_2CuO_4 were also reported in [23]. The very limited number of experiments performed during the course of this work, as shown in table 1, confirms that this is the only compound formed in the system. No attempt was made to reinvestigate the melting relations of this system because it does not have any great effect on the phase equilibria of the ternary system with SrO.

3.2 The System SrO-CuO

Phase equilibria in the high CuO portion of the system were shown in [16], where the new compound "$Sr_{14}Cu_{24}O_{41}$" ($S_{14}C_{24}$) was proven to exist along with the previously reported $SrCuO_2$ [24] and Sr_2CuO_3 [25]. Refined unit cell dimensions and standard x-ray powder diffraction data for the last two phases were recently reported: $SrCuO_2$ (SC) [26] is orthorhombic (Cmcm) with $a = 3.5730(2)$, $b = 16.3313(8)$, $c = 3.9136(2)$ Å; Sr_2CuO_3 (JCPDS 34-283) is also orthorhombic (Immm) $a = 3.4957$, $b = 12.684$, $c = 3.9064$ Å. The unit cell dimensions of $Sr_{14}Cu_{24}O_{41}$ ($S_{14}C_{24}$) [16,17] indicate that it is face centered orthorhombic with $a = 11.483(1)$, $b = 13.399(1)$ and $c = 3.9356(3)$ Å; there are also some superstructure peaks in the pattern which may possibly be indexed on an incommensurate cell that has a c-axis which is about 7 times that of the subcell. The partially indexed x-ray powder diffraction data is given in table 3 and the pattern is illustrated in figure 1.

Determinations of the melting relations in the high-SrO portion of the system were complicated by charge-capsule reactions (table 1). Specimens of $SrCuO_2$ and Sr_2CuO_3 (SC and S_2C) were calcined to single phase and then small portions reheated in 3-mm diameter unsealed Pt tubes; Au capsules could not be used because the melting points of interest were higher than that of Au (1063 °C). Even though these experiments had a maximum duration of no more than 10 min at high-temperature, some CuO always alloyed with the Pt even at

Table 1a. Experimental data for the ternary system SrO-Bi_2O_3-CuO

Spec. no.	Composition, mole percent[a]			Temperature of heat treatment; °C[b]		Visual observation	Results of x-ray diffraction[c]
	SrO	$\frac{1}{2}Bi_2O_3$	CuO	Initial	Final		
	75.0	12.5	12.5	700			
				750			$SrCO_3+S_3B+$“7:2:2”
				800			$S_3B+SrCO_3+S_2C+$“7:2:2”$_{tr}$
				850			$S_3B+S_2C(+SrO?)$
					900		$S_3B+S_2C(+SrO?)$
	65	10	25	700			
				750			$SrCO_3+CuO+$“7:2:2”$+S_{14}C_{24}+S_3B_{tr}$
				800			“7:2:2”$+S_2C+S_3B+CuO_{tr}$
				850			S_2C+S_3B+“7:2:2”
				900			$S_2C+SC+S_3B_{2tr}+$“7:2:2”$_{tr}$
	64.29	28.57	7.14				
	$SrCO_3:S_2C:S_3B_2$			800×3			$S_3B+S_3B_2+$“7:2:2”
	1: 1 :2			800×5			$S_3B+S_3B_2+$“7:2:2”
#1[d]	63.63	18.18	18.18	700			
				750			
				800			“7:2:2”$+S_3B+S_3B_2+S_2C+SC+CuO$
				800×3			“7:2:2”$+S_3B+S_3B_2+SC+S_2C$
				800×6			“7:2:2”$+S_3B+S_3B_2+SC+S_2C$
				850			$S_3B_2+S_2C+$“7:2:2”$+SC+S_3B$
#2	*$S_2C:S_3B_2$*				875×1		$S_3B_2+S_2C+X(30.25^\circ)$
	2:1				875×2		$S_3B_2+S_2C+X(30.25^\circ)$
					875×4		$S_3B_2+S_2C+X(30.25^\circ)_{tr}$
#3	*$S_2C:S_3B_2$*			800×3			$S_3B+S_3B_2+$“7:2:2”$+S_2C+SC$
	2:1			800×5			S_3B+“7:2:2”$+SC+S_2C_{tr}+S_3B_{2tr}$
					900×3		$S_3B_2+S_2C+S_3B_{tr}+X(30.25^\circ)_{tr}$
#1	63.33	5.00	31.67				
	$\frac{1}{2}Bi_2O_3:S_2C$			750			
	1.00:6.33			850			
					900		$S_2C+SC+S_3B_2+X_{tr}$
					950		$S_2C+SC+S_3B_2+X_{tr}$
#2	*$\frac{1}{2}Bi_2O_3:S_2C$*				875×5		$S_2C+SC+S_3B_2+X$
	1.00:6.33						
#1	60	10	30				
	$\frac{1}{2}Bi_2O_3:S_2C$			750			
	1:3			850			
					900		$S_2C+SC+S_3B_2+X_{tr}$
					950		$S_2C+SC+S_3B_2+X_{tr}$
#2	*$\frac{1}{2}Bi_2O_3:S_2C$*				875×5		$S_2C+SC+S_3B_2+X$
	1:3						
#1	60	20	20	700			
				750			“7:2:2”$+S_3B+CuO+SrCO_3$
				800			“7:2:2”$+SC+S_2C$
				850			$SC+S_2C+unk(11^\circ)+$“7:2:2”
					900		$SC+S_2C+unk(11^\circ)$
					900×3		$S_3B_2+SC+S_2C$

Table 1a. Experimental data for the ternary system SrO-Bi_2O_3-CuO—Continued

Spec. no.	Composition, mole percent[a]			Temperature of heat treatment; °C[b]		Visual observation	Results of x-ray diffraction[c]
	SrO	$\frac{1}{2}Bi_2O_3$	CuO	Initial	Final		
#2				700			
				750			
				800			"7:2:2"$+S_3B_2+SC+S_2C+S_3B+CuO$
				800×3			"7:2:2"$+S_3B_2+SC+S_2C+S_3B$
					800×6		"7:2:2"$+S_3B_2+SC+S_2C+S_3B$
					850		$S_3B_2+S_2C+SC+$"7:2:2"
#3	*$S_2C{:}S_2B_2$*			700			
	2:1			750			
				800			S_3B_2+SC+"7:2:2"$+S_2C+S_3B$
				800×3			S_3B_2+SC+"7:2:2"$+S_2C+S_3B$
					800×6		"7:2:2"$+S_3B_2+SC+S_2C+S_3B$
					850		$S_3B_2+S_2C+SC+$"7:2:2"
	57.14	28.57	14.29	700			
				850			
					875		$S_3B_2+SC+2{:}2{:}1_{tr}$
					900		$S_3B_2+SC+2{:}2{:}1_{tr}$
					900×3		$S_3B_2+SC+2{:}2{:}1_{tr}$
	55	35	10		875(Ag/Pd[e])		$S_3B_2+2{:}2{:}1+X$
					900(Ag/Pd[e])		$S_3B_2+2{:}2{:}1+X$
	55	20	25				
	$SC{:}S_3B_2$				875		$SC+S_3B_2+8{:}4{:}5$
	2.5:1.0				875×2		$SC+S_3B_2+8{:}4{:}5$
					875×4		$SC+S_3B_2+8{:}4{:}5_{tr}$
#1	55	10	35				
	$\frac{1}{2}Bi_2O_3{:}S_2C{:}SC$			750			
	2:4:3			850			
					900		$SC+S_2C+S_3B_2$
					950		$SC+S_2C+S_3B_2$
#2	*$\frac{1}{2}Bi_2O_3{:}S_2C{:}SC$*				875×5		$SC+S_2C+S_3B_2+X$
	2:4:3						
	50	40	10	850			$S_3B_2+2{:}2{:}1$
					875		$S_3B_2+2{:}2{:}1$
#1	50	35	15	875			$S_3B_2+2{:}2{:}1$
					900		$S_3B_2+2{:}2{:}1+8{:}4{:}5+SC_{tr}$
					900-3days		$S_3B_2+2{:}2{:}1+3{:}2{:}2+8{:}4{:}5+SC$
					900×3		$S_3B_2+2{:}2{:}1+8{:}4{:}5+3{:}2{:}2+SC$
#2	*$S_2B_2{:}SC$*			650			
	1.1667:1.0000			750			
				800			$2{:}2{:}1+S_3B_2+SC$
					875		$2{:}2{:}1+S_3B_2+SC$
#1	50	25	25	700			
				750×2			$SrCO_3+CuO+S_3B+S_{14}C_{24}+$"7:2:2"
					750×4(Au[f])		$*+SC_{tr}+S_{14}C_{24tr}$
					800(Au[f])		$*+8{:}4{:}5_{tr}+SC_{tr}+S_{14}C_{24tr}$
					800×2(Au[f])		$*+8{:}4{:}5_{tr}+SC_{tr}+S_{14}C_{24tr}$
					850(Au[f])		$8{:}4{:}5+*+SC_{tr}$
					850×2(Au[f])		$8{:}4{:}5+S_3B_2+SC$
					850×3(Au[f])		$8{:}4{:}5+S_3B_2+SC$
					880×1(Au[f])		$8{:}4{:}5+S_3B_2+SC$
					900(Au[f])		$8{:}4{:}5+S_3B_2+SC$

Table 1a. Experimental data for the ternary system SrO-Bi$_2$O$_3$-CuO—Continued

Spec. no.	Composition, mole percent[a] SrO	$\frac{1}{2}$Bi$_2$O$_3$	CuO	Temperature of heat treatment; °C[b] Initial	Final	Visual observation	Results of x-ray diffraction[c]
#2	$SC{:}S_2B_2$			880×1			SC+2:2:1+S$_3$B$_2$
	1.0:0.5			880×5			8:4:5+2:2:1+S$_3$B$_2$+SC
				900×3			8:4:5+S$_3$B$_2$+SC
#3				650			
				750			
				800			S$_3$B$_2$+SC+2:2:1
					875		SC+2:2:1+S$_3$B$_2$+8:4:5
					900(Au[f])		SC+8:4:5+S$_3$B$_2$
					900×3(Au[f])		SC+8:4:5+S$_3$B$_2$
					900×6(Au$_f$)		SC+8:4:5+S$_3$B$_2$
					925(Au[f])		SC+8:4:5+S$_3$B$_2$
					950(Au[f])	part.melt	SC+S$_3$B$_2$+Rav
				950(Au[f])			
					900(Au[f])		SC+S$_3$B$_2$+8:4:5
					875(Au[f])		SC+S$_3$B$_2$+8:4:5
	50.00	16.50	33.50	650			
				750			SrCO$_3$+CuO+"7:2:2"+SC$_{tr}$
				800			CuO+SC+"7:2:2"+S$_{14}$C$_{24}$
				850			SC+S$_3$B$_2$+2:2:1+S$_2$C
					875		SC+S$_3$B$_2$+2:2:1
					900		SC+S$_3$B$_2$+2:2:1+8:4:5
					900×3		SC+S$_3$B$_2$+8:4:5
#1	48.75	5.00	46.25				
	$SC{:}SB_2$			750			
	18.5:1.0			850			
					900		SC+2:2:1+8:4:5
					950	sl. melting	SC+Rav+S$_3$B$_{2tr}$
#2	$SC{:}SB_2$						
	18.5:1.0				875×5		SC+8:4:5+X
#1	47.5	10.0	42.5				
	$SC{:}SB_2$			750			
	8.5:1.0			850			
					900		SC+2:2:1+3:2:2+8:4:5$_{tr}$
					950	part.melt	SC+Rav+S$_3$B$_{2tr}$
#2	$SC{:}SB_2$				875×5		SC+8:4:5+3:2:2
	8.5:1.0						
#1	47.06	23.53	29.41				
	(8:4:5)			700			
				750×2			SrCO$_3$+CuO+Rav+unk(4.40°)
					800(Au[f])		SrCO$_3$+CuO+Rav+unk(4.40°) +unk(4.80°)
					850(Au[f])		unk(4.80°)+CuO+SrCO$_3$
					850×2(Au[f])		unk(4.80°)+CuO+SrCO$_3$
					875(Au[f])		
					900(Au[f])		2:2:1+Rav+SC
				900(Au[f])			unk(4.40°)+unk(4.80°)+CuO

Table 1a. Experimental data for the ternary system $SrO-Bi_2O_3-CuO$—Continued

Spec. no.	Composition, mole percent^{a}			Temperature of heat treatment; °C^{b}		Visual observation	Results of x-ray diffraction^{c}
	SrO	$\frac{1}{2}Bi_2O_3$	CuO	Initial	Final		
#2				875			$S_3B_2+2:2:1+SC+S_{14}C_{24}+Rav$ $+3:2:2+S_3B$
					900		$S_3B_2+SC+2:2:1+3:2:2+8:4:5$
					900×2		$S_3B_2+SC+2:2:1+3:2:2+8:4:5$
					950	part.melt	$S_3B_2+Rav+SC$
#3L^{g}				650			$B_2C+SrCO_3+CuO$
				750			
				850			$2:2:1+S_3B_2+SC+3:2:2+S_{14}C_{24}$
					850×2		$2:2:1+S_3B_2+SC+3:2:2+S_{14}C_{24}$
				450			
				850×2			
					900×1		$8:4:5+2:2:1+SC$
					900×4		$8:4:5+2:2:1+SC_{tr}$
					925		$8:4:5+SC_{tr}$
#4				850			
				1250^{h}		comp.melt	
					$900(0_2^{i})$		8:4:5
					$925(0_2^{i})$		8:4:5
#1	45	20	35	850			
				875			
					875×7		$SC+3:2:2+S_{14}Cu_{24}$
					900		$SC+Rav+S_3B_2+8:4:5$
					900×3		$SC+3:2:2$
#2				875			
					900		$3:2:2+SC+2:2:1$
#3	*SC:SB$_2$* 3.5:1.0			800			
				875×1			$SC+S_{14}C_{24tr}$
					875×6		$SC+2:2:1+8:4:5$
	45	45	10	700			
				800			
				850			
					875		$S_2B_2+2:2:1$
	45	35	20	700			
				800			
				850			
					875		$2:2:1+S_3B_2+SC$
					900		$2:2:1+S_3B_2+SC$
	44.44	33.33	22.22	700			
				850			$2:2:1+S_3B_2+SC+S_{14}C_{24}$
				875			$2:2:1+S_3B_2+SC+S_{14}C_{24}+3:2:2_{tr}$
					900		$2:2:1+S_3B_2+8:4:5+3:2:2+SC_{tr}$
					900×3		S_3B_2+Rav
	44	36	20	700			
				800			
				850			
					875		$2:2:1+S_3B_2+SC$
					900		$2:2:1+S_3B_2+SC$

Table 1a. Experimental data for the ternary system $SrO-Bi_2O_3-CuO$—Continued

Spec. no.	Composition, mole percent[a] SrO	$\frac{1}{2}Bi_2O_3$	CuO	Temperature of heat treatment; °C[b] Initial	Final	Visual observation	Results of x-ray diffraction[c]
	43.75	25.00	31.25	700			
				750			
				850			
					875		3:2:2+SC+$S_{14}C_{24}$+S_3B_2
					900		3:2:2+SC+$S_{14}C_{24}$+2:2:1$_{tr}$
					900×2		3:2:2+SC+$S_{14}C_{24tr}$
	43.62	32.98	23.40	700			
				750			
				850			
					875		2:2:1+3:2:2+$S_{14}C_{24}$+SC
					900		2:2:1+3:2:2+SC+8:4:5$_{tr}$
	43	37	20	700			
				800			
				850			
					875		2:2:1+SC+S_3B_2
					900		2:2:1+SC+S_3B_2
	42.86	32.65	24.49	700			
				750			
				850			
					875		2:2:1+3:2:2+$S_{14}C_{24}$+SC
					900		2:2:1+3:2:2+$S_{14}C_{24}$+SC
#1	42.86	28.57	28.57	700			
	(3:2:2)			850			
				875			2:2:1+SC+$S_{14}C_{24}$+3:2:2+S_3B_{2tr}
					900×3(Au[f])		2:2:1+SC+8:4:5+3:2:2+S_3B_{2tr}
					900×6(Au[f])		2:2:1+8:4:5+S_3B_2
					900×8(Au[f])		2:2:1+8:4:5+S_3B_2
#2				700			
				750			
				850			
				875			2:2:1+SC+$S_{14}C_{24}$+3:2:2+S_3B_2
					900		3:2:2+SC_{tr}+$S_{14}C_{24tr}$
					900×2		3:2:2+SC_{tr}+$S_{14}C_{24tr}$
					925(O_2[i])		3:2:2+$S_{14}C_{24tr}$
					925×2(O_2[i])		3:2:2+$S_{14}C_{24tr}$
					950(O_2[i])	part.melt	Rav+8:4:5+SC
#3L[g]					900×2		2:2:1+3:2:2+SC
					900×3		2:2:1+3:2:2+SC
	42.5	47.5	10	800			S_2B_2+Rav
					875		2:2:1+S_2B_2+Tet
					925	comp.melt	Rav+Tet
	42.16	32.35	25.49	700			
				750			
				850			
					875		2:2:1+3:2:2+$S_{14}C_{24}$+SC
					900		2:2:1+3:2:2+$S_{14}C_{24tr}$+SC_{tr}
	42	40	18	700			
				850			
					875		2:2:1+S_3B_2+$S_{14}C_{24tr}$

Table 1a. Experimental data for the ternary system SrO-Bi_2O_3-CuO—Continued

Spec. no.	Composition, mole percent[a]			Temperature of heat treatment; °C[b]		Visual observation	Results of x-ray diffraction[c]
	SrO	$\frac{1}{2}Bi_2O_3$	CuO	Initial	Final		
	42	41	17	700			
				850			
					875		2:2:1+S_3B_2+S_2B_2
	42	38	20	700			
				800			
				850			
					875		2:1:1+$S_{14}C_{24}$+SC
					900		2:2:1+SC
	41.67	33.33	25.00	700			
				750			
				850			
					875		2:2:1+$S_{14}C_{24}$+3:2:2+SC_{tr}
					900		2:2:1+3:2:2+$S_{14}C_{24tr}$
					900×2		2:2:1+3:2:2+$S_{14}C_{24tr}$
					900(O_2[i])		2:2:1+3:2:2+$S_{14}C_{24}$[j]
					925(Au[f])	part.melt	Rav+SC_{tr}
					925(O_2[i])	no melting	2:2:1+3:2:2+$S_{14}C_{24}$
	41	44	15	700			
				850			
					875		2:2:1+Rav+S_2B_2
					900		2:2:1+S_2B_2+Rav
	41	43	16	700			
				850			
					875		2:2:1+S_2B_2+Rav
					900		2:2:1+S_2B_2
	41	42	17	700			
				850			
					875		2:2:1+S_2B_2
					900		2:2:1+S_2B_{2tr}
	41	41	18	700			
				850			
					870		2:2:1+S_3B_{2tr}
					900		2:2:1+$S_{14}C_{24tr}$
					925	part.melt	2:2:1+Rav
					889[k]		Rav+2:2:1
	41	40	19	700			
				850			2:2:1
					870		2:2:1+$S_{14}C_{24tr}$
					900		2:2:1+$S_{14}C_{24tr}$
					900(Au[f])Q		2:2:1+Rav
	41	39	20	700			
				800			
				850			
					875		2:2:1+$S_{14}C_{24}$
					900		2:2:1+$S_{14}C_{24}$

Table 1a. Experimental data for the ternary system SrO-Bi_2O_3-CuO—Continued

Spec. no.	Composition, mole percent[a]			Temperature of heat treatment; °C[b]		Visual observation	Results of x-ray diffraction[c]
	SrO	$\frac{1}{2}Bi_2O_3$	CuO	Initial	Final		
	40.67	40.32	19.00				
	$S_{\bullet}B_{\bullet}:S_2B_2:CuO$						
	1.00:0.45:1.00			880			2:2:1+Rav
					880×5		2:2:1+Rav
					900		2:2:1+Rav
	40.5	49.5	10.0	750			S_2B_2+SB_2+Rav
				800			Rav+S_2B_2+Tet
				850			Rav+S_2B_2+Tet
					875		Tet+Rav+2:2:1
	40.5	40.5	19.0	700			
				850			
					870		2:2:1+$S_{14}C_{24tr}$
					900		2:2:1+$S_{14}C_{24tr}$+Rav_{tr}
				925			
					889[k]	part.melt	2:2:1+Rav
	40	41	19	700			
				850			
					870		2:2:1+Rav
					900		2:2:1+Rav_{tr}
#1	40	40	20	650			
				750			Rav+S_2B_2
				800			2:2:1+S_2B_2+Rav
					850		2:2:1+$S_{14}C_{24tr}$+Rav_{tr}
					870		2:2:1+$S_{14}C_{24tr}$+Rav_{tr}
					900		2:2:1+$S_{14}C_{24tr}$+Rav_{tr}
#2				650			
				750			
				800			
				850			
				870			
					900		2:2:1+$S_{14}C_{24tr}$+Rav_{tr}
					900(Au[f])Q		2:2:1+Rav
#3	$SC:SB_2$						
	1:1				850×1		Rav+SC+2:2:1+SB_{2tr}+S_2B_{2tr}
					850×2		2:2:1+Rav+SC_{tr}+$S_{14}C_{24tr}$
#4	$SC:SB_2$						
	1:1			650			
				750			
				800			
					875		2:2:1+Rav+$S_{14}C_{24tr}$
					925		2:2:1+Rav+$S_{14}C_{24tr}$
#5	$S_2B_2:CuO$						
	1:1			880			Rav+2:2:1
				880×5			2:2:1+Rav
					900(0_2[i])		Rav+2:2:1
					950	comp.melt	
					875		2:2:1+Rav[l]
					900-PO_2=		
					0.15[m]		2:2:1+Rav[m]

Table 1a. Experimental data for the ternary system SrO-Bi_2O_3-CuO—Continued

Spec. no.	Composition, mole percent[a]			Temperature of heat treatment; °C[b]		Visual observation	Results of x-ray diffraction[c]
	SrO	$\frac{1}{2}Bi_2O_3$	CuO	Initial	Final		
#6				800(O_2[i])			
				850(O_2[i])			Rav+2:2:1
					900(O_2[i])		Rav+2:2:1
#7				850			
				1250[h]		comp.melt	Rav+S_3B_2
					800		Rav+2:2:1_{tr}
					850		Rav+2:2:1_{tr}[n]
					900		Rav+2:2:1[n]
					900×2		Rav+2:2:1[n]
					900×3		Rav+2:2:1
					900(O_2[i])		Rav
					925(O_2[i])		Rav
	40	20	40	650			
				750			
				800			Rav+2:2:1+CuO+S_2B_2+X
					850		2:2:1+$S_{14}C_{24}$+SC
					900		2:2:1+3:2:2+$S_{14}C_{24}$+SC_{tr}
				650			
				750			
					900(Au[f])		Rav+SC+S_2B_2+$S_{14}C_{24}$
					900×3(Au[f])		8:4:5+SC+Rav
					950		Rav+SC+S_2B_2+X
	38	42	20				
	S_2B_2:Tet:CuO						
	1.00:0.45:1.00				880×1		Rav+2:2:1
					880×5		Rav+2:2:1
	37	44	19	700			
				850			
					900		Rav+2:2:1
	37	43	20	700			
				850			
					900		Rav+2:2:1
					870		Rav+2:2:1
	36.66	53.33	10.00	700			
				750			Rav+SB_2+S_2B_2
				850			Rav+SB_2+Tet
					875	part.melt	Rav+SB_2+Tet
	36.66	36.66	26.66	650			
				750			Rav+S_2B_2+CuO
				800			Rav+2:2:1+CuO+$S_{14}C_{24}$
				850			2:2:1+Rav+CuO+$S_{14}C_{24}$
					870		2:2:1+Rav+CuO+$S_{14}C_{24}$
					900		2:2:1+Rav+CuO+$S_{14}C_{24}$
	36.15	44.50	19.35				
	S·B·:$\frac{1}{2}Bi_2O_3$:SC						
	0.7000:1.4444:1.0000			880			Rav
					880×5		Rav

Table 1a. Experimental data for the ternary system SrO-Bi$_2$O$_3$-CuO—Continued

Spec. no.	Composition, mole percent[a]			Temperature of heat treatment; °C[b]		Visual observation	Results of x-ray diffraction[c]
	SrO	$\frac{1}{2}$Bi$_2$O$_3$	CuO	Initial	Final		
	36	45	19	700			
				850			
					900		Rav+2:2:1
#1	36	44	20	700			
				750			Rav+S_2B_2+SB_2
				875×7			Rav
					880(Au[f])		Rav
					880×2(Au[f])		Rav
					900×3		Rav
#2	*Tet:CuO*			800			
	9:5				875		Rav
					875×5		Rav
#3	*Rhomb:SC*			875×5			Rav+2:2:1
	1.00:1.25					950	comp.melt
					875		Rav+2:2:1
	35.29	43.14	21.57	800			
	Tet:CuO			875			Rav+CuO
	9.0:5.5				875×5		Rav+CuO
	35	48	17	700			
				850			
					875		Rav+Rhomb$_{tr}$
	35	47	18	700			
				850			
					875		Rav+Rhomb$_{tr}$
	35	46	19	700			
				850			
					875		Rav+Rhomb
	35	45	20	700			
				850			
				875			Rav
					900×3(Au[f])		Rav
	35	5	60	700			
				850			
					900		$S_{14}C_{24}$+Rav+CuO
	34.66	55.33	10.00	700			
				750			
				800			SB_2+Rav
				850			SB_2+Rav
					875	part.melt	SB_2+Rav
	34	47	19	700			
				800			
					875		Rav

Table 1a. Experimental data for the ternary system SrO-Bi_2O_3-CuO—Continued

Spec. no.	Composition, mole percent[a]			Temperature of heat treatment; °C[b]		Visual observation	Results of x-ray diffraction[c]
	SrO	$\frac{1}{2}Bi_2O_3$	CuO	Initial	Final		
	34	46	20				
	$\frac{1}{2}Bi_2O_3$:Tet:SC						
	1.4444:0.7:1.0			880			Rav
				880×1			Rav
				880×2			Rav
				880×5			Rav
					900	part.melt	Rav
					1000	comp.melt	Rav
#1	33.33	33.33	33.33	800(12hr)			
					900(2hr)[p]		Rav+CuO+2:2:1+$S_{14}C_{24}$
#2				650			
				750			Rav+CuO+$S_{14}C_{24}$
				800			Rav+CuO+$S_{14}C_{24}$+2:2:1_{tr}
				850			Rav+CuO+2:2:1+$S_{14}C_{24}$
					870		Rav+CuO+2:2:1+$S_{14}C_{24}$
					900		Rav+CuO+2:2:1+$S_{14}C_{24}$
#3	*$\frac{1}{2}Bi_2O_3$:SC*			800			Rav+SC+CuO+$S_{14}C_{24}$
	1:1			850			Rav+CuO+$S_{14}C_{24}$
#4	*$\frac{1}{2}Bi_2O_3$:SC*			650			
	1:1			750			
				800			
					875		Rav+$S_{14}C_{24}$+CuO
					900×3(Au[f])		2:2:1+Rav+$S_{14}C_{24tr}$
	33	47	20	700			
				850			
					875		Rav
	32	48	20				
	$\frac{1}{2}Bi_2O_3$:Tet:SC						
	1.6667:0.6000:1.0000			880×1			Rav+$Rhomb_{tr}$
				880×5			Rav+Rhomb
	32	46	22				
	$\frac{1}{2}Bi_2O_3$:Tet:SC						
	1.5353:0.4545:1.0			880×2			Rav+CuO
				880×5			Rav+CuO
	31.842	5.000	63.158	700			
				850			
					900		$S_{14}C_{24}$+Rav+CuO
	31.33	58.66	10.00	700			
				750			
					850		Rhomb+Rav
					875	comp.melt	Rhomb+Rav
#1	30.75	47.25	22.00				
	$\frac{1}{2}Bi_2O_3$:Tet:SC			750			
	1.6616:0.3977:1.0			850			
					900	Slight melt	Rav+Rhomb

Table 1a. Experimental data for the ternary system SrO-Bi_2O_3-CuO—Continued

Spec. no.	Composition, mole percent[a] SrO	$\frac{1}{2}Bi_2O_3$	CuO	Temperature of heat treatment; °C[b] Initial	Final	Visual observation	Results of x-ray diffraction[c]
#2				700			
				850			
					875		Rav
	30	50	20				
	$\frac{1}{2}Bi_2O_3$:Tet:SC						
	1.8888:0.5000:1.0000			880			Rav+Rhomb
					880×5		Rav+Rhomb
	30	47	23				
	$\frac{1}{2}Bi_2O_3$:Tet:SC						
	1.6715:0.3043:1.0000			880×2			Rav+CuO+Rhomb
				880×5			Rav+CuO+Rhomb
	30	45	25				
	$\frac{1}{2}Bi_2O_3$:Tet:SC						
	1.5555:0.2000:1.0000			880×2			Rav+CuO
					880×5		Rav+CuO
	28	48	24				
	$SrCO_3$:$\frac{1}{2}Bi_2O_3$:Tet						
	1.0000:1.7963:0.1667			880×2			Rhom+Rav+CuO_{tr}
				880×5			Rhom+Rav+CuO_{tr}
	20.0	46.5	33.5	650			
				750			
					800		Rav+Rhomb+CuO
					850	consid.melt	Rav+Rhomb+CuO_{tr}
	10.00	56.66	33.33	700			
				750			Rhomb+B_2C+CuO
					800		Rhomb+B_2C+CuO

[a] Starting materials: $SrCO_3$, Bi_2O_3,CuO, except when listed in italics. Compositions given in italics were formulated from the listed prereacted compounds or compositions. S•B•=$Sr_{1.2407}Bi_{1.2222}O_{3.074}$, Rhomb=$SrBi_{2.75}O_{5.125}$, Tet=$SrBi_{1.22}O_{2.83}$.

[b] Specimens were given all previous heat treatments listed in the initial column, sequentially, and held at temperature 16–24 h, with grinding in-between, for the number of times shown and then reheated at the final temperature overnight. Specimens were heated as pellets on Au foil or MgO single crystal plates, except as indicated. In general, only a small portion of the specimen used for the initial (calcined) heat treatments was used to make sequential "final" heat treatments. Q=quenched.

[c] Compounds are listed in order of estimated amounts, most prevalent first.

tr=trace, just barely discernible
$B_2C=Bi_2CuO_4$
$S_2C=Sr_2CuO_3$
$SC=SrCuO_2$
$S_{14}C_{24}=Sr_{14}Cu_{24}O_{41}$
Rhomb=rhombohedral solid solution
$SB_2=SrBi_2O_4$
Tet=Tetragonal solid solution near $SrBi_{1.22}O_{2.83}$
$S_2B_2=Sr_2Bi_2O_5$
$S_3B_2=Sr_3Bi_2O_6$
$S_3B=Sr_6Bi_2O_9$
2:2:1=$Sr_2Bi_2CuO_6$
Rav=Raveau-type solid solution, $\sim Sr_{1.8-x}Bi_{2.2+x}CuO_z$
8:4:5=$Sr_8Bi_4Cu_5O_{19+x}$
3:2:2=$Sr_3Bi_2Cu_2O_8$
X,unk=phases of unknown composition
"7:2:2"=unknown phase, probably oxycarbonate with diffraction peaks a ~18.40 ° and ~21.27 ° 2θ
*=unknown phase, probably an oxycarbonate, with diffraction peaks a 4.40 ° and 5.68 ° plus major peaks at 30.50 ° and 32.45 ° 2θ

Footnotes to table 1a—Continued

[d] These specimens are numbered when more than one batch of a given oxide ratio were prepared.

[e] Specimens were heated in 70Ag/30Pd tubes, which caused the appearance of unknown phases due to reaction with the tube.

[f] Specimens were contained in 3-mm diameter Au tubes. Excessive heat treatment in such tubes resulted in appreciable loss of Cu to the surrounding Au tube.

[g] L = Specimen prepared by an organic precursor route utilizing lactic acid.

[h] The specimen was melted in an Al_2O_3 crucible and poured onto an Al chill plate.

[i] Specimen heated in one atmosphere pure oxygen instead of in air.

[j] Increase in amount of $S_{14}C_{24}$ relative to 3:2:2; indicates that the 3:2:2 phase is not favored by higher oxygen partial pressure.

[k] Specimen cooled from 925 to 889 °C at 1 °C/h.

[l] Amount of 2:2:1 phase not increased.

[m] Specimen heated in atmosphere of mixed Argon/Oxygen with the partial pressure of oxygen equal to 0.15 atm; amount of 2:2:1 phase greatly increased.

[n] Amount of 2:2:1 phase increased relative to previous heat treatment.

[p] This specimen was prepared as described in reference [30].

Table 1b. Experimental conditions for crystal growth experiments

Charge	Flux	Container	Temperature cycle	Results
$SrO:1/2Bi_2O_3$ 4 : 1 98 wt%	(KNa)Cl 2 wt%	sealed small diameter Au	800 °C 16 h	
$SrO:1/2Bi_2O_3$ 4 : 1 90 wt%	(KNa)Cl 10 wt%	sealed small diameter Au	800 °C 16 h	
$SrO:1/2Bi_2O_3$ 4 : 1 80 wt%	(KNa)Cl 20 wt%	sealed small diameter Au	1025→650 °C @ 5 °C/h	
$Sr_6Bi_2O_9$		open small diameter Au	925→900 °C @ 0.3 °C/h	
$Sr_6Bi_2O_9$ 98 wt%	(KNa)Cl 2 wt%	sealed small diameter Au	900 °C 16 h	
$Sr_6Bi_2O_9$ 98 wt%	(KNa)Cl 2 wt%	sealed small diameter Au	800 °C 16 h	
$Sr_6Bi_2O_9$ 90 wt%	(KNa)Cl 10 wt%	sealed small diameter Au	800 °C 16 h	S_3B oxychloride
$Sr_6Bi_2O_9$ 80 wt%	(KNa)Cl 20 wt%	sealed small diameter Au	1025→650 °C @ 5 °C/hr	S_3B_2 xtls hydrate after long exposure to air
$Sr_6Bi_2O_9$ 80 wt%	(KNa)Cl 20 wt%	sealed small diameter Au	950→650 °C @ 4 °C/h	
$SrO:1/2Bi_2O_3$ 2 : 1 98 wt%	(KNa)Cl 2 wt%	sealed small diameter Au	800 °C 16 h	
$SrO:1/2Bi_2O_3$ 2 : 1 90 wt%	(KNa)Cl 10 wt%	sealed small diameter Au	800 °C 16 h	
$Sr_2Bi_2O_5$		sealed small diameter Pt	925 °C 162 h	S_2B_2 Partially melted

Table 1b. Experimental conditions for crystal growth experiments—Continued

Charge	Flux	Container	Temperature cycle	Results
$Sr_2Bi_2O_5$		sealed small diameter Au	1025→950 °C @ 1 °/h	b.c. Tet
$Sr_2Bi_2O_5$		sealed small diameter Au	1025→900 °C @ 1 °C/h	b.c. Tet
$Sr_2Bi_2O_5$		sealed small diameter Au	1025→900 °C @ 1 °/h; 875 °C–225 h	S_2B_2
$Sr_2Bi_2O_5$ 98 wt%	(KNa)Cl 2 wt%	sealed small diameter Au	900→640 °C @ 3 °C/h	S_2B_2
$Sr_2Bi_2O_5$ 90 wt%	(KNa)Cl 10 wt%	sealed small diameter Au	900→640 °C @ 3 °C/h	S_2B_2
$Sr_2Bi_2O_5$ 80 wt%	(KNa)Cl 20 wt%	sealed small diameter Au	900→640 °C @ 3 °C/h	
$Sr_2Bi_2O_5$ 50 wt%	(KNa)Cl 50 wt%	sealed small diameter Au	900→640 °C @ 3 °C/h	
$SrBi_2O_4$ 80 wt%	(KNa)Cl 20 wt%	sealed large diameter Au	900→850 °C @ 3 °C/h	
$SrBi_2O_4$ 80 wt%	(KNa)Cl 20 wt%	sealed large diameter Au	900→700 °C @ 3 °C/h	
$SrBi_2O_4$ 20 wt%	(KNa)Cl 80 wt%	sealed small diameter Au	800→645 °C @ 1 °C/h	SB_2
$SrBi_2O_4$ 50 wt%	(KNa)Cl 50 wt%	sealed small diameter Au	800→645 °C @ 1 °C/h	SB_2
$SrBi_2O_4$ 20 wt%	(KNa)Cl 80 wt%	sealed Pt	740→570 °C @ 6 °C/h	SB_2
$SrO:1/2Bi_2O_3:CuO$ 3 : 1 : 1 90 wt%	(KNa)Cl 10 wt%	sealed small diameter Au	900 °C 16 h	xtals soluble in H_2O
$SrO:1/2Bi_2O_3:CuO$ 2 : 1 : 1		large diameter Pt	950→615 °C @ 1 °C/min	
$SrO:1/2Bi_2O_3:CuO$ 2 : 1 : 1 90 wt%	(KNa)Cl 10 wt%	sealed small diameter Au	900 °C 16 h	
$SrO:1/2Bi_2O_3:CuO$ 2 : 1 : 1 90 wt%	(KNa)Cl 10 wt%	sealed small diameter Au	900→650 °C @ 3 °C/h	partially melted needlelike xtals of 8:4:5
$SrO:1/2Bi_2O_3:CuO$ 2 : 1 : 1 90 wt%	$2NaF:SrF_2$ 50.86:49.14 10 wt%	sealed small diameter Au	900→650 °C 3 °C/h	Partially melted Rav
$SrO:1/2Bi_2O_3:CuO$ 45 : 45 : 10		Ag/Pd small diameter tube	950→800 °C @ 1 °C/h	

Table 1b. Experimental conditions for crystal growth experiments—Continued

Charge	Flux	Container	Temperature cycle	Results
$Sr_3Bi_2Cu_2O_8$ 90 wt%	(KNa)Cl 10 wt%	sealed small diameter Au	900 °C 16 h	xtals not soluble in H_2O
SrO:1/2Bi_2O_3:CuO 42.5 : 47.5 : 10		Ag/Pd small diameter tube	950→800 °C @ 1 °C/h	
SrO:1/2Bi_2O_3:CuO 41 : 41 : 18		sealed small diameter Au	925→900 °C @ 1 °C/h	
SrO:1/2Bi_2O_3:CuO 41 : 40 : 19		open small diameter Au	900→450 °C @ 1 °C/h	
SrO:1/2Bi_2O_3:CuO 40.5 : 49.5 : 10		Ag/Pd small diameter tube	950→800 °C @ 1 °C/h	
SrO:1/2Bi_2O_3:CuO 40.5 : 40.5 : 19		sealed small diameter Au	925→900 °C @ 1 °C/h	2:2:1+ Rav
$Sr_2Bi_2CuO_6$		Ag/Pd small diameter tube	950→800 °C @ 1 °C/h	Rav+Tet
$Sr_2Bi_2CuO_6$		Pt small diameter tube	950→800 °C @ 1 °C/h	
$Sr_2Bi_2CuO_6$		sealed small diameter Au	950→800 °C @ 1 °C/h	Rav
$Sr_2Bi_2CuO_6$		open small diameter Au	950→400 °C @ 1 °C/h	
$Sr_2Bi_2CuO_6$ 90 wt%	(KNa)Cl 10 wt%	sealed small diameter Au	900 °C 16 h	Rav completely melted
$Sr_2Bi_2CuO_6$ 98 wt%	NaF:KF 42:58 2 wt%	sealed small diameter Au	900 °C 3 d	Rav
$Sr_2Bi_2CuO_6$ 90 wt%	NaF:KF 42:58 10 wt %	sealed small diameter Au	900→650 °C @ 3 °C/h	Rav
$Sr_2Bi_2CuO_6$ 90 wt%	2NaF:SrF_2 50.86:49.14 10 wt%	sealed small diameter Au	850→650 °C @ 3 °C/h	Rav
$Sr_2Bi_2CuO_6$ 90 wt%	2NaF:CaF_2 51.73:48.28 10 wt%	sealed small diameter Au	900→650 °C 3 °C/h	Rav
SrO:1/2Bi_2O_3:CuO 3 : 2 : 3 80 wt%	(KNa)Cl 20 wt%	sealed small diameter Au	1025→650 °C @ 5 °C/min	
SrO:1/2Bi_2O_3:CuO 36 : 44 : 20 Rav		Ag/Pd small diameter tube	950→800 °C @ 1 °C/h	
SrO:1/2Bi_2O_3:CuO 1 : 1 : 1		large diameter Pt	950→615 °C @ 1 °C/min	
SrO:1/2Bi_2O_3:CuO 1 : 1 : 1 80 wt%	(KNa)Cl 20 wt%	sealed small diameter Au	1025→650 °C @ 5 °C/min	

Table 2. Crystallographic data

Phase formula	Unit cell parameters (Å)				Symmetry	Space group	Reference
	a	*b*	*c*	β°			
Bi_2CuO_4	8.510		5.814		Tet	P4/ncc	23
$SrCuO_2$	3.5730(2)	16.3313(8)	3.9136(2)		Orth	Cmcm	26
Sr_2CuO_3	3.4957	12.684	3.9064		Orth	Immm	JCPDS[a] 34-283
$Sr_{14}Cu_{24}O_{41}$	11.483(1)	13.399(1)	3.9356(3)[b]		Orth	Fmmm	This work
~Rhomb-SS[c] $Sr_xBi_{1-x}O_{(3-x)/2}$ $0.1 \leqslant x \leqslant 0.265$	3.979		28.51		Rhomb		27[d]
$SrBi_2O_4$	19.301(2)	4.3563(5)	6.1049(7)	94.85(1)	Mon	C2/m	This work
~Tet-SS $SrBi_{1.22}O_{2.83}$	13.239(2)		4.257(1)		Tet	I4/m	27
$Sr_2Bi_2O_5$	3.8262(2)	14.307(1)	6.1713(4)		Orth	Cmcm	This work
$Sr_3Bi_2O_6$	12.526(1)		18.331(2)		Rhomb	R$\bar{3}$m	This work
$Sr_6Bi_2O_9$	6.009		58.663		Rhomb[e]		This work
$Sr_2Bi_2CuO_6$	24.493(2)	5.4223(5)	21.959(2)	105.40(1)	Mon	C2/m	18
Raveau-SS $Sr_{1.8-x}Bi_{2.2+x}Cu_{1\pm x/2}O_z$ $0 \leqslant x \leqslant 0.15$	26.889(9)	5.384(2)	26.933(8)	113.67(3)	Mon	C2	This work[f]
$Sr_8Bi_4Cu_5O_{19+x}$	33.991(3)	24.095(2)	5.3677(5)		Orth	Fmmm	This work
$Sr_3Bi_2Cu_2O_8$	24.937(7)	5.395(2)	19.094(7)	96.97(3)	Mon	C2/m	This work

[a] Joint Committee for Powder Diffraction Standards, X-Ray Diffraction card file.
[b] Contains superstructure with c′=7c.
[c] -SS=solid solution.
[d] Unit cell dimensions for x=0.19.
[e] Apparently a subcell.
[f] Unit cell dimensions for x=0.

temperatures well below melting. Partial melting was assumed to have occurred when the x-ray powder diffraction pattern of a quenched specimen indicated an abrupt change in the phase fraction of a second phase. Both $SrCuO_2$ and Sr_2CuO_3 melt incongruently: $SrCuO_2$ melts to liquid plus Sr_2CuO_3 at ~1085 °C, and Sr_2CuO_3 melts to liquid plus SrO, at ~1225 °C. The phase equilibria diagram constructed from the data in table 1 and the previously reported experiments [16] is shown in figure 2.

3.3 The System SrO-Bi_2O_3

The phase equilibria diagram for the system SrO-Bi_2O_3 was reported in [27] and redrawn as figure 6428 in PDFC [22] and figure 3 (where the scale is changed to $\frac{1}{2}Bi_2O_3$:CuO instead of the original Bi_2O_3:CuO, to be consistent with the other phase diagrams in this report). Considerable effort was made to study the phase relations of this binary. Complete experimental results are published in [28], and the results are shown in figures 4a and 4b

Table 3. X-ray powder diffraction data for $Sr_{14}Cu_{24}O_{41}$

d obs(Å)	Rel *I*(%)	2θ obs	2θ calc[a]	*hkl*
6.68	2	13.25	13.22	020
5.72	<1	15.48	15.45	200
4.352	2	20.39	20.38	220
3.596	6	24.74	24.75	111
3.347	12	26.61	26.61	040
3.021[b]	1	29.55		
2.8879	100	30.94	30.91	240
2.8608	66	31.24	31.22	131
2.6853	52	33.34	33.30	311
2.6339	10	34.01	34.00	420
2.6049[b]	1	34.40		
2.4245[b]	1	37.05		
2.3364	38	38.50	38.47	331
2.2834[b]	1	39.43		
2.2324	1	40.37	40.39	060
2.1742	42	41.50	41.47	151
2.0801	1	43.47	43.48	260
1.9878[b]	3	45.60		
1.9718	13	45.99	45.96	002
1.9582	6	46.33		
1.9103	14	47.56	47.55	600
1.8920	6	48.05	48.04	022
1.8657	2	48.77	48.78	202
1.8361	17	49.61	49.57	620
1.8108	46	50.35	50.32	531
1.7975	3	50.75	50.76	222
1.7610	2	51.88	51.87	460
1.7413[b]	2	52.51		
1.7096[b]	2	53.56		
1.7026	3	53.80	53.81	171
1.6733	15	54.82	54.81	080
1.6599	2	55.30	55.32	640
1.6290	16	56.44	56.42	642
1.5934	9	57.82	57.82	551
1.5789	2	58.40	58.39	422
1.5696	13	58.78	58.79	371
1.5542[b]	1	59.42		
1.5117[b]	1	61.27		
1.5037	1	61.63	61.65	711
1.4783	4	62.81	62.82	062
1.4624	11	63.57	63.59	442
1.4518	9	64.09	64.11	660
1.4422[b]	3	64.57		
1.4327	15	65.05	65.05	731
1.4017	5	66.67	66.69	820
1.3731	11	68.25	68.28	602
1.3450	4	69.88	69.90	622

[a] Calculated from an orthorhombic unit cell, $a=11.466(2)$; $b=13.389(2)$ and $c=3.9458(6)$ Å.

[b] Superstructure peak.

(compare with fig. 3). The major differences between our new diagram and the one presented in [27] are: 1) the occurrence of a new compound which is estimated to have the stoichiometry $Sr_6Bi_2O_9$ (fig. 4a); 2) the presence of a high temperature polymorph of $SrBi_2O_4$ (fig. 4b) which becomes stable between 800 and 825 °C and melts incongruently at 940±5 °C; and 3) the determination of melting relations in the region of 20–50 mol percent SrO.

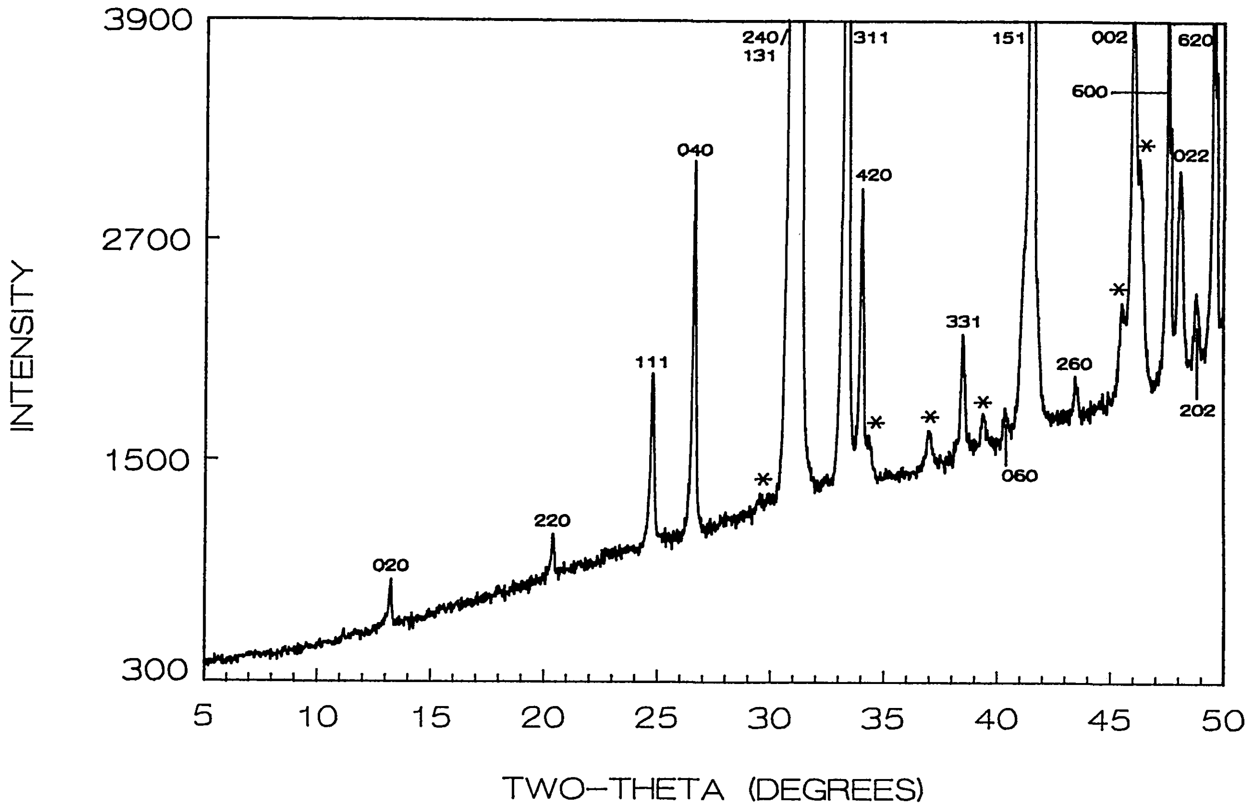

Figure 1. X-ray powder diffraction pattern of $Sr_{14}Cu_{24}O_{41}$ (cooled from 925 °C). *Superstructure peaks.

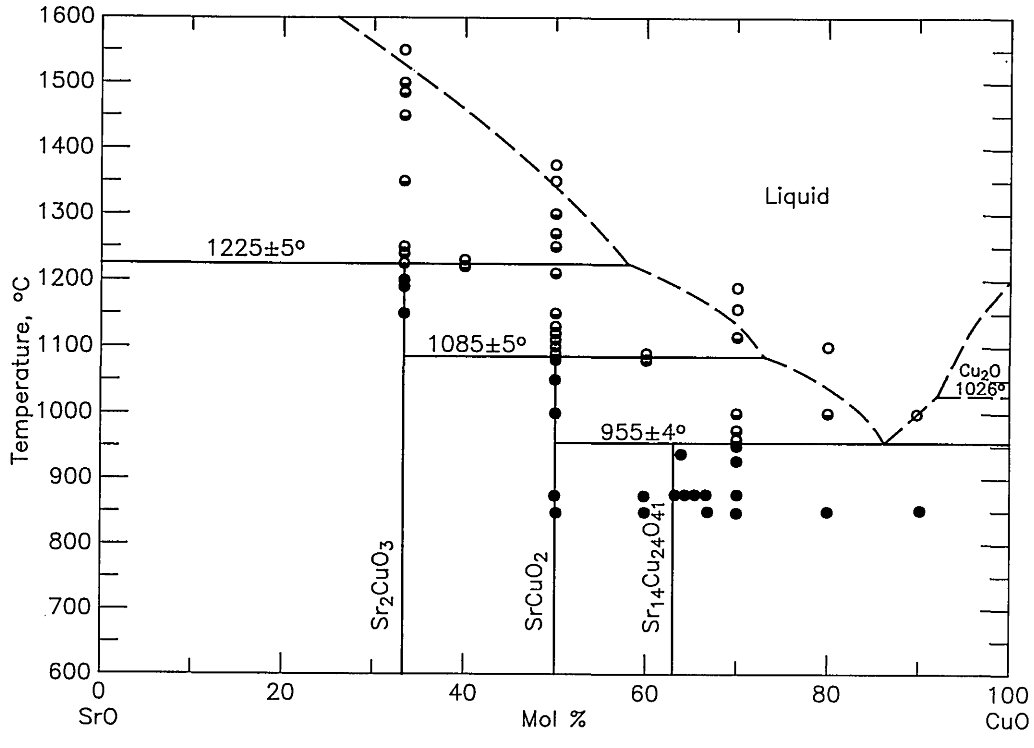

Figure 2. Phase diagram for the system SrO-CuO ●-not melted, ◒-partially melted, O-completely melted.

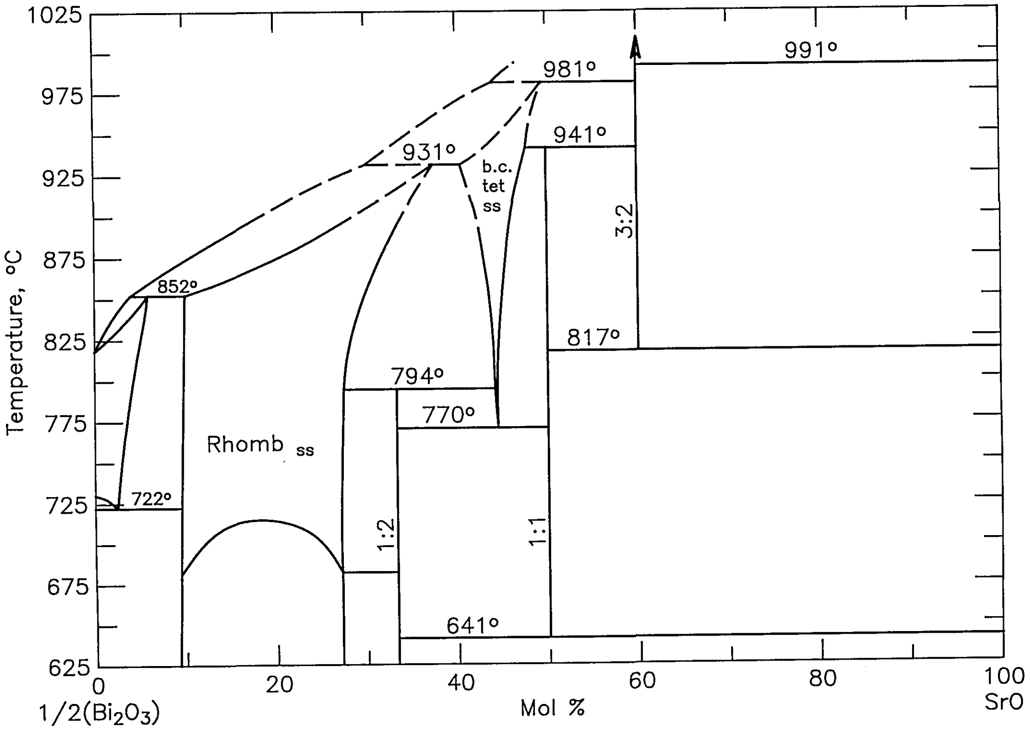

Figure 3. Phase diagram for the system SrO-$\frac{1}{2}$Bi$_2$O$_3$ modified from that published in [27].

3.3.1 Rhombohedral Solid Solution (Sillen Phase-Rhomb) The rhombohedral solid solution was first reported by Sillen [29] and it was later shown by Levin and Roth [30] that the solidus temperature is increased when SrO is added to face-centered-cubic (fcc) Bi_2O_3, or when it is added to the rhombohedral solid solution phase. Melting relations in the SrO-rich region of the Sillen phase field were previously [27] represented schematically (by dashed lines) as a melting loop, but the experiments reported in [28] indicate a congruent melting point between 25–30 mol% SrO and 950–960 °C. Guillermo et al. [27] reported that a phase transition occurred from one rhombohedral phase to another, but as this has not been confirmed by quench data, such possible polymorphism is ignored in the present work. X-ray diffraction data for this phase are well established [27] and will not be summarized here.

3.3.2 $SrBi_2O_4$ (SB_2) $SrBi_2O_4$ appears to have both high- and low-temperature polymorphs with a transition point at about 825 °C. The high-temperatures form melts incongruently to liquid plus the tetragonal solid solution (next section) between 940 and 945 °C. In the high to low-temperature transition, sharp x-ray diffraction peaks in a powder pattern of the low-temperature phase become broad and diffuse when specimens are quenched from about 825–940 °C. Also, a few maxima (e.g., 202) that are present in patterns from the low-temperature phase have drastically reduced intensities in patterns from samples that were quenched from above 825 °C. The indexed x-ray powder diffraction data for low-$SrBi_2O_4$ are listed in table 4. The patterns for both low-temperature and high-temperature $SrBi_2O_4$ are shown in figure 5. The observed broadening of diffraction maxima in the pattern from the quenched sample suggests that the high-temperature polymorph, perhaps orthorhombic, was not successfully quenched. The presence of broad rather than sharp peaks suggests a small domain size in samples quenched from above 825 °C.

Very small single crystals of low-temperature $SrBi_2O_4$ were prepared (table 1b) by heating a prereacted powder sample of $SrBi_2O_4$ plus a 1:1 NaCl:KCl flux (80/20 flux/charge ratio) in a sealed Pt tube. The specimen was heated to 740 °C and cooled to 570 °C at 6 °/h. After the flux was dissolved with H_2O, a very thin flat platelet was

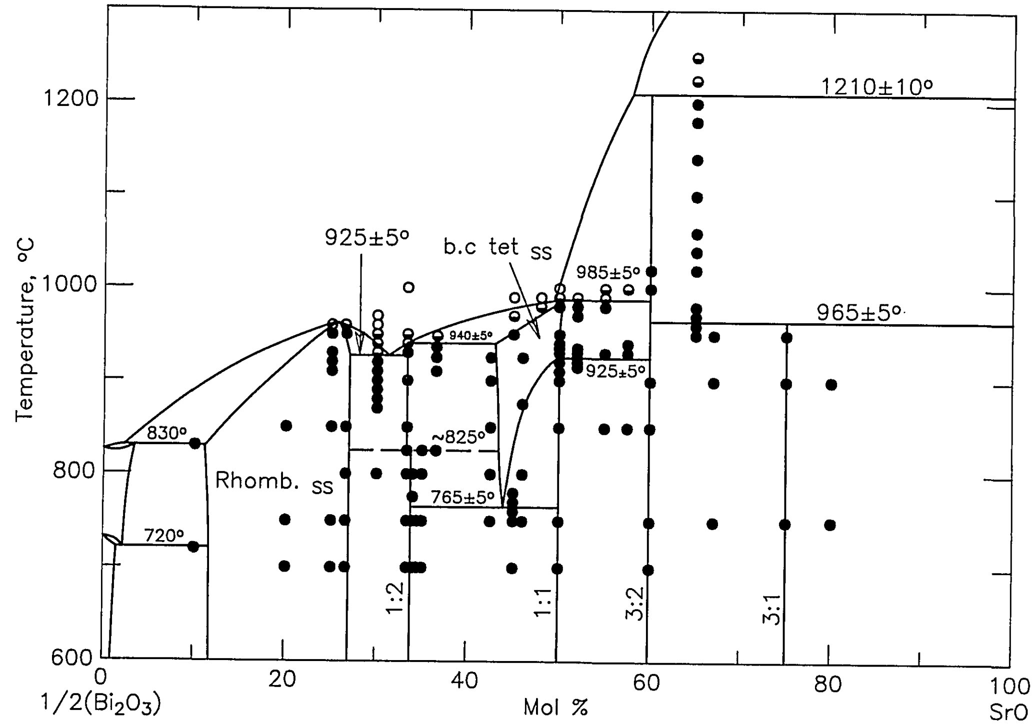

Figure 4a. Phase diagram for the system SrO-$\frac{1}{2}$Bi$_2$O$_3$ as reported in [28] ●-not melted, ⊖-partially melted, O-completely melted.

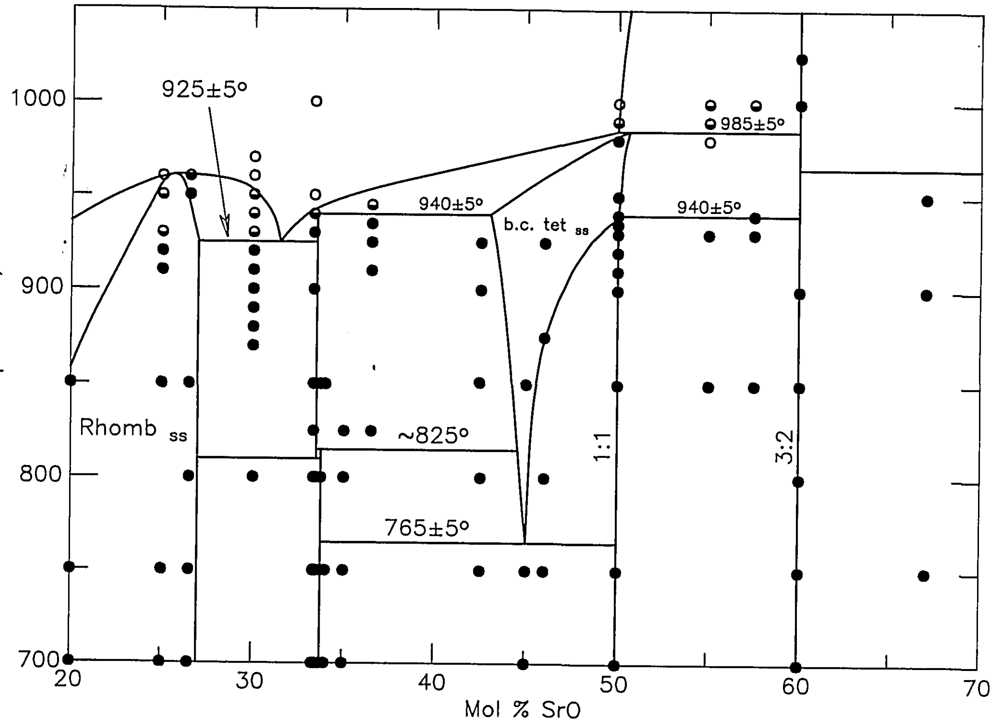

Figure 4b. Enlargement of figure 4a showing polymorphism of SrBi$_2$O$_4$.

Table 4. X-ray powder diffraction data for the compound $SrBi_2O_4$

d obs(Å)	Rel *I*(%)	2θ obs	2θ calc[a]	*hkl*
9.64	9	9.17	9.19	200
6.09	4	14.53	14.55	001
5.36	1	16.54	16.56	$20\bar{1}$
4.813	22	18.42	18.44	400
3.626	7	24.53	24.53	401
3.606	6	24.67	24.69	310
3.454	29	25.77	25.78	111
3.205	97	27.81	27.81	600
3.168	100	28.15	28.16	$31\bar{1}$
3.040	93	29.36	29.38	311
2.9743	15	30.02	30.03	$20\bar{2}$
2.9417	3	30.36	30.38	$60\bar{1}$
2.8326	6	31.56	31.57	202
2.7421	13	32.63	32.63	601
2.6728	7	33.50	33.51	$51\bar{1}$
2.5454	1	35.23	35.25	511
2.4781	7	36.22	36.23	402
2.4526	3	36.61	36.63	112
2.4051	1	37.36	37.38	800
2.3065	19	39.02	39.03	$60\bar{2}$
2.2724	5	39.63	39.64	312
2.1782	34	41.42	41.42	020
2.1196	22	42.62	42.59 42.64	711 602
2.0501	1	44.14	44.13	021
2.0291	2	44.62	44.62	512
2.0197	3	44.84	44.86	$20\bar{3}$
1.9841	5	45.69	45.69	420
1.9686	5	46.07	46.07	$80\bar{2}$
1.9191	19	47.33	47.35	910
1.8701	33	48.65	48.63	$91\bar{1}$
1.8427	8	49.42	49.40	$11\bar{3}$
1.8145	17	50.24	50.25	403
1.8018	43	50.62	50.63	620
1.7909	30	50.95	50.95	911
1.7705	16	51.58	51.57	022
1.7569	11	52.01	52.00	$22\bar{2}$
1.7318	9	52.82	52.81	313
1.7270	8	52.98	53.00	222
1.7096	10	53.56	53.53	$51\bar{3}$
1.7058	12	53.69	53.70	621
1.6812	3	54.54	54.54	$91\bar{2}$
1.6514	2	55.61	55.60	603
1.6357	5	56.19	56.18	422
1.6107	6	57.14	57.12	513
1.6023	11	57.47	57.45	12,0,0
1.5831	19	58.23	58.22	622
1.5691	7	58.80	58.77	912
1.5670	6	58.89	58.90	10,0,2

[a] Calculated on the basis of a monoclinic cell, C2/m, $a=19.301(2)$, $b=4.3563(5)$, $c=6.1049(7)$ Å, $\beta=94.85(1)°$.

picked and single crystal x-ray precession photographs were taken (fig. 6) of it. The precession data indicate that the phase is C-centered monoclinic, probably C2/m, and unit cell dimensions refined from x-ray powder diffraction data are $a=19.301(2)$, $b=4.3563(5)$, $c=6.1049(7)$ Å, $\beta=94.85(1)°$. Larger crystals were obtained from both 80:20 and 50:50 flux/charge ratios by cooling from 800 °C to 645 °C at 1°/h.

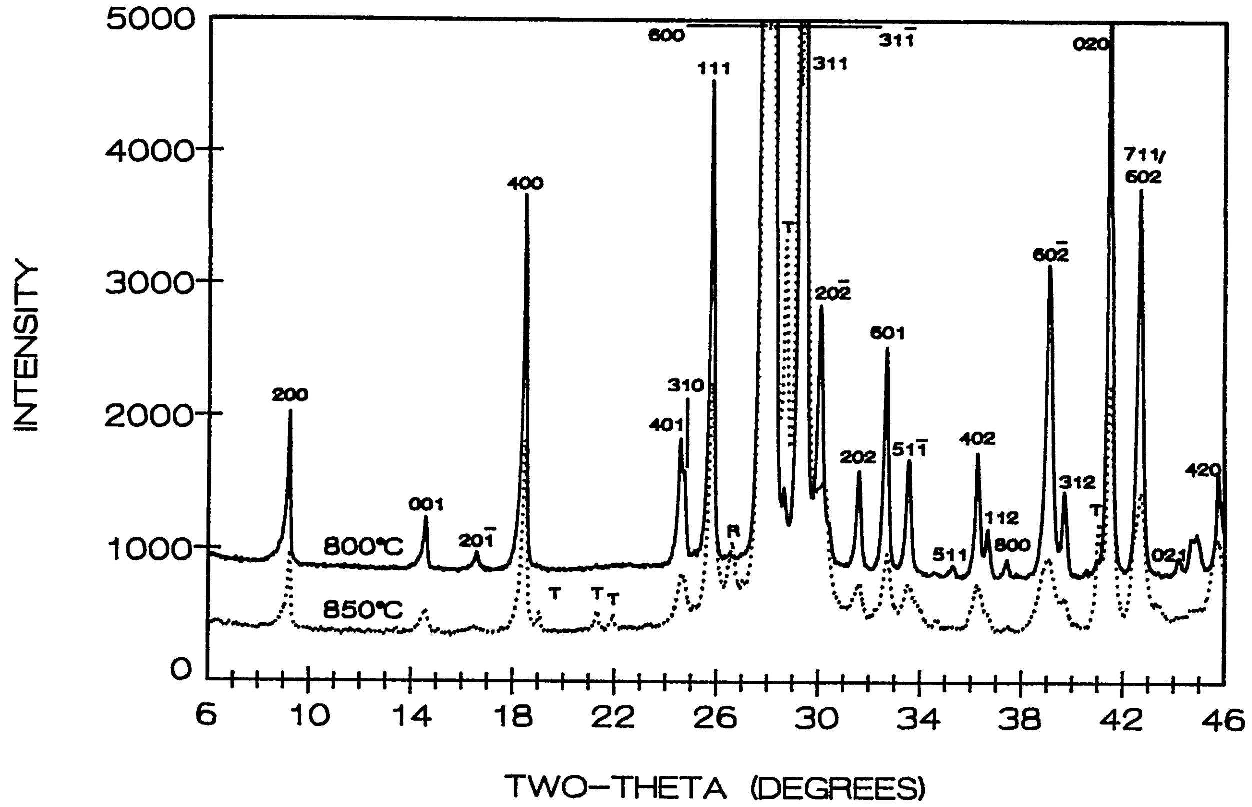

Figure 5. X-ray powder diffraction patterns for low-temperature (cooled from 800 °C) solid line and high-temperature $SrBi_2O_4$ (cooled from 850 °C) dotted line. T=tetragonal phase, R=rhombohedral phase.

3.3.3 The Tetragonal Solid Solution Near $SrBi_{1.22}O_{2.83}$ (Tet) This phase was previously reported [27] with space group I4/m, $a=13.239(2)$, $c=4.257(1)$ Å. Experiments during the course of this study agree reasonably well with those previously reported, except for the region near the solidus where we find the single phase region extends to compositions with at least 50 mol percent SrO. The x-ray powder diffraction data was previously reported [27]. Very large single crystals were obtained by cooling the $Sr_2Bi_2O_5$ composition from above the melting point to ~950 °C.

3.3.4 $Sr_2Bi_2O_5(S_2B_2)$ The compound $Sr_2Bi_2O_5$ was reported [27] to be orthorhombic, space group Pcmm with $a=14.293(2)$, $b=7.651(2)$ and $c=6.172(1)$ Å. Although precession photographs collected from very small crystals in the present study show evidence of only $\frac{1}{2}$ the b axis reported in [27] (see fig. 7), much larger crystals showed a very weak superstructure and a doubled b-axis. The subcell space group is apparently Cmcm and in this orientation $a=3.8262(2)$, $b=14.307(1)$, $c=6.1713(4)$ Å as obtained from a least-squares refinement of the powder data. The indexed powder data are given in table 5 and illustrated in figure 8. Apparently the superstructure destroys the subcell symmetry of the C-centering, showing such peaks as (1/2, 16, 0) and (1 1/2, 0, 1) resulting in a space group symmetry consistant with Pbnm. Very large single crystals were obtained by cooling the $Sr_2Bi_2O_5$ composition from above the melting point to ~900 °C, and annealing large fragments at 850 °C—258 h.

3.3.5 $Sr_3Bi_2O_6(S_3B_2)$ $Sr_3Bi_2O_6$ melts incongruently between 1200 and 1220 °C. Single crystals are formed in many compositions in the ternary system with CuO when heated above ~900 °C. Apparently, this phase has a large primary phase field in the ternary system. For example, single crystals were obtained from $SrO{:}\frac{1}{2}Bi_2O_3{:}CuO$ 55:35:10 at 900 °C and from $SrO{:}\frac{1}{2}Bi_2O_3$ 57.5:42.5 at 1000 °C. These crystals often react slowly with atmospheric moisture. The best crystals were obtained using an NaCl:KCl flux with 4/1 flux/$Sr_6Bi_2O_9$ ratio cooled

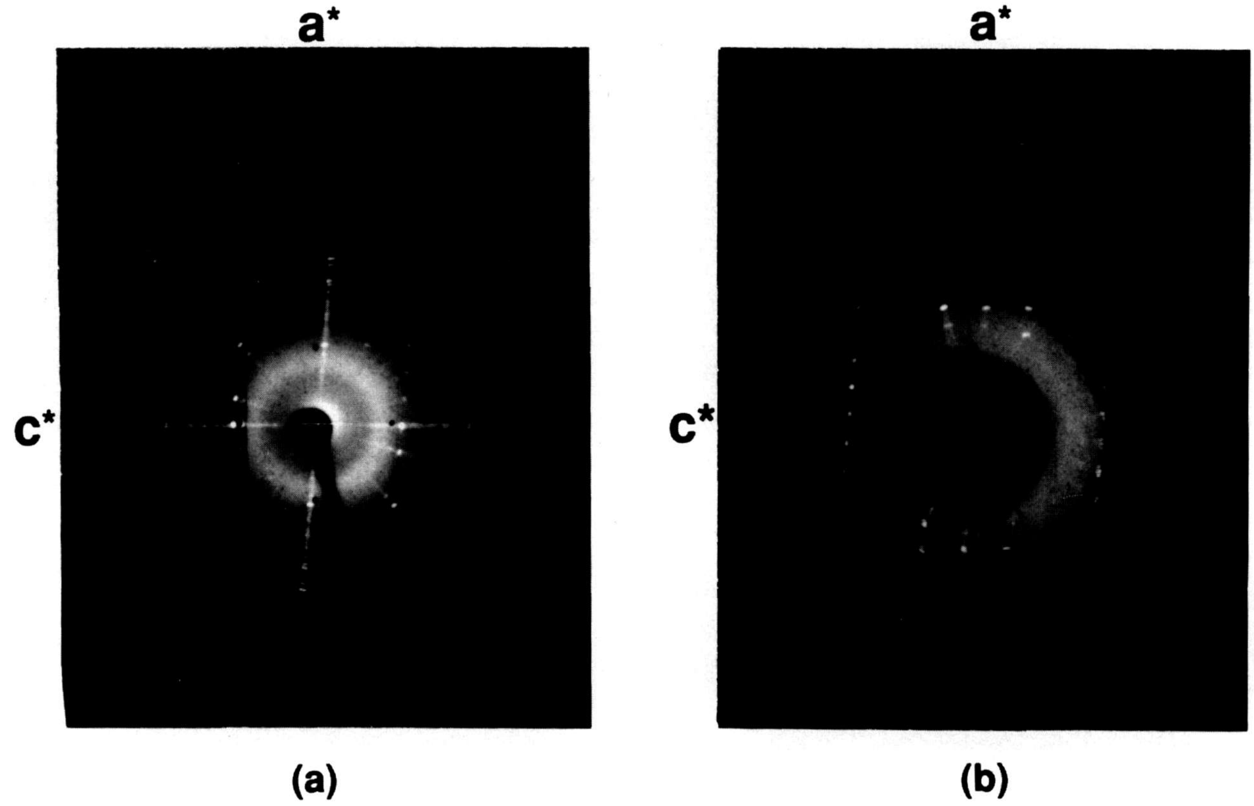

Figure 6. X-ray precession photographs for $SrBi_2O_4$ (a) *h0l*, (b) *hll*.

from 1025 to 650 °C at 5 °/h (table 1b). These crystals are colorless and easily recognized because of their very low birefringence in polarized light. All these crystals were found (see precession photographs, fig. 9) to be rhombohedral probably $R\bar{3}m$, with unit cell dimensions refined from the x-ray diffraction powder data (table 6, fig. 10) $a = 12.526(1)$, $c = 18.331(2)$ Å.

3.3.6 $Sr_6Bi_2O_9(S_3B)$ Previous workers [27] did not report any binary compound with more than 60 mole percent SrO; however, $Sr_6Bi_2O_9$ appears to be stable between about 750 and 950 °C, and it decomposes between 950 and 975 °C to $Sr_3Bi_2O_6 + SrO$. Single crystals were obtained by heating a prereacted specimen plus 1:1 NaCl:KCl flux (flux/charge ratio = 10/90). X-ray precession photographs (fig. 11) indicate an apparently rhombohedral unit cell with $a = 6.009$ and $c = 58.633$ Å. This appears, however, to be a subcell and even a doubled a-axis (as suggested by electron diffraction data) does not account for all of the diffraction maxima observed in an x-ray powder diffraction pattern of the prereacted mix (table 7, fig. 12). The crystals may actually be an oxychloride phase and the pseudocell suggested in table 7 does not fit the observed data very accurately. The reaction $Sr_6Bi_2O_9 \rightarrow (975\ °C) \rightarrow Sr_3Bi_2O_6 + 3SrO$ is completely reversible i.e., with material that was decomposed, $Sr_6Bi_2O_9 \rightarrow Sr_3Bi_2O_6 + 3SrO$ at 975 °C, one can perform the back reaction, $Sr_3Bi_2O_6 + 3SrO \rightarrow (900\ °C) \rightarrow Sr_6Bi_2O_9$, with or without intermediate grinding (and exposure to atmospheric CO_2).

3.4 The System $SrO{:}\frac{1}{2}Bi_2O_3{:}CuO$

Phase relations in the nominally ternary system are shown in figure 13 and experimental data are reported in table 1. Figure 14 is an enlargement of the triangular region of figure 13 that is delineated by dots. Many of the experiments listed in table 1 yield apparently conflicting and often confusing results, precisely because the experimental system is not strictly ternary in air and/or in contact with various capsule materials such as Au, Pt or 70Ag30Pd. Reproducibility of experiments in this system is exceedingly difficult to achieve, and it is often impossible to reproduce the results published

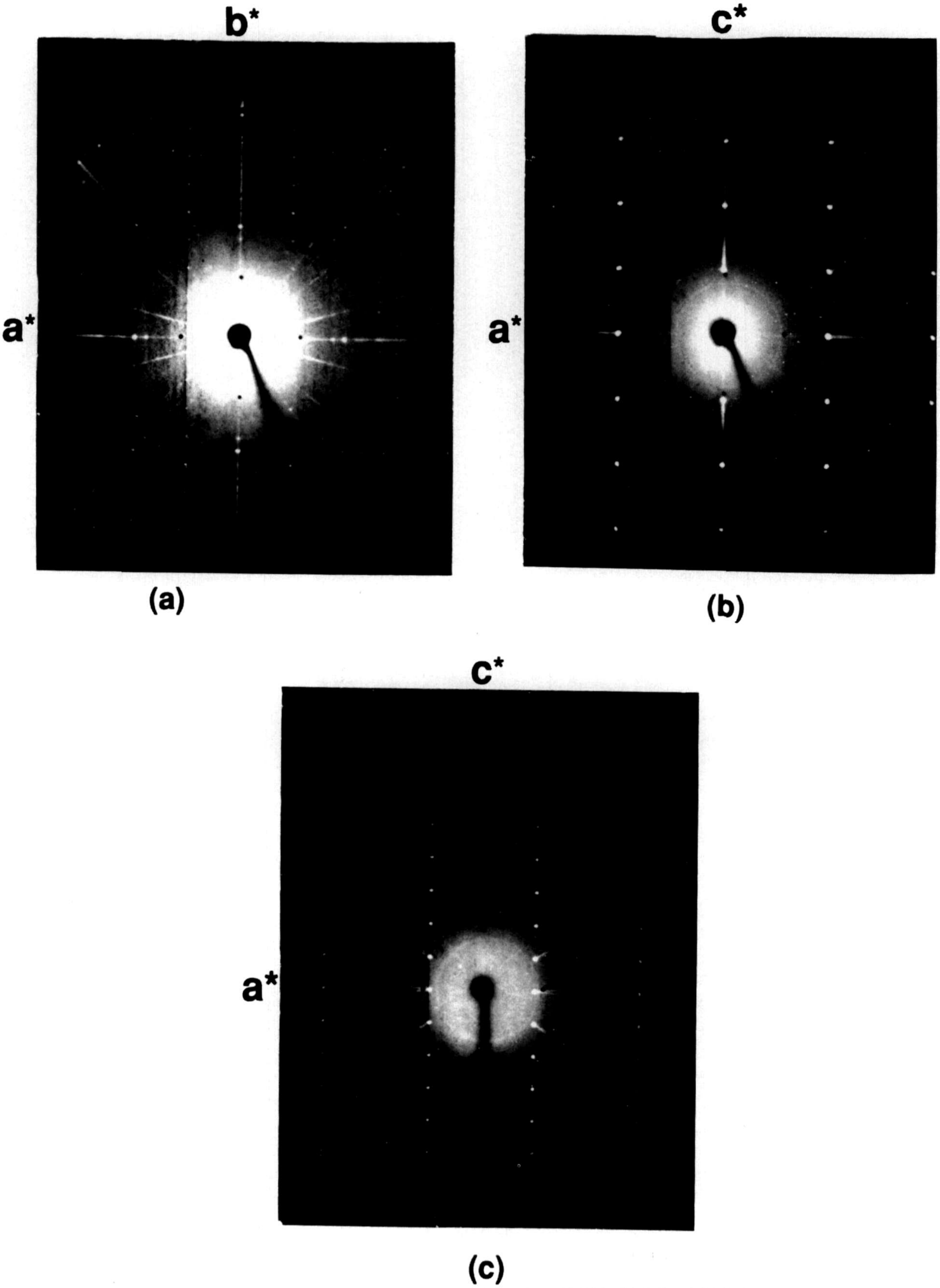

Figure 7. X-ray precession photographs of $Sr_2Bi_2O_5$ (a) *hk0*, (b) *h0l* and (c) *h1l*.

Table 5. X-ray powder diffraction data for the compound $Sr_2Bi_2O_5$

d obs(Å)	Rel *I*(%)	2*θ* obs	2*θ* calc[a]	*hkl*
7.161	17	12.35	12.3	020
4.676	15	18.96	18.98	021
3.697	32	24.05	24.06	110
3.171	1	28.11	28.12	111
3.094	100	28.84	28.83	041
2.9842	10	29.92	29.92	130
2.8319	8	31.57	31.55	022
2.6865	23	33.33	33.32	131
2.3857	1	37.67	37.69	060
2.3684	11	37.96	37.95	112
2.3373	<1	38.49	38.50	042
2.2918	9	39.28	39.29	150
2.2254	2	40.50	40.52	061
2.1466	26	42.06	42.09	132
1.9767	1	45.88	45.87	023
1.9122	8	47.51	47.49	200
1.8873	2	48.18	48.19	062
1.8401	8	49.50	49.51	152
1.8030	5	50.59	50.59	170
1.7979	8	50.74	50.75	113
1.7827	17	51.20	51.19	043
1.7712	2	51.56	51.58	221
1.7306	7	52.86	52.86	171
1.6936	5	54.11	54.10	133
1.6873	1	54.33	54.34	240
1.6271	17	56.51	56.51	241
1.5849	<1	56.16	58.14	222
1.5570	5	59.31	59.32	172
1.5472	7	59.72	59.71	082
1.5424	7	59.92	59.91	004

[a] Calculated on the basis of an orthorhombic unit cell, Cmcm, $a=3.8262(2)$, $b=14.307(1)$, $c=6.1713(4)$ Å.

by others. In some cases this may be because insufficient experimental details were given; however, attempts to reproduce our own experiments have sometimes lead to slightly different results. Experimental results are greatly affected by the factors outlined below.

(1) Compositional changes caused by reaction with Au or other containers;

(2) Volatilization of Bi_2O_3;

(3) CO_2 in some phases at the lower temperatures (e.g., $SrCO_3$ does not decompose in air until about 875 °C);

(4) Oxidation/reduction reactions involving atmospheric O_2, CO_2, or H_2O;

(5) Difficulties related to the very disparate melting behaviors of various compounds and the end members. For example, Bi_2O_3 melts at ~825 °C but CuO decomposes in air to form Cu_2O at about 1020 °C which melts at about 1210 °C. Also, The Sr-cuprates react very slowly at temperatures below the melting points of Bi_2O_3 and Bi_2CuO_4. Thus, it was often necessary to prepare specimens from prereacted compounds (or mixtures of compounds) instead of the end members.

(6) Persistence of apparently unstable three phase assemblages within single phase regions. Typically, it is not possible to homogenize single phase ternary samples to the point that all detectable traces of additional phases are eliminated from x-ray powder patterns.

Therefore, it should be emphasized that the diagram in figure 13 is a composite of subsolidus data that is neither strictly ternary nor strictly isothermal. The region below the join that connects CuO to the SrO-poor end of the rhombohedral Sillen phase field contains phases which melt below 850 °C, and some phases in the low CuO portion of the system begin to melt between ~875 and 900 °C. Also, specimens of one composition which are near the $SrBi_2O_4$:Raveau-solid-solution join showed evidence of melting between 850 and 875°C. All other compositions start to melt above at least 900 °C and many start melting slightly above 925 °C.

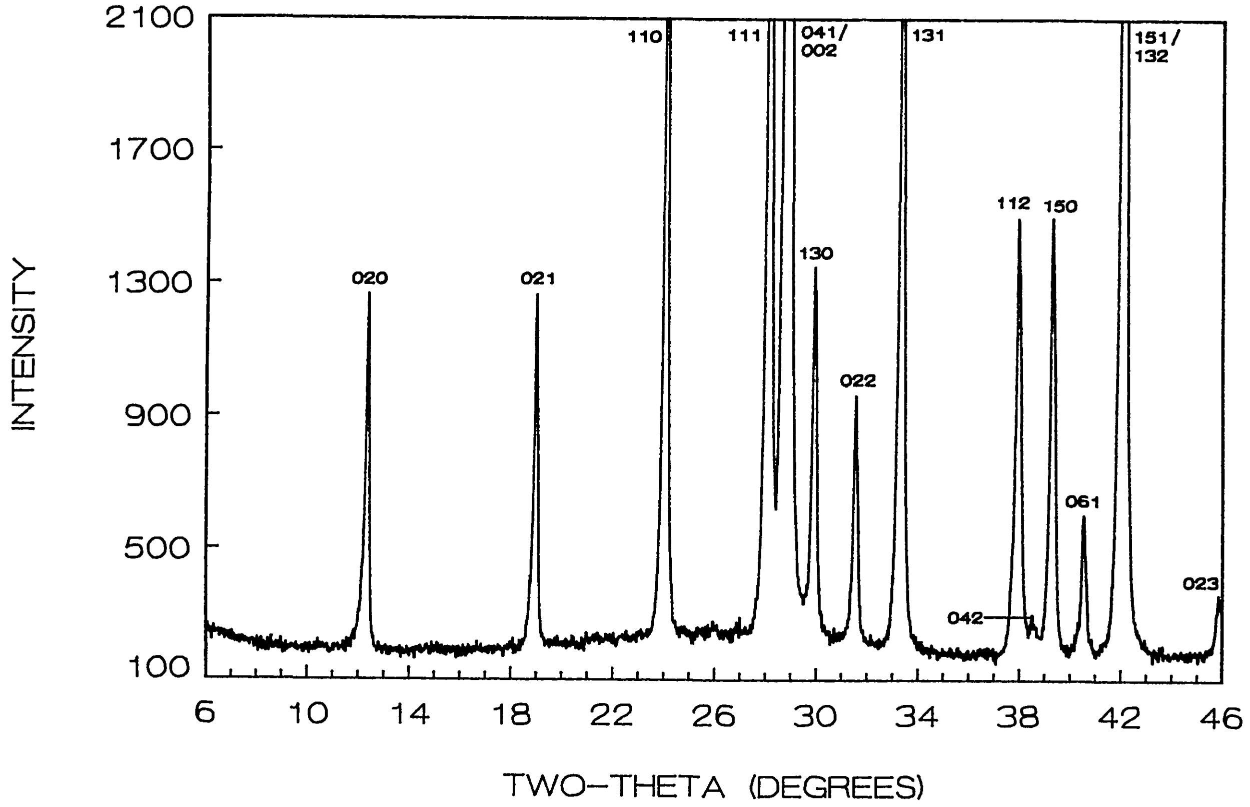

Figure 8. X-ray powder diffraction pattern of $Sr_2Bi_2O_5$ (cooled from 900 °C).

3.4.1 $Sr_2Bi_2CuO_6$(S_2B_2C-2:2:1) This compound should nominally be the end member with $n=1$ of the homologous series $Sr_2Bi_2Ca_{n-1}Cu_nO_{2n+4}$. However, the x-ray powder diffraction pattern for this composition does not match at all with the predicted tetragonal subcell for a compound of this structure type. The predicted type of x-ray pattern is only found in specimens that are grossly deficient in SrO (i.e., compositions corresponding to the Raveau solid solution region—see below). The compound which occurs at approximately $Sr_2Bi_2CuO_6$ has been characterized by electron diffraction and x-ray powder and single crystal diffraction and the results reported elsewhere [18]. The compound was found to be monoclinic, space group C2/m (or Cm) with $a=24.493(2)$, $b=5.4223(5)$, $c=21.959(2)$ Å, $\beta=105.40(1)°$. The actual composition with Sr:Bi:Cu ratio of 2:2:1 always contains a small amount of $Sr_{14}Cu_{24}O_{41}$ and probably also some of the Raveau-type phase. Therefore, this compound is shown in figures 13 and 14 as being slightly deficient in CuO (less than 1 mol percent) and having a small homogeneity region. The x-ray powder diffraction data, single crystal precession photographs and electron microscopy data, along with figure 14, were previously published [18]. This phase appears to have a subcell with c-subcell ($\sim$5.49 Å) $\frac{1}{4}c$-supercell; electron microscopy data for some grains indicate an incommensurate superstructure. The x-ray diffraction data for compositions with only 19 mol percent CuO do not yield satisfactory least-squares refinements. It is possible that the observed incommensurate modulation is an equilibrium phenomenon dependent on composition, although it is equally likely to be due to a non-equilibrium chemical inhomogeneity.

3.4.2 The Raveau-Type Solid Solution (Rav) A two-phase region is shown in figure 14 (after [18]) between the 2:2:1 phase and the region referred to as the Raveau-type solid solution. This nomenclature is used because, structurally, the Raveau-type phase most closely resembles the $n=1$ end member of the series $Sr_2Bi_2Ca_{n-1}Cu_nO_{2n+4}$ and because Raveau and coworkers were the first to report superconductivity in this system [31]. This phase often forms

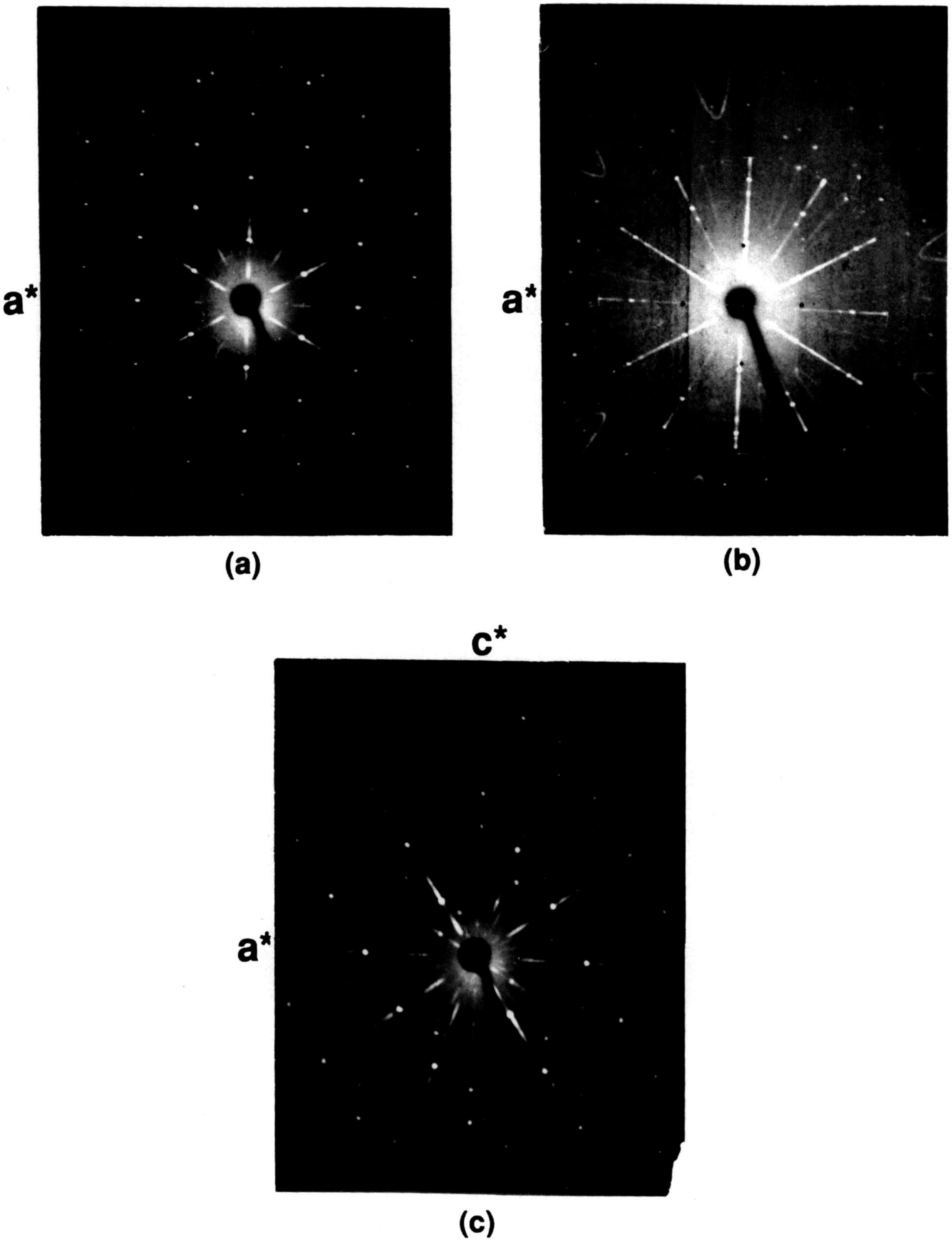

Figure 9. X-ray precession photographs of $Sr_3Bi_2O_6$ (a) *hk0*, (b) unscreened *hk0* and (c) *h0l*.

Table 6. X-ray powder diffraction data for the compound $Sr_3Bi_2O_6$

d obs(Å)	Rel *I*(%)	2*θ* obs	2*θ* calc[a]	*hkl*
9.32	2	9.48	9.47	101
6.997	2	12.64	12.63	012
6.100	4	14.51	14.49	003
4.662	16	19.02	19.00	202
4.371	14	20.30	20.29	113
4.217	8	21.05	21.03	104
4.001	11	22.20	22.20	211
3.740	9	23.77	23.76	122
3.1326	100	28.47	28.48	220
3.0394	85	29.36	29.38	205
2.9694	6	30.07	30.08	131
2.8582	4	31.27	31.27	312
2.7861	3	32.10	32.09	223
2.7454	2	32.59	32.58	116
2.7347	2	32.72	32.74	125
2.6013	7	34.45	34.46	042
2.5150	8	35.67	35.67	134
2.4024	1	37.40	37.42	232
2.3588	26	38.12	38.13	027
2.3329	2	38.56	38.54	404
2.3265	2	38.67	38.68	315
2.2420	3	40.19	40.19	018
2.2073	5	40.85	40.85	413
			40.86	217
2.1797	63	41.39	41.38	045
2.1552	2	41.88	41.90	051
2.1111	2	42.80	42.79	502
			42.81	208
2.0377	2	44.42	44.43	241
			44.44	009
2.0011	11	45.28	45.29	422
			45.30	128
1.9767	6	45.87	45.90	333
			45.91	137
1.9376	7	46.85	46.86	511
			46.87	119
1.9062	4	47.67	47.68	152
1.8832	12	48.29	48.27	407
1.8711	7	48.62	48.62	244
			48.62	416
1.8230	9	49.99	49.99	318
1.8087	24	50.41	50.44	600
1.7893	46	51.00	51.00	425
1.7753	9	51.43	51.44	431
			51.45	309
1.7512	3	52.19	52.21	342
			52.22	048
1.7367	40	52.66	52.66	0,2,10
1.7248	4	53.05	53.09	336
1.7200	4	53.21	53.20	155
1.6855	5	54.39	54.38	238
1.6146	9	56.99	57.00	247
1.5931	4	57.83	57.84	2,0,11
1.5667	24	58.90	58.94	440
1.5569	5	59.31	59.35	164
			59.35	606
1.5443	9	59.84	59.85	701
			59.86	419

[a] Calculated on the basis of a rhombohedral unit cell $a=12.526(1)$, $c=18.331(2)$ Å.

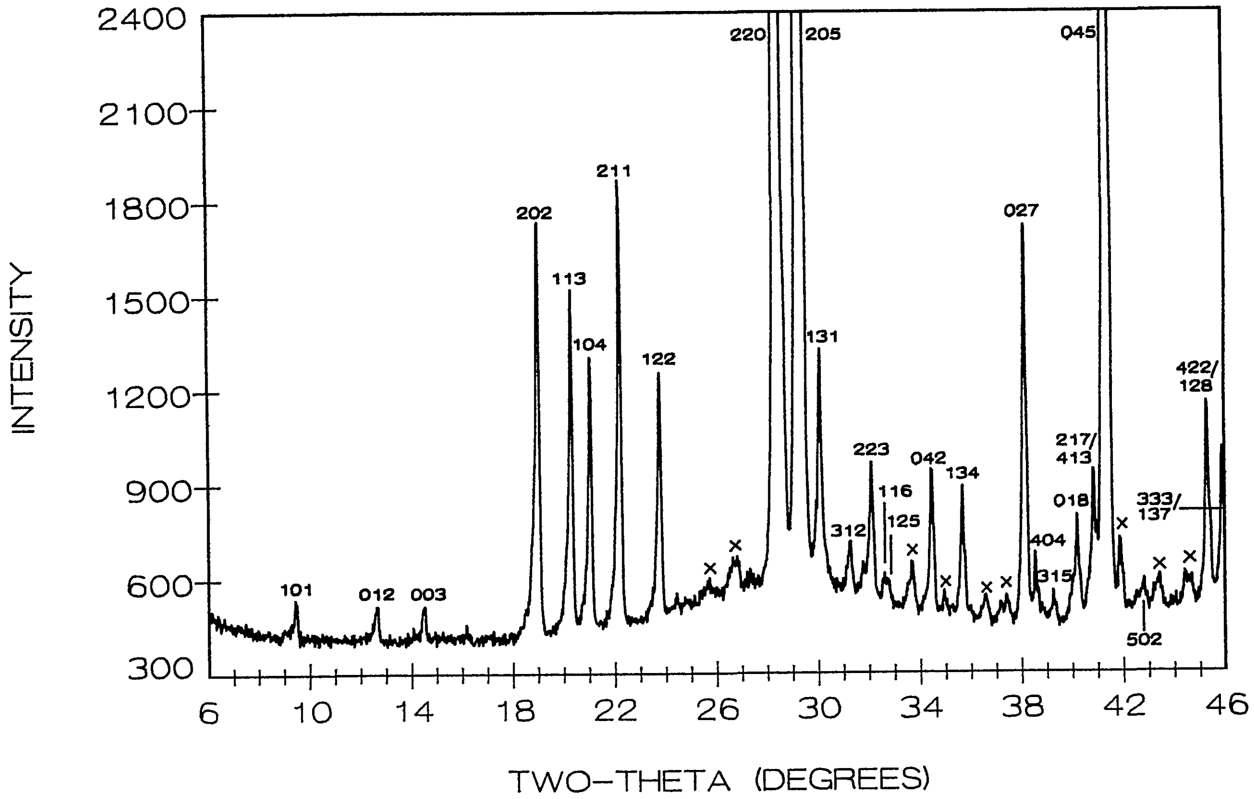

Figure 10. X-ray powder diffraction pattern of $Sr_3Bi_2O_6$ (cooled from 975 °C). X=unidentified peaks-probably due to hydration.

metastably as an almost single-phase product when compositions near the indicated equilibrium single-phase region are synthesized by cooling from a melt. For example, a melt of 2:2:1 composition first crystallizes as the Raveau solid solution and reacts to form the 2:2:1 phase only after subsequent heating and grinding (table 1); similarly, when a mixture of composition 3:2:2 was prepared by a lactate route, the Raveau solid solution was the first crystalline phase to form; but, the 3:2:2 phase replaced it after subsequent heating and grinding (table 1). The crystals formed from melts of Raveau solid solution, or similar compositions (outside the equilibrium Raveau field), are always very platy and micaceous and form "books" of crystals not well ordered in the direction perpendicular to the plates. They always have one long crystallographic axis of about 26.6 Å and the x-ray powder diffraction data can be roughly fit to a pseudotetragonal subcell with $a=5.3$ Å. Several unit cells have been reported for this phase, either pseudotetragonal or pseudoorthorhombic [32,33].

Crystals that were picked from various ternary melts (with or without chloride flux) were invariably non-single and appear to have a monoclinic superstructure. The phase formed using 1:1 NaF:KF flux, however, yielded crystals with apparent orthorhombic symmetry and a very strange incommensurate superstructure (fig. 15). Onoda and Sato [34] obtained a monoclinic superstructure for a crystal that was grown from a melt of 1:1:1 composition (Sr:Bi:Cu = 1:1:1) which was heated in an Al_2O_3 crucible. They report a nominal composition for the crystal of Sr:Bi:Cu 4:6:3, well outside the equilibrium single-phase region reported in figures 13 and 14. The unit cell reported for this phase [34] is C-centered monoclinic with $a=26.856$, $b=5.380$, $c=26.908$ Å, $\beta=113.55°$; no data were reported on the extent of contamination from the Al_2O_3 crucible. A calculated powder pattern based on their structure determination [34] was obtained from M. Onoda (private communication) and these data were used to index the x-ray powder diffraction pattern of the composition with Sr:Bi:Cu ratios of 36:44:20 (near the SrO-rich end of the Raveau solid solution region). All of the superstructure lines observed for this composition can be completely accounted for by *hkl*'s with intensities *very* similar to those calculated by Onoda. For a C-centered monoclinic cell, the unit cell dimen-

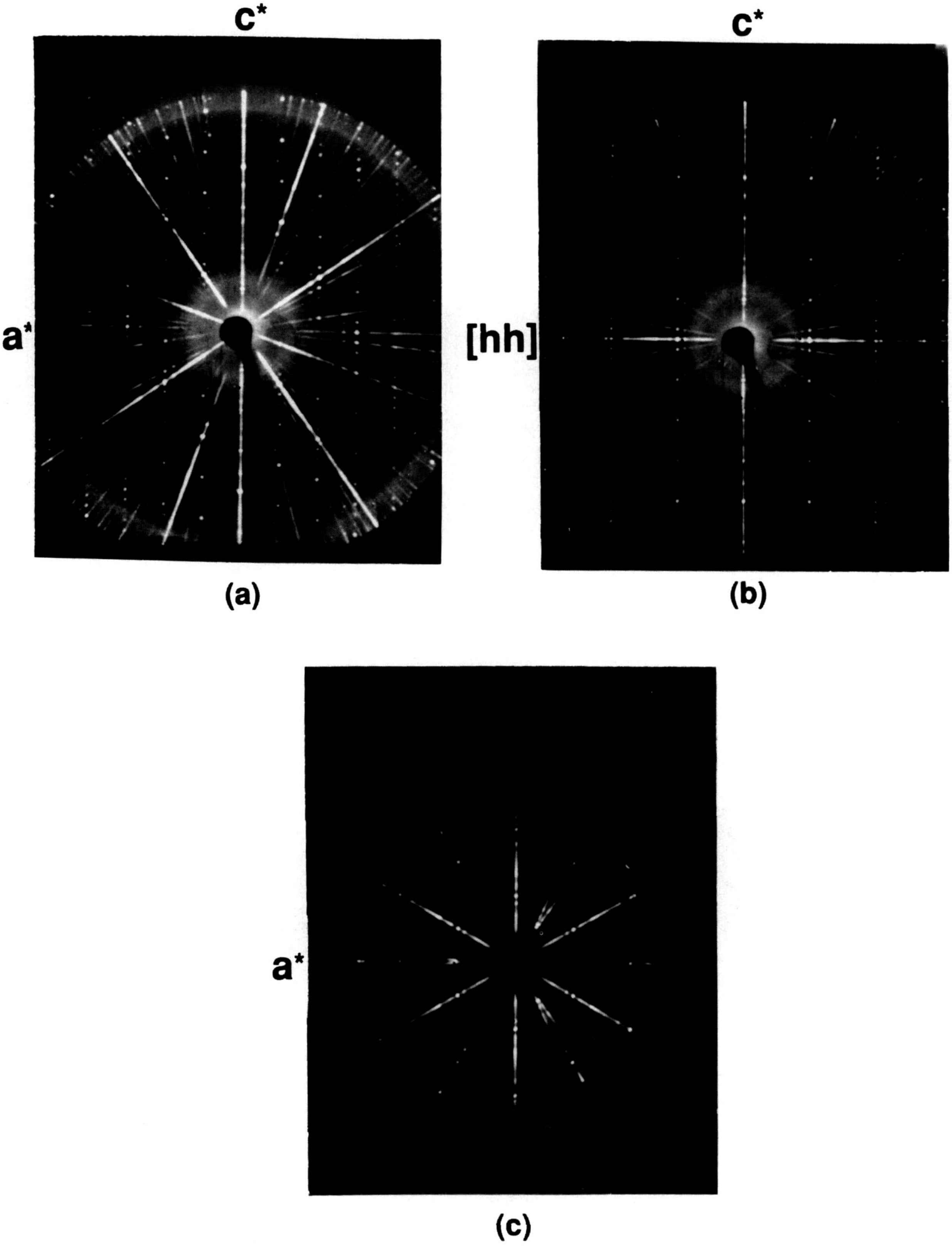

Figure 11. X-ray precession photograph of "$Sr_6Bi_2O_9$" (a) *h0l*, (b) *hhl* and (c) unscreened *hk0*.

Table 7. X-ray powder diffraction data for the compound $Sr_6Bi_2O_9$

d obs(Å)	Rel I(%)	2θ obs	2θ calc[a]	*hkl*[b]
4.891	18	18.12	18.13	0,0,12
4.777	1	18.56		
4.397	1	20.18		
4.258	12	20.85	20.93	018
4.197	6	21.15		
3.810	1	23.33		
3.589	1	24.79		
3.396	3	26.22	26.13	1,0,13
3.318	1	26.85		
3.271	1	27.24		
3.218	1	27.70		
3.184	1	28.00		
3.092	1	28.85		
3.0105	58	29.65	29.74	110
2.9997	61	29.76	29.79	1,0,16
2.9859	100	29.90		
2.8779	1	31.05		
2.8493	1	31.37		
2.7283	1	32.80		
2.6437	5	33.88	33.74	1,0,19
2.5615	16	35.00	35.05	1,1,12
2.5357	9	35.37		
2.4827	2	36.15		
2.4436	4	36.75	36.74	0,0,24
2.4075	1	37.32		
2.3829	2	37.72		
2.3672	2	37.98		
2.3383	1	38.55		
2.2974	1	39.18		
2.2603	6	39.85	39.99	0,2,13
2.2308	1	40.40		
2.1272	32	42.46	42.60	0,2,16
2.0953	15	43.14		
2.0452	2	44.25		
2.0146	1	44.96		
1.9952	4	45.42		
1.9845	3	45.68		
1.9550	4	46.41		
1.9502	6	46.53		
1.9415	8	46.75		
1.9337	10	46.95		
1.9054	4	47.69		
1.9006	5	47.82		
1.8629	4	48.85		
1.8452	2	49.35		
1.8118	2	50.32		
1.8001	3	50.67		
1.7509	3	52.20		
1.7364	18	52.67		
1.7318	35	52.82	52.77	300
1.7188	21	53.25		
1.7031	2	53.78		
1.6838	2	54.45		
1.6557	2	55.45		
1.6354	9	56.20		
1.6295	4	56.42		
1.6156	3	56.95		
1.5884	1	58.02		
1.5802	2	58.35		
1.5600	2	59.18		

---

[a] Calculated on the basis of a rhombohedral subcell with $a=6.009$, $c=58.663$ Å.

[b] Based on the intensities observed in single crystal precession photographs, figure 11.

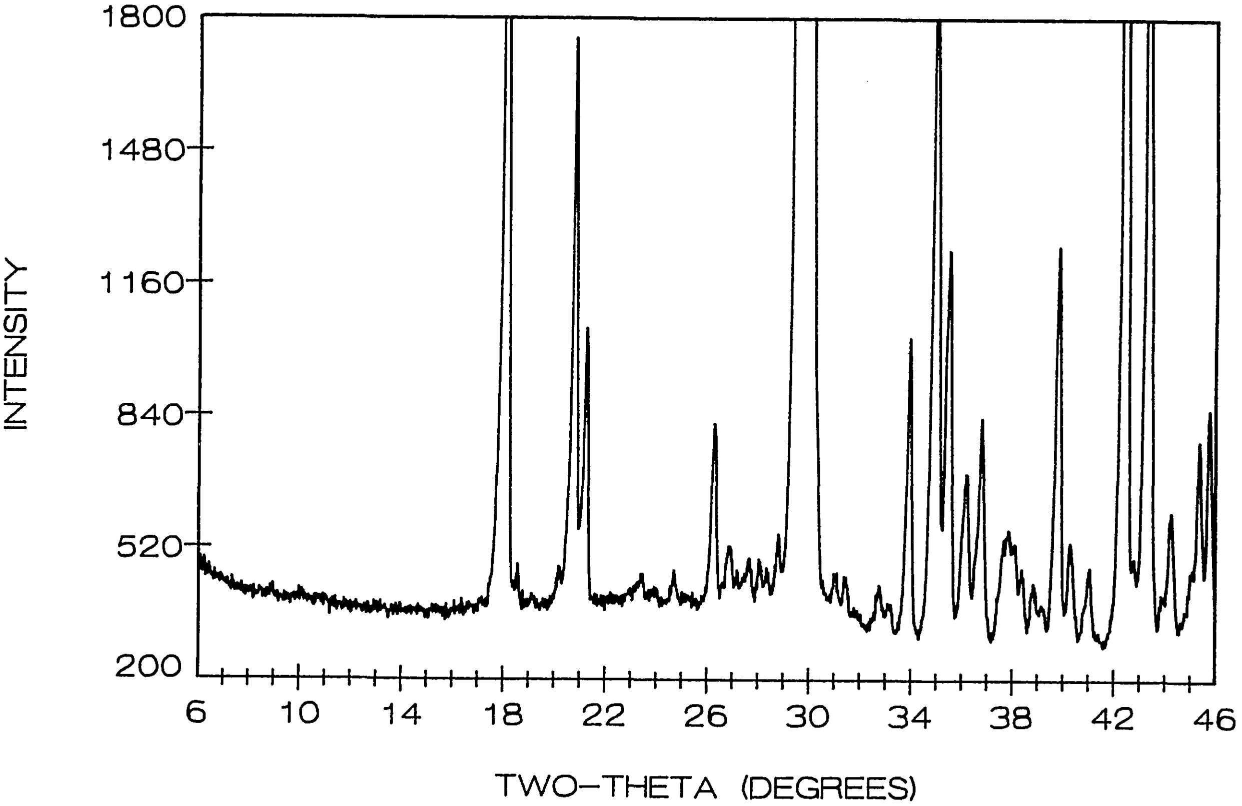

Figure 12. X-ray powder diffraction pattern of $Sr_6Bi_2O_9$ (heated to 975 °C then cooled to 900 °C, held for 24 h and cooled to room temperature).

sions obtained by least-squares analysis of this x-ray powder data (table 8, fig. 16) are $a = 26.889(9)$, $b = 5.384(2)$, $c = 26.933(8)$ Å, $\beta = 113.67(3)°$.

It should be noted, however, that powder patterns for more Bi-rich Raveau-type solid solutions display superstructure peaks which deviate widely from those observed for the 36:44:20 composition. At present it is not known if this is truly a region of solid solution or a collection of smaller regions (separated by two and/or three phase fields) in which several structurally related phases are stable. New specimens are currently being prepared at very close intervals in this Raveau-type region in order to determine the true crystal chemistry of this important "phase." These results will be reported in the near future [35].

The Raveau solid solution region extends along a line with approximately 20 mol percent CuO according to the formula $Sr_{1.8-x}Bi_{2.2+x}CuO_z$ with $\sim 0.0 < x < \sim 0.15$. This is slightly at odds with the results of Saggio et al. [36] who reported the formula $Sr_{1.8+x}Bi_{2.2-x}CuO_z$ with $0.0 < x < 0.08$ which corresponds to negative values of x in our formula. Their samples were annealed at 800 °C and premixed with 0.5 weight percent Li_2CO_3. It is not known if the differences between their results and ours are due to the temperature difference, the time of "equilibration," or to the presence of Li_2CO_3. They also report [36] that only the high SrO end of the solid solution exhibits superconductivity based on the data of Akimitsu et al. [37] which were obtained from specimens that were heated twice at 880 °C for 12 h. This preparation should probably have yielded results similar to ours, but we failed to find evidence of superconductivity at temperatures above 10 K. It is possible that superconductivity only occurs in metastable Raveau-type solutions that have compositions which lie outside the equilibrium "single phase" field.

The Raveau-type solid solution also exhibits non-stoichiometry with respect to its CuO concentration. The solid solution region corresponds approximately to the formula $Sr_{1.8-x}Bi_{2.2+x}Cu_{1\pm x/2}O_z$. Of course, there is no *a priori* reason why the CuO concentration must be structurally controlled by the Sr/Bi ratio.

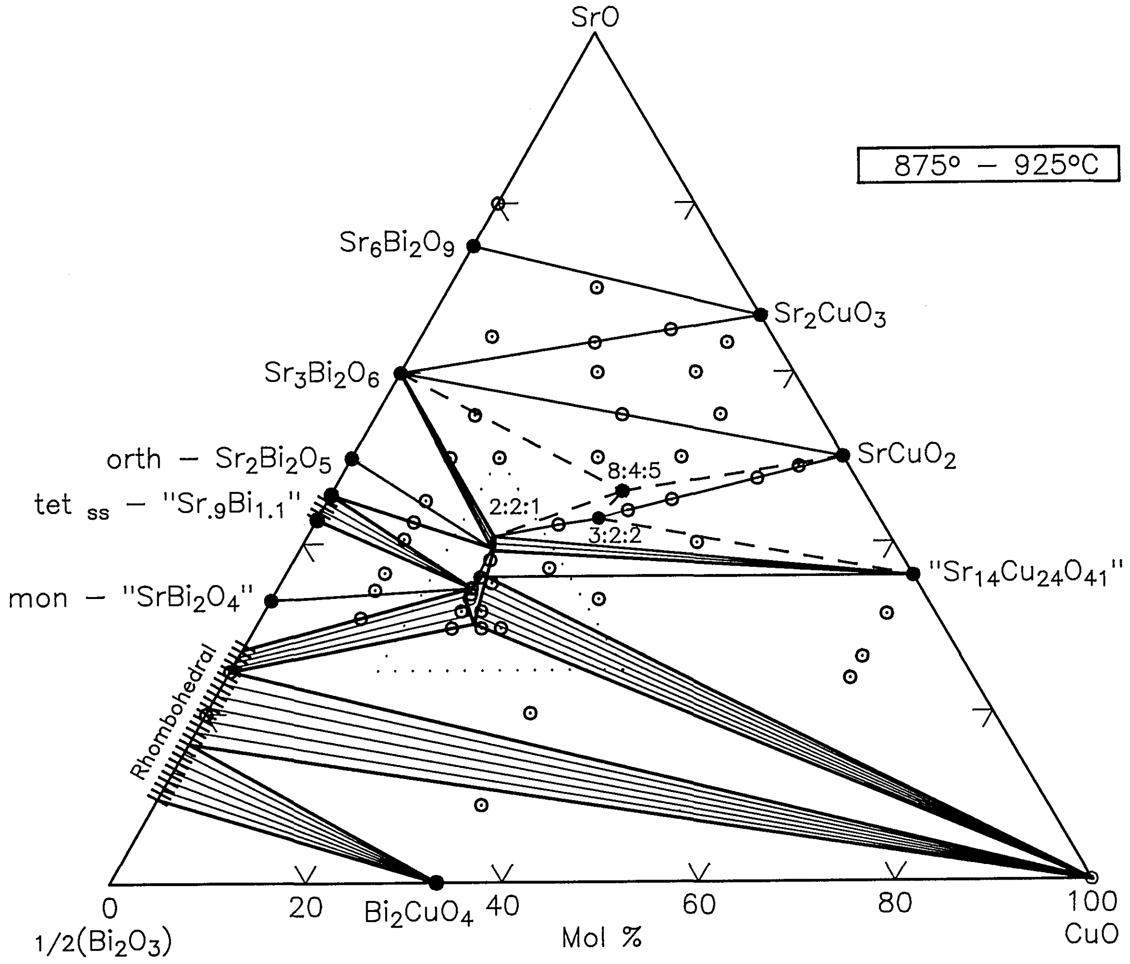

Figure 13. Phase diagram for the system SrO-$\frac{1}{2}Bi_2O_3$-CuO. O-compositions studied, ●-compounds. This diagram represents subsolidus conditions, although Bi_2O_3 melts at 825 °C and therefore partial melting occurs below 875 °C in most compositions below the join CuO-Rhomb. In addition, some melting was found at 875 °C for the composition 34.66:55.33:10.

Chakoumakos et al. [38] reported the results of a study of Raveau-type single crystals that were grown under oxygen from CuO-rich melts in crucibles of various compositions. Incomensurate superstructure peaks (related to orthorhombic symmetry) were found to vary systematically with the SrO content. Superconductivity was found to be related to excess oxygen and to the concentration of impurities including Al_2O_3. The superstructure peaks occurred with modulation of $\sim 1/5b^*$ plus a c^* component varying from $0.29c^*$ to $0.65c^*$ (where * represents the reciprocal vector direction). The observed formula for these crystals was reported as $Bi_2Sr_{2-x}CuO_{6-y}$. These crystals (and most if not all melt-grown, Raveau-type crystals) are probably metastable since they have compositions well outside the equilibrium range shown in figures 13 and 14. It should be noted, however, that Chakoumakos et al. grew their crystals under oxygen rather than air, so the relevant single-phase region may be similar but will not be identical to that in figures 13 and 14.

3.4.3 $Sr_8Bi_4Cu_5O_{19+x}$ ($S_8B_4C_5$-8:4:5) This phase was apparently first described [39] as a compound with the composition $Sr_4Bi_2Cu_2O_{9+z}$ (Sr:Bi:Cu=2:1:1); however, an examination of the reported unindexed x-ray powder diffraction data indicate that modest amounts of both S_3B_2 and SC were present in this sample. All of our experiments with the 2:1:1 composition yielded three phases when equilibrated in air at subsolidus temperatures, although the minority phases that were observed depended upon the heat treatment (table 1). Small single crystals of this new phase were obtained from a specimen of 2:1:1 that was mixed with 10 weight percent 1:1 NaCl:KCl flux and sealed in a gold tube that was heated at 900 °C for 1 h then cooled to 650 °C at 3 °C/h. The crystals are needle-like suggesting that one crystallographic axis is

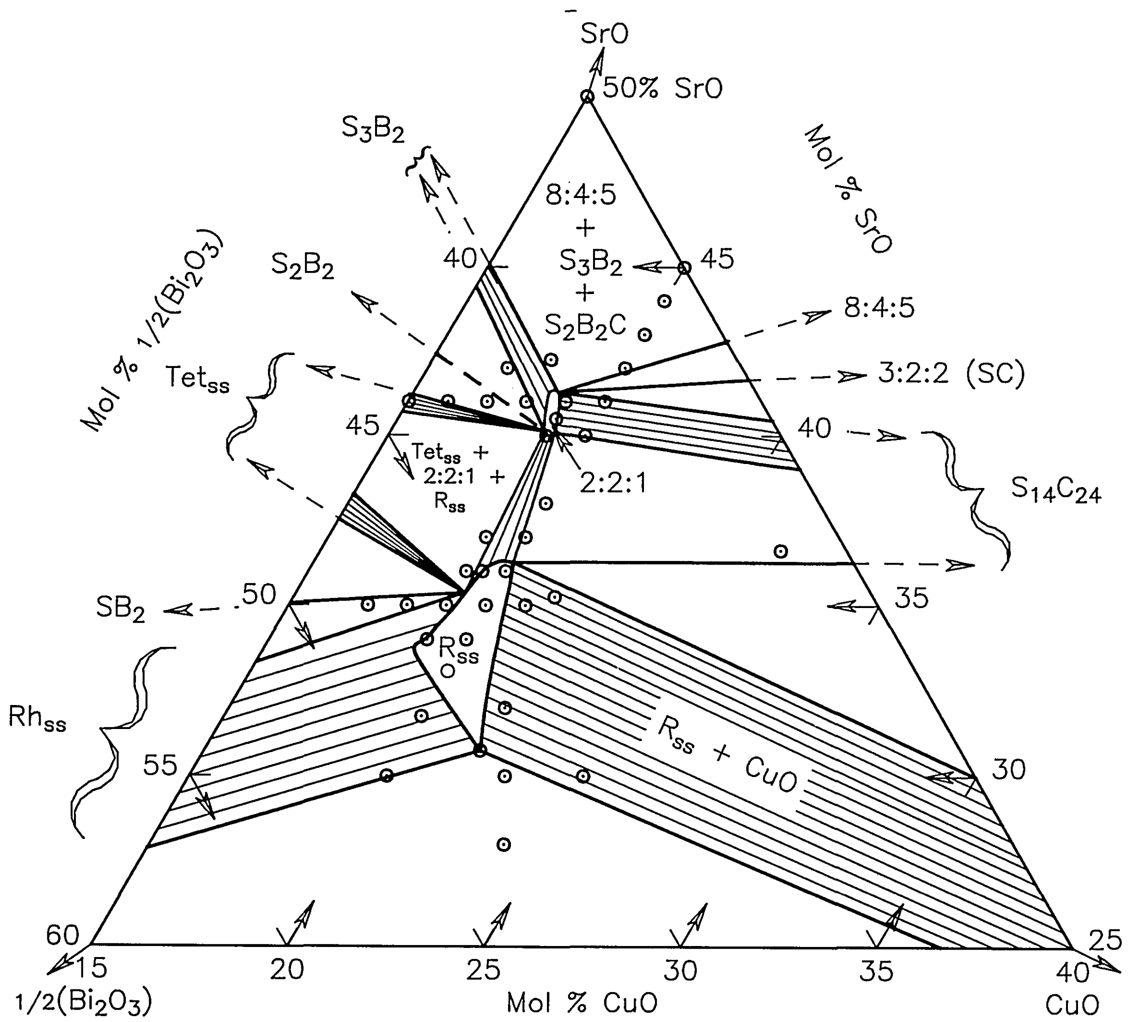

Figure 14. An enlargement of the triangular region of the phase diagram in figure 13 that is delineated by dots.

probably much shorter than the others, and x-ray precession photographs (fig. 17) revealed that it is orthorhombic (space group Fmmm) with a, b, c parameters of approximately 33.98, 24.02, 5.364 Å, respectively. The crystal structure of this phase has been solved by Fuertes et al. [40] who describe its chemistry as $Bi_4Sr_8Cu_5O_{19+x}$, and its unit cell as orthorhombic with $a = 5.373(2)$, $b = 33.907(6)$, $c = 23.966(4)$ Å. Obviously, the diffraction data in figure 17 indicate that this is the same phase as the one reported in [39,40].

Single-phase specimens of $Sr_8Bi_4Cu_5O_{19+x}$ were only obtained in this laboratory when the starting materials were annealed in one atmosphere of oxygen. The unit cell refined from the data obtained from the 8:4:5 specimen (table 9, fig. 18) is orthorhombic Fmmm with $a = 33.991(3)$, $b = 24.095(2)$, $c = 5.3677(5)$. Clearly the published structure of this phase [40] requires more than the 19 oxygen atoms per formula unit that are implied by an 8:4:5 ratio. The smaller unit cell obtained by [40] was also found in the present work when an 8:4:5 specimen was melted in an Al_2O_3 crucible (as were the crystals reported by [40]) poured onto an Al plate and annealed in air or oxygen. Attempts to supply the excess oxygen by the substitution of some La^{+3} for some of the Sr^{+2} as suggested by R. J. Cava (private communication) was only partially successful, never resulting in a completely single-phase specimen when heated in air.

3.4.4 $Sr_3Bi_2Cu_2O_8$ ($S_3B_2C_2$-3:2:2) Extrapolation based on the general formula for the homologous series of Bi-containing high-T_c phases, $A_2Ca_{n-1}B_2Cu_nO_{2n+4}$, predicts the formula $Sr_2CaBi_2Cu_2O_8$ (2:1:2:2) for the phase with $n = 2$, and a c-axis of ~30.6 Å which implies $d(002)$

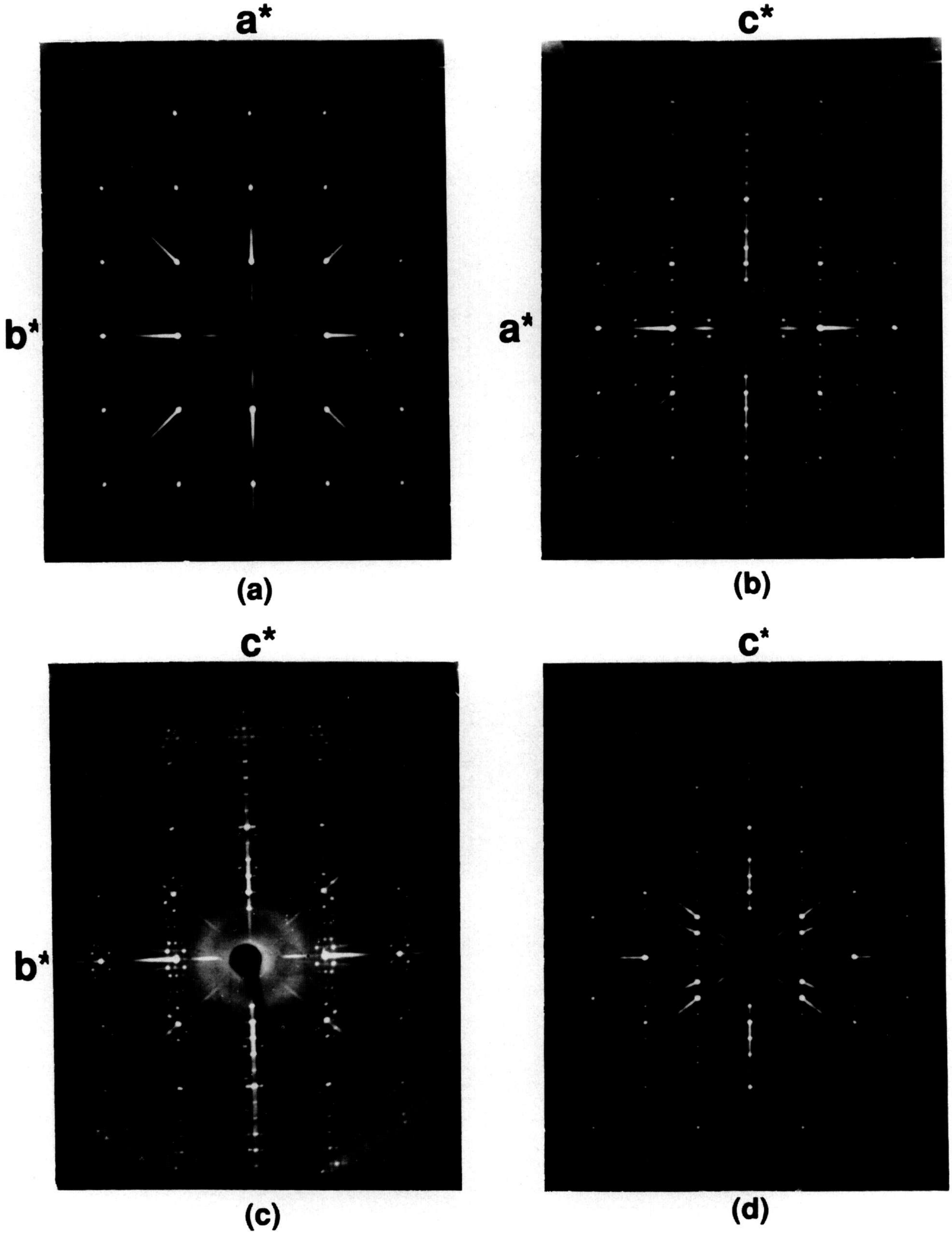

(a) (b) (c) (d)

Figure 15. X-ray precession photographs of an orthorhombic/incommensurate Raveau solid solution phase that was grown in 1:1 NaF:KF flux. Original composition=$Sr_2Bi_2CuO_6$ (a) *hk0*, (b) *h0l*, (c) *0kl* and (d) *hhl*.

Table 8. X-ray powder diffraction data for the Raveau-type phase at the composition $Sr_{1.8}Bi_{2.2}CuO_{6.1}$[a]

d obs(Å)	Rel *I*(%)	2*θ* obs	2*θ* calc[b]	*hkl*[c]
12.35	6	7.15	7.17	200
6.16	1	14.37	14.38	400
5.47	1	16.20	16.17	401
5.26	3	16.83	16.84	110
4.50	1	19.70	19.70	310
4.348	2	20.41	20.44	$60\bar{1}$
4.183	2	21.22	21.22	$11\bar{4}$
4.105	34	21.63	21.63	600
3.761	2	23.64	23.62 23.62	$31\bar{5}$ $11\bar{5}$
3.632	4	24.49	24.45 24.47	$51\bar{4}$ 510
3.457	58	25.75	25.76 25.78	$51\bar{5}$ 115
3.384	1	26.32	26.32	$11\bar{6}$
3.239	4	27.52	27.50	$51\bar{6}$
3.220	6	27.68	27.70	$80\bar{1}$
3.092	24	28.85	28.85	$71\bar{4}$
3.081	66	28.96	28.96	800
3.013	100	29.63	29.62 29.64	$71\bar{5}$ 315
2.9427	5	30.35	30.32	710
2.9380	5	30.40	30.41	$20\bar{9}$
2.9025	11	30.78	30.81	$71\bar{6}$
2.7929	3	32.02	32.05	514
2.7462	2	32.58	32.54	316
2.6924	58	33.25	33.24 33.25	$4,0,\overline{10}$ 020
2.6317	2	34.04	34.04 34.05 34.06	$6,0,\overline{10}$ $2,0,\overline{10}$ 220
2.5831	7	34.70	34.68 34.70	$91\bar{5}$ 515
2.5560	2	35.08	35.11	$10,0,\bar{1}$
2.4623	15	36.46	36.45	10,0,0
2.4481	5	36.68	36.71	$4,0,\overline{11}$
2.4182	5	37.15	37.15	$6,0,\overline{11}$
2.3565	5	38.16	38.12	10,0,1

[a] Oxygen content not certain.

[b] Calculated from monoclinic unit cell $a=26.889(9)$, $b=5.384(2)$, $c=26.933(3)$ Å, $\beta=113.67(3)°$.

[c] Indexed based on single crystal F_{obs} data received from M. Onoda [34].

~5.78 ° 2*θ* for Cu*K*α radiation. It is known that Sr^{+2} can substitute for some of the Ca^{+2} up to at least 3:3:4:4 [40]. If *all* the Ca^{+2} were replaced by Sr^{+2}, the chemical formula would degenerate to 3:2:2 or $Sr_3Bi_2Cu_2O_8$; but, attempts to synthesis the $n=2$ phase at this composition have failed. The presence of a small peak at ~5.75 ° 2*θ* was noted during the first low temperature calcination of specimens prepared by decomposition of lactate precursor powders with 3:2:2 composition. However, the peak at ~5.75 ° 2*θ* disappears after subsequent heat treatments which suggests that it is associated with a metastable phase.

Compositions of 3:2:2 prepared by conventional solid state techniques yield a new phase that has an x-ray powder diffraction pattern (table 10, fig. 19) which resembles both the Raveau-type solid solution and the 2:2:1 phase in some respects. The low angle peak occurs at about the same value as for the Raveau solid solution ($d \sim 12.35$ Å, $2\theta \sim 7.15°$), but there is a very small peak at a *d*-value of twice that ($d \sim 24.7$ Å, $2\theta \sim 3.58°$). The strong (113) Raveau-type tetragonal subcell peak at ~25.75° 2*θ* is not present and, instead, a strong peak occurs at ~26.85° 2*θ*, similar to the 2:2:1 compound. In addition, there are considerable differences between

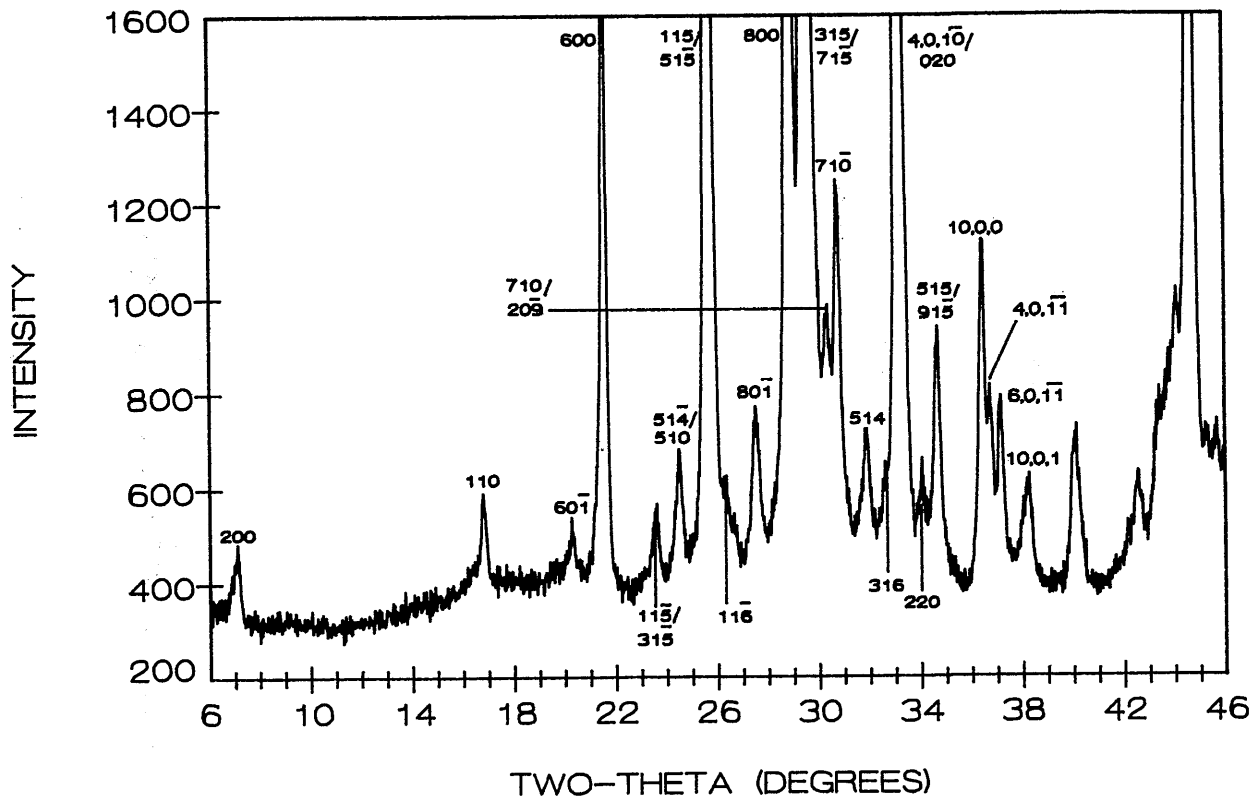

Figure 16. X-ray powder diffraction pattern of the Raveau phase from the composition $Sr_9Bi_{11}Cu_5O_{30.5\pm x}$ (cooled from 875 °C).

this pattern and both the Raveau solid solution and $Sr_2Bi_2CuO_6$, which indicate that $Sr_3Bi_2Cu_2O_8$ is a unique phase. As yet, no single crystals of this phase have been synthesized. The pattern in figure 19 shows the presence of a small amount of $Sr_{14}Cu_{24}O_{41}$, indicating some probable nonstoichiometry in the composition. The diffraction maxima in this pattern have been indexed with comparison to the 2:2:1 and Raveau solid solution with a C-centered monoclinic unit cell, $a=24.937(7)$, $b=5.395(2)$, $c=19.094(7)$ Å, and $\beta=96.97(3)°$. This commensurate cell probably represents only a subcell of an incommensurate non-stoichiometric phase.

3.4.5 Miscellaneous Phases of Unknown Composition Two phases high in SrO content at approximate Sr:Bi:Cu ratios of 9:4:1 and 7:2:2 were reported by Saggio et al. [36], and two different phases at 4:2:1 and 2:1:1 were reported by Casais et al. [39]. Of these, we only found evidence for the phase reported at 7:2:2 composition, and then only at temperatures below 875 °C. The Saggio et al. data [36] are complicated by their use of the 0.5 wt% Li_2CO_3 "as a mineralizer." Peaks corresponding to the d-spacings reported for the composition 9:4:1 were not present in our specimens except when we included 0.5 wt% Li_2CO_3, and the binary phase $Sr_6Bi_2O_9$ (that was not reported by Saggio et al. [36]) is only present when Li_2CO_3 is absent. We therefore conclude that the "9:4:1-phase" is not present in the ternary system. Some of the low-angle d-spacings reported for the "7:2:2-phase" (4.82 Å$=18.40°$ 2θ and 4.17 Å$=21.27°$ 2θ) in samples that were heated at 800 °C were observed in patterns from samples that we heated at temperatures below ~875 °C (table 1). Because $SrCO_3$ does not decompose until ~875 °C, these results suggest the presence of one or more oxycarbonate phases. The first two d-spacings as well as the strongest peak reported as a "4:2:1" phase [38] ($d=4.91$, 4.25 and 3.004 Å) are apparently due to the phase $Sr_6Bi_2O_9(S_3B)$.

In summary, we interpret the evidence for these four reported phases as follows:

9:4:1-mostly due to reaction with Li_2CO_3;

7:2:2-multiphase due to reaction with Li_2CO_3 plus a Sr:Bi:Cu-oxycarbonate;

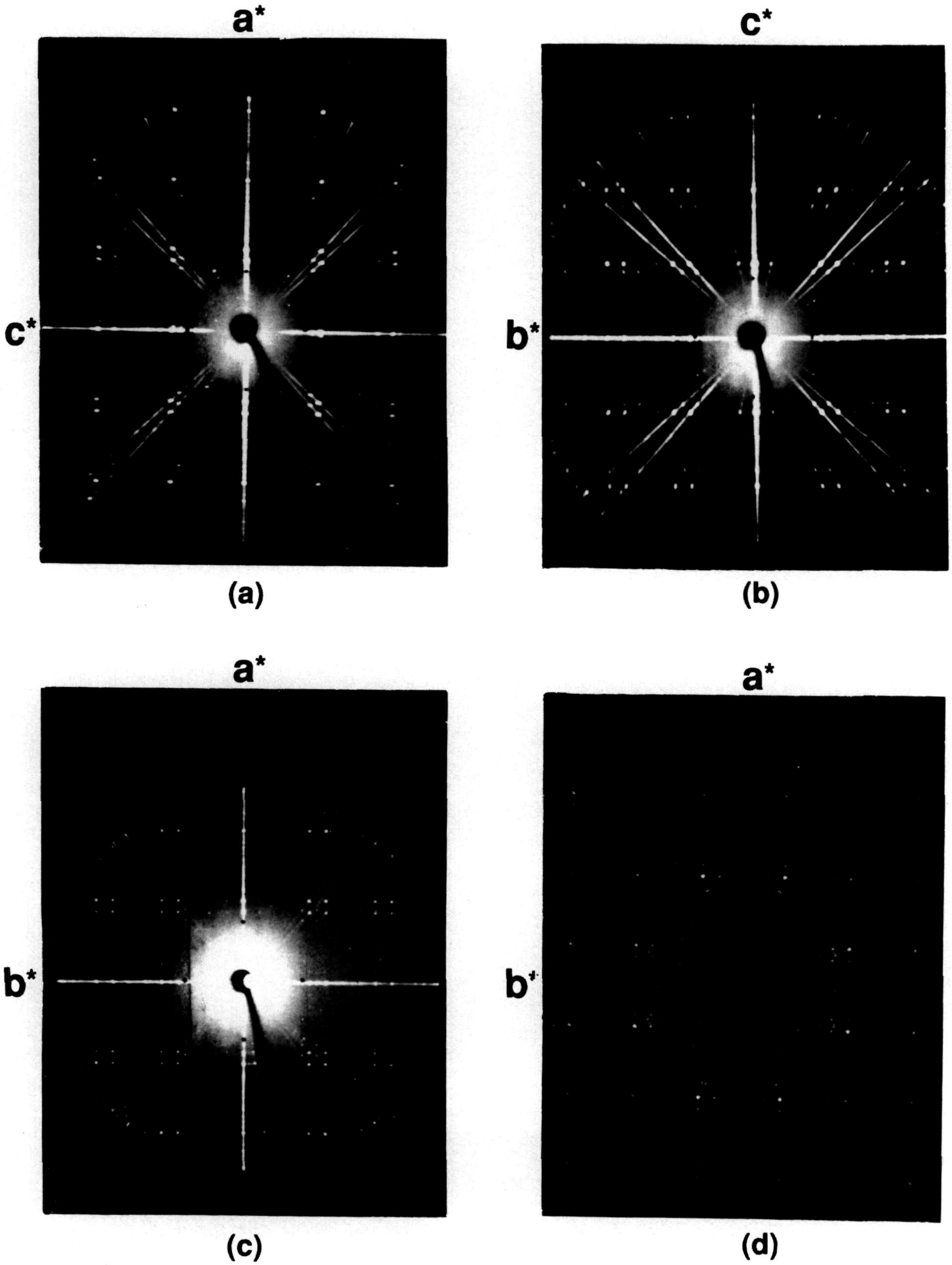

Figure 17. X-ray precession photographs of 8:4:5 (a) *h0l*, (b) *0kl*, (c) *hk0* and (d) *hk1*.

Table 9. X-ray powder diffraction data for the compound $Sr_8Bi_4Cu_5O_{19+x}$[a]

d obs(Å)	Rel I(%)	2θ obs	2θ calc[b]	hkl[c]
17.05	3	5.18	5.20	200
12.08	3	7.31	7.33	020
9.85	1	8.97	8.99	220
5.668	<1	15.62	15.63	600
4.425	2	20.05	20.05	131
4.253	2	20.87	20.89	800
4.153	2	21.38	21.39	511
4.015	4	22.12	22.12	060
3.911	3	22.72	22.73	260
3.729	13	23.84	23.83	531
3.559	1	25.00	24.98	711
3.418	2	26.05	26.04	351
3.288	33	27.10	27.12	731
3.173	23	28.10	28.11	551
3.011	27	29.65	29.64	080
2.9665	4	30.10	30.11	280
2.8861	100	30.96	30.95	171
2.8317	11	31.57	31.56	12,0,0
2.7569	2	32.45	32.44	12,2,0
2.6837	35	33.36	33.36	002
2.6498	1	33.80	33.78	202
2.6182	3	34.22	34.20	022
	4	34.40[d]		
2.5903	1	34.60	34.62	222
2.4881	2	36.07	36.07	771
2.4264	27	37.02	37.00	14,0,0
2.4080	24	37.31	37.29	0,10,0
2.3793	3	37.78	37.77	14,2,0
2.3417	1	38.41	38.42	11,5,1
2.3145	1	38.88	38.88	12,6,0
2.2571	2	39.91	39.93	13,3,1
2.2303	1	40.41	40.39	062
2.2125	1	40.75	40.75	262
2.1485	2	42.02	42.02	791
2.1244	4	42.52	42.52	16,0,0
2.1135	3	42.75	42.77	13,5,1
2.0639	14	43.83	43.84	12,8,0
2.0077	14	45.12	45.12	0,12,0
2.0036	14	45.22	45.22	082
1.9474	24	46.60	46.58	12,0,2
1.9443	23	46.68	46.70	5,11,1
1.9164	20	47.40	47.42	15,5,1
1.8909	2	48.08	48.10	14,8,0
1.8715	21	48.61	48.61	7,11,1
1.8351	8	49.64	49.63	12,10,0
1.8001	19	50.67	50.66	14,0,2
1.7935	21	50.87	50.89	0,10,2
1.7875	12	51.05	51.08	9,11,1
1.7525	3	52.15	52.14	12,6,2
1.7494	4	52.25	52.24	1,13,1
1.7264	3	53.00	53.02	513
1.7099	9	53.55	53.54	14,10,0
1.6967	7	54.00	54.01	5,13,1
1.6915	7	54.18	54.18	533
1.6604	10	55.28	55.28	19,3,1
1.6478	27	55.74	55.73	7,13,1
1.6437	21	55.89	55.90	733
1.6359	10	56.18	56.18	12,8,2
1.6288	5	56.45	56.46	553
1.6007	25	57.53	57.53	19,5,1
1.5851	26	58.15	58.14	753
1.5453	13	59.80	59.79 59.81	14,8,2 22,0,0

[a] Oxygen content based on structure derived by [40].

[b] Calculated by least-square analysis from orthorhombic unit cell, Fmmm, $a=33.991(3)$, $b=24.095(2)$, $c=5.3677(5)$ Å.

[c] Indexed with the aid of the single crystal precession photographs, figure 17 and intensities calculated from the published structure [40].

[d] $SrCuO_2$.

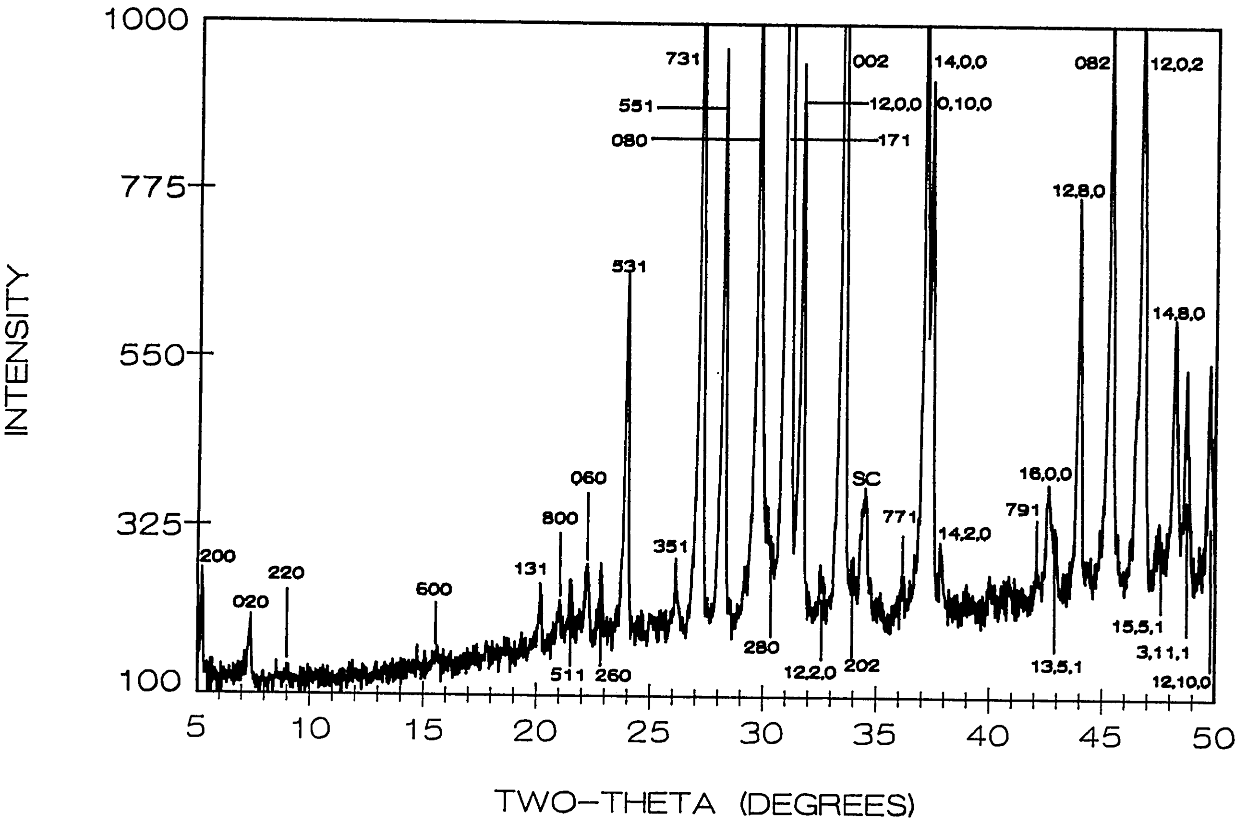

Figure 18. X-ray powder diffraction pattern of $Sr_8Bi_4Cu_5O_{19+x}$ (cooled from 925 °C in O_2).

4:2:1-$Sr_6Bi_2O_9$+other phases; and
2:1:1-$Sr_8Bi_4Cu_5O_{19+x}+S_3B_2$+SC

On heating above about 850 °C, the diffraction maxima characterizing the 7:2:2 "phase" start to disappear and are ultimately replaced by at least one other strong maximum at ~30.25° 2θ the origin of which is still unknown. At the 3:1:1 composition (table 1) the 7:2:2-type phase is very prevalent at 750 and 800 °C; however, as it starts to decompose at 850 °C, another peak arises at ~11.00° 2θ which persists even at 900 °C after the first heat treatment but finally disappears after three overnight anneals. The origin of this ~11.00° peak is also unknown but it appears to indicate a metastable phase that forms during decarbonation and subsequently decomposes.

At the 2:1:1 and 8:4:5 compositions it was found that preliminary low-temperature annealing was actually detrimental to the formation of an equilibrium assemblage. Apparently, an oxycarbonate phase characterized by small peaks at $2\theta=4.40°$ and 5.60° with strong peaks at 30.50° and 32.45° is formed first with repeated heating at 750°C; further heat treatments at 800 °C produce a new peak at ~4.80° as the 4.40° peak gradually disappears. These are gradually replaced by peaks from the 2:2:1 and Raveau solid solution plus $SrCuO_2$, but the 8:4:5 phase which should form is not found. Note, however, that when this sample was put in an Al_2O_3 crucible, melted and reheated at 900 °C, the 8:4:5 phase did form. Apparently, the formation of these oxycarbonates blocks the nucleation of 8:4:5.

Four ternary phases were reported in this system by Ikeda et al. [42]. These are essentially the same phases as those reported here, although the compositions do not always agree. The formula given for the Raveau phase solid solution differs somewhat from that used here. The formula for $Sr_2Bi_2CuO_6$ is given as $Sr_{16}Bi_{17}Cu_7O_z$, considerably deficient in SrO and occurring in the region clearly shown by our work to contain three phases. The x-ray diffraction pattern shown for their $Sr_3Bi_2Cu_2O_z$ clearly shows evidence of the $Sr_{14}Cu_{24}O_{41}$ phase, as do our own patterns of this composition. Unit cell dimensions and symmetry given by Ikeda et al. [42] and Saggio et al. [36] for their ternary phases are clearly based on intuition rather than single crystal data and should be considered suspect.

Table 10. X-ray powder diffraction data for the compound $Sr_3Bi_2Cu_2O_8$[a]

d obs(Å)	Rel *I*(%)	2*θ* obs	2*θ* calc[b]	*hkl*
24.7[c]	1	3.57		
12.35	3	7.15	7.14	200
5.26	2	16.84	16.81	110
5.12	1	17.32	17.33	$11\bar{1}$
4.120	10	21.55	21.52	600
4.064[c]	2	21.85		
3.992	2	22.25	22.22	113
3.625	9	25.54	24.54	602
3.573	2	24.90	24.92	$11\bar{4}$
3.315	48	26.87	26.86	$60\bar{4}$
3.124	11	28.55	28.63	$11\bar{5}$
3.095	33	28.82	28.83	800
3.053	2	29.20	29.23	$80\bar{2}$
3.043	2	29.33	29.32	513
2.9220	100	30.57	30.57	$80\bar{3}$
2.8031	1	31.90	31.79	315
2.7082	26	33.05	33.06	007
2.6963	60	33.20	33.19	020
2.6324	4	34.03	34.04	$71\bar{4}$
2.5581	2	35.05	35.07	$22\bar{2}$
2.5518	2	35.14	35.11	$80\bar{5}$
2.5281	3	35.48	35.56	222
2.4748	20	36.27	36.26	10,0,0
2.4384	16	36.83	36.85	$91\bar{2}$
2.3933	3	37.55	37.55	$31\bar{7}$
2.2571	3	39.91	39.91	317
2.0993	2	43.05		
2.0629	5	43.85		
2.0334	34	44.52		
1.9877	4	45.60		
1.9815	3	45.75		
1.9125	41	47.50		
1.8919	2	48.05		
1.8539	2	49.10		
1.8239	13	49.96		
1.8090	14	50.40		
1.7908	3	50.95		
1.7875	2	51.05		
1.7360	5	52.68		
1.7232	3	53.10		
1.6857	18	54.38		
1.6532	12	55.54		
1.6388	4	56.07		
1.6279	18	56.48		
1.5971	24	57.67		
1.5744	19	58.58		
1.5620	8	59.09		
1.5475	6	59.70		

[a] Heated to 925 °C in flowing O_2 on Au foil. Total oxygen content uncertain.

[b] Calculated on the basis of a C-centered monoclinic cell with $a=24.937(7)$, $b=5.395(2)$, $c=19.094(7)$ Å, $\beta=96.97(3)°$.

[c] Superstructure peaks.

3.4.6 Deduction of Ternary Compatibility (Alkemade) Lines This ternary system is remarkable for the gross irreproducibility of the experimental results. Attainment of equilibrium for each of the ternary compounds that we represent as stable is very difficult and time consuming. Nevertheless, equilibrium can generally be more easily achieved in ternary combinations furthest from the compositions of the stable ternary phases. For this reason the deduction of the compatibility joins is some-

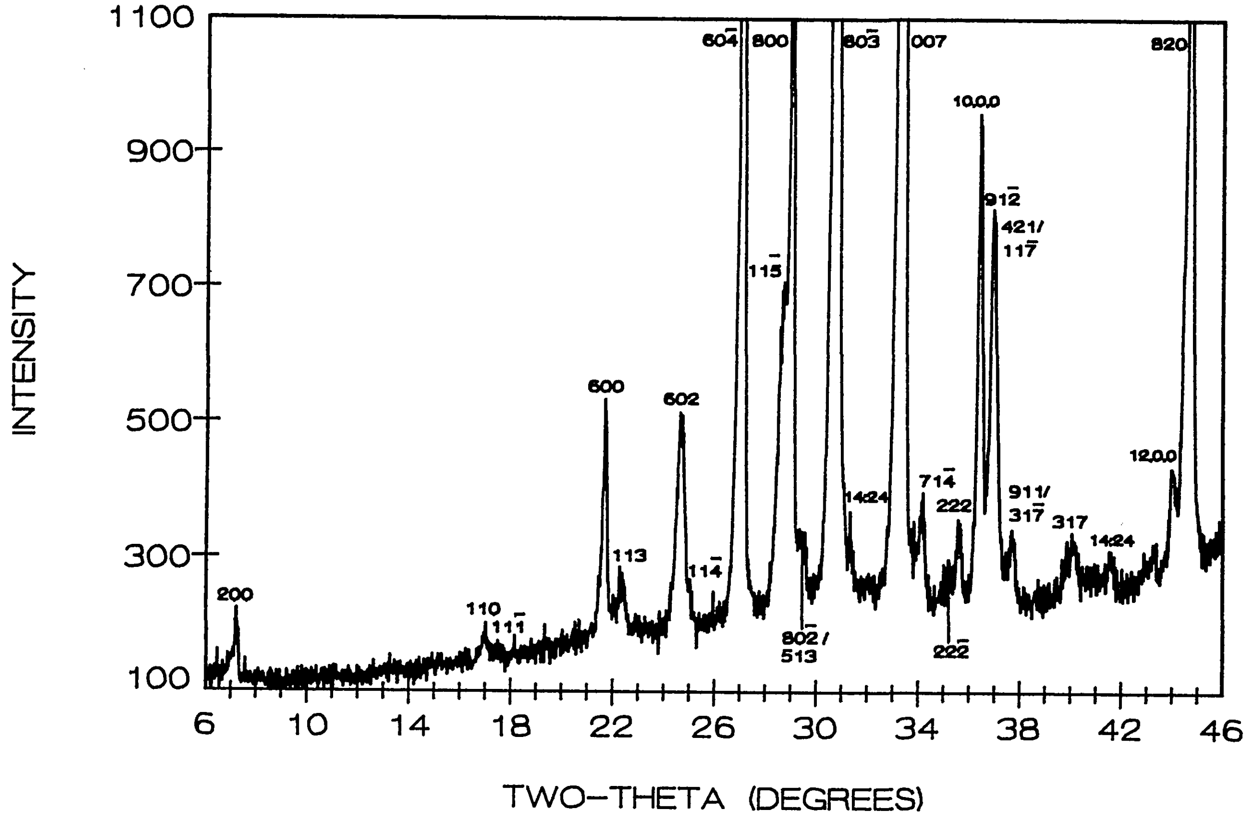

Figure 19. X-ray powder diffraction pattern of $Sr_3Bi_2Cu_2O_8$ (cooled from 925 °C in O_2).

what more reliable than one might suppose based on the difficulties inherent in determining the true compositions of the ternary phases.

Some generalizations can be made concerning both the data in table 1 and the interpretations behind our construction of figures 13 and 14. Because there is a two phase region involving CuO and the rhombohedral Sillen-phase solid solution, the compound Bi_2CuO_4 and the low melting eutectics of the Bi_2O_3-CuO binary system are not involved in most of the ternary equilibria. Also, CuO is in equilibrium with most or all of the compositions comprising the Raveau-type solid solution region. Therefore, the 1:1:1 composition (reported by Raveau [31] as superconducting) is in the middle of a ternary phase field bounded by CuO, Raveau solid solution and $S_{14}C_{24}$. The compound $Sr_{14}Cu_{24}O_{41}$ is in equilibrium with all three of the ternary phases related to the structurally homologous series $A_2Ca_{n-1}B_2Cu_nO_{2n+4}$: $Sr_2Bi_2CuO_6$, $Sr_3Bi_2Cu_2O_8$ and $Sr_{1.8-x}Bi_{2.2+x}Cu_{1\pm x/2}O_z$ (i.e., 2:2:1, 3:2:2 and the Raveau solid solution), but not with the structurally dissimilar phase $Sr_8Bi_4Cu_5O_{19+z}$ (8:4:5) or any of the SrO-Bi_2O_3 binary phases. The compound $SrCuO_2$ is in equilibrium with all three of the ternary compounds except for the Raveau-type solid solution while Sr_2CuO_3 is compatible only with the two high SrO content binary phases but not with any of the ternary phases. Joins describing compatibility conditions for the 8:4:5 and 3:2:2 phases are left as dashed lines because of the difficulty in determining equilibrium three phase assemblages.

4. Acknowledgments

Thanks are due to L. Bendersky, for electron diffraction investigations and to N. M. Hwang for experimental details in the binary systems.

About the authors: Robert S. Roth is a research chemist with the NIST Ceramics Division. Claudia J. Rawn is a materials research engineer with the NIST Ceramics Division. Benjamin P. Burton is a metallurgist with the NIST Metallurgy Division. Frank Beech was a research chemist with the Reactor Division at NIST and now is at University College, London, England.

5. References

[1] Bednorz, J. G. and Müller, K. A., Z. Phys. B-Condensed Matter **64**, 189 (1986).

[2] Takagi, H., Uchida, S., Kitazawa, K., and Tanaka, T., Jap. J. Appl. Phys. Lett. **26**, L123 (1987).

[3] Cava, R. J., VanDover, R. B., Batlog, B., and Rietman, E. A., Phys. Rev. Lett. **58**, 408 (1987).

[4] Wu, M. K., Asburn, J. R., Torng, C. J., Hor, P. H., Meng, R. L., Gao, L., Huang, Z. J., Wang, Y. Q., and Chu, C. W., Phys. Rev. Lett. **58**, 908 (1987).

[5] Cava, R. J., Batlog, B., VanDover, R. B., Murphy, D. W., Sunshine, S. A., Siegrist, T., Remeika, J. R., Rietman, E. A., Zahurak, S., and Espinosa, G. P., Phys. Rev. Lett. **58**, 1676 (1987).

[6] Roth, R. S., Davis, K. L., and Dennis, J. R., Ad. Ceram. Mat. **2**, 295 (1987).

[7] Roth, R. S., Rawn, C. J., Beech, F., Whitler, J. D., and Anderson, J. O., Ceramic Superconductors II, Ed. Yan, M. F., Amer. Ceram. Soc., Westerville, Ohio (1988) pp. 13–26.

[8] Maeda, H., Tanaka, Y., Fukutomi, M., and Asano, T., Jap. J. Appl. Phys. **27**, L209 (1988).

[9] Sheng, Z. Z. and Hermann, A. M., Nature **332**, 55 (1988).

[10] Subramanian, M. A., Torardi, C. C., Gopalakrishnan, J., Gai, P. L., Calabrese, T. C., Askew, T. R., Flippen, R. B., and Sleight, A. W., Science **242**, 249 (1988).

[11] Cava, R. J., Batlogg, B., Krajewski, J. J., Rupp, L. W., Schneemeyer, L. F., Siegist, T., vanDover, R. B., Marsh, P., Peck, W. F., Jr., Gallegher, P. K., Glarum, S. H., Marshall, J. H., Farrow, R. C., Waszczak, J. V., Hull, R., and Treor, P., Nature **336**, 211 (1988).

[12] Cava, R. J., Batlogg, B., Kajewski, J. J., Farrow, R., Rupp, L. W., Jr., White, A. E., Short, K., Peck, W. F., and Kometari, T., Nature **332**, 814 (1988).

[13] Tokura, Y., Takagi, H., and Uchida, S., Nature **337**, 345 (1989).

[14] Roth, R. S., Rawn, C. J., Ritter, J. J., and Burton, B. P., J. Amer. Ceram. Soc. **72**, 1545 (1989).

[15] Siegrist, T., Zahurak, S. M., Murphy, D. W., and Roth, R. S., Nature **334**, 231 (1988).

[16] Roth, R. S., Rawn, C. J., Whitler, J. D., Chiang, C. K., and Wong-Ng, W. K., J. Amer. Ceram. Soc. **72**, 395 (1989).

[17] Siegrist, T., Schneemeyer, L. F., Sunshine, S. A., Waszczak, J. V., and Roth, R. S., Mat. Res. Bull. **23**, 1429, (1988).

[18] Roth, R. S., Rawn, C. J., and Bendersky, L. A., J. Mater. Res. **5**, 46 (1990).

[19] Roth, R. S., Rawn, C. J., Burton, B. P., and Beech, F. (to be published).

[20] Roth, R. S. and Rawn, C. J. (to be published).

[21] Kakhan, B. G., Lazarev, V. B., and Shaplygin, I. S., Zh. Neorg. Khim **24**, 1663 (1979) Russ. J. Inorg. Chem. (Engl. Transl.) **24**, 922 (1979).

[22] Phase Diagrams for Ceramists, Vol. 6, Roth, R. S., Dennis, J. R., and McMurdie, H. F., Eds., Amer. Ceram. Soc., Westerville, OH (1987).

[23] Bovin, J. C., Thomas, D., and Tridot, G., Compt. Rend. **226C**, 1105 (1973).

[24] Teske, C. L. and Müller-Bushbaum, H., Z. Anorg. Allg. Chem. **379**, 234 (1970).

[25] Teske, C. L. and Müller-Bushbaum, H., Z. Anorg. Allg. Chem. **371**, 325 (1969).

[26] Wong-Ng, W.K., McMurdie, H. F., Paretzkin, B., Hubbard, C. R., and Dragoo, A. L., Powd. Diff. **3**, 117 (1988).

[27] Guillermo, R., Conflant, P., Bovin, J. C., and Thomas, D., Rev. Chim. Min. **15**, 153 (1978).

[28] Huang, N. M., and Roth, R. S. (to be published, J. Amer. Ceram. Soc.).

[29] Sillen, L. G. and Aurivillius, B., Z. Krist. **101**, 483 (1943).

[30] Levin, E. M. and Roth, R. S., J. Res. Natl. Bur. Stand. (U.S.) **68**, 197 (1964).

[31] Michel, C., Hervieu, M., Borel, M. M., Grandin, A., Deslandes, F., Provost, T., and Raveau, B., Z. Phys. B **68**, 421 (1987).

[32] Torardi, C. C., Subramanian, M. A., Calabrese, J. C., Gopalakrishnan, J., McCarron, E. M., Morriessey, K. J., Askew, T. R., Flippen, R. B., Chowdhry, V., and Sleight, A. W., Phys. Rev. B **38**, 225 (1988).

[33] Torrance, J. B., Tokura, Y., LaPlaca, S. J., Huang, T. C., Savoy, R. J., and Nazzal, A. I., Solid State Commun. **66**, 703 (1988).

[34] Onoda, M. and Sato, M., Solid State Commun. **67**, 799 (1988).

[35] Roth, R. S. and Rawn, C. J. (to be published).

[36] Saggio, J. A., Sugata, K., Hahn, J., Hwu, S. J., Poeppelmeir, K. R., and Mason, T. O., J. Amer. Ceram. Soc. Commun. **72**, 849 (1989).

[37] Akimitsu, J., Yamazaki, A., Sawa, H., and Fujiki, H., Jap. J. Appl. Phys. **26**, L208 (1987).

[38] Chakoumakos, B. C., Budai, J. D., Sales, B. C., and Sonder, E., In High-Temperature Superconductors: Relationships Between Properties, Structure and Solid-State Chemistry, edited by Torrance, J. B., Kitazawa, K., Tarascon, J. M., Jorgensen, J. R., and Thompson, M., Materials Research Society Symposium Proceedings Vol. 156 (Materials Research Society, Pittsburgh, PA, 1989) pp. 329–335.

[39] Casais, M. T., Cascales, C., Castro, A., de Pedro, M., Rasines, I., Domarco, G., Maza, J., Miguelez, F., Ponte, J., Torron, C., Veira, J. A., Vidal, F., and Campa, J. A., Proc. of E.-MRS Fall Meeting, Nov 8–10, 1988, Strasbourg, France. Symp. A: High Temperature Superconductors Preparation and Applications, paper A IV-38.

[40] Fuertes, A., Miravitlles, C., Gonzalez-Calbet, J., Vallet-Regi, M., Obradors, X., and Rodriguez-Carvajal, J., Physica C **157**, 525 (1989).

[41] Tarascon, J. M., LePage, Y., Barboux, P., Bagley, B. G., Greene, L. H., McKinnon, W. R., Hull, G. W., Giroud, M., and Hwang, D. M., Phys. Rev B **37**, 9382 (1988).

[42] Ikeda, Y., Ito, H., Shimomura, S., Oue, Y., Inaba, K., Hiroi, Z., and Takano, M., Physica C **159**, 93 (1989).

Volume 95, Number 3, May–June 1990
Journal of Research of the National Institute of Standards and Technology

[J. Res. Natl. Inst. Stand. Technol. 95, 337 (1990)]

Scattered Light and Other Corrections in Absorption Coefficient Measurements in the Vacuum Ultraviolet: A Systems Approach

Volume 95 Number 3 May–June 1990

R. Klein, W. Braun, and A. Fahr

National Institute of Standards
and Technology,
Gaithersburg, MD 20899

A. Mele

University of Rome,
Ple. A. Moro 5,
00185 Rome, Italy

and

H. Okabe

Howard University,
Washington DC 20059

A systems approach in which computer automation is applied to a vacuum ultraviolet spectrometer and auxiliary components is described. The errors associated with the measurement of gaseous absorption coefficients in the vacuum ultraviolet are considered. The presence of scattered light introduces large errors particularly at those wavelengths where the source used is characterized by low intensity. In the case of a D_2 light source this occurs in the region 120 to 130 nm. Simple considerations explain the variation of the absorption coefficient determinations in the presence of scattered light and lead to an appropriate treatment of the data to eliminate the error. Experimental results are presented illustrating the efficiency and precision obtainable with the present approach.

Key words: absorption coefficient; computer automation; error analysis; instrument; vacuum.

Accepted: March 2, 1990

1. Introduction

Accurate absorption coefficients in the vacuum ultra violet region for a variety of gases are required in many applications such as in the assessment of the photochemistry of man-made halocarbons in the stratosphere [1] and chemical vapor deposition of organometallic compounds [2,3]. The absorption coefficient at a wavelength λ is expressed by the well known relationship

$$\epsilon_\lambda = -(1/pl)\ln(I_\lambda/I_{0\lambda}) \qquad (1)$$

for gases that conform to Beer's law. It is obvious that the quality of the measurement of the absorption coefficient depends on the precision and accuracy of p, l, I, and I_0, the pressure of the gas, length of the absorbing path, and the intensities of the light signals with and without the absorbing gas, respectively. Reference has been made to error analysis in absorption coefficient measurements in the vuv region by Mount et al. [4]. Simon et al. [1] have also considered errors in their investigation of halogenated hydrocarbons in the uv where the values of ϵ are small and difficult to measure. Both Simon et al. [1] and Gillotay et al. [5] presented error budgets based on p, l, I/I_0, T, and impurities.

Since I_λ and $I_{0\lambda}$ in eq (1) are usually determined from separate wavelength scans, the precision in ϵ_λ can be adversely affected by lack of wavelength reproducibility, especially in those regions of the spectrum where $dI_{0\lambda}/d\lambda$ is large. Further it is unavoidable that scattered light is included in the measurement of both I and I_0, introducing errors in ϵ. The errors can be large depending upon the ratio of the scattered to the transmitted light. Errors in the absorption coefficient measurements must be considered with respect to the specific experimental configuration employed (single beam or double beam, for example). McPherson[1] provides a dual beam attachment for their monochromators. This device utilizes an oscillating mirror to direct the beam alternately through twin cells, one of which is used for establishing a reference, I_r. The I and I_0 signals are obtained using the other cell and individually ratioed with I_r to remove variations of the resultant ratios ($I_\lambda/I_{r\lambda}$ and $I_{0\lambda}/I_{r\lambda}$) in separate wavelength scans. This technique has been used and discussed by a number of workers [6,7,8]. The measurements described in the present paper are based on a single beam instrument system. High lamp stability and wavelength reproducibility offset the need for a reference beam. We will also show that the presence of a sharp-line spectrum is essential for scattered light diagnosis and correction. In the present work, error analysis for measurements of ϵ in the uv to the vuv will be considered in detail, and a method is developed for obtaining more accurate values of ϵ in regions where scattered light is not negligible. We have used a systems approach wherein computer control and analysis lead to increased accuracy and efficiency.

2. Experimental

The central part of the system is a 1-m normal incidence McPherson vacuum monochromator employing a 600 lines/mm grating blazed at 150 nm. A Hamamatsu D_2 lamp with a stabilized power supply is the source of vacuum uv radiation. A MgF_2 window on the lamp limits the low wavelength cutoff at about 115 nm. The light detector is a solar blind Hamamatsu R1220 side-on photomultiplier tube (PMT) fitted with a MgF_2 window. The photomultiplier housing [9] permits vacuum operation. Five absorption cells fitted with LiF windows and covering the range from 0.2 to 20 cm in length are arranged in a cylindrical (turret) array so that any one may be interposed in the light path. Two MgF_2 windows and two LiF windows establish the lower limit of usable light intensity down to about 119 nm. For the present apparatus the signal to noise ratio of the light signal is about 1% (shot noise limited) for integration times of about 1 s [10]. The monochromator wavelength drive is controlled by a stepping motor with 800 steps per revolution. A gear train is employed such that 16 steps are equivalent to 0.1 nm wavelength change. Gas pressure in the cells is monitored with a diaphragm gauge calibrated by an oil manometer. A block diagram of the apparatus is given in figure 1.

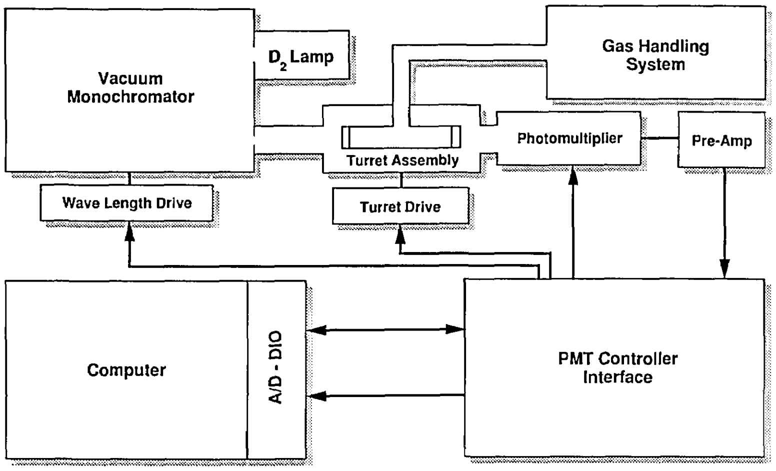

Figure 1. Schematic diagram of the vacuum ultra-violet absorption coefficient acquisition system.

---

[1] Certain commercial equipment, instruments, or materials are identified in this paper to specify adequately the experimental procedure. Such identification does not imply recommendation or endorsement by the National Institute of Standards and Technology, nor does it imply that the materials or equipment identified are necessarily the best available for the purpose.

The current from the PMT developed by the light signal is processed by a current to voltage pre-amp (with output impedance of 50 Ω) at the PMT. The pre-amp output is connected to a PMT-controller interface module. The PMT-controller interface consists in part of a follower-amp and filter-amp where the signal is amplified by 10 and processed by a programmable voltage amplifier (with binary gain from 2^0–2^7). The resulting voltage signal is received by an A/D-DIO (analogue to digital—digital input output) interface board within an IBM compatible PC. The PMT-controller interface contains shaping and latching circuits. These process the digital logic signals (from the A/D-DIO board) used to control the programable amplifier and the stepping motors. The proper functioning of all components can be assessed through a computer test program.

Initially all measurements were made in a single scan, analyzed and displayed in real time. Prior to each run all cells were intercompared (with no sample) to compensate for any imbalance in transmission. At each wavelength an I_λ and $I_{0\lambda}$ were determined sequentially by rotating the turret from a given filled cell to an empty reference cell. An absorption coefficient was determined to form the basis of a choice of a cell of optimum length ($I/I_0 \approx 0.5$). The wavelength was advanced and the cell of optimum length was then interposed for the measurement. The operation of changing the turret from a given cell to the reference cell and the requirement to measure the cell imbalance at each wavelength added considerably to the effective data acquisition time. The final procedure adopted was simplified as follows. The measurement was performed in two separate scans. The light intensity was monitored with the same cell, first under vacuum and then with the absorbing gas. The data obtained in each scan were stored and later analyzed.

3. Analysis of Measurement Errors

From the theory of propagation of errors applied to eq (1), the error in ϵ, is in part

$$d\epsilon_\lambda = (1/pl)[(\ln(I_\lambda/I_{0\lambda}))^2\{(dp/p)^2+(dl/l)^2\} + (dI_\lambda/I_\lambda)^2+(dI_{0\lambda}/I_{0\lambda})^2]^{1/2}. \qquad (2)$$

Errors in the pressure and cell length measurements can be held to less than 1%. In consideration of the measurement system used, the short and long term variations of I_0 need to be examined. A particular I_0 value is obtained from the signal from the PMT. At a given wavelength setting the signal is recorded and stored by way of 1000 A/D conversions. The values, acquired in about 1 s are averaged, and the standard deviation, σ, is calculated. Typical values at 120 nm are $I_0=0.2747\times10^{-2}\pm0.2\times10^{-4}$ and at 161.4 nm $I_0=3.3815\pm0.727\times10^{-3}$, where the errors represent $\sigma/(1000)^{1/2}$, which we denote as ($\sigma_{\text{av.}}$). This short time fluctuation is small and is entirely associated with shot noise as verified by noting that the ratio $\sigma_{\text{av.}}$ (120 nm)/$\sigma_{\text{av.}}$ (161.4 nm) is equal to the square root of the ratio of the above two light source signals. The long term stability was determined through measurements over 1-h periods. This is shown in figure 2. Similar drifts in I signals are observed. The long term downward drift of about 1% per hour in the light source constitutes a systematic error for which correction can be made. Warm-up periods of at least 20 min are necessary to maintain the level of stability shown in figure 2. As the I and I_0 scans are usually taken within minutes the drift shown in figure 2 is usually small enough not to warrant correction. There is an additional error due to scattered light, much larger percentage-wise in I than in I_0. This will be discussed in some detail. Another possible source of error is that of the wavelength setting. Even a fraction of an angstrom difference in settings in subsequent determinations involving I and I_0 leads to errors, particularly in those regions where $dI_0/d\lambda$ is large. Because the wavelength drive is controlled by a stepping motor with one pulse equivalent to 0.00625 nm, very precise settings can be achieved, and manual re-settings are eliminated. Since a computer controlled stepping motor is used to advance and rewind the grating drive any irreproducibility in successive wavelength scans is likely to be due to backlash in the connecting gear train. Most of the backlash can be corrected between successive scans by rewinding to below the starting wavelength and then advancing to the starting position. Figure 3 shows two subsequent scans of the lamp spectrum between 121 and 122 nm where the Lyman-α line is the spectral feature. The two curves in this figure are virtually superimposable. It is noted that shifts of even less than one tenth of the spectral line width produces a significant detrimental effect on an absorption coefficient measurement.

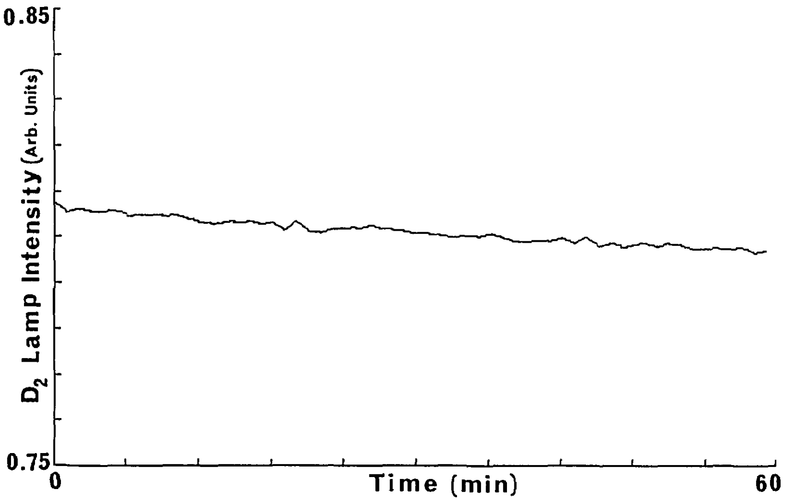

Figure 2. Deuterium lamp stability over a 1-h period.

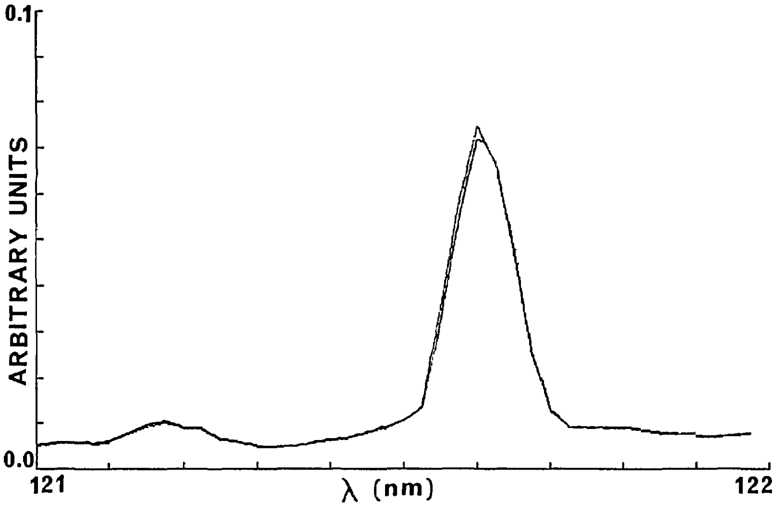

Figure 3. Separate scans of the deuterium lamp demonstrating wavelength reproducibility.

Wavelength setting and scattered light errors aside, the percentage error in ϵ is

$$d\epsilon_\lambda/\epsilon=[(dp/p)^2+(dl/l)^2+(\ln(I_\lambda/I_{0\lambda}))^{-2}\{(dI_\lambda/I_\lambda)^2+(dI_{0\lambda}/I_{0\lambda})^2\}]^{1/2}. \quad (3)$$

As an example, if the percentage errors in p, l, I, and I_0 are taken as 1.0, 0.5, 1.0, and 1.0 with $I/I_0=0.5$, the percentage error in ϵ is about 2%. This error limit can be achieved routinely, and with extreme care a percentage error of 1% or less can be obtained. Figure 4 shows that in two repeat determinations of the spectrum of oxygen between 190 and 195 nm excellent agreement is observed. This agreement is remarkable in view of the fact that there is only about 1% absorption and hence the stability of the light source must be about 0.1% over the data acquisition time. On the other hand, a comparison of two absorption coefficient determinations using acetone, one with the 0.64-cm cell and the other with a 2.0-cm cell showed a 2% discrepancy. If the 2.0-cm cell were chosen as the standard, the nominal 0.64-cm cell would in fact be 0.653 cm. This is an indication of the sensitivity of the measurements. Finally as far as errors are concerned, it can be inferred from eq (3) that the absorption coefficient measurements are subject to relatively large percentage errors when the absorption, $(I_0-I)/I_0$, is close to zero or one.

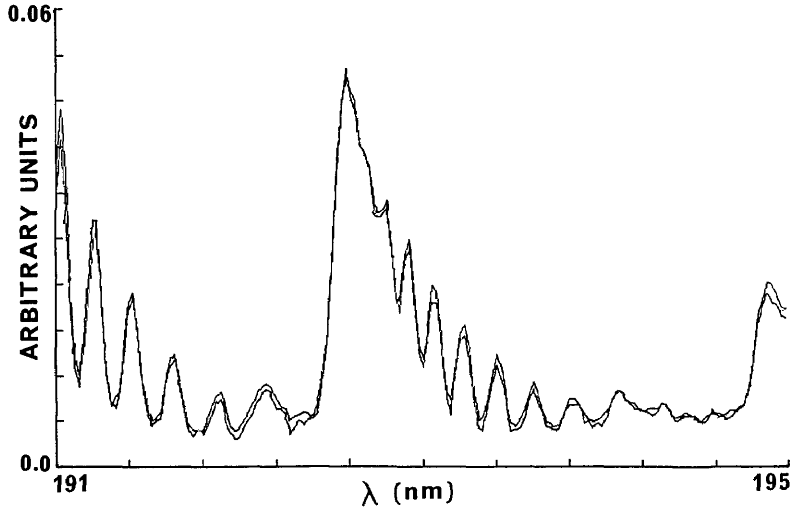

Figure 4. Scans of Schumann-Runge absorption coefficients of oxygen at 79 and 165 Torr using a 20-cm cell demonstrating reproducibility.

4. Method of Correction for Scattered Light

Because of scattered light the efficiency of a grating in isolating a specific wavelength interval is not 100%. For gratings that have deteriorated through long use the efficiency may be considerably less. This presents no difficulty in absorption coefficient measurements where the light intensity is so high that the scattered light is negligible in comparison. Problems are encountered, i.e., obtaining erroneous absorption coefficient values, when the scattered light cannot be ignored. This is the case in the 120–130 nm region of the deuterium lamp spectrum. The presence of scattered light can be convincingly demonstrated through measurements of the transmitted light through a cell filled with an absorbent sufficient to effectively eliminate light at a prescribed wavelength. Scattered light was demonstrated through the use of a 20-cm cell filled with various compounds, acetylene for example, which show high absorption coefficients at wavelengths up to 200 nm. The detector signals are shown in figure 5 for a particular grating. The signals display a non-zero intensity and very little variation over a broad spectral range. Gases absorbing less strongly at longer wavelengths show, as expected, a higher value for the light background.

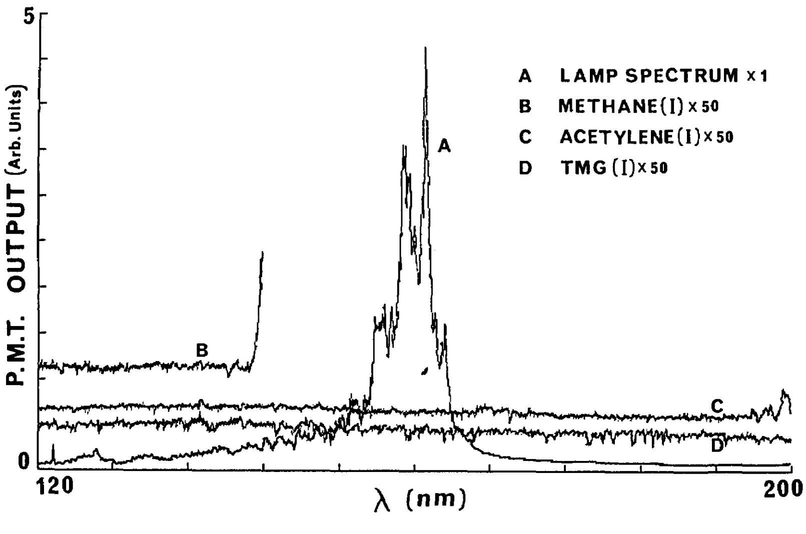

Figure 5. Scattered light from deuterium lamp remaining after absorption by methane, acetylene and trimethyl gallium.

The absorption coefficient of acetone between 120 and 130 nm without correction for scattered light is shown in figure 6. It is also noted in figure 6 that the absorption coefficient-wavelength curve has characteristics similar to the lamp spectrum in this wavelength region (but not elsewhere). The basis for this effect, the presence of scattered light which is not an insignificant part of the signal, is examined and an appropriate corrective procedure formulated. That the presence of scattered light can lead to an absorption coefficient spectrum which has superimposed on it certain features of the spectrum of the source lamp is easily shown. If A is the scattered light intensity, then the measured absorption coefficient will be of the form

$$\epsilon=-(1/pl)\ln[(I+A)/(I_0+A)] \qquad (4)$$

where $\epsilon_0=-(1/pl)\ln(I/I_0)$. It will be assumed that A is negligibly small with respect to I_0. Then $-(1/pl)\ln[(I/I_0)(1+A/I)]$ can be approximated by

$$\epsilon=\epsilon_0-A/(plI). \qquad (5)$$

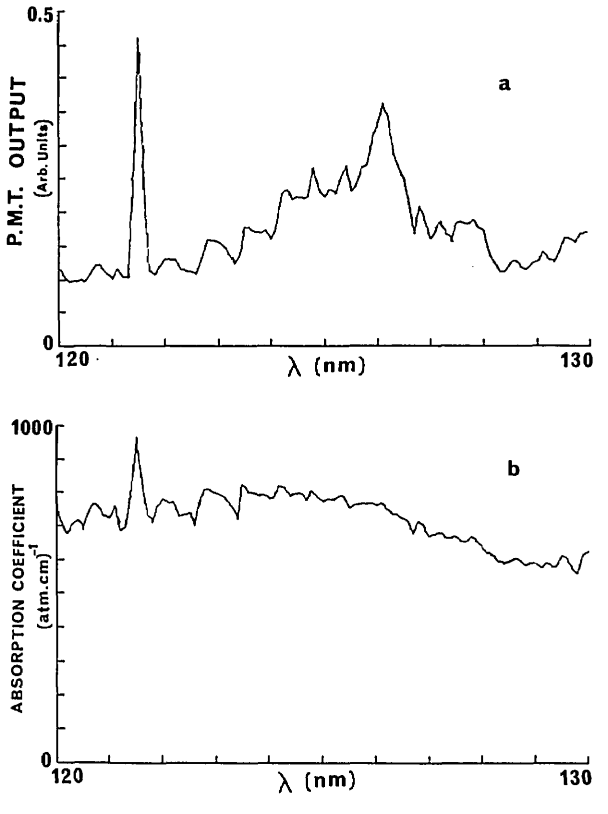

Figure 6. Absorption coefficients of acetone between 120 and 130 nm without scattered light correction showing features of the deuterium lamp spectrum.

I is related to the lamp spectrum so that its inverse, subtracted from e_0, gives an apparent coefficient that has the appearance of an absorption spectrum upon which the lamp spectrum is superimposed. The effect of the scattered light leads to an absorption coefficient that is less than the true value ϵ_0.

Obviously the correction for the scattered light requires subtraction from the *measured* I the quantity A. Aside from some indication of a minimum of this subtraction, as obtained from figure 5, a criterion must be found to establish the precise value of A to be subtracted. The spectral distribution of the scattered light is not known although it is likely to be concentrated in the 160 to 170 nm spectral region, since this is where the D_2 lamp radiation is most intense. The scattered light is of course attenuated by the presence of the absorbing gas in the cell. The scattered light correction for ethane at 6.59 Torr was found to be 25% lower than that at 0.61 Torr, for example. All the factors for calculating the amount of scattered light ultimately detected by the PMT are not available. Fortunately, the presence of the sharp Lyman-α peak at 121.6 nm in the deuterium lamp spectrum presents an appropriate approach to the solution of the problem. This is illustrated with the following model. It is assumed that over the wavelength region where scattered light may not be neglected, the true absorption coefficient spectrum is taken as constant. The light source spectrum is also assumed constant except for a single triangular spike (approximating the Lyman-α line). A value of 10 is assigned to I_0, 1.0 to I, and 0.3 to A, the scattered light, and 1.0 to the product pl (fig. 7). If I' refers to the directly observed value of the intensity after

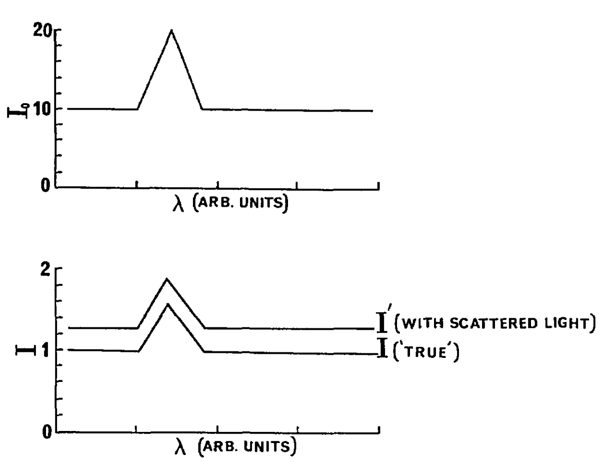

Figure 7. Model for I and I_0 with simulated Lyman-α line with and without scattered light.

absorption then I is $I'-A$. A corrective term B applied to I' will give $\epsilon=\epsilon_0-C/(plI)$ where $C=A-B$ will be positive, zero, or negative depending on the choice of B. Figure 8 illustrates each of these cases. The criterion for the correct value of B is the complete elimination of the spike. The validity of this model is shown in figure 9 where the absorption spectrum of ethane was established over the 121–122 nm region. An appropriate value of B was found, and hence an accurate value of ϵ_0 could be established.

It can be seen from figure 9 that if no scattered light correction is made there is about 15% error at the Lyman-α peak and more than 100% elsewhere in the 121–120 range. This is in accord with the expression derived from eq (3), namely $d\epsilon/\epsilon=(A/I)/\ln(I/I_0)$, and with about 5% and 50% scattered light on and off the Lyman-α peak respectively [6]. We have also found that an estimate for the correction obtained from the residual light through a high pressure absorbing gas is not appropriate and is generally about half that derived by the procedure shown in figure 9.

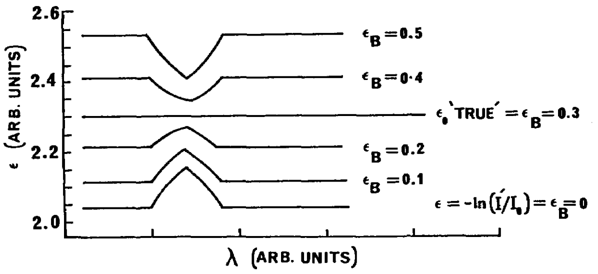

Figure 8. Model, based on figure 7, of the effect of the scattered light correction on the calculated absorption coefficient.

5. Summary

An automated control and data acquisition system for the measurement of absorption coefficients in the vuv region of the spectrum is described. Further, an error analysis for these measurements has been made. It shows that besides the obvious contributions of errors in the pressure and cell length determinations, scattered light contributes to the error budget especially in regions of low light source intensities. Corrections for the latter can be made if a sharp line in the source, such as Lyman-α in the D_2 lamp output, is present. System automation permits the achievement of precise wavelength reproducibility and fast data acquisition, processing and recording. The system approach described here for obtaining absorption coefficients in the vuv is shown to provide an improvement not only in the accuracy and precision but also in the efficiency with which these measurements can be made.

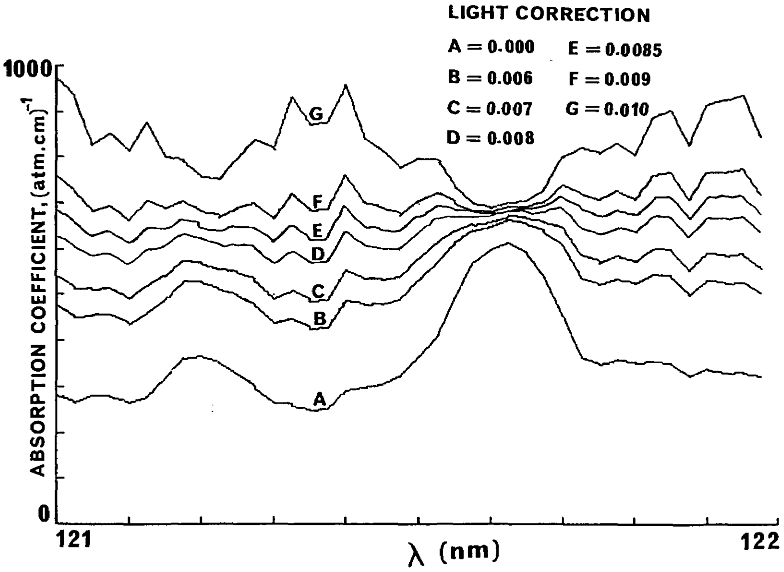

Figure 9. Effect of the scattered light correction on the absorption coefficient of ethane between 121 and 122 nm. Pressure ethane, 2.26 Torr; cell, 0.64 cm.

6. Acknowledgment

This work was supported by the Army Research Office under Grant No. MIPR 119-89.

About the authors: Ralph Klein, Walter Braun, and Askar Fahr are with the Chemical Kinetics Division, NIST. Aldo Mele is Professor of Chemistry at the University of Rome, Italy. He has had past associations with NBS/NIST. Most recently he was a visiting scientist with the Chemical Kinetics Division from June to December, 1989. His permanent address is Department of Chemistry, University of Rome, Ple. A. Moro 5, 00185, Rome, Italy. Hideo Okabe, formerly from NBS/NIST, is Research Professor at the Department of Chemistry and Materials Science, Reseach Center of Excellence, Howard University. He is also a guest scientist in the Chemical Kinetics Division, NIST. Dr. Okabe's address at Howard is Department of Chemistry, Howard University, Washington DC 20059.

7. References

[1] Simon, P. C., Gillotay, D., Vanlaethem-Meuree, N., and Wisemberg, J., J. Atm. Chem. **7**, 107 (1988).

[2] Urisu, T. and Kyuragi, H., J. Vac. Sci. Technol. **B5**, 1436 (1987).

[3] Moss, S. J. and Ledwith, A., The Chemistry of the Semiconductor Industry, Blackie (Chapman and Hall), NY (1987) p. 98.

[4] Mount, G. H., Warden, E. S., and Moos, H. W., Astrophys. J. **214**, L47 (1977).

[5] Gillotay, D. and Simon, P. C., Planet. Space Sci. **37**, 105 (1989).

[6] Gillotay, D., Jenouvrier, A., Coquart, B., Merienne, M. F., and Simon, P. C., Planet. Space Sci. **37**, 1127 (1989).

[7] Lombos, B. A., Sauvageau, P., and Sandorfy, C., J. Molec. Spectrosc. **24**, 253 (1967).

[8] Myer, J. A. and Samson, J. A. R., J. Chem. Phys. **52**, 266 (1970).

[9] Braun, W., Klein, R., Fahr, A., and Mele, A., Photomultiplier Housing for Vacuum Operation of Side-on 1P28-Type Tubes, in press.

[10] The absolute amount of light and the percent scattered light depend on the condition of the instrument. For example, the D_2 lamp deteriorates slowly, losing half its intensity over about 100 h. Window contamination also seriously affects transmission. Depending on the gases the cell is exposed to and total contact time, the cell windows must be replaced at various intervals.

Volume 95, Number 3, May–June 1990
Journal of Research of the National Institute of Standards and Technology

Conference Reports

HYPERTEXT STANDARDIZATION WORKSHOP Gaithersburg, MD January 16–18, 1990

Report prepared by

Jean Baronas

National Computer Systems Laboratory,
National Institute of Standards and Technology,
Gaithersburg, MD 20899

1. Introduction

Hypertext systems and technology are being developed and used by numerous industrial, academic and Government organizations today. "A Hypertext is a network of information nodes connected by means of relational links. A Hypertext System is a configuration of hardware and software that presents a Hypertext to users and allows them to manage and access the information that it contains," as stated in reference [1]. The nodes in these systems may contain text, graphics, audio, and video, as well as source code or other forms of data. The nodes are meant to be viewed through an interactive browser and manipulated through a structure editor [2].

The members of the National Institute of Standards and Technology (NIST) National Computer Systems Laboratory (NCSL) Hypertext Competence Project (initiated in October 1988) held a Hypertext Standardization Workshop at NIST, on January 16–18, 1990, to provide opportunities for Hypertext system designers and users to discuss directions, timing, and requirements for Hypertext standardization. The Workshop was attended by 65 representatives from Hypertext system development and user communities. Workshop participants made progress toward generating a plan for Hypertext standards development which includes reference models, information interchange between different systems, and user requirements.

The Workshop program committee, comprised of members of the NIST Hypertext Competence Project, published a "Call for Papers" and then selected papers to be presented in the Workshop plenary sessions from responses to the "Call." The papers that were presented in the Workshop included approaches to solutions for Hypertext modelling and standards, such as "The Trellis Hypertext Reference Model" by Richard Furuta and David Stotts of the University of Maryland at College Park, MD, "The Dexter Hypertext Reference Model" by Frank Halasz of the Xerox Palo Alto Research Center, Palo Alto, CA, and Mayer Schwartz of Tektronix Laboratories, Beaverton, OR, and "A Formal Model of Hypertext" by Danny Lange of the Technical University of Denmark. A total of 14 papers were presented during plenary sessions at the Workshop which covered aspects of the following:

Workshop Paper Topic Overview

1) Descriptions of Hypertext systems using reference models,
2) Approaches to interchanging Hypertext documents and databases between heterogeneous systems, and

3) Applications of already-existing document processing standards within the Hypertext domain.

The presentations made during the Workshop plenary sessions provided the basis for interesting discussions in break-out sessions that were run in parallel and followed the plenary sessions. The participants formed the Hypertext Models Discussion Group, Data Interchange Discussion Group, and the User Requirements Discussion Group for the break-out sessions.

2. The Hypertext Models Discussion Group

The Hypertext Models Discussion Group members defined a reference model as a "description of some domain that can be used to compare existing implementations in that domain, design new implementations, map out possible areas for standardization and show their relation to one another," see reference [3]. The Group wrote a development plan for standardization, analyzed the differences and similarities of the before-mentioned Trellis, Dexter and Lange models, and organized the following taxonomy of Hypertext concepts.

Taxonomy of Hypertext Concepts

1) Entities (objects) that a Hypertext system must manipulate,
2) Properties of entities or of the entire Hypertext system,
3) Functions or operations including knowledge modification, navigation, system's tailoring, interfaces, versioning, access control, and
4) Abstractions including schema, type, class, object, data models, encapsulation, layer.

The Group began ranking the concepts by their importance to Hypertext systems, took inventory of existing systems, and constructed an implementation model which is comprised of layers that represent system characteristics that are essential to Hypertext researchers and standards developers and those that should be covered by standardization efforts that are ongoing in other disciplines.

The Hypertext Models Discussion Group also developed a reference model to map out the areas where standards are needed. It represents a ranking of the most popular concepts in Hypertext systems, i.e., how central each is to Hypertext, to focus standardizing on those concepts that have the most widespread use. To select the area for standards development, the group analyzed the intersection of Hypertext features with the most widespread use and those that would be best standardized by members of other research communities, such as the computer human interface, database, object oriented programming, and windowing domains.

3. The Hypertext Data Interchange Discussion Group

The Hypertext Data Interchange Group discussions focused on making a distinction between delivery and archival interchange concepts. The Group summarized that a delivery interchange standard could be one that is usable by a conforming Hypertext system, without translation. In the near term, such a standard would be difficult to achieve due to the different data storage and indexing approaches that exist in various commercially-available Hypertext systems, in addition to the different methods of data representation and presentation that are used.

The development of an archival interchange standard was discussed. In this approach, the user would store Hypertext in a vendor-specific format at both the source and target systems, with a translation to and from the "archival interchange" format. Changes or updates would be stored in the archival store before reaching the other platforms. The Group suggests that the development of the "archival interchange" approach could be done in the nearer term, as compared with the "delivery interchange" approach.

The Group discussed the interchange formats that were covered by Workshop contributions and noted that all adopted the concept of partitioning interchange into data objects, Hypertext anchors, and links. The contributions were written with different terminology; however, there was a fundamental conformance to the layering approaches that they represented. According to reference [4] "Most of the proposals included the Standard Generalized Markup Language (SGML) or SGML-like systems as a basis for tagging text. It was agreed that SGML was a reasonable basis for further interchange experiments between existing Hypertext systems." The Hypertext Data Interchange Group also identified other Hypertext characteristics that are fundamental to interchange and suggested that they be discussed in future standards sessions.

4. The Hypertext User Requirements Group

The Hypertext User Requirements Group overviewed Hypertext applications and identified factors that account for different Hypertext design concepts (enabling technology, document standards initiatives, market pressure, and increased academic interest). The Group discussed two different views of what it termed the Hypertext Design Space: a dimensional view and an edit or not to edit view. The dimensional view includes the user dimension (single users vs. groups, vs. multiple users that are unrelated), the information dimension (creation vs. conversion), the task dimension (specific vs. general), and the interface dimension (static vs. dynamic). The edit or not to edit view covers a framework for understanding Hypertext Design Space that partitions applications by whether or not users can edit the content of Hypertext units, and the links between them, from those that are read-only, i.e., the user can only browse (read) the units and the links cannot be changed.

The Group concluded that users and manufacturers would benefit from the development of shared specifications for Hypertext functions that are carried out by a Hypertext user interface on entities that are managed by a Hypertext storage layer. Such specifications would be useful if they had the following characteristics:

Hypertext User Specifications Characteristics

1) Fit in proposed Hypertext Reference Model,
2) Maintain independence from presentation specifications, and
3) Define operational semantics of the system.

The Group maintained that if these specification goals are satisfied, standards for Hypertext functions can be organized into subsets that fit into different parts of the Hypertext Design Space. An initial list of functions that can be used to define the interoperability of Hypertext systems within a given Hypertext Design Space includes those that effect a Hypertext unit, link, or composite unit follows:

Initial List of User Functions

1) Create,
2) Edit,
3) Delete,
4) Publish,
5) Indicate current unit,
6) Move to another unit,
7) Indicate presence of an expandable structure.

Another phase of the Group discussions included the importance of developing definitions and rules for various user functions. The User Requirements Group concluded their work by listing research agenda that are needed to help define semantics for Hypertext functions and new measures for Hypertext that describe characteristics which are relevant to user performance. These agenda include the following.

Hypertext Research Agenda

1) Evaluating hypertextability of a document or a document collection,
2) Validating Hypertext conversion which includes methods and tools for measuring the amount of Hypertext that has been successfully converted,
3) Measuring Hypertext readability, and
4) Analyzing the intellectual property issues of Hypertext.

5. Recommended Directions for Hypertext Standards

In the final plenary session, the Workshop participants discussed the possibilities of establishing a more formal Hypertext study group within accredited standards bodies. Major conclusions made in the final plenary discussions can be summarized as the following.

Workshop Conclusions

1) The discussion groups should continue efforts,
2) NIST should sponsor a follow-up workshop,
3) Decision should be made as to the development of a standards committee with official status in American National Standards Institute (ANSI).

6. Workshop Proceedings

More detailed reports from the discussion groups, in addition to the technical papers that were presented during the Workshop plenary sessions are published in NIST Special Publication

Number 500-178, Proceedings of the Hypertext Standardization Workshop; January 16-18, 1990; National Institute of Standards and Technology, edited by Judi Moline et al. March 1990, which is available from the United States Government Printing Office, Superintendent of Documents, Washington, DC 20042.

7. NIST Hypertext Systems and Applications Workshop, October 1989

Preliminary to the Workshop, the Competence Project sponsored a Hypertext Systems and Applications Workshop at NIST on October 23, 1989, which consisted of overviews of Hypertext systems and applications, in addition to discussion of the need for a Hypertext reference model and the pursuit of Hypertext standardization. Hypertext system vendors provided system demonstrations for the October 1989 Workshop participants. The Hypertext Standardization Workshop was held in response to the request for the beginning of discussions of Hypertext standardization that prevailed in the October Workshop. Both events shared NIST Hypertext Competence Project research with NIST staff members and built close relationships between industry and Competence Project personnel. For further information, please contact Jean Baronas, NIST, Technology Building, Room B263, Gaithersburg, MD 20899, telephone: 301-975-3338, electronic mail: baronas@asl.ncsl.nist.gov.

The author, Jean Baronas, is a technical staff member in the NCSL and is also a member of the NIST Hypertext Competence Project. Other project members are Len Gallagher (Project Leader), Judi Moline, and Dan Benini of the NCSL.

8. References

[1] Moline, Judi, ed. Proceedings of the Hypertext Standardization Workshop, January 16-18, 1990, Natl. Inst. Stand. Technol. Spec. Publ. 500-178 (1990) p. 10.

[2] Smith, John and Weiss, Stephen, Hypertext, Communications of the Association for Computing Machinery (CACM), July, 1988, 31/7:816.

[3] Moline, Judi, ed. Proceedings of the Hypertext Standardization Workshop, January 16-18, 1990, Natl. Inst. Stand. Technol. Spec. Publ. 500-178 (1990) p. 9.

[4] Ibid. pp. 21-22.

Volume 95, Number 3, May-June 1990
Journal of Research of the National Institute of Standards and Technology

Conference Reports

SIXTH INTERNATIONAL CONFERENCE ON HIGH TEMPERATURES—CHEMISTRY OF INORGANIC MATERIALS

Gaithersburg, MD

April 3–7, 1989

Report prepared by

J. W. Hastie

Metallurgy Division,
Materials Science and Engineering Laboratory,
National Institute of Standards and Technology,
Gaithersburg, MD 20899

This conference was the sixth of a series, sponsored by the International Union of Pure and Applied Chemistry (IUPAC) Commission II.3 on High Temperature and Solid State Chemistry, and which is held about every 3 years.

The NIST meeting represented only the second occasion that this conference series had been held in the U.S.A. Attendance, exceeding 170, included participants from 19 countries, and 130 papers were presented.

1. About the Conference

The conference program emphasized the basic chemical science and measurement issues underlying the characterization, processing, and performance of materials at high temperatures. Each of the major classes of materials was considered, including high performance alloys, ceramics, composites, and specialized forms such as films, coatings, clusters, powders, slags, fluxes, etc. in addition, individual substances, namely the elements and their compounds, were discussed in detail. Seven plenary lectures and 68 invited talks were given as well as 61 poster presentations and computer-based demonstrations. Also, Prof. Leo Brewer, one of the foremost pioneers of the field, gave an overview of the conference proceedings together with his perspective on the "Role of Chemistry in High-Temperature Materials Science and Technology." During the conference sessions, many of the hot issues of the day were also discussed, including cold fusion, high-temperature superconductors, low pressure production of diamond films, etc.

Participation by the leading international researchers in the field was particularly strong in the materials-related areas of measurement techniques, thermochemistry and models, processing and synthesis, and performance under extreme environments. Of special interest were the topics on databases and phase equilibria models, processing—mainly from the vapor phase, and high power laser-materials interactions.

The conferees were welcomed by Dr. Lyle Schwartz, Director of the Institute for Materials Science and Engineering (IMSE) (now Materials Science and Engineering Laboratory), who also gave an overview of pertinent NIST and IMSE research activities. Prof. Jean Drowart of the Free University of Brussels, Belgium, addressed the meeting on behalf of IUPAC and gave a fascinating account of "7000 Years of High Temperature Materials Chemistry."

A few representative technical highlights from each of the main conference sessions are given in the following discussion.

2. Advances in Measurement Techniques

Three areas were given special emphasis. These were spectroscopic probes, diffractometry, and physicochemical methods. The types of spectroscopic probes discussed included Raman and related laser spectroscopic methods for *in situ* molecular-level or phase-specific monitoring of hot surfaces. Examples were considered in the areas of corrosion, oxide superconductor processing, and in Raman imaging of ceramic crack suppression due to phase transformation toughening (see fig. 1). An interesting novel application of *in situ* optical emission spectroscopic analysis of molten steel, using a laser-induced plasma-forming technique, was also discussed (see fig. 2). These effectively nonintrusive methods also have potential as process monitoring probes for intelligent processing in addition to their utility in experimental systems.

In the area of diffractometry, *in situ* analysis of material structures at high temperatures, using x-ray and neutron sources, was described. Atom probe chemical analysis on alloy surfaces using field-ion microscopy was also discussed.

Physicochemical techniques have traditionally been key to the characterization of materials at high temperatures and significant recent advances have occurred in this area. Methods have been developed which effectively eliminate containment problems. For instance, with liquid metals, transient microsecond time scale techniques have been applied to accurate measurements of melting points and heat capacities at very high temperatures. For steady state measurements, electromagnetic levitation may be used as, for instance, with emissivity and optical constant measurements. Another transient technique that was discussed by a number of researchers throughout the conference is the pulsed laser-heating approach to the production of vapor species for mass and optical spectroscopic characterization.

3. Thermochemistry and Models

This session was particularly well represented by the leaders in the field. Progress on development of thermodynamic databases was reviewed by researchers from the United States, U.S.S.R., Canada, France, Sweden and the United Kingdom. While the databases developed thus far are incomplete they are still sufficiently extensive to allow their use in thermochemical and phase equilibria models for many high-temperature alloy, ceramic, composite, slag, glass, and other systems. A key element in these models is the description of nonideal mixing, present in many practical systems. Among the various models considered, those accounting for ordering or formation of liquid associates appear particularly promising (see fig. 3). In one of the presentations, direct experimental (neutron diffraction) evidence was presented for ordering in liquid alloys (see fig. 4). Many papers were presented dealing with experimental determinations of thermochemical data and applications of the data to materials process development.

4. Processing and Synthesis

The chemical basis for high temperature processing and synthesis of materials is a rapidly growing area of research and representative work in the field was discussed. An area of significant promise for the design of new or improved materials is that of molecular/atomic clusters. These species, with properties intermediate between molecular and bulk material, are key reaction intermediates to most deposition and condensation processes. They also serve as model structures for surfaces owing to their intrinsic high ratio of surface to bulk atoms. Their unique reactivity as a function of cluster size was indicated by several speakers (see fig. 5).

The session on CVD and other vapor phase-based processes was particularly exciting. Thermochemical, kinetic, transport models, whereby the processing of films (diamond, semiconductor, ceramic, alloy, etc.) could be optimized, were described (see fig. 6).

5. Performance Under Extreme Environments

The important related areas of hot and high temperature corrosion were discussed for both alloy and ceramic materials. In particular, the key role of chemical reaction and solubility was demonstrated (see fig. 7).

Another area where materials are subject to extreme conditions is that of laser-materials interactions. There are many areas of science and technology that require an improved understanding of this interaction, including design of laser resistant materials, laser deposition of films, laser etching for electronic devices, laser stimulated chemical processing, laser welding, and laser heating for containerless studies of thermochemistry at ultra-high temperatures. This latter case has special significance to providing thermodynamic data for nuclear reactor excursions (see fig. 8) and for materials data for advanced aerospace applications.

6. Additional Information

A three volume proceedings (1350 pages) is being published by Humana Press, Clifton, NJ. Many of the conference presentations will appear in these volumes. Also included are a few articles, not presented at the conference, in order to provide a more complete coverage of certain topics. This will be the first generally available publication for this subject area and the proceedings should be of considerable interest to researchers, students, and others interested in the scientifically challenging, and technologically indispensable, interplay between materials and high temperatures.

The next meeting in the series is scheduled to be held in 1991 in Orleans, France and will be chaired by J. P. Coutures.

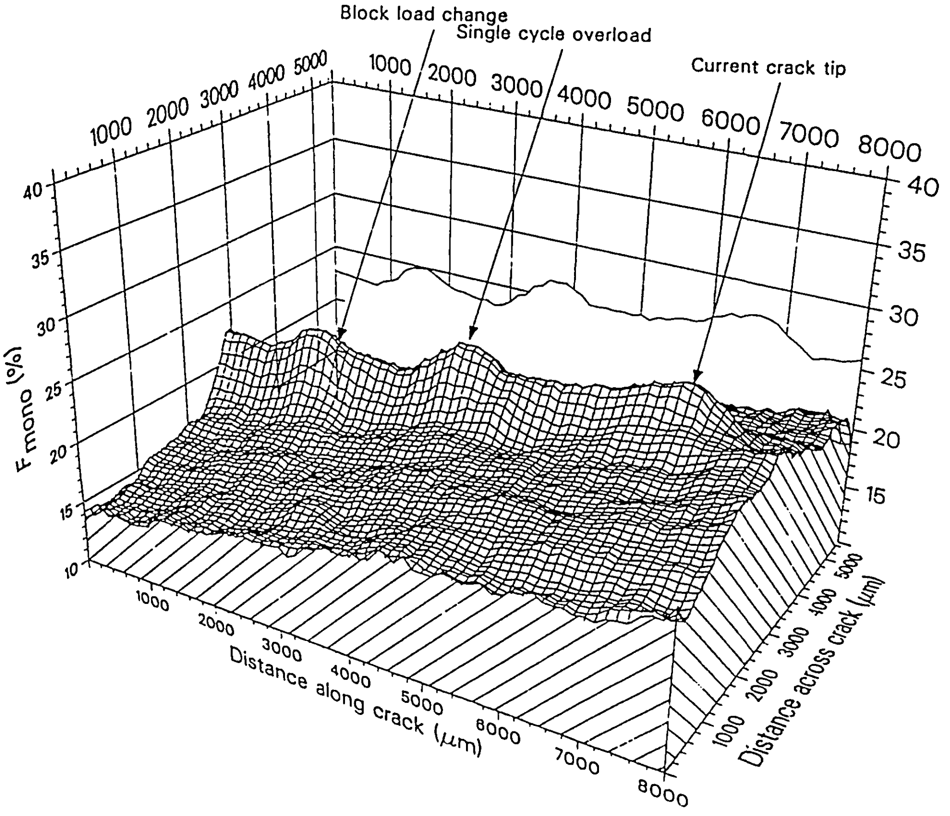

Figure 1. A map of the monoclinic phase fraction of a zirconia specimen subjected to an applied stress and crack growth. The stress history of the material is revealed in the extent and degree of transformation of the transformed zone. Large stresses induce a larger transformed zone around the crack tip that remains after the crack tip moves forward. (Taken from Rosenblatt et al., paper 4.)

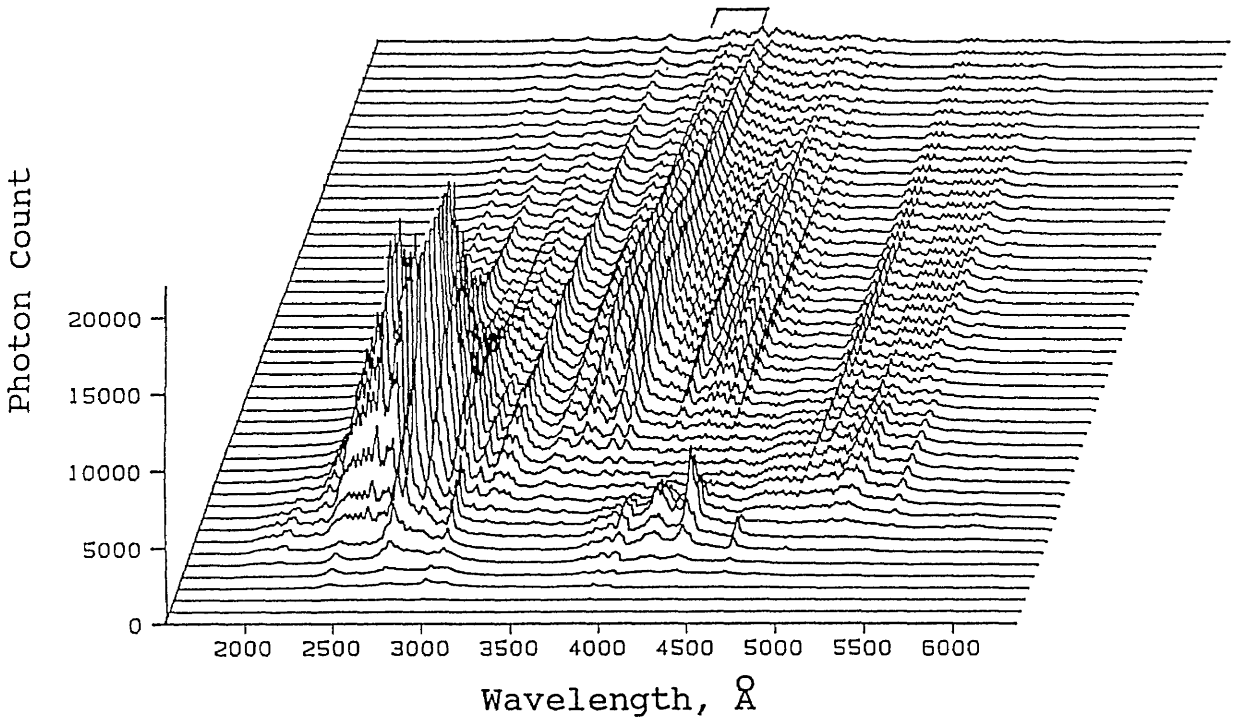

Figure 2. Time-resolved emission spectra from a laser produced plasma plume generated off a specialty steel alloy target. Each trace represents a 20 ns exposure spectrum covering the spectral range of 1850 to 6200 Å. Each successive trace is delayed by 20 ns and the 50 traces shown cover the first 1 μs of the plume. The laser energy is 3.38 J and the ambient gas is argon at 0.015 Torr at room temperature. (Taken from Kim, paper 5.)

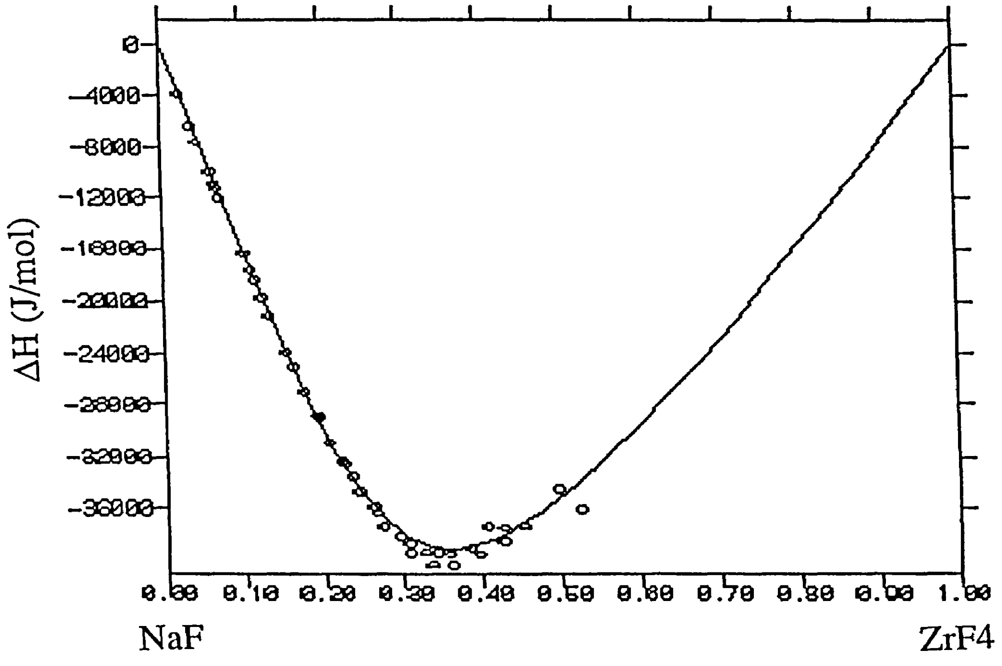

Figure 3. Enthalpy of mixing of the NaF-ZrF$_4$ system. Data points are experimental and line is calculated using an associated liquid model. (Taken from Gaune-Escard et al., paper 35.)

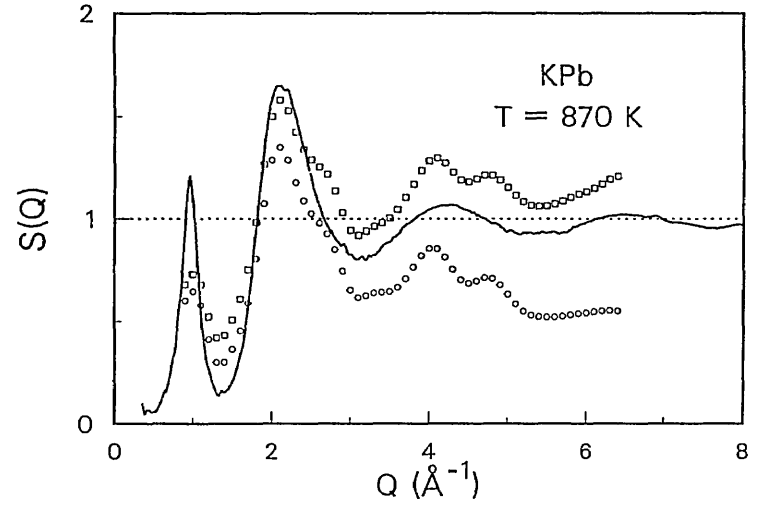

Figure 4. Structure factors, $S(Q)$, for liquid KPb. Solid line: $S(Q)$ from diffraction measurements on SEPD; Points $S_\Delta(Q) = {}_{-\Delta}\int^{\Delta} S(Q,E)$ from inelastic scattering measurements on LRMECS: (□)$\Delta = 40$ meV, (o)$\Delta = 5$ meV. (Taken from Saboungi et al., paper 27.)

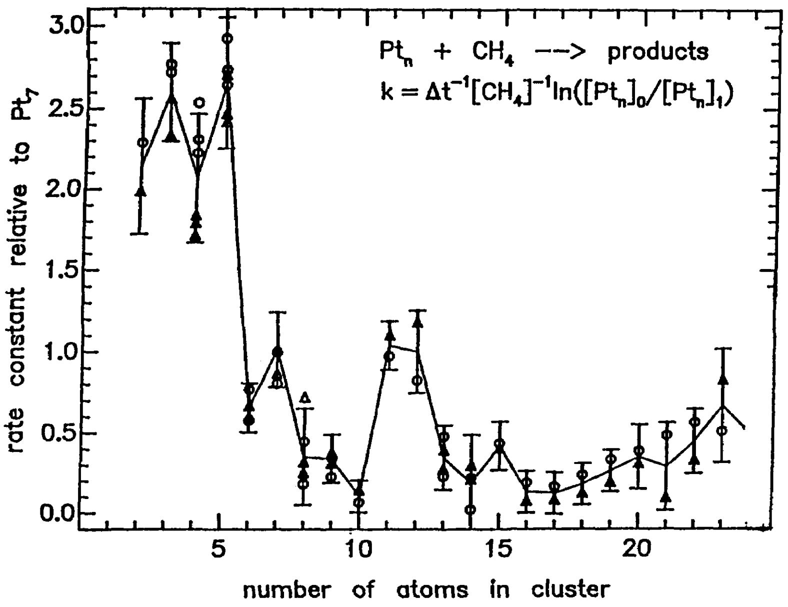

Figure 5. Reaction rate of Pt_x with CH_4, normalized to Pt_7. (Taken from Kaldor et al., paper 77.)

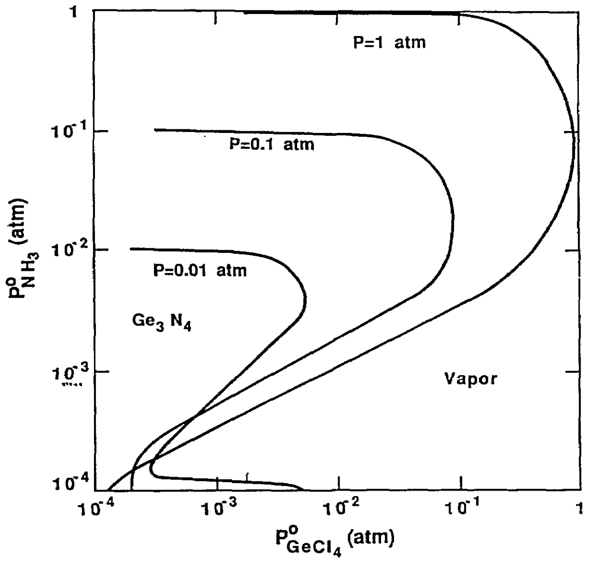

Figure 6. Phase fields for deposition of Ge_3N_4 as a function of deposition temperature and the feed ratio $P^0_{NH_3}/P^0_{GeCl_4}$ for the $GeCl_4$-NH_3-N_2 system. $P=1$ atm and $P^0_{GeCl_4}=10^{-2}$ atm. (Taken from Anderson et al., paper 105.)

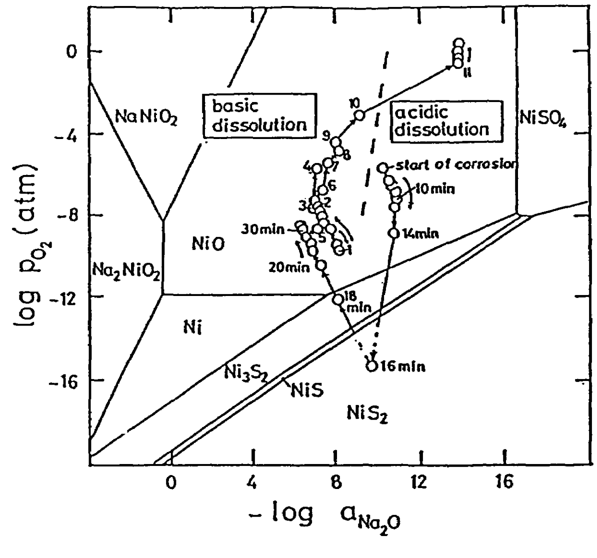

Figure 7. Trace of basicity and oxygen activity measured for preoxidized 99% Ni covered with a Na_2SO_4 film at 900 °C in 0.1% SO_2-O_2 gas atmosphere (preoxidized at 900 °C for 4 h in O_2). Numbers designate reaction time in hours except as indicated. Severe corrosion conditions. (Taken from Rapp, paper 115.)

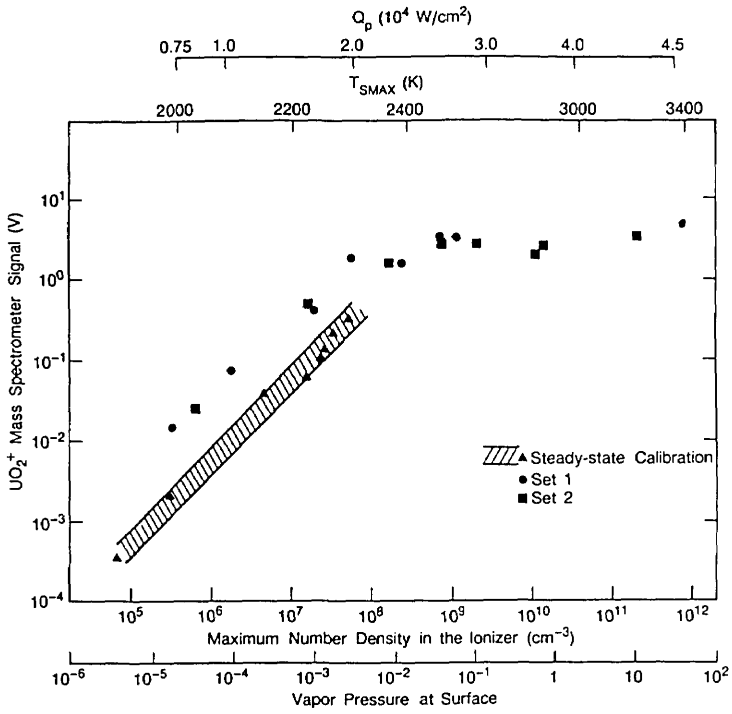

Figure 8. Maximum UO_2^+ signals from the mass spectrometer for laser pulses of varying strength. Q_p is the peak absorbed power density, and T_{smax} is the measured maximum surface temperature in the pulse. The scale designating the maximum number density in the ionizer of the mass spectrometer was calculated from measured ion intensities and the vapor pressure (Torr) is that of UO_2 at the peak surface temperature. The hatched area represents the range of results of the steady-state calibrations. (Taken from Olander, paper 123.)

7. List of Papers Presented at the Conference

ADVANCES IN MEASUREMENT TECHNIQUES

Spectroscopic Probes

1. *R. J. M. Anderson* and J. C. Hamilton—(Sandia National Lab., United States) **Nonlinear Optical Spectroscopy as a Probe of Properties and Processes at Surfaces and Interfaces**
2. *K. F. McCarty*, D. R. Boehme, D. S. Ginley, E. L. Venturini, and B. Morosin (Sandia National Labs., United States) **High-Temperature Processing of Oxide Superconductors: A Raman Scattering Study**
3. *M. D. Allendorf*—(Sandia National Labs., United States) **Temperature Measurements in Silica-Laden Flames by Spontaneous Raman Scattering**
4. *G. M. Rosenblatt* and D. K. Veirs —(Lawrence Berkeley Lab., United States) **Recent Developments using Imaging Detectors for Raman Characterization of High Temperature Materials**
5. *Y. W. Kim*—(Lehigh Univ., United States) **Laser Plasma Plume Analysis in High Temperature Condensed Phases**
6. *Y. Shiraishi* and K. Kusabiraki—(Tohoku Univ., Japan) **Infrared Spectrum of High Temperature Melts by Means of Emission Spectroscopy**
7. *I. R. Beattie*, N. Binsted, W. Levason, J. S. Ogden, M. D. Spicer, and N. A. Young—(Univ. Southhampton, United Kingdom) **EXAFS, Matrix Isolation and High Temperature Chemistry**

Diffractometry

8. *H. F. Franzen* and S.-J. Kim—(Iowa State Univ., United States) **High Temperature X-Ray Diffraction and Landau Theory Investigations of Thermal Symmetry-Breaking Transitions: The W Point of Fm3m and the Structure of NbN$_{1-x}$**
9. *R. D. Shull* and J. P. Cline—(NIST, United States) **High Temperature X-Ray Diffractometry of Ti-Al Alloy Phase Transitions**
10. *J. Faber, Jr.* and R. L. Hitterman—(Argonne National Lab., United States) **High Temperature insitu Neutron Diffraction Studies of the Defect Structure of Non-stoichiometric Oxides**
11. *P. P. Camus*—(NIST, United States) **Field-Ion Microscopy and Atom Probe Chemical Analysis**

Physico-Chemical Methods

12. *A. Cezairliyan*—(NIST, United States) **A Microsecond-Resolution Transient Technique for Thermophysical Measurements on Liquid Refractory Metals**
13. *R. H. Hauge*, S. Krishnan, G. P. Hansen, and J. L. Margrave—(Rice Univ., United States) **Emissivities and Optical Constants of Electromagnetically Levitated Liquid Metals as Functions of Temperature and Wavelength**
14. *M. Shamsuddin*[1]—(Banaras Hindu Univ., India) **Techniques for Measurement of Thermodynamic Properties of Chalcogenides**
15. *M. V. Korobov*[1], E. B. Rudnyi, O. M. Vovk, E. A. Kibicheva and L. N. Sidorov—(Moscow State Univ., U.S.S.R) **Ion Equilibria—A New Technique for Measurement of Low O$_2$ Partial Pressures**
16. *M. A. Frisch* and E. A. Giess —(IBM Yorktown Heights, United States) **Kinetics of Water Desorption from Glass Powders Studied by Knudsen Effusion Mass Spectrometry**
17. *K. A. Gingerich*, M. J. Stickney, and M. S. Chandrasekharaiah—(Texas A&M Univ., United States) **A Novel Vapor Source for the Thermodynamic Study of Alloys with a High Temperature Mass Spectrometer**
18. *D. Bostrom, B. Lindblom*, E. Rosen, and M. Sodelund—(Univ. Umea, Sweden) **The Zero Point Technique: An Improved Method to Determine Equilibrium Oxygen Partial Pressure of Slow Reacting Chemical Systems at High Temperatures**
19. *K. Zmbov*, J. W. Hastie, D. W. Bonnell, and D. L. Hildenbrand—(Boris Kidric Inst., Yugoslavia) **Mass Spectrometric Analysis of LiF and AgCl Vaporization and Temperature Dependent Electron Impact Fragmentation**

THERMOCHEMISTRY AND MODELS

Databases and Phase Equilibria Models

20. *L. V. Gurvich*—(Institute of High Temperature, U.S.S.R.) **Reference Books and Databanks on the Thermodynamic Properties of Inorganic Substances**
21. *M. W. Chase* and R. D. Levin—(NIST, United States) **Thermodynamic Properties of the Alkaline Earth Hydroxides: A JANAF Case History**
22. *I. Ansara*—(Domaine Univ., France) **Thermodynamic Modeling of Solution Phases and Phase Diagram Calculations**
23. *A. D. Pelton*, W. T. Thompson, and C. W. Bale—(Ecole Polytechnique, Canada) **Thermodynamic Databases for Multicomponent Solution-Modeling and Data Evaluations**
24. *M. H. Rand*, R. H. Davies, A. T. Dinsdale, T. G. Chart, and T. I. Berry—(Harwell Lab. Didcot, United Kingdom) **Application of MTDATA to the Modeling of Multicomponent Equilibria**
25. *B. Jonsson* and B. Sundman —(Royal Institute of Technology, Sweden) **Thermochemical Applications of THERMO-CALC**
26. *M. Seapan* and J. Y. Lo—(Oklahoma State Univ., United States) **A Simulation Model to Predict Slag Composition in a Coal Fired Boiler**
27. *M. L. Saboungi*, G. K. Johnson, and D. L. Price—(Argonne National Lab., United States) **Ordering in Some Liquid Alloys**
28. *M. Ramanathan*, S. Ness, and D. Kalmanovitch—(Univ. of North Dakota, United States) **New Techniques for Thermochemical Phase Equilibrium Predictions in Coal Ash Systems**
29. *R. G. Reddy* and H. Hu—(Univ. Nevada-Reno, United States) **Modeling of Viscosities of Alkali-, Alkaline-Earth Metal Oxide and Silicate Melts**
30. *M. W. Chase*, F. Glasser, and A. Bernstein—(NIST, United States) **PC Demonstration of Thermodynamic Databases**
31. *L. V. Gurvich*, V. S. Iorish and V. S. Youngman—(Institute of High Temperature, U.S.S.R.) **Extended and Updated Data Bank on Thermodynamic Properties of Inorganic Substances**
32. *D. W. Bonnell* and J. W. Hastie—(NIST, United States) **A Predictive Slag Phase Equilibria Model**
33. *H. M. Ondik*—(NIST, United States) **The NIST—ACerS Ceramic Phase Diagram Data Base**
34. *M. Gaune-Escard*, J. P. Bros, and G. Hatem—(Univ. de Provence, France) **Thermosalt, A Thermodynamic Data Bank for Molten Mixtures**
35. *M. Gaune-Escard* and G. Hatem—(Univ. de Provence, France) **Thermodynamic Modelling of High Temperature Melts and Phase Diagram Calculations**

Phase Equilibria Experimental and Applications

36. *P. W. Gilles* and G. F. Kessinger—(Univ. of Kansas, United States) **The High Temperature Vaporization and Thermodynamics of the Magneli Phases of the Titanium-Oxygen System**
37. *C. B. Alcock*—(Univ. Notre Dame, United States) **Strontium Oxide Activities in Oxide Ceramics**
38. *J.-C. Lin* and Y. A. Chang—(Univ. Wisconsin, United States) **Thermodynamics, Kinetics and Interface Morphology of Reactions Between Metals and III-V Compound Semiconductors**
39. *E. Kaldis*—(ETH-Zurich, Switzerland) **Thermodynamic Instabilities in High-Temperature Compounds With Intermediate Valence**
40. C. K. Mathews[1]—(Indira Gandhi Centre for Atomic Research, India) **Recent Studies on Thermochemistry and Phase Equilibria in Alkali Metal Systems**
41. *M. Iwase*, M. F. Jiang, and E. Ichise—(Kyoto Univ., Japan) **Thermochemistry of the System MO+MX$_2$+Fe$_x$O (M=Ca, Sr, Ba, and X=F, Cl)**
42. A. I. Saitzev, N. V. Korolev, and B. M. Mogutnov[1]—(I. P. Bardin Research Institute, U.S.S.R.) **Thermodynamic Properties and Phase Equilibria at High Temperatures in CaO-CaF$_2$, Al$_2$O$_3$-CaO, and CaF$_2$-Al$_2$O$_3$-CaO Systems**
43. *H. Ipser*, R. Krachler, G. Hanninger, and K. L. Komarek—(Univ. of Vienna, Austria) **Thermodynamic Properties of NiAs-Type Co$_{1\pm x}$Sb and Ni$_{1\pm x}$Sb**
44. A. I. Saitzev, M. A. Semchenko, and B. M. Mogutnov[1]—(I. P. Bardin Central Research Institute, U.S.S.R.) **Thermodynamic Properties and Phase Equilibria at High Temperatures in Fe-Cr and Fe-Mn Systems**
45. *M. Pelino*, A. Florindi, and M. Petroni—(Univ. dell'Aquila, Italy) **Study of the Decomposition Process of α-Goethite by Thermal Gravimetry "in Vacuo"**
46. *L. P. Cook*, E. R. Plante, D. W. Bonnell, and J. W. Hastie—(NIST, United States) **Reaction of Liquid Li, Al and Mg with Gaseous Cl$_2$, O$_2$ and F$_2$**
47. *R. H. Hauge*, M. Sampson, J. L. Margrave, J. Porter, and G. Reynolds—(Rice Univ., United States) **Mass Spectrometric Studies of the Vaporization Behavior of SrZrO$_3$, SrHfO$_3$, Yttria Stabilized Hafnia and Ir$_{0.4}$Al$_{0.6}$**
48. *K. Hilpert* and M. Miller - (Nuclear Research Center, Federal Republic of Germany) **Chemical Vapor Transport and Complexation in the NaI-ScI$_3$ System**
49. *K. Hilpert*, S. R. Dharwadkar, D. Kobertz, V. Venugopal, and H. Nickel—(Nuclear Research Center, Federal Republic of Germany) **Differential Thermal Analysis and Knudsen Effusion Mass Spectrometry in the Determination of Phase Equilibrium Diagrams in Nickel Based Superalloys**
50. *J. C. Liu*, M. P. Brady, and E. D. Verink, Jr.—(Univ. of Florida, United States) **Phase Stability and Kinetics Study in High Temperature Oxidation of Nb Ti-Al Alloys**
51. *D. Hoelzer* and F. Ebrahimi—(Univ. of Florida, United States) **Phase Stability in the Nb-Ti-Al Ternary System**
52. *E. M. Foltyn*—(Los Alamos National Lab., United States) **Allotropic Transitions in Neptunium Metal by Differential Thermal Analysis**
53. *B. M. Mogutnov*,[1] A. I. Saitzev, and N. V. Korolev—(I. P. Bardin Central Research Institute for Ferrous Metallurgy, U.S.S.R.) **The Vapor Pressures and the Heats of Sublimation of CaF$_2$ and SrF$_2$**
54. *B. M. Mogutov*[1] and A. I. Saitzev—(I. P. Bardin Central Research Institute for Ferrous Metallurgy, U.S.S.R.) **The Vapor Pressures and the Heats of Sublimation of Some Rare Earth Metals**
55. *J. M. Leitnaker*, R. W. Nichols, and B. S. Lankford—(Martin Marietta Energy Systems Oak Ridge, United States) **Reactions of Aluminum with Uranium Fluorides and Oxyfluorides**

Basic Data Determinations

56. *J. Drowart*, A. V. Gucht, S. Smoes—(Free Univ. Brussels, Belgium) **Mass Spectrometric Investigation of Systems Far From Thermodynamic Equilibrium Using the Knudsen Effusion Method**
57. *L. N. Gorokhov*, A. M. Emelyanov, and M. V. Milushin—(High Temp. Inst.,U.S.S.R.) **Knudsen Effusion Mass Spectrometry Determination of Metal Hydroxide Stabilities**
58. *V. L. Stolyarova*—(Silicate Inst. Academy of Sciences, U.S.S.R.) **Mass Spectrometric Study and Calculation of Thermodynamic Properties of Glass-Forming Oxide Systems**
59. *C. E. Myers*, G. A. Murray, R. J. Kematick, and M. A. Frisch—(State Univ. New York at Binghamton, United States) **Comparison of Knudsen Vaporization by Magnetic and Quadrupole Mass Spectrometric Techniques**
60. *J. G. Edwards* and J. K. R. Weber—(Univ. of Toledo, United States) **Vaporization Chemistry in the CaS-Ga$_2$S$_3$ System**
61. *G. Balducci*, G. De Maria, G. Gigli, and M. Guido—(Univ. di Roma 'La Sapienza', Italy) **Vaporization Behavior of Molten Alkali Metal Metavanadates**
62. *J. K. Gibson* and R. G. Haire—(Oak Ridge National Lab., United States) **Knudsen Effusion Investigation of the Thermal Decomposition of Transplutonium Hydrides**
63. *P. W. Gilles* and M. A. Williamson—(Univ. of Kansas, United States) **Vaporization Chemistry of the Vanadium Selenides**
64. *R. G. Haire* and J. K. Gibson—(Oak Ridge National Lab., United States) **On the Enthalpies of Sublimation of Einsteinium and Fermium**
65. *D. L. Hildenbrand*, K. H. Lau, and R. D. Brittain—(SRI International, United States) **Mechanistic Aspects of Metal Sulfate Decomposition Processes**
66. *K. Hilpert* and K. Ruthardt—(Nuclear Research Centre, Federal Republic of Germany) **Determination of the Enthalpy of Dissociation of the Molecule CrPb by High Sensitivity Knudsen Effusion Mass Spectrometry**

67. *P. D. Kleinschmidt* and K. Axler—(Los Alamos National Lab., United States) **Activity and Free Energy of Formation of the Compound $CaCsCl_3$**
68. *P. C. Nordine*, R. A. Schiffman, and J. K. R. Weber—(Intersonics, Inc., United States) **Vapor Pressure of Boron**
69. *G. N. Papatheodorou* and L. Nalbandian—(Institute of Chemical Engineering and High Temperature Chemical Processes, Greece) **Raman Spectra and Vibrational Analysis of the Fe_2Cl_6, $FeAlCl_6$, Au_2Cl_6 and $AuAlCl_6$ Vapor Molecules**
70. M. Shamsuddin and A. Nasar[1]—(Banaras Hindu Univ., India) **Thermodynamic Properties of Cadmium Telluride**
71. *V. L. Stolyarova*, I. Y. Archakov, and M. M.Shultz—(Institute of Silicate Chemistry of the Academy of Sciences, U.S.S.R.) **High Temperature Mass Spectrometric Study of the Thermodynamic Properties of Borosilicate Systems**
72. *M. E. Jacox* and W. E. Thompson—(NIST, United States) **The Production and Spectroscopy of Small Polyatomic Molecular Ions Isolated in Solid Neon**
73. M. Shamsuddin,[1] A. Nasar, and V. B. Tare—(Banaras Hindu Univ., India) **Electrical Conductivity and Defect Structure of Cadmium Telluride**
74. *M. Gaune-Escard* and A. Bogacz—(Univ. de Provence, France) **Calorimetric Investigation of $NdCl_3$ and of $NdCl_3$-MCl Mixtures**
75. *J. P. Bros*, D. El Allam, M. Gaune-Escard, and E. Hayer—(Univ. de Provence, France) **Enthalpies of Formations of Ni- and Pd-Based Ternary Alloys**
76. *C. B. Coughanowr*, T. J. Anderson, and J. J. Egan—(Univ. of Florida, United States) **Thermodynamic Investigation of the Al-Sb and Al-In Systems by Solid State Electrochemistry**

PROCESSING AND SYNTHESIS

Clusters as Reaction Intermediates and Model Structures

77. *A. Kaldor*—(Exxon Research and Engineering, United States) **Clusters as Intermediates for New Materials**
78. *F. W. Froben*, T. M. Chandrasekhar and J. Kolenda—(Freie Univ. Berlin, Federal Republic of Germany) **Cluster Production by Laser Material Interaction With Optical Spectroscopic Characterization**
79. *M. Vala*, T. M. Chandrasekhar, and J. Szczepanski—(Univ. of Florida, United States) **Spectroscopy and Structure of Small Carbon Clusters**
80. *K. G. Weil* and A. Hartman—(Technische Hochschule Darmstadt, Federal Republic of Germany) **Mechanism of Cluster Formation during Evaporation of Alloys**
81. *K. Hilpert* and D. Kath—(Nuclear Research Centre, Federal Republic of Germany) **Investigation of Small Alkali Metal Clusters by Knudsen Effusion Mass Spectrometry using Broad Band Photoionization**
82. *T. C. DeVore* and J. L. Gole—(James Madison Univ., United States) **Oxidation of Small Metal Clusters**
83. *R. S. Berry*, H.-P. Cheng, and J. Rose—(Univ. of Chicago, United States) **Freezing and Melting of Metallic and Salt-Like Clusters**
84. *E. Blaisten-Barojas* and M. Nyden—(NIST, United States) **Thermal Fragmentation of Long Carbon Chains**
85. *K. A. Gingerich*, J. E. Kingcade, Jr., and I. Shim—(Texas A&M Univ., United States) **Bond Energies and Nature of Bonding in Small Transition Metal Semiconductor Clusters**
86. *P. J. Ficalora* and J. H. Hawley—(Rensselaer Polytechnic Institute, United States) **Heterogeneous Formation of Aluminum Vapor Clusters**

Nucleation and Growth of Small Particles

87. *J. Schoonman*, R. A. Bauer, and J. G. M. Becht—(Delft Univ. Technology, The Netherlands) **Laser-Chemical Vapor Precipitation of Ultrafine Ceramic Powders: Si and Si_3N_4**
88. *N. Shimo* and K. Yoshihara—(Idemitsu Kosan Central Research Labs., Japan) **Laser Production of Metallic Fine Particles from Organometallic Compounds**
89. *J. L. Katz* and M. D. Donohue—(Johns Hopkins Univ., United States) **Nucleation with Simultaneous Chemical Reaction**
90. *P. R. Buerki*, T. Troxler, and S. Leutwyler—(Univ. Bern, Federal Republic of Germany) **Synthesis of Ultrafine Si_3N_4 Particles by CO_2-Laser Induced Gas Phase Reactions**
91. *M. R. Zachariah* and H. G. Semerjian—(NIST, United States) **Experimental and Numerical Studies of Refractory Particle Formation in Flames: Application to Silica Growth**

Processing, Mainly from the Vapor Phase

92. *K. E. Spear*—(Pennsylvania State Univ., United States) **The Role of High Temperature Chemistry in CVD Processing**
93. *C. Bernard*—(ENSEEG Domaine Univ., France) **Thermochemical Modeling of Vapor Deposition**
94. *Y. K. Rao* and Y. Do—(Univ. of Washington, United States) **Modeling of Chemical Vapor Deposition (or Etching) in Closed Systems**
95. *F. W. Smith*, M. Sommer, and K. Mui—(City College of the City Univ. of New York, United States) **Thermodynamic Analysis of the Chemical Vapor Deposition of Diamond Films**
96. *J. E. Butler*—(Naval Research Lab., United States) **The Chemical Vapor Deposition of Synthetic Diamond**
97. *E. Schnedler* and H. Greiner—(Phillips GmbH Forschungslaboratorium Aachen, Federal Republic of Germany) **Modelling of High Temperature Transport Reactions**
98. *J.-O. Carlsson*—(Uppsala Univ., Sweden) **Area Selective and Phase-Selective CVD on Patterned Substrates**
99. *R. Naslain* and F. Langlais—(Lab. des Composites Thermostructuraux, France) **Fundamental and Practical Aspects of the Chemical Vapor Infiltration of Porous Substrates**
100. *T. H. Baum* and C. E. Larson—(IBM Almaden Research Center, United States) **Laser Chemical Vapor Deposition of High Purity Metals**
101. *U. B. Pal* and S. C. Singhal—(Westinghouse R&D Center, United States) **Growth of Perovskite Films by Electrochemical Vapor Deposition**
102. *J. S. Horwitz* and M. C. Lin—(U.S. Naval Research Lab., United States) **Laser and Mass Spectrometric Studies of the Mechanism of Silicon Single Crystal Etching Reactions**
103. *Z. A. Munir*—(Univ. of California Davis, United States) **The Utilization of Combustion Processes for the Synthesis of High Temperature Materials**
104. *K. L. Komarek* and H. Blaha—(Institute of Inorganic Chemistry, Austria) **The Reduction of Silica With Graphite**
105. *T. J. Anderson*, J. L. Ponthenier, and F. Defoort—(Univ. of Florida, United States) **Thermodynamic Analysis of Ge_3N_4 Chemical Vapor Deposition**
106. *Z. H. Kafafi* and R. S. Pong—(Naval Research Lab., United States) **The Activation of the C-H Bond of Allene by Ground State Atomic Iron**
107. *T. C. DeVore*, M. L. Smith, and J. C. Fagerli—(James Madison Univ., United States) **Chemical Vapor Transported Species Resulting from the Oxidation of Hot W, Mo Filaments by N_2O, O_2, $POCl_3$, and K_2Cl0_4**

Process Models and Materials by Design

108. *P. J. Spencer* and H. Holleck—(Lehrstuhl fur Theoretische Huttenkunde, Federal Republic of Germany) **Application of a Thermochemical Data Bank System to the Calculation of Metastable Phase Formation During PVD of Carbide, Nitride and Boride Coatings**
109. *P. R. Strutt* and G.-M. Chow—(Univ. of Connecticut, United States) **Ultrafine Composite Synthesis by Laser-Induced Reactive Evaporation and Rapid Condensation**
110. *J. W. Mitchell* and G. Cadet—(AT&T Bell Labs., United States) **Microwave Discharge Synthesis and Characterization of Materials**
111. *J. D. Corbett*, E. Garcia, Y.-U. Kwon, and A. Guloy—(Iowa State Univ., United States) **Chemical Clusters from Solid State Systems at High-Temperatures—Interstitials as a Means to Stability and Versatility**
112. *P. K. Khowash* and D. E. Ellis—(Northwestern Univ., United States) **Impurity Defect Structure in Alpha–Alumina**
113. *N. Zacchetti*, G. Fierro, G. M. Ingo, A. Mazzarano, S. Sturlese—(Centro Sviluppo Materiali SpA, Italy) **High Temperature Stability of CeO_2-Y_2O_3 Stabilized Zirconia Plasma Spray Powders: XPS and DTA Investigations**
114. *N. Zacchetti* and G. M. Ingo—(Centro Sviluppo Materiali SpA, Italy) **XPS Investigation on the Chemical Structure and Growth Model of Amorphous Silicon Nitride (a-SiNx)**

PERFORMANCE UNDER EXTREME ENVIRONMENTS

Hot Corrosion

115. *R. A. Rapp*—(Ohio State Univ., United States) **Hot Corrosion of Materials**
116. *R. L. Jones*—(Naval Research Lab., United States) **Oxide Acid-Base Reactions in Ceramic Corrosion**
117. *N. S. Jacobson*, J. E. Marra, E. R. Kreidler, and M. J. McNallan,—(NASA Lewis Research Center, United States), **High Temperature Reactions of Ceramics and Metals with Chlorine and Oxygen**
118. *N. Birks*, D. L. Rishel, and F. S. Pettit—(Univ. of Pittsburg, United States) **Erosion and Corrosion of Metals in Sulfurous Atmospheres**
119. *I. Tomizuka*, H. Numata, H. Harada, Y. Koizumi, and M. Yamazaki— (National Research Institute for Metals, Japan) **Effects in Processing History and Minor Element Contents on Hot-Corrosion Behavior of a Power-Metallurgically Prepared Nickel-Base Superalloy**
120. *W. Boersma-Klein* and J. Kistemaker—(FOM-Institute for Atomic and Molecular Physics, The Netherlands) **Material Transport at the Interface of a Graphite Wall and a U-C-F Gas/Liquid Mixture**
121. *E. Franconi*, M. Rubel, and B. Emmoth—(Associazione EURATOM-ENEA sulla Fusione Centro Ricerche Energia Frascati, Italy) **Deuterium Implanted in C+SiC and CL589OPT Materials**
122. *V. U. Kodash*, P. S. Kisley, and V. J. Shemet—(Institute of Superhard Materials, Academy of Sciences, U.S.S.R.) **High Temperature Oxidation of Molybdenum Aluminosilicides**

High Power Laser-Materials Interactions

123. *D. R. Olander*, S. K. Yagnik, and C. H. Tsai—(Univ. of California, United States) **Laser-Pulse-Vaporization of Uranium Dioxide and Other Refractory Materials**
124. *J. L. Lyman*, D. A Cremers, R. D. Dixon, R. C. Estler, G. K. Lewis, R. E. Muenchausen, N. S. Nogar, M. Piltch—(Los Alamos National Lab., United States) **Direct Laser/Materials Interaction: Laser Ablation of Superconductor Materials and Laser Welding**
125. *M. J. Berry*, T. D. Kunz, R. F. Menefee, and L. G. Fredin—(Rice Univ., United States) **Laser Probe Absorption Spectroscopy Measurements on Laser Induced Plumes**
126. *Y. Nishina* and A. Kasuya—(Materials Research Institute, Japan) **Space/Time Resolved Spectroscopic Analysis on High Power Laser-Materials Interaction**
127. *R. W. Dreyfus*—(IBM, Yorktown Heights, United States) **Interactive Effects in Excimer Laser Photoablation**
128. *K.-S. Lyu*, J. Kralik, and Y. W. Kim—(Lehigh Univ., United States) **Laser Produced High Temperature States for Iron**
129. *P. K. Schenck*, D. W. Bonnell, and J. W. Hastie—(NIST, United States) **Insitu Analysis of Laser-Induced Vapor Plumes**

CONFERENCE WRAP-UP

130. *L. Brewer*—(Univ. of California Berkeley, United States) A Conference Overview with a Personal Perspective on the Role of Chemistry in High Temperature Materials Science and Technology

---

[1] Paper presented in absentia.

Volume 95, Number 3, May–June 1990
Journal of Research of the National Institute of Standards and Technology

News Briefs

General Developments

NIST SOLVES WELD PROBLEMS IN ATOM SMASHER

NIST investigators have solved problems with weld cracks during construction of a massive steel toroid at the Fermi National Accelerator Laboratory in Batavia, IL. The toroid, a 45×35×35 ft energy measurement device, was designed to determine the momentum of muons emerging from high-energy collisions produced by the atom smasher. But recurrent cracks in welds in walls of the toroid caused safety and structural concerns, and Fermi Lab asked NIST for help. A NIST team found the cracking was due to overload of the highly constrained steel forging. They made a series of recommendations to improve the welds. The recommendations were adopted, and the toroid was completed with no further cracking. For a copy of a paper describing this investigation, contact Jo Emery, Division 104, NIST, Boulder, CO 80303; telephone: 303/497-3237. Ask for paper no. 6-90.

AGENDA DEFINED FOR INTELLIGENT PROCESSING OF STEEL

A NIST report summarizes the research agenda for the intelligent processing of steel, which was developed at a workshop on "Intelligent Processing of Primary Metals," sponsored by NIST, the Department of Energy, and the American Iron and Steel Institute (AISI). The agenda was developed after officials from industry, universities, and government defined the key elements producers need for the intelligent processing of steel, assessed the status of available technologies, and outlined strategies for implementing their use. Experts at the workshop recommended applying intelligent processing concepts in three generic areas: production and refining of primary metal (iron, steel, and aluminum), production of near-net shape products, and the finishing and coating of metals to yield final properties. The findings have been reviewed by an AISI advisory committee, which recommended that priorities be determined and a long-term research program be established with an industry consensus. For a copy of the workshop report, Intelligent Processing for Primary Metals (NIST SP 772), send a self-addressed mailing label to James Early, B309 Materials Bldg., NIST, Gaithersburg, MD 20899; telephone: 301/975-6113.

NARROWEST SPECTRAL LINE PRODUCED

Researchers at NIST have made the narrowest known observation of an optical spectral line. To do it, they developed the narrowest line-width laser ever produced. Their work represents a big step towards an optical frequency time standard which would be 10,000-times more accurate than the best current standard (based on a microwave-range frequency of the cesium atom). For a variety of reasons, a time standard in the optical frequency range would be very useful, and the more narrow the observed line, the more accurate the standard. At present, the limiting factor is the inability to build a very narrowly tuned laser as a probe for the spectral line. The NIST researchers isolated a single, laser-cooled mercury ion in an electromagnetic trap and probed it with a newly designed laser with an effective linewidth of about 86 Hz at a wavelength of 563 nm. The frequency observation was more than 10 times narrower than any previous such attempt. A time standard based on such a system could be accurate to a part in 10^{18}, compared with the current standard accurate to a part in 10^{13}. For a copy of the paper describing this work, contact Jo Emery, Div. 104, NIST, Boulder, Colo. 80303; telephone: 303/497-3237. Request paper no. 13-90.

SYMPOSIUM ON OPTICAL FIBER MEASUREMENTS SCHEDULED

NIST, in cooperation with the Institute of Electrical and Electronics Engineers Optical Communications Committee and the Optical Society of America, will sponsor the 6th biennial Symposium on Optical Fiber Measurements on Sept. 11-12, 1990, in Boulder, CO. The symposium will be devoted entirely to measurements on fiber, related components, and systems. Typical topics will include telecommunications fibers, fiber lasers and amplifiers, fibers for sensors, couplers, connectors, multiplexers, integrated optics, sources, detectors, modulators, switches, long haul systems, LANs, subscriber loops, field and laboratory instrumentation, and standards. For more information, contact the General Chairman, Douglas L. Franzen, NIST Div. 724.02, Boulder, CO 80303 or call 303/497-3346.

CANADA AND U.S. WEIGHTS AND MEASURES COORDINATE PLANNING

The NIST Office of Weights and Measures (OWM) and the Canadian Division of Weights and Measures have developed plans to coordinate their programs and to work toward uniformity in the regulation of weights and measures in the two countries.

Senior representatives of the Canadian Weights and Measures Division have been members of the National Conference on Weights and Measures (NCWM) for several years. Recently, OWM has been working with its Canadian counterpart and, through the exchange of letters and visits, has developed an agreement of cooperation. The agreement includes plans for representatives of each country to participate in the technical and policy development activities of the other. OWM staff have attended meetings of the Canadians to: (1) gain understanding of the Canadian program; and (2) contribute technically and administratively to the Canadian program.

PHASE EQUILIBRIA AND CRYSTAL CHEMISTRY IN SYSTEMS CONTAINING HIGH-T_C SUPERCONDUCTIVITY: THE SYSTEM Sr-Ca-Bi-Cu-O

Phase equilibria studies of the binary and ternary boundary systems for the complex four component system SrO-CaO-Bi_2O_3-CuO have been completed. Phase diagrams have been prepared for publication for the binary systems SrO-CuO, SrO-Bi_2O_3, CaO-CuO, and CaO-Bi_2O_3 and for the ternary systems SrO-CaO-CuO, SrO-Bi_2O_3-CuO, CaO-Bi_2O_3-CuO, and SrO-CaO-Bi_2O_3. Precise unit cell dimensions and standard x-ray powder diffraction data have been collected and prepared for publication for most of the binary and ternary phases. Whenever possible, small single crystals have been synthesized for each phase and characterized as to symmetry and space group. In collaboration with industry scientists, crystal structure determinations are in progress for most of these crystals prepared at NIST. Thus, precise information has been obtained on the geometric nature of the Bi-coordination. Surprisingly, several of the phases show threefold coordination of oxygen around the bismuth ion. Examination of the structure of such phases as $Ca_4Bi_6O_13$ and $Sr_2Bi_2O_5$ has afforded an opportunity to study aspects of the Bi-geometry and bonding not possible in the complex superconductors containing the rigid covalent Cu-O network.

ULTRA-HIGH STRENGTH WELDABLE Al-Cu-Li ALLOYS

A weldable aluminum alloy, which has recently been developed by industry, has twice the strength of currently used weldable alloys. At the same time, the density is lower and the elastic modulus is improved. This alloy, containing copper and lithium with minor amounts of silver, magnesium and zirconium, is targeted for use on the Advanced Launch System, the Space Shuttle, and other aerospace vehicles where weldability is required for containment of cryogenic liquid propellant. The use of such a high-strength alloy would allow substantial weight savings and corresponding increases in payload capacity.

The microstructural basis for these alloy properties is presently under study in a collaborative research effort between NIST and industry. Microstructural studies have been conducted using analytical electron microscopy techniques. The ultrahigh strength arises from a fine, dense precipitation of at least three types of strengthening phases: θ' (Al_2Cu), S' (Al_2CuMg), and T_1 (Al_2CuLi). Further, there are indications of a fourth, previously unknown precipitate. These phases reside in a matrix of aluminum solid solution and each has a different habit and habit plane. This intricate microstructure leads to high strength by making dislocation motion complex and difficult.

Microstructures resulting from various alloy processing conditions are being correlated with mechanical properties, at cryogenic and room temperature, and with corrosion resistance in critical environments. With an understanding of the basis for properties, processing conditions and alloy composition can be optimized to improve the performance of the alloy system. The understanding and correlations obtained in this work are expected to have applications to a large number of aluminum alloys.

UNIVERSITY OF MINNESOTA TO PARTICIPATE IN CNRF INSTRUMENT DEVELOPMENT

The University of Minnesota will participate with NIST in the development and use of two high-resolution instruments at the Cold Neutron Research Facility (CNRF).

The instruments are the 30-m cold neutron small-angle scattering spectrometer and the cold neutron reflectometer. The former is further along in construction and, on commissioning later this year, will be the first state-of-the-art high-resolution SANS instrument available in the United States. The reflectometer is in its final design phase and is expected to be installed in early 1991. It, too, will be a state-of-the-art instrument, with expected measurement sensitivity down to $\sim 5\times10^{-7}$ in reflectivity.

These instruments are expected to play a major role in the elucidation of the structure and microstructure of polymers and other materials as well as surface and interfacial structure and interactions—areas of considerable interest both to scientists of the University of Minnesota and NIST. Neutron reflectometry measurements at poorer sensitivities already have provided important information on surfaces, interfaces, and thin films for systems as diverse as magnetic films and multilayers, and diblock copolymers. In addition to its powerful role in the study of micro- and macromolecular structures, SANS also has been used to study a wide variety of interfacial problems, including internal surface adsorption in controlled pore glasses and micellar growth and aggregation.

POLYMER FILMS USED IN RADIATION DOSIMETERS ANALYZED

Scientists at NIST have used high sensitivity dielectric loss measurements to evaluate polymer films to be used in the construction of radiation dosimeters. The work is being carried out for the Federal Emergency Management Agency, which maintains large quantities of dosimeters to be used in the event of a nuclear emergency. It is important that the electrical leakage characteristics of the polymer, typically polystyrene, not be altered after short exposure to high levels of ionizing radiation in any manner which would change the dosimeter's response. The leakage characteristics tend to be dominated by adventitious impurities introduced during polymerization or subsequent processing rather than being an intrinsic property of the polymer. Dielectric loss measurements have enabled selection of materials with the appropriate electrical characteristics before exposure to ionizing radiation. These materials now are being irradiated for further evaluation.

UNITED STATES AND FRANCE AGREE ON EQUIVALENCE OF LUMINOUS INTENSITY STANDARDS

A series of agreements that recognize the equivalence of the practical realizations of a number of SI units by the national standardizing laboratories of the United States and France have been signed.

Typical is the reciprocity agreement on luminous intensity which states that the national standards for the practical realization of the candela in the United States and France are equivalent to each other within an uncertainty of 1 part in 100 (three standard deviation estimate). Within the same limit of uncertainty, the NIST and BNM units are believed to be smaller than the SI unit by 4 and 5 parts in 1,000, respectively.

These estimates are based on data contributed by NIST and BNM to an international intercomparison of photometric base units, which was conducted by the Consultative Committee for Photometry and Radiometry between 1984 and 1986. Overall, the intercomparison showed 0.8 percent agreement (one standard deviation) of independent luminous intensity scale realizations by 15 national laboratories, and 0.6 percent agreement of luminous flux realizations by 11 national laboratories. The NIST candela and lumen agreed with the world mean within quoted uncertainty limits and were shown to be consistent with one another within 0.5 percent.

The U.S./French SI unit equivalency agreements will remain in effect for an unlimited period but may be withdrawn by either party at any time. These agreements will facilitate the sale of products between the United States and France if traceability to national standards of the relevant SI units is required.

ABSOLUTE CRYOGENIC RADIOMETER

An absolute cryogenic radiometer, constructed in the United Kingdom as part of a joint NIST-NPL (National Physical Laboratory) project, has arrived in the United States. The instrument is to be used in a series of collaborative measurements involving the two laboratories. These measurements are being used to compare this radiometer with a similar instrument at NPL and to carry out a collaborative long-term effort to develop transfer standard detectors and working standard detectors. The first intercomparison of the instruments was accomplished before the NIST radiometer was transferred to the United States. The results indicated that the two instruments measured optical power in a consistent manner, within the expected accuracy.

The instrument will be set up at NIST in a specially prepared laboratory that is designed to minimize dust and electrical noise and will provide a stable temperature environment. The instrument will serve as the absolute radiometric base for NIST and will accommodate calibration and research activities being carried out at NIST. The long-term goal of this program is to improve the calibrations provided by NIST and make available more accurate laboratory standards for use in a wide range of radiometric activities. It is expected that the instrument will be in operation this year and start to make an impact on NIST programs immediately after commissioning. The instrument has a demonstrated level of accuracy of at least 0.01 percent in work carried out over the last few years by the NPL staff.

AIR POLLUTION TRACER EXPERIMENT

NIST scientists in collaboration with researchers at the University of Maryland, have developed a new method for air pollution source apportionment. This technique involves tagging the emissions from combustion sources with a small amount of an enriched isotope of a rare earth element. In the case of coal-fired power plants the tracer is injected into the stack as an organic complex dissolved in an organic solvent. For sources that burn oil, the tracer can be directly mixed with the fuel. Air particulate samples are then taken and the isotopic composition measured by thermal ionization mass spectrometry.

This technique is currently being used as part of the Environmental Protection Agency's (EPA) Integrated Air Cancer Project to study the emissions from residential heating oil furnaces and diesel trucks. For this experiment, extremely small amounts of two isotopes of samarium (Sm) were used. Samarium 149 was added to a supply of home heating oil and ^{150}Sm was added to a supply of diesel fuel. In both cases, the final concentration of tracer in the fuel was a few parts per billion.

Samples from the sources and receptor sites, including filters from air samplers, vegetation, soil, and rain samples, were collected during the winter of 1989. The absolute amounts and isotopic enrichment of the Sm isotopes will be determined by high-precision isotope dilution thermal ionization mass spectrometry. This experiment should provide a quantitative measure of the dispersion of particulates as a function of both their source and size. These data will help EPA to assess the relative impacts of these two emission sources on human health.

CLUSTERS OF ATOMS SHOW METALLIC BEHAVIOR

When metal atoms are brought together to form clusters, transition to the metallic state must occur at some critical cluster size or number of atoms. This transition is noted by the change from isolated electrons (and electronic states) in each metal atom to completely delocalized electrons in the metal cluster. Using scanning tunneling electron microscopy (STM), NIST scientists have observed this transition and determined the critical size for Fe clusters on GaAs surfaces.

Molecular beam epitaxy was used to deposit quantities of Fe on GaAs below the number of atoms needed to form one continuous layer of Fe. The STM shows that this process generates localized clusters of Fe, up to several hundred atoms in size, growing on the GaAs surface. It was found that clusters of fewer than about 13 Fe atoms were nonmetallic or semiconducting in nature, and that clusters of more than 35 Fe atoms clearly exhibited metallic behavior. These measurements also have revealed evanescent electronic states in the GaAs band gap at the metal-semiconductor interface. The electron tunneling characteristics at the edges of the clusters show that the electronic states of the metallic clusters "leak out" into the semiconductor region where there are usually no electronic states within the band gap. These measurements are the first clear experimental observation of metal-induced gap states, shown previously in theoretical modeling of metal-semiconductor interfaces.

HIGH-T_C SUPERCONDUCTIVITY THEORY ELIMINATES LARGE CLASS OF PROPOSED MECHANISMS

The discovery of high-temperature, copper oxide superconductors was not anticipated by existing theories of superconductivity, and no attempt to explain the phenomenon has been fully successful. A number of theories invoke electronic excitations to mediate an attractive interaction between electrons near the Fermi surface. Such mechanisms might account for the high values of T_c, since electronic excitations are characterized by much higher energies than the lattice vibrations responsible for low-T_c superconductivity. However, recent theoretical work in collaboration with researchers from the University of California at Berkeley, has shown that many proposed electronic mechanisms are not appropriate.

The standard BCS theory of superconductivity is not applicable to the high-T_c oxides. The properties of high-T_c compounds must be examined within a generalization of the BCS theory, which involves solving equations derived by Eliashberg. The scientiests solved the Eliashberg equations in a model that represents strong electronic interactions in a fairly general way, yet also accounts for specific materials properties by incorporation of experimental data.

Their main finding is that the appropriate constants required to fit experimental data are much too small. Thus, *electronic mechanisms of this type* are inconsistent with the predictions of the standard strong-coupling theory of superconductivity as applied to known high-T_c compounds. This means that the agent of high-temperature superconductivity still remains un-identified. Some simplifications made to the model, such as the assumption of isotropic interactions, could change their results; but this would indicate a major deficiency in existing simple models. The possibility that the Eliashberg formalism is inapplicable would have far-reaching implications because it would place strong-coupling theories of high-T_c superconductivity outside the realm of tested physical theory.

FEDERAL INFORMATION PROCESSING STANDARD (FIPS) FOR COBOL REVISED

The Secretary of Commerce has approved a revision of FIPS 21-2, COBOL, to be published as FIPS 21-3. To be effective June 29, 1990, the revised standard adopts American National Standard Programming Language COBOL, ANSI X3.23-1985 and X3.23A-1989 for federal agency use. FIPS 21-3 adds an intrinsic function facility to the COBOL specifications. FIPS COBOL is one of the high-level programming language standards provided for use by all federal agencies. The language is especially suited for applications that emphasize the manipulation of characters, records, files, and input/output (in contrast to those primarily concerned with scientific and numeric computations).

NIST PUBLISHES RESEARCH RESULTS ON DIRECT IMAGE STORAGE TECHNOLOGY

Direct image storage technology promises to provide substantial improvements in the transmission and storage of forms. NISTIR 89-4177, Decoding Bar Codes from Image Data, describes a process of direct decoding of the bar code in a scanned image which simplifies paper handling and systems design. In work done for the Bureau of the Census, researchers developed software to provide portable "C" programs which demonstrate the feasibility of directly decoding bar codes from raster images.

Three distinct decoding algorithms were developed and tested: a scan method which decodes a single scan line without prior image processing; a global histogram averaging method which takes into account information from the entire image maximizing reliability at the expense of processing time; and a hybrid method which samples the original bar code into a collection of representative scan lines. These methods are fully portable and can be incorporated into a wide range of image applications.

REPORT DESCRIBES GRAPHICS APPLICATION PROGRAMMER'S INTERFACE STANDARDS AND CALS

NISTIR 89-4199, Graphics Application Programmer's Interface Standards and CALS, focuses on two graphics application programmer's interface (API) standards of interest to CALS (Computer-Aided Acquisition and Logistic Support): program-mer's hierarchical interactive graphics system and programmer's imaging kernel. API standards are tool boxes of graphics functions used by application programmers who develop graphics programs.

The primary purpose of a graphics API standard is to provide portability for an application program across a wide range of computers, operating systems, programming languages, and interactive graphics devices. Other benefits of API standards include reducing software development and lifecycle costs and reducing programmer time and costs since many of the functions currently performed by the application program can be performed by the API standard.

NIST DEVELOPS FACT SHEET ON THE DATA ENCRYPTION STANDARD (DES)

In response to the many questions received from federal agencies about DES, NIST has developed a fact sheet covering all aspects of the standard and its applicability. Federal Information Processing Standard (FIPS) 46, Data Encryption Standard, was issued in 1977 and has been reaffirmed twice; the current FIPS 46-1 reaffirms the standard until 1993. Subject to agency waivers, the use of DES is mandatory for all federal agencies, including defense agencies, for the protection of sensitive unclassified data communications (except information covered by 10 U.S.C. Section 2315) when the agency determines that cryptographic protection is required.

CD-ROM VERSION OF THE DEFENSE ADVANCED PROJECTS AGENCY'S (DARPA) RESOURCE MANAGEMENT CONTINUOUS SPEECH CORPUS COMPLETED

NIST has completed the preparation and public availability of a CD-ROM version of DARPA's Resource Management Continuous Speech Corpus. This speech database has been in use within the DARPA speech research community since 1987, and a series of benchmark performance assessment tests has been conducted using designated training and test sets in conjunction with scoring software that provides a basis for a uniform reporting standard.

The CD-ROM discs that are now publicly available contain all speaker-dependent and speaker-independent system training and benchmark test material used to date, together with the latest version of the scoring software and other tools. Arrangements have been made with NTIS (National Technical Information Service) for public sale of these CD-ROM releases, both domestically and abroad.

REPORT INTRODUCES CONCEPT OF A HETEROGENEOUS COMPUTING ENVIRONMENT

Computer networks are becoming larger not only in the number of nodes connected but also in the geographic area spanned. Networks are also becoming more diverse in the variety of equipment from which the network is implemented. NIST Special Publication 500-176, Introduction to Heterogeneous Computing Environments, characterizes heterogeneous computing environments from the point of view of the generic services provided. The report introduces the types of technical standards necessary in a heterogeneous computing environment and illustrates how such standards can be used to provide services.

NIST DEVELOPS NEW RATING PROCEDURE FOR MIXED AIR-SOURCE HEAT PUMPS TO AIR CONDITIONING INDUSTRY

A recently completed NIST rating procedure for mixed air-source heat pumps was presented to a special meeting of the Unitary Equipment Committee of the Air-Conditioning and Refrigeration Institute. Mixed air-source heat pumps are those that are not designed and tested as a single system. An outdoor section of compressor and condenser is used with a separate indoor section of evaporator and fan, typically in a retrofit application. A rating procedure is necessary for utilities' rebate programs where the amount of rebate is governed by the predicted efficiency of the new system. The rating procedure developed by NIST enables the manufacturer and/or designer to calculate the seasonal performance of such units from prior tests on a complete system that included the outdoor unit plus relevant engineering performance data on the indoor refrigerant-to-air heat exchanger and indoor fan. The procedure will be adopted by the U.S. Department of Energy in their mandatory minimum standards program and used extensively throughout the industry.

ROLE OF TURBULENCE CLARIFIED IN FLAME SPREAD

Prof. A. C. Fernandez-Pello (U.C., Berkeley) under a grant from NIST has quantitatively shown for the first time the role of turbulence on flame spread rate over materials. Although this work emphasizes the influence of free stream turbulence on a laminar boundary layer flame, it clearly shows the effect is to decrease flame length and increase flame heat flux. This quantification of the effects allows rate predictions based on the general theory of flame spread. The implications of this work are significant to the interpretation and reproducibility of standardized flame spread tests, and on the need to understand more fully turbulent flame spread in real fires.

UNSTABLE SOIL A CULPRIT IN LOMA PRIETA QUAKE

Unexpectedly severe damage to buildings in the San Francisco Bay area during last October's Loma Prieta earthquake underscores the lesson that structures sited on unstable soil deposits need to be assessed to determine their earthquake safety, according to a recent NIST report. "Lifelines," such as bridges, highways, and water and gas pipelines, also are vulnerable to earthquakes and should be assessed as well. NIST investigated the earthquake at the request of Congress. Not surprisingly, NIST found that older wood-framed dwellings and unreinforced masonry buildings that had not been strengthened sustained substantial damage. Somewhat unexpected, however, was that many structures in the Bay area of San Francisco, 60 to 70 miles away from the earthquake's epicenter, suffered severe damage, including some buildings constructed using modern seismic safety practices. To a large extent, these damages occurred to structures located on unstable soil deposits. Most buildings on firmer ground sustained little or no damage. Since 1971, NIST has participated in nine earthquake investigations.

REPORT SUMMARIZES NIST ELECTRIC ENERGY RESEARCH

A summary of numerous investigations aimed at improving measurement science for the electrical power industry is contained in a report now available. The document, prepared for the U.S. Department of Energy, covers four major research projects. One of these examines the measurement of ions in the vicinity of dc high-voltage transmission lines and in biological exposure facilities that simulate a transmission line environment. Another project is concerned with the behavior of the compressed gas insulators (dielectrics) used in high-voltage power systems. Understanding the breakdown of liquid dielectrics such as the oil used as an insulator in power transformers is the goal of another project. (The summary for this research includes a description of a novel high-speed camera designed at NIST to record the random events that take place in the nanosecond range of breakdown phenomena.) A fourth project aims to improve the measurement of fast transient pulses such as lightning and power surges. The free publication, Research for Electric Energy Systems—An Annual Report, is available from the Center for Electronics and Electrical Engineering, B344 Metrology Bldg., NIST, Gaithersburg, MD 20899.

SMALL SHOP AUTOMATION: A HANDS-ON SEMINAR

Shop owners, managers, and foremen examined computer software designed to automate small plant production in the first "Shop of the 90's" seminar held at NIST. Participants used commercially available automation software that is ready to run on personal computers. The hands-on demonstrations covered computer-aided process planning and computer-aided cost estimation, as well as programs devised to speed manufacture such as computer-aided design and computer-aided manufacturing packages. Direct numerical control, the process that transmits machine codes to the computer-driven shop machines, also were discussed. Representatives of state and regional technology transfer centers were on hand to review their automation and technology transfer efforts. Seminar participants left with a good idea of how to build a computer-integrated manufacturing system for their small job shop. For more information contact: Adrian Moll, Rm. 136 Shops Bldg., NIST, Gaithersburg, MD 20899; telephone: 301/975-6504.

NEW VIDEO PROFILES QUALITY AWARD WINNERS

The 1989 winners of the Malcolm Baldrige National Quality Award—Milliken & Company and Xerox Corporation Business Products and Systems—are profiled in a new videotape, "The Malcolm Baldrige National Quality Award—1989." Produced under NIST supervision, the 14 1/2-minute tape in VHS format highlights the award and the management philosophies of the two firms. Also covered are the management approaches that contributed to their choice as recipients of the award for total quality management. The videotape, funded by the Foundation for the Malcolm Baldrige National Quality Award, is available for $10 through the American Society for Quality Control, Customer Service, 1-800-952-6587.

NIST, INDUSTRIAL COMPANY SIGN OPTICAL FIBER SENSOR RESEARCH AGREEMENT

NIST and an industrial company have begun a cooperative program to develop components for optical fiber current sensors. These electric current sensors have potential applications in the electric power industry, electromagnetic pulse and interference testing, and general electronic instrumentation. Having no electrical parts, fiber current sensors are especially attractive in applications where current must be measured at high voltage or in the presence of electromagnetic interference. NIST has developed certain technologies in this field, including methods for improving the properties of fiber coils for sensing. A guest scientist from the industrial company will spend a year working with researchers at the NIST Boulder Laboratories. NIST will share its knowledge with the company, and the visiting scientist will participate in further developmental work in fabrication, packaging, and characterization of the coils. The goal of cooperative research programs, which exist in many different fields of research at NIST, is to accelerate the transfer of federally generated technology to commercial enterprise.

SPRINKLERS IN CHEM LABS CAN PROTECT LIVES, PROPERTY

During a fire in a chemical laboratory, lives and property as well as critical scientific experiments are at risk within seconds. Researchers at NIST recently conducted a series of full-scale fire tests in chemical labs to examine the potential of quick response sprinklers to improve life safety and protect property. The tests were part of a project to help the National Institutes of Health develop sprinkler design criteria for its chemical labs. In a test in an unsprinklered laboratory, the NIST researchers found that within 38 s all combustible material in the lab was burning, creating lethal conditions and extensively damaging the laboratory. In contrast, both the standard and quick response sprinklers effectively controlled the fires and reduced temperatures as well as carbon monoxide and carbon dioxide levels. A report, Quick Response Sprinklers in Chemical Laboratories: Fire Test Results (NISTIR 89-4200), is available from the National Technical Information Service, Springfield, VA 22161 for $17 prepaid. Order by PB #90-151721/AS.

NEW APPARATUS FOR STUDYING METALS

Over the past 20 years the steel industry has developed thermomechanically processed (TMP), high-strength, low-alloy steel plates which are strong, tough, and easily welded. Production of TMP plates, however, requires careful control over each step. To assist the steel industry, NIST scientists have devised a laboratory-scale, hot-deformation-apparatus to simulate the thermal and mechanical treatments metal receives during a rolling or forging operation. The apparatus has advantages of economy, versatility, and reproducibility. It has been used successfully to perform the direct-quenching simulation of the ASTM A710 plate steel and forging simulation of the directly cooled microalloyed AISI 1522 and 1141 steels. More information is contained in Development of a Computer-Controlled Hot-Deformation Apparatus at NIST (NISTIR 89-3925). Order from the National Technical Information Service, Springfield, VA 22161. Order by PB #90-149964 for $23 prepaid or $8 for microfiche.

NEW PUBLICATIONS DISCUSS ADVANCES

To maintain our lead in biotechnology research and commercialize the results of that research, the United States needs a strong base of generic technology in bioprocess engineering. Two recent publications, co-edited by NIST personnel, make significant contributions to that base. Frontiers in Bioprocessing, contains 35 papers originally presented at a NIST-NASA conference. Areas covered include process integration, fermentation control, sensor development, free-fluid bioseparations, chromatography, and emerging technologies. One chapter, written by NIST researchers, discusses the rapidly expanding interest in applying microbial processing for metal dissolution and recovery from ores and wastes. The publication is available from CRC Press Inc., Boca Raton, FL 33431. The second publication, Downstream Processing and Bioseparation, discusses the increasingly important role played by downstream processing in the commercialization of biotechnology. Two chapters, written by NIST personnel, discuss aqueous two-phase extraction systems for recovering and purifying proteins, enzymes, and other molecules. The publication is part of the American Chemical Society Symposium Series, Vol. no. 419, and is available from ACS, Distribution Office, Dept. 225, Washington, DC 20036.

MIT TO PARTICIPATE IN NEUTRON DIFFRACTOMETER DEVELOPMENT

The Massachusetts Institute of Technology (MIT) will participate with NIST in the development and use of a new powder neutron diffractometer for materials research at the NIST reactor.

The new 32-detector ultra-high resolution powder diffractometers to be installed at the BT-1 thermal neutron port. It will replace the 5-detector instrument currently in use. The new instrument will be a world-class diffractometer with state-of-the-art capabilities in resolution, versatility, and data collection efficiency.

As is generally well-known now, Rietveld analysis of neutron powder diffraction provides details of atomic arrangements in condensed materials which is not possible with other diffraction methods. With this capability, this experimental station is expected to play a major role in research programs of mutual interest to NIST and MIT. Of particular initial interest in the collaborative program are structural studies of graphite intercalation compounds and fast-ion conductors, and advanced ceramics.

INTERIM U.S. ADOPTION OF HUNGARIAN RADIONUCLIDE STANDARDS

Cooperation between the Hungarian National Office of Measures (OMH) and NIST will allow NIST to adopt radionuclidic standards developed in OMH's respected Radionuclide Metrology Section until direct activity measurement of the radionuclides can be made in this country. This interim adoption will give NIST a means of performing accurate measurement-traceability tests of U.S. commercial calibration-material suppliers and nuclear-power radiochemistry departments much sooner. Because of this cooperation, resources in the NIST radioactivity group can now be focused on the establishment of national standards for new radionuclides being introduced into nuclear medicine. An ampoule of ^{106}Ru$-$^{106}Rh has been sent to OMH, together with a test ampoule of ^{144}Ce$-$^{144}Pr recently standardized here. Arrangements are being made for the transfer of standardizations of ^{86}Rb, ^{65}Zn, ^{182}Ta, and ^{192}Ir during the year with ^{141}Ce included to compare with a recent NIST value.

MARINE BIOGEOCHEMICAL SULFUR CYCLE AND GLOBAL WARMING

NIST scientists in collaboration with researchers from the University of Washington, helped determine the sulfur isotopic composition in atmospheric samples collected over the Pacific Ocean. The results of these findings may provide additional constraints on global warming models.

Dimethyl sulfide (DMS) and non-sea-salt sulfate samples were collected on a NOAA cruise in the Pacific Ocean. Dimethyl sulfide, produced by oceanic bacteria, is believed to be the major precursor to other sulfur-containing species that are a primary source of cloud condensation nuclei. The biogeochemical sulfur cycle as now defined has been postulated as a temperature-regulating feedback system for the Earth. Global warming will induce the formation of more DMS, followed by more cloud condensation nuclei and more clouds, and hence compensative cooling.

The first determinations of the sulfur isotopic composition of DMS and non-sea-salt sulfate were made in January. These measurements were made using the NIST thermal ionization procedure for sulfur which is based on the formation of the stable AsS^+ molecular ion. Since As is mononuclidic, no corrections to the measured isotopic ratios are necessary. These first measurements of the sulfur isotopic composition of DMS and non-sea-sulfate indicate that the two species are isotopically distinctive from sea-salt sulfate. These results provide an important additional link between DMS and the cloud condensation nuclei.

NIST XUV OPTICS FACILITY USED IN X-RAY LITHOGRAPHY DEMONSTRATION

A novel projection XUV lithography system has been used by industry to form a printed image (on a resist) with 0.1 μm features. NIST characterized the reflective multilayer optics of the system, which forms a 20:1 reduced image on the resist. The work is part of a large industrial effort to develop a short wavelength (13 nm) lithography technique capable of fabricating semiconductor devices with 0.1 μm components, nearly an order of magnitude smaller than presently possible.

A key development in soft x-ray science that has made XUV projection lithography a possibility is the XUV multilayer reflector first demonstrated about a decade ago. XUV optical systems based on multilayer mirrors are now revolutionizing soft x-ray technology.

The NIST Synchrotron Ultraviolet Radiation Facility (SURF II) is ideally suited as a source to support the development of multilayer systems and soft x-ray projection lithography. The spectral region of interest for these technologies, 4-40 nm, is the region of highest spectral output power of SURF II, and the extremely small beam cross-section of this source allows the establishment of a very high quality test facility for optical components. Scientists at NIST evaluated the quality of the multilayer mirrors—the reflectivity was 38 percent at 13.2 nm, about two orders of magnitude larger than conventional optics.

NIST also has provided measurements to numerous collaborators engaged in developing XUV telescopes, monochromators, and new multilayer combinations.

NIST SCIENTISTS SOLVE FUNDAMENTAL PROBLEM IN GENE CLONING AND EXPRESSION

The ability to express a gene at high levels to produce large quantities of protein in bacteria using recombinant DNA technology is one of the biotechnology industry's core technologies. However, not all genes can be cloned in expression systems for reasons that until now have been unclear. NIST scientists report that current high-expression techniques fail to work with genes that produce protein products lethal to bacterial cells, because of "leaky" vector transcription.

Working with the gene that codes for the enzyme adenylate cyclase, scientists demonstrated that increasing the level of enzyme in the cell from 0.004 percent to 0.20 percent of total protein was lethal to the cell. The lethal problem could be overcome in the case of adenylate cyclase by using a bacterial cell that had a defective receptor protein for cyclic AMP, the product of adenylate cyclase catalysis. To solve this problem in the general case for all lethal gene products, the researchers used DNA technology to engineer a new generation of expression vectors that block "leaky" transcription. Using this system it was demonstrated that adenylate cyclase could be expressed in normal bacterial cells at very high levels (up to 30 percent of total cell protein). This means that the amount of protein previously produced from a 1,000 L fermenter can now be isolated from 1-L of cells. This technology should be useful for other genes that have been demonstrated to be difficult to express in bacterial cells, such as the HIV protease and human cystic fibrosis gene.

NIST INVESTIGATES APPLICATION OF MULTI-ATTRIBUTE DECISION MODEL TO FIRE PROTECTION INVESTMENT ALTERNATIVES

A NIST scientist investigated the use of the analytic hierarchy process (AHP) model for making choices among alternative fire protection strategies in buildings. The AHP, a multiattribute decision support model, has the advantage that it allows the decision-maker to combine quantitative and qualitative criteria. Quantitative criteria may include system price, future costs, insurance, and property tax savings. Qualitative criteria may include attitudes towards risk and aesthetics, and exposure of the individual building and its occupants to risk of death, injury, and property loss. In the application of the model, the decision-maker weights all relevant criteria and alternatives by comparing them in a pairwise fashion. The pairwise comparisons elicit user-specific information; this is an advantage for fire protection decisions which involve unique combinations of risk exposure and attitude. The AHP model combines the weights resulting from the comparisons and assigns to the investment alternatives a ranking that reflects the decision-maker's particular situation. Two hypothetical case studies apply the method to a choice among smoke detectors, a sprinkler system, and a combination of the two. The NIST report "Risk Exposure and Risk Attitude of Homeowners in Fire Protection Investment Decisions," lays the groundwork for possible development of specialized computer software to apply the AHP model to a wide variety of fire protection measures.

NIST ESTABLISHES NEW MICROWAVE POWER SERVICES

NIST has announced new special-test measurement service for power measurements for 3.5-mm coaxial connectors in the range 2 to 26.5 GHz. The approach used to establish the service was to employ existing coaxial and waveguide power standards as a base and to adapt them to 3.5-mm coaxial connectors with precision adapters. The scattering parameters of these connectors were determined with measurements on division-developed dual six-port automatic network analyzers, using a mixed-connector calibration technique. A number of measurements were carried out to demonstrate consistency, with the result that the efficiency of the adapter when connected to a power standard contributes no more than 1 percent to the overall uncertainty of the measurement of 1.5 to 2 percent. The division also completed work on dual six-port systems covering the waveguide bands WR42/28 (18 to 40 GHz) and WR22 (33 to 50 GHz) and is now providing special-test services for power and scattering parameters over these ranges. These new six-port based services offer improvements in sensitivity and accuracy of up to one order of magnitude over measurements available from tuned-reflectometer manual systems.

NASREM ARCHITECTURE ADOPTED FOR NEXT GENERATION CONTROLLER

The NIST/NASA Standard Reference Model for Telerobotic Control System Architecture (NASREM) developed by NIST for the NASA Space Station Flight Telerobotic Servicer has been adopted for the next generation controller (NGC) for the Air Force Wright R&D Center. The Air Force NGC program is part of a national initiative to revitalize the U.S. machine tool industry. The NGC will be an open-system, real-time computer control system for machine tools, robots, and coordinate measuring machines. NIST will develop a task vocabulary and syntax at each level of the NASREM hierarchical architecture as the basis for a NGC "Neutral Manufacturing Language."

STATE-OF-THE-ART ROBOTIC WORKSTATION TRANSFERRED TO MARE ISLAND NAVAL SHIPYARD

NIST transferred a robotic flexible manufacturing workstation, developed in its Automated Manufacturing Research Facility (AMRF), to the Mare Island Naval Shipyard located north of San Francisco, CA. By applying the research and technology developed in the turning workstation, the state-of-the-art small-batch workstation is designed to produce critical component parts for the U.S. Navy. The development of this advanced workstation, partially supported by Naval Sea System Command, the Navy Manufacturing Technology program, and NIST, launches the Navy into the forefront of advanced flexible manufacturing. This development and further research will yield applications at seven other naval shipyards in the United States.

This robotic workstation is driven totally by process plans and data. It has many capabilities and sophisticated features including hierarchical control architecture, in-process gaging, robotic material handling, robotic assembling of pallets, flexible workholding, and an intelligent robot gripper. With in-process inspection built into the workstation, scrap parts are virtually eliminated. The workstation can improve productivity five-fold over existing technology and practices currently employed by the U.S. Navy. This automated workstation can produce parts continuously, unattended, and on a part-on-demand basis so that no inventory of parts needs to be maintained.

NIST JOINTLY SPONSORS ROUNDTABLE ON INTERNATIONAL CONSTRUCTION STANDARDS AND PRACTICES

Twenty-seven U.S. private- and public-sector design and construction community leaders met for a 1-day roundtable on "International Harmonization of Construction Standards and Practices—Assets or Liabilities for Competitiveness." They identified actions to enhance the effectiveness of U.S. construction:

- A national certification and testing system is essential to provide for mutual recognition for international trade.
- Strengthened U.S. participation in international standardization. The international standard soon will be the basis for acceptance of products and services internationally and domestically. Federal participation is appropriate.
- SI conversion is needed. Most of the world's trade activities are in metric units. The U.S. construction industry must convert to be competitive.
- Effective communication is fundamental to industry and government policy makers on the importance of international harmonization of construction standards and practices.

TENSILE PROPERTIES OF INDIUM DETERMINED

Indium, the softest metal known that is stable in air, and its alloys are used in many high-technology applications because their excellent wetting properties enable reliable joining of glass, ceramics, and metals. Indium is also a superconductor below about 3.4 K. Curiously for an engineering material, there are no data on its mechanical strength in tension. NIST has performed extensive tensile tests on 99.99 wt% pure indium, cast in a nitrogen atmosphere into cylindrical tensile specimens of 13-mm reduced-section diameter. The specimens were tested at 4, 10, 76, and 295 K. Some specimens were studied metallographically before and after testing to determine characteristics such as grain size and precipitate structure, mode of failure, and recrystallization. Data on the yield strength, tensile strength, elongation, and reduction in area are given in "Tensile Strength and Ductility of Indium," published in Materials Science and Engineering A, 102 (1988). Copies of the paper, no. 15-90 are available from Jo Emery, Div. 104, NIST, Boulder, CO 80303; telephone: 303/497-3237.

ANTENNA DATA ANALYSIS AND RESEARCH USING PCs

NIST researchers have developed a new software package that allows scientists, engineers, and programmers to make complex antenna computations on personal computers. The package, termed Planar Near Field Codes, has a highly modular structure and can be used to address diverse research problems. A recent publication describes some of the inner workings of the FORTRAN codes, the data management schemes, and the structure of the input/output sections. The structure of the codes is open so that a user can incorporate a new application into the package relatively easily. The publication includes some basic research problems to illustrate the use and effectiveness of the codes. Planar Near-Field Codes for Personal Computers (NISTIR 89-3929) is available from the National Technical Information Service, Springfield, VA 22161. Order by PB #90-155839 for $17 prepaid. To order the software package, available for $1500, contact Lorant A. Muth, Div. 723.05, NIST, Boulder, CO 80303; telephone: 303/497-3603.

CALIBRATING THE SPACE TELESCOPE

NIST researchers provided a suite of state-of-the-art radiometric calibrations for the Hubble Space Telescope (HST). Because everything discovered by astronomy depends on analyzing light from distant stars and exotic objects, extremely accurate instrument calibrations are essential to the space telescope mission. Scientists at NIST aided in the design of a special optical simulator to test the HST Faint Object Spectrograph and calibrated the simulator for brightness. They then calibrated the special light sources used to test the overall sensitivity of the telescope's optics and measuring instruments. In addition, the researchers provided special wavelength and brightness calibrations for an on-board standard lamp, part of the HST High-Resolution Spectrograph. The latter will make it possible to identify the particular element associated with individual spectral lines, to estimate the speed of the element to within a km/s and to account for any changes in instrument calibrations while in space. NIST is the only source in the world for radiometric calibrations of short-wavelength vacuum ultraviolet radiation, which are essential for space-based astronomy.

USING THE SPACE TELESCOPE

Two NIST scientists at the Joint Institute for Laboratory Astrophysics (JILA) have obtained observing time on the Hubble Space Telescope. An astronomer and co-investigator on the Goddard High Resolution Spectrograph instrument, will make high-precision measurements of the deuterium-to-hydrogen ratio for intersteller gas, an important test of some models of the origin of the universe. He will also study six stars of very low mass to learn whether they have atmospheres which resemble the sun's—such stars are too faint to observe from Earth and can be studied only from space. An astrophysicist, will work with colleagues at JILA and the University of Munich to measure the ultraviolet spectrum of hot stars in the Magellanic Clouds, the galaxies nearest to our own. With this data they will be able to study the origin and evolution of these stars which, unlike stars in our own galaxy, appear to contain a much lower abundance of elements heavier than hydrogen. JILA is a joint operation of NIST and the University of Colorado and is located on the university's campus in Boulder, CO.

NIST EXPERT SYSTEM HELPS DIAGNOSE CAUSE OF CRACKS

To help diagnose the causes of cracks in concrete, NIST researchers have developed a prototype expert system known as "CRACKS." An expert system is a computer program that incorporates facts along with experts' opinions and guidelines. In addition, CRACKS includes a database for maintaining information describing a structure and an "image base" for storing digitized photographs and drawings of cracking. CRACKS also can be used to measure the rate of deterioration of a structure by comparing observations over time. While CRACKS is not yet available commercially, it is available for review and comment. Contact Lawrence J. Kaetzel, B348 Building Research Bldg., NIST, Gaithersburg, MD 20899; telephone: 301/975-5912. A report describing CRACKS is available from the National Technical Information Service, Springfield, VA 22161 for $15. Order Integrating Knowledge for the Identification of Cracks in Concrete Using An Expert System Shell and Extensions (NISTIR 89-4206) by PB #90-151234/AS.

COMMERCE APPROVES REVISION OF POSIX

The Secretary of Commerce has approved a revised version of the Federal Information Processing Standard (FIPS) for POSIX which adopts the final IEEE (Institute of Electrical and Electronics Engineers) standard for portable operating system interface. Issued as FIPS 151-1, this version replaces an earlier one based on an IEEE draft standard. POSIX defines the interface, or link, between applications and computer operating systems based on UNIX. NIST considers POSIX as the first step toward a more open software environment for federal agencies. FIPS 151-1 will be available from the National Technical Information Service, Springfield, VA 22161; telephone: 703/487-4600.

ASTM APPROVES NIST TEST AS A NEW FIRE STANDARD

A new way to predict flame spread over a material, developed by researchers at NIST, has been approved as a standard from the American Society for Testing and Materials. Flame spread is a key factor in predicting the growth of a fire. Current tests measure flammability—how far and how fast a flame will spread over a particular material—and then rank the material with others. But, these results are arbitrary and, in some cases, differ from one test to another. The NIST method determines the basic physical properties of a material that enable it to ignite and spread the flames. They include ignition temperature, thermal properties (the ease in which a material heats up), and the minimum temperature of the material needed to allow the flame to spread. These properties can be used in mathematical or computer models to predict the behavior of many materials, including a composite or one which has additives, over a wide range of fire conditions.

Calibration Services

LOW-BACKGROUND INFRARED (LBIR) CALIBRATION FACILITY

NIST recently completed the construction of the LBIR facility. The first calibration of a low-background blackbody has been completed, and a second one has been started. The facility uses an absolute cryogenic radiometer as a fundamental radiometric standard with which to calibrate the temperature and radiant output of blackbody sources. The sensitivity of the detector is at the nanowatt level with flat response to approximately 50 μm. The blackbody and the radiometer are contained in a cryogenically cooled vacuum chamber, which is maintained at about 20 K while it is being operated. This allows low power sources to be calibrated.

Development programs are under way to provide more sensitive detectors for these calibration endeavors and to develop spectral capability for the facility. The spectral capability would be used to fully characterize blackbody sources as well as to allow scientists to characterize the spectral response of detectors.

The facility is available for calibration or research activities on a scheduled basis.

Standard Reference Materials

STANDARD REFERENCE MATERIAL 1804—EIGHTEEN TOXIC VOLATILE ORGANIC COMPOUNDS IN NITROGEN

NIST announced the availability of SRM 1804 intended for the calibration of instruments used for the determination of toxic volatile organic compounds (VOCs) in stationary source emissions. SRM 1804 is a mixture of 18 toxic VOCs, collectively designated as EPA Group 5, in a nitrogen matrix. It should be useful for providing quality assurance and accuracy to measurements of VOCs in air monitoring and research programs and for the development and evaluation of methods used for such measurements.

This SRM was developed through joint support of NIST and the Atmospheric Research and Exposure Assessment Laboratory of the U.S. Environmental Protection Agency in Research Triangle Park (EPA/AREAL/RTP), North Carolina.

SRM 1804 is supplied in an aluminum cylinder with a pressure of 12.4 MPa (1800 psi) with a deliverable volume of 3.6 m^3 (127 ft^3) at normal temperature and pressure. The cylinder conforms to DOT specifications and is equipped with a stainless steel CGA-350 packless valve.

NEW BROCHURES FOR SEMICONDUCTOR AND COATING SRMS

Two new NIST brochures offer quick access to special listings of important standard reference materials (SRMs) for the producers of semiconductors and the manufacturers of coated metal materials. Standard Reference Materials for Semiconductor Manufacturing Technology lists a series of SRMs for use in characterizing semiconductor materials and processes. The SRMs include a series of silicon resistivity materials for calibrating four-probe and eddy-current test equipment, sizing materials for calibrating optical and scanning electron microscopes, SRMs for mechanical testing, optical measurements, x-ray and photographic films, x-ray diffraction, and the chemical analysis of materials. Standard Reference Materials for Coating Thickness Materials contains a listing of SRMs for calibrating various coating thickness gages. There are materials for calibrating non-magnetic coating on magnetic substrate—copper and chromium on steel, magnetic coating on magnetic substrate—nickel on steel, gold coating on glass sealing alloy, gold coating on nickel, and solder coating on copper. Copies of the new SRM brochures are available from the Standard Reference Materials Program, Rm. 204 Bldg. 202, NIST, Gaithersburg, MD 20899; telephone: 301/975-OSRM (6776).

NIST ANNOUNCES NEW RADIOCHROMIC DYE STANDARD

Standard Reference Material (SRM) 4500 is a new calibration standard for the radiation processing industry. Based on research at NIST, radiochromic dyes change color—blue in this case—when irradiated, and the color intensity increases linearly with radiation dose. They can be used for standardizing measurements of absorbed dose in many radiation processing applications, such as sterilizing medical devices, curing polymer and elastomer materials, testing electronics, and for extending the shelf-life of foods. SRM 4500 consists of a set of flame-sealed amber glass ampoules, each containing 5 mL of solution of a radiochromic dye. These standards are for calibrating cobalt-60 and cesium-137 sources of gamma radiation for absorbed dose in the range from 50 Gy to 5 kGy (5–500 krad). SRM 4500 is available for $698 from the Office of Standard Reference Materials, Rm. 204 Bldg. 202, NIST, Gaithersburg, MD 20899; telephone: 301/975-6776, FAX: 301/948-3730.

1990-91 SRM CATALOG PUBLISHED

The NIST Standard Reference Materials Catalog 1990-91 (SP 260) lists approximately 1,100 standard reference materials (SRMs) available from the institute. Materials certified for their chemical and physical properties include cements, ores, metals, glass, plastics, food, and environmental standards. Also certified are nutrition and clinical health standards to calibrate instruments that measure marijuana and cholesterol in human urine and serum, fat-soluble vitamins and cholesterol in food products, and levels of the enzyme aspartate aminotransferase (AST) to detect heart attacks. New materials listed include polyethylene samples for evaluating the performance of plastic gas pipe, a reference material for calibrating non-destructive evaluation systems to detect fatigue cracks and flaws, and sets of low-energy and high-energy test blocks for calibrating Charpy V-notch impact machines. The catalog contains an alphabetical index and a complete numerical listing of the latest renewal SRMs and their certificate dates. Prices for the SRMs are published separately in annual supplements. Copies of SP 260 are available from the Office of Standard Reference Materials, Rm. 204 Bldg. 202, NIST, Gaithersburg, MD 20899; telephone: 301/975-6776.

Standard Reference Data

STANDARD REFERENCE DATA DIRECTORY UPDATED

The Standard Reference Data Program, which evaluates data on the physical and chemical properties of substances, is an important part of NIST's measurement services program for science and industry. Standard Reference Data Publications 1987-1989 (SP 708, Supplement 2) updates the 1964-1984 directory of publications and computerized databases prepared through the National Standard Reference Data System (NSRDS), established in 1963. The supplement contains new information on reprints and supplements from the Journal of Physical and Chemical Reference Data, other NSRDS data compilations, critical bibliographies and indexes from other publishers, and databases available in printed form, on magnetic tape, disks, and through on-line computer networks. Author, materials, and property indexes, as well as ordering information and price lists, are included. To obtain a copy of SP 708, Supplement 2, send a self-addressed mailing label to: Standard Reference Data Program, A323 Physics Bldg., NIST, Gaithersburg, MD 20899; telephone: 301/975-2208.

NEW ION THERMOCHEMISTRY DATABASE AVAILABLE FOR PCs

A new computerized database package with thermodynamic information on the positive and negative ions in the gas phase has been developed by NIST. Designed for personal computers (PCs), NIST Standard Reference Database 19A and 19B, Positive and Negative Ion Energetics, provides rapid access to important information on charged atoms and molecules. Evaluated data on the thermochemistry of positive ions and negative ions are presented separately in the database package, each with its own software and documentation. Database 19A, Positive Ion Energetics, contains approximately 5,000 values for ionization energies of molecules and radicals, along with enthalpies or heats of formation of the corresponding neutral species and ions. Values for proton affinities of about 1,000 molecules also are provided. Database 19B, Negative Ion Energetics, includes data on electron affinities and gas phase acidities of molecules, and enthalpies of the molecules and corresponding ions. Data on about 2,000 species are given. The NIST ion energetics database package is available for $130 from the Office of Standard Reference Data Programs, A323 Physics Bldg., NIST, Gaithersburg, MD 20899; telephone: 301/975-2208.

NEW PC DATA FILE ON ATOMIC RADIATION ANNOUNCED

Space scientists, astrophysicists, combustion and fusion engineers, designers of laser systems, and plasma scientists and modelers now have a new reference that can be stored on personal computers (PCs) for analyzing the properties of plasmas and the performance of hot gaseous systems. NIST Standard Reference Database 24, Atomic Transition Probabilities Data File, Scandium Through Nickel, contains numerical data on eight iron-group elements—atomic numbers 21 to 28—that were published in Supplements 3 and 4 to Volume 17 (1988) of the Journal of Physical and Chemical Reference Data. The iron-group elements are of particular interest to space scientists who use atomic spectroscopy techniques to determine the temperatures of stars. The database contains two types of files: numerical files, or tables containing atomic transition probabilities and spectral identification data; and files of references pertaining to the numeric tables. The data file is available for $125 from the Office of Standard Reference Data Programs, A323 Physics Bldg., NIST, Gaithersburg, MD 20899; telephone: 301/975-2208.

Calendar

August 6-9, 1990

NORTH AMERICAN ISDN USERS' FORUM (NIU-FORUM)

Location: National Institute of
Standards and Technology
Gaithersburg, MD

Integrated Services Digital Network (ISDN) is a telecommunications technology which can be used to send and receive voice, data, and pictures simultaneously over digital telephone lines. However, there is work to be done before this technology develops. User-defined applications, implementation agreements for the existing standards, and tests are needed to allow for a transparent, ubiquitous, and user-driven ISDN. NIST has formed with private industry (both manufacturing and prospective users of ISDN technology) a new organization to find ways to promote the implementation of ISDN standards in interoperable products and services, and to identify potential ISDN applications. This is the North American ISDN Users' Forum (NIU-Forum). This meeting of the forum will begin with one day of tutorials on August 6. The tutorials will focus on facsimile, imaging, optical disk, multimedia, optical character recognition, ISDN audiodata teleconferencing, satellites and ISDN, and an introduction to the NIU-Forum. The forum, held August 6-9, will consist of joint workshops for the users and implementors. The users' workshops will continue to identify, define and prioritize user applications of ISDN. The implementors' workshops will continue defining implementation agreements for ISDN. Working group meetings will discuss issues related to the use and implementation of ISDN technology. Manufacturers and service providers are invited to participate in this workshop. For registration information, please call Lori Phillips on (301) 975-3881.

Contact: Dawn Hoffman, B364 Materials Building, NIST, Gaithersburg, MD 20899, 301/975-2937.

August 17–22, 1990

INTERNATIONAL CONFERENCE ON THE CHEMISTRY OF ELECTRONIC CERAMIC MATERIALS

Location: Sojourner Inn, Teton Village
Jackson, WY

Materials chemistry has evolved from the more identifiable disciplines of inorganic and solid state chemistry, ceramics, and materials science. It is inherently interdisciplinary, attracting scientists from many different backgrounds, such as materials science, physical, inorganic, and organo-metallic chemistry, physics, ceramics, and mineralogy. This conference will bring together major national and international researchers to bridge the gap between those primarily interested in the pure chemistry of inorganic solids and those interested in the physical and electronic properties of ceramics. One of the primary goals of the conference will be to evaluate our current understanding of the chemistry of electronic ceramic materials and to assess the state of a field that has become one of the most important areas of advanced materials research. Tentative sessions will include: chemistry of dielectric ceramics; electrical, magnetic, and optical materials; chemical precursors and catalysts; crystal chemistry, new materials, and defects; high-T_c superconductors; and structure and chemical bonding. Sponsored by NIST, the Office of Naval Research, and NASA.

Contact: Robert Roth, B126 Materials Building, NIST, Gaithersburg, MD 20899, 301/975-6116.